# Impact dampers for structural dynamic control

Li, Kuinian

*Award date:*
2004

*Awarding institution:*
University of Bath

# IMPACT DAMPERS FOR STRUCTURAL DYNAMIC CONTROL

Kuinian Li

A thesis submitted for the degree of Doctor of Philosophy

University of Bath

Department of Architecture and Civil Engineering

October 2004



Kuinian Li





ProQuest LLC
789 East Eisenhower Parkway
P.O. Box 1346
Ann Arbor, MI 48106-1346

# CONTENTS

## Abstract

An impact damper consists of a freely moving mass constrained by stops attached to a structure to be controlled. During dynamic excitation collisions between the mass and the stops result in exchange of momentum and dissipation of energy, thus, reducing the dynamic response of the structure. Experimental and numerical studies on the interaction of an impact damper with primary structure have been carried out. An experimental investigation on a MDOF primary structure equipped with an impact damper showed the effectiveness of impact damper but also revealed the intrinsic shortcoming of a conventional impact damper, i.e. high contact force and associated high acceleration and noise caused by collision. To solve this problem and make impact dampers applicable in civil engineering, a new type of impact damper, a buffered impact damper (BID), has been developed and investigated. Experimental studies and numerical simulations have demonstrated that, compared with a conventional impact damper, a BID can not only significantly reduce the contact force and associated acceleration and noise caused by collision but also significantly enhance the vibration control effect. The controlling mechanism of a BID is investigated and a method for the design of the buffer of a BID is developed to make a BID easy to use in engineering practice. The interaction of an impact damper with a primary structure is modelled using a spring-damper model of the impact surface. A novel method is developed to determine the parameters of the spring and damper making use of the experimentally measured contact time and coefficient of restitution of an impact. A high precision direct integration scheme for non-linear systems has also been developed for numerical simulation. The advantage of the spring-damper model over the conventional impulse momentum model of impact is demonstrated by comparison of numerical simulations with experimental results. The accuracy and effectiveness of the algorithm and simulation is also verified.

## Acknowledgements

I wish to express my gratitude to my supervisor, Dr A. P. Darby, for his sustained encouragement and guidance throughout the duration of this project. It was his experience and inspiration that kept the research going.

I would also like to thank the EPSRC who provided the financial funding for running this research.

Thanks are given to Mr Brian Purnell who helped with the construction of the shaking table and the manufacturing of the test structures.

Thanks are also given to Mr Brian Smith who did the proofreading of the thesis and helped with the grammatical checking and wording.

Finally, I would like to thank my wife, my son and my parents for their understanding and encouragement.

## Notation

### Chapter 1

| | |
|---|---|
| $c_r$ | coefficient of restitution |
| $d$ | clearance of impact damper |
| $m$ | impact damper mass |
| $\mu$ | mass ratio |
| $\varsigma$ | damping ratio |

### Chapter 2

| | |
|---|---|
| $c_b$ | damping of the damper of the spring-damper model |
| $k_b$ | stiffness of the spring of the spring-damper model |
| $r$ | frequency ration |
| $T_c$ | contact time of impact |
| $x$ | time varying displacement in Cartesian co-ordinates |
| $\dot{x}$ | 1st time derivative of $x$ |
| $\ddot{x}$ | 2nd time derivative of $x$ |
| $x_g$ | displacement of ground (base) |
| $\ddot{x}_g$ | acceleration of ground (base) |
| $y$ | relative displacement |
| $\dot{y}$ | 1st time derivative of $y$ |
| $\ddot{y}$ | 2nd time derivative of $y$ |
| $\mathbf{C}$ | damping matrix |
| $\mathbf{f}$ | excitation force vector |
| $\mathbf{K}$ | stiffness matrix |
| $\mathbf{M}$ | mass matrix |
| $\mathbf{x}$ | vector of displacement |
| $\dot{\mathbf{x}}$ | 1st time derivative of $\mathbf{x}$ |
| $\ddot{\mathbf{x}}$ | 2nd time derivative of $\mathbf{x}$ |
| $\mathbf{y}$ | vector of relative displacement |
| $\dot{\mathbf{y}}$ | 1st time derivative of $\mathbf{y}$ |
| $\ddot{\mathbf{y}}$ | 2nd time derivative of $\mathbf{y}$ |

**Chapter 3**

| | |
|---|---|
| $\mathbf{x}_0$ | initial displacement vector |
| $\dot{\mathbf{x}}_0$ | initial velocity vector |
| $\tau$ | time-step of integration |

**Chapter 4**

| | |
|---|---|
| $e$ | error between $Y$ and $Y_{ref}$ |
| $K_d$ | gain of derivative controller |
| $K_i$ | gain of integral controller |
| $K_p$ | gain of proportional controller |
| $T_s$ | period of sampling |
| $u$ | output signal of controller |
| $Y$ | measured output signal |
| $Y_{ref}$ | reference signal |

**Chapter 6**

| | |
|---|---|
| $f_c$ | contact force |
| $F_m$ | maximum contact force |
| $I$ | impulse momentum |

**Chapter 7**

| | |
|---|---|
| $T_0$ | total time of simulation |

## Abbreviations

| | |
|---|---|
| DOF(s) | degree(s) of freedom |
| SDOF | single degree of freedom |
| MDOF | multi-degree of freedom |
| TMD | tuned mass damper |
| Eq | equation |
| HPD | high precision direct integration |
| Kutta 4 | $4^{th}$ order Runge-Kutta explicit algorithm |
| HPD-L | high precision direct integration with linear approximation of loading |
| HPD-C | high precision direct integration with cubic approximation of loading |
| HPD-NL | high precision direct integration for non-linear system |
| PID | proportional-integral-derivative |
| PSD | power spectral density |
| BID | buffered impact damper |
| IMM | impulse momentum model of impact |
| SDM | spring-damper model of impact |
| SUIT | single-unit impact damper |
| TUID | twin-unit impact damper |
| MUID | multi-unit impact damper |
| TPMD | tuned pendulum mass damper |
| HPID | hybrid pendulum impact damper |

## List of Figures

### Chapter 1



### Chapter2



### Chapter 3

**Chapter 4**

**Chapter 5**

**Chapter 6**

**Chapter 7**

**Chapter 8**

**Chapter 9**

## List of Tables

# Chapter 1

# Introduction

The built environment is inevitably subject to environmental disturbances, such as wind and earthquakes. As civil engineering structures become taller or span further, the need to control their dynamic response with respect to both wind induced disturbances and earthquake ground motions becomes more and more important. To protect structures, the traditional approach to seismic design is to resist the imposed dynamic load by providing a combination of strength and ductility. In many ways this traditional approach views the transient dynamic disturbance as an equivalent static lateral load that must be resisted by the structure itself. By discarding this notion and considering the actual dynamic characteristics of environmental disturbance, many new and innovative concepts of structural protection have been advanced and are at various stages of development.

## 1.1 Motivation of research

According to different approaches employed to manage the energy associated with transient environmental events, modern structural protective systems can be divided into three groups, as shown in table 1.1.

Table 1.1: Structural Protective Systems

| Seismic Isolation | Passive Control | Semi-active/Active Control |
|---|---|---|
| Lead Rubber Bearings | Visco-elastic Dampers | Active bracing System |
| Sliding Friction Pendulum | Tuned Mass Dampers | Variable Stiffness/Damping |
| bearings | Tuned Liquid Dampers | Smart Materials |
| | Metallic dampers | |
| | Friction dampers | |

Seismic isolation has been widely applied in practice in many parts of the world [1] [2]. A seismic isolation system is an isolation layer placed at the foundation of a structure. It

can partially reflect and partially absorb the earthquake energy before this energy can be transmitted to the structure, which leads to a reduction of energy dissipation demanded by the structural system itself. It is clear, however, that seismic isolation can only be easily used in newly built structures and is only applicable against earthquakes, not wind loading.

At the other end of the spectrum as shown in Table 1.1 are semi-active and active control systems. The motion of the structure is controlled by action of these systems using some external energy source. They can be used for the alleviation of both wind and seismic response of the structure. Considerable attention has been paid to theoretical and practical aspects of semi-active and active control of structures. However, unlike in mechanical systems, it is rarely applied in civil engineering practice, due to the fact that an external energy supply is required and because they tend to be mechanically complex. The most important thing for all structural protective systems is that they can respond reliably and as expected whenever a random environmental disturbance, such as an earthquake, occurs during the whole service life of the structure.

The basic function of a passive control device when incorporated into a structure is to absorb a portion of the input energy, thereby reducing energy dissipation demand on the primary structure and minimizing possible structural damage. Unlike a seismic isolation system, however, these devices can be effective against wind-induced motion as well as those due to earthquakes. Moreover, passive energy dissipation devices can be used not only in new buildings but in retrofitting of existing buildings also. They may also be easy to set, maintain, repair and alter. Contrary to semi-active or active control systems, passive energy dissipation devices have no need for an external power source. All these characteristics make them attractive to civil engineering application.

Great efforts have been undertaken to develop the concept of energy dissipation into a workable technology, and many such devices have been installed in structures throughout the world. Passive energy dissipation devices reduce the dynamic response of a structure by either dissipating energy, e.g., by using plasticity of metal components [3], friction properties [4], viscous fluids (e.g., a dashpot) [5] or by altering the frequency response of the structure, e.g., by adding a tuned mass damper [6] to move the resonant frequency of the primary system away from the excitation frequency.

Tuned mass dampers (TMD) were first applied in mechanical engineering systems in which an operating frequency is in resonance with a machine's fundamental frequency. Building structures, however, are subjected to environmental loads, such as winds and earthquakes, which possess many frequency components. Hence, modes other than the fundamental mode of the structure can be excited to a high degree, which can not be reduced effectively by an optimally tuned damper. Although TMD can be effective on not just one frequency but over a narrow bandwidth by introducing damping, for example, the intrinsic limitation of TMD can not be eliminated unless a servomechanism is added to form an active TMD. To solve this problem, multiple tuned dampers and non-linear strategies (e.g., the use of cubic stiffness springs) have been investigated [7]. However, the problem associated with achieving damping over a large frequency range is still there. The vibration control effectiveness of TMD, especially for seismic application is still controversial [8].

One method of achieving high levels of damping over a wide frequency range is the use of an impact vibration damper. Although it has received little attention from structural engineers, impact dampers have been used to reduce vibrations in machinery by mechanical engineers for a number of years [9]. Impact dampers are variants on the commonly used tuned mass damper. However, rather than being connected to the primary structure via a spring or damping mechanism, the damper mass of an impact damper is allowed to move freely, in a constrained manner, so that on impact with stops attached to the primary structure momentum is exchanged and energy dissipated as much higher frequency components and as noise and heat. Such a damping system is shown diagrammatically in Figure 1.1.

The advantages of impact dampers lie in the unique feature that its motion is synchronised to the excitation frequency, and maximum reduction in dynamic response can be achieved over a large frequency range, not just near resonance [10]. This point is emphasised by Sadek [11], who recommended the use of impact dampers for machine tool applications. The drawback with impact dampers is that large accelerations are applied to the structure under control at the moment of impact. This could be less of an issue for controlling the response of a structure under earthquake loading since the duration of an earthquake is short and occupancy comfort can be sacrificed in favour of

maintaining structural integrity and reducing costly structural damage. However, this is an important issue particularly if the impact damper is to be used to reduce the effect of wind-induced disturbances, since occupancy comfort must be maintained and damage to contents must be negligible.

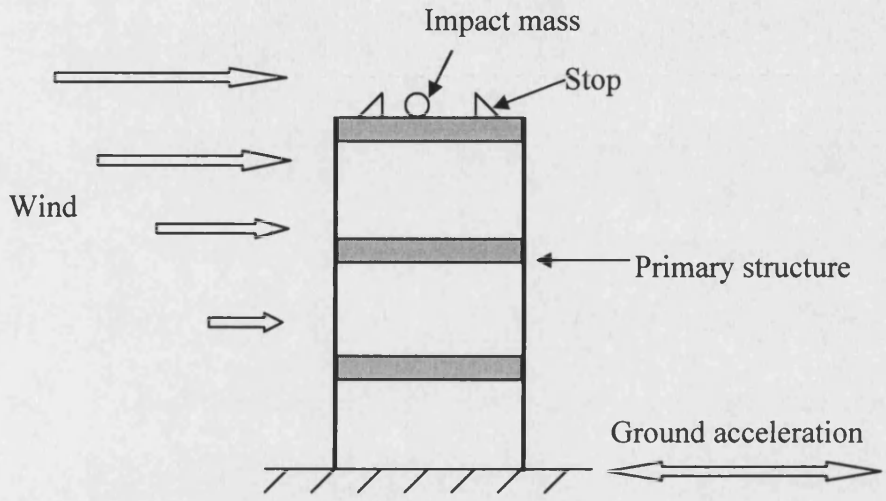


Figure 1.1: Structure equipped with impact damper subject to dynamic loading

The motivating factors to initiate research in the subject of impact dampers for structural protection are:

- stringent requirements for effective and reliable passive control devices for structural protection
- the limitations associated with the structural protection systems currently available
- the successful application of impact dampers in mechanical engineering and the need to further understand the mechanics of impact dampers to advance this dynamic control method and make it accessible to the civil engineering community.

## 1.2 Theory of impact dampers

The first publication on the theory of impact dampers was that by Lieber and Jensen [12], who considered only perfect plastic impact between the impact mass and primary structure. Ten years later Grubin [13] introduced the coefficient of restitution to

describe the impact between the damper mass and the stops and developed a theoretical analysis of forced vibration of a single-degree-of-freedom (SDOF) system fitted with an impact damper. The theory was based on the assumption of steady state motion with two equispaced impacts per cycle. Arnold [14] presented a theoretical and experimental investigation of the same problem based on similar assumptions except that damping of the main system was not included. By replacing the impact force with a Fourier series and introducing a phase angle into the expression for the excitation force, tedious numerical calculations were avoided. However, appreciable discrepancies between theoretical and experimental results were noted. Warburton [15] further simplified the analysis by avoiding the use of Fourier series but including the use of an unknown phase angle.

Theoretical analysis up to that time had been confined to the case of an impact damper attached to a SDOF primary system subjected to sinusoidal excitation, as shown in Figure 1.2

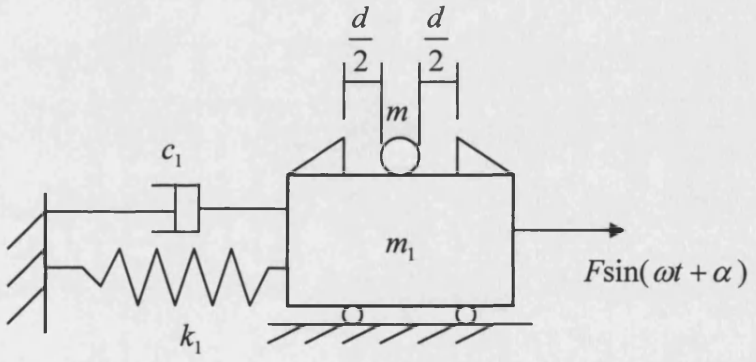


Figure 1.2: Harmonically excited SDOF system with impact damper

The equation of motion of the primary system between impacts is:

$$m_1\ddot{x} + c_1\dot{x} + k_1 x = F\sin(\omega t + \alpha) \tag{1.1}$$

A closed form solution of Eq(1.1) was derived on the assumption of steady state motion with two equispaced impacts per cycle. Subsequent analysis of the same problem is given by Masri and Caughey [16] for a damped oscillator and by Egle [17] for an undamped oscillator, with stability analysis presented in both cases.

After careful experimentation, Sadek [18] found that equally spaced impacts hardly ever occur even away from resonance. Masri [19] attempted an extension to unevenly spaced impacts but maintaining the assumption of two impacts per loading cycle. Popplewell and Bapat[20] elaborated on Masri's work and proposed an algorithm for the computation of stable periodic motions involving any number of impacts. Supposing that $N$ impacts happen in a loading period, the time $t_i$ $(i=1,2,...N)$ at which the $i^{th}$ impact happens is taken as unknown. A group of linear equations can be formed and solved so that the displacement response of the main mass in a loading period is obtained. Bapat [21] further applied this method to study the general motion of an inclined impact damper with friction, as shown in Figure 1.3. In a similar vein, Xu Zhiwei [22] developed a simulation of a vertical impact damper system, as shown in Figure 1.4.

Thomas [23] extended the work of Sadek [18] to the case where the impacting mass is coupled to the main system by means of a linear spring, as shown in Figure 1.5. Strictly speaking, it is a tuned mass damper with position-limiting stops, although impacts could happen between the damper mass and the stop.

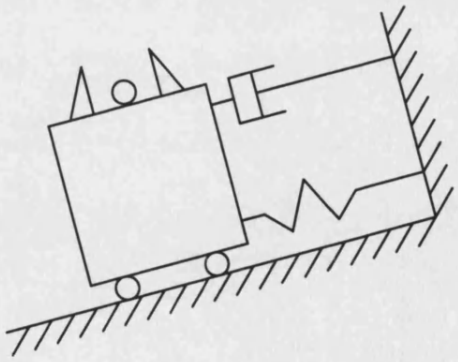

Figure 1.3: Inclined impact damper

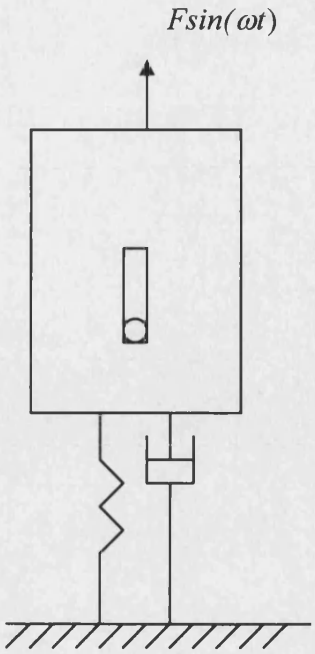


Figure 1.4: Model of vertical Impact damper System

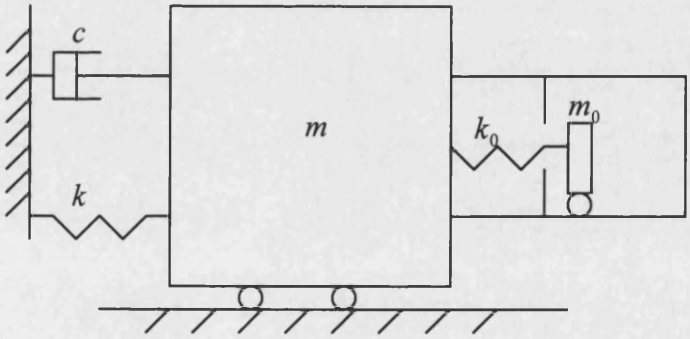


Figure 1.5: Impact damper with a spring supported auxiliary mass

Bapat [24] developed non-linear equations governing $N$ impacts per cycle of a SDOF oscillator under a sinusoidal and bias force. The coefficient of restitution can be constant or velocity dependent.

As an extension of a single unit impact damper, multi-unit impact dampers, as shown in Figure 1.6, have been studied theoretically and numerically by Bapat [25]. Multi-unit impact dampers have the advantage that they can reduce the velocity discontinuity of the primary system significantly, which means the high acceleration or contact force occurring at the moments of collision of single unit impact damper can be reduced with

an multi-unit impact damper. The study also revealed that in periodic motion with identical units, impacts occur in clusters and are not uniformly distributed in time.

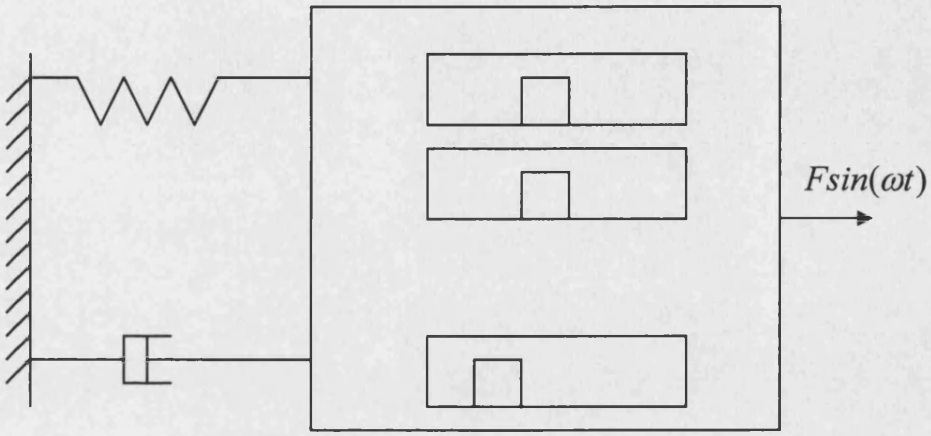


Figure 1.6: Model of Multi-unit Impact Damper

Nigm *et al.* [26] extended the theoretical analysis of the steady state vibrational motion to multi-degree-of-freedom (MDOF) systems equipped with an impact damper, based on the assumption that two generally distributed impacts occur in each cycle. The model is as shown in Figure 1.7.

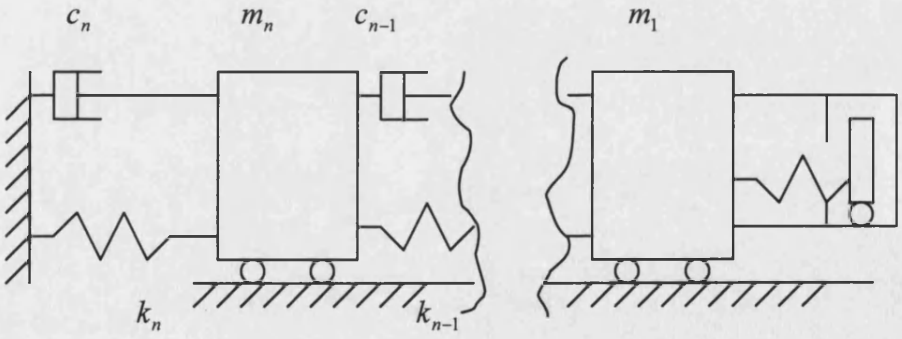


Figure 1.7: Impact damper attached to a MDOF system

Between the impacts the system was treated as linear and modelled as:

$$\mathbf{M}\ddot{\mathbf{X}} + \mathbf{C}\dot{\mathbf{X}} + \mathbf{K}\mathbf{X} = \mathbf{F}\cos(\omega t + \alpha) \tag{1.2}$$

Besides the great deal of work done on sinusoidal excitation, Masri [27] performed numerical simulations on the response of impact dampers to stationary random excitation and found that an impact damper is effective in reducing the vibration amplitude levels resulting from random excitation. Aoki S., *et al.* [28] studied the effect of impact dampers with hysteretic damping subject to earthquake excitation. An analytical method for the random response of the primary system with impact dampers is proposed. The energy loss and duration of each collision was dealt with by introducing the hysteretic characteristic.

Ma [29] performed numerical simulation of MDOF systems, equipped with an impact damper, under random excitation, by using a standard fourth order Runge-Kutta finite difference scheme to integrate the equations of motion between impacts. A very small time step was taken to accurately time collision events.

### 1.3 Modelling of impact dynamics

Both Eq(1.1) for SDOF primary structures and Eq(1.2) for MDOF primary structures are valid only between impacts. To model a structure equipped with an impact damper, modelling of the impact process is required and it is the key to the modelling of such a system. The impulse momentum model, or coefficient of restitution model as it is sometimes called, has been employed in most investigations on impact dampers up to now. The impulse momentum model stems from rigid body dynamics so it does not consider elastic deformation during the process of impact. The primary assumption on which this model is based is that the colliding bodies are perfectly rigid; consequently, the duration of impact must be zero, or instantaneous, and, therefore, the contact time of impact cannot be taken into consideration.

Two limit cases are considered in the elementary studies of impact modelling: a perfectly elastic impact and a perfectly inelastic impact. The former case implies that the kinetic energy of the system is conserved. The latter case assumes that the two colliding bodies coalesce, to move as a single mass, after impact. The velocity of the combined mass can then be predicted using only the conservation of momentum. In the first publication on the theory of impact dampers [12], the collision of the damper mass with the stops was modelled by perfectly inelastic impact. Most impacts in practice are neither perfectly elastic nor fully inelastic. The coefficient of restitution was introduced

to express the partial loss of the initial kinetic energy. The coefficient of restitution is a dimensionless coefficient between *0* and *1*, where *0* corresponds to a fully inelastic impact and *1* to a perfectly elastic impact. It is a global measure of the energy loss during impact and may incorporate different forms of dissipation such as viscoelastic work performed on the materials of the impacting bodies, plastic deformation of contact surfaces and vibration in the two bodies. The coefficient of restitution is not an intrinsic material property. It depends on the materials of the impacting bodies, their surface geometry and the impact velocity [30]. The impulse momentum model governs the impact process with the law of conservation of momentum plus the relation of the velocities before and after the impact, which is given by the coefficient of restitution. The major advantage of this model lies in its mathematical simplicity and it can lead to a reasonable approximation for impact behaviour occurring between hard metal objects, where the elastic deformation and contact time is very small. However, if the collisions happen not between two hard metal objects and, therefore, both elastic deformation during impact and the contact time are not negligible, this model will fail, since the assumptions upon which the model is formed are not met. It is worth pointing out that this problem cannot be solved by measures such as making the coefficient of restitution a function of velocity, rather than constant.

Two other possible methods for modelling impacts macroscopically, where the post-impact motion of the impact bodies is of primary concern, are the elastic model and the spring-damper model [31] respectively. Unlike the rigid body impulse momentum model, which is limited by an assumption of point contact, the elastic model is based on a finite area of contact [32]. This model is limited to treating only collisions between spherical-like objects. Moreover, in the elastic model of impact, all normal impact is assumed to be perfectly elastic, giving a coefficient of restitution of unity. Another assumption of this model is that materials of the impact bodies are similar and behave in a linear elastic manner. All these assumptions make the elastic model problematic in the modelling of an impact damper.

The spring-damper model has been developed by conceptualising the actual process of impact in a simple way. In the spring-damper model, the impact is modelled as the compression of a spring acting between the two impact bodies and perpendicular to the plane of impact [33] [31]. The energy loss that occurs during impact can be modelled

with a damper placed in parallel with the spring. The spring-damper model results from conceptual reasoning rather than the physical impact process. It is easy to understand. Additionally, the limitations of the elastic model or impulse momentum model are inherently removed and the actual behaviour can be accurately modelled given appropriate model parameters. However, finding the parameters *a priori* is a difficult task [31], since they do not correspond directly to material properties, which makes the spring-damper model problematic to implement even though it appears attractive. Therefore, in order to use this technique, a method for finding the parameters of the model must be developed.

### 1.4 Stability of systems with impact dampers

In the investigation of the dynamic behaviour of systems equipped with impact dampers, the stability of such systems is an important aspect to deal with. A simple stability criterion was developed by Egle [17] for the case of a sinusoidally excited SDOF primary structure equipped with an impact damper, as shown in Figure 1.2. The dependence of the stability boundaries on the parameters of the impact damper was shown such that the stability criterion is given by:

$$\frac{-AB \pm A^2(A^2+1-B^2)^{1/2}}{AB \pm (A^2+1-B)^{1/2}} > 0 \tag{1.3}$$

Here: $A = \frac{\pi}{2}(1+\mu)^{-1}(1+c_r)(1-c_r)^{-1}[1+(2\mu r/\pi)\tan(\pi/2r)]$

$$B = \frac{1}{2}(d/x_{st})(1-r^2),\ r = \frac{\omega}{\omega_1},\ \mu = \frac{m}{m_1},\ x_{st} = \frac{F}{k_1},\ \omega_1 = \sqrt{\frac{k_1}{m_1}}$$

where $c_r$ is the coefficient of restitution and the other parameters as defined in Figure 1.2.

Masri [34] developed an analytical solution for single unit and multi-unit impact dampers and applied the concept of error propagation in the difference equation to ascertain whether or not these periodic motions were asymptotically stable. The stability

boundaries were presented in terms of the coefficient of restitution and clearance parameters. Bapat C.N., *et al.* [35] extended Masri's work in studying the stability of the periodic motions, including symmetric and un-symmetric motions.

Instead of using the method of error propagation exploited by many investigators, Dowell, *et al* [36] and Shaw S. W., *et al.* [37] exploit the Poincaré map and bifurcation theory to study stability. The existence and stability of sub-harmonic motions and non-linear phenomena, such as cascades of period-doubling bifurcation and the existence of chaotic motion, were found.

Whiston [38] analysed the vibro-impacting response of a one-dimensional linear oscillator under harmonic excitation. The model used is a SDOF system in which the motion of the damper mass is studied while the motion of the primary mass is subjected to harmonic excitation. Sung, *et al.* [39] used a two-degree-of-freedom model to analyse the dynamic behaviour, observing the bifurcation phenomena by using a Poincaré map.

Peterka [40][41] evaluated the motion of a harmonically excited SDOF primary structure equipped with an impact damper by numerical simulation. Periodic, quasiperiodic and chaotic impact motions are explained by time series, phase trajectories, bifurcation diagrams and Poincaré map.

It should be pointed out that all the studies published are on the stability of a sinusoidally excited SDOF primary structure equipped with an impact damper. The stability of a MDOF primary structure equipped with an impact damper has not been investigated due to its mathematical complexity, especially when the structure undergoes excitation other than sinusoidal excitation.

### 1.5 Experimental studies

Many experimental studies on impact dampers have been carried out for testing specific practical applications or for checking theoretical/analytical results. Thomas *et al.* [42] tested a single unit impact damper used to improve the chatter performance of a cantilever boring bar during a machining process. The research showed that the impact damper could improve the chatter performance of the boring bar and that the impact damper was not sensitive to the excitation frequency. Hong *et al.* [43] experimentally studied a single unit impact damper used to mitigate the oscillation of an industrial

robot manipulator. It demonstrated the effectiveness of the impact damper in reducing vibrations of a flexible arm by up to 95%. Jo *et al.* [44] studied multi-unit impact dampers for reducing vortex-induced vibrations of highway light poles. In their study, the researchers determined that increasing the mass ratio increased damping. It was found that the arm of the light pole undergoes greater flexural vibration in-plane than out-of-plane. Consequently, providing additional in-plane damping was more difficult.

The behaviour of a multi-unit impact damper, subject to harmonic excitation, was also studied experimentally by Masri, *et al.* [45]. The experiments showed that, compared with a single impact damper, the multi-unit impact damper reduced noise and local damage to the structure and improved effectiveness.

Ekwaro-Osire *et al.* [46] carried out experimental studies on an impact damper for both free and forced vibration. For free vibrations, the effect of system parameters on the rate of decay of vibration was shown. Constant frequency and frequency sweep experiments were conducted to study the dynamics of the system under forced vibration. The effects of mass ratio, clearance and excitation amplitude on system dynamics and impact damper effectiveness were investigated.

A study of a hybrid impact damper, as shown in Figure 1.8, was conducted by Collette [47]. The effectiveness of combing a tuned mass damper with a single unit impact damper (a pendulum impact damper to be exact) applied to a three-storey building model under random excitation was investigated. The sensitivity of its effectiveness to variation of clearance, coefficient of restitution, and mass ratio were studied. The results show that it seems to be a cheap alternative to the tuned mass damper. However, as the author pointed out, its practical use may be limited by the geometric requirement to suspend the impact damper in the tuned mass damper. One interesting point that this research demonstrated is that the introduction of the impact damper reduces the effectiveness of the optimal TMD.

Semercigil *et al.* [48] also carried out experiments with a tuned mass damper/impact damper combination. The excitation applied on the primary system was provided by striking it with a pendulum released at a predetermined distance. Experiments on a SDOF primary system and a 2 DOF primary system were carried out. The emphasis was on the control effect of the impact damper on the response of a secondary tuned mass damper system. In addition, the control effect of the TMD on the primary system was

also observed. However, the control effect of the impact damper on the primary system was negligible for the 2-DOF systems.

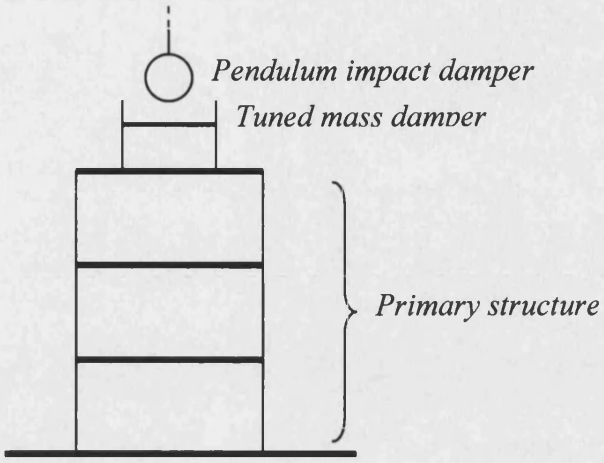


Figure 1.8: A combined tuned absorber and pendulum impact damper

To apply impact dampers for civil engineering, model tests and modifications of impact dampers have been carried out to minimize the large accelerations which are applied to the primary structure at the moment of impact. Popplewell, *et al.* [49] studied the performance of a resilient bean bag damper, as shown in Figure 1.9, for sinusoidal excitation. The research showed that, compared with a single mass impact damper the bean bag damper is not only a better attenuator of the resonant displacement of a lightly damped oscillator but the contact forces and the noise generated by collision are also reduced.

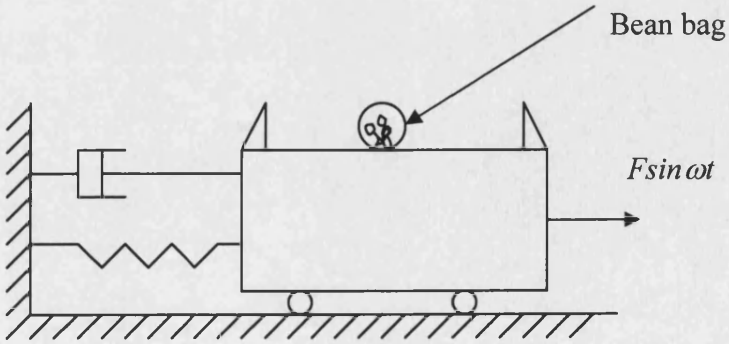


Figure 1.9: Bean bag impact damper

Araki *et al.* [50] used a bed of granular material as an impactor in a SDOF system subjected to external sinusoidal excitation, as shown in Figure 1.10.

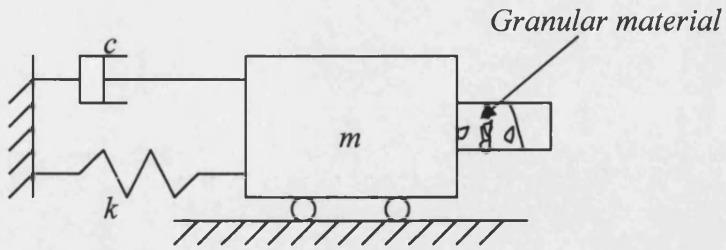


Figure 1.10: Impact damper with granular materials

The characteristics of the damper and the influence of some parameters on its performance were investigated experimentally. Papalou *et al.* [51] investigated the behaviour of a particle impact damper under wide band random excitation. The influence of the total auxiliary mass ratio, particle material type, particle size, container dimensions, intensity and direction of excitation were investigated. It is found that, by replacing the solid particle in the container of a single-mass impact damper by a number of particles of equal mass, significant improvements are achieved with respect to reduction of high noise levels and interface material deterioration. It also reveals that the level of excitation plays a very important role in such a damper, especially when smaller size particles are used. Tomlinson *et al.* [52] also studied the damping characteristics of particle dampers. This study clearly shows that the damping levels of a particle damper are dependent on the geometry of the device and the resulting motion of the particles arising from the level of the input excitation.

## 1.6 Practical applications in engineering

The study of impact dampers originated from its engineering application. The first publication describing a practical application of an impact damper was that by Paget [9], which was based upon a US patent granted in 1931. The impact damper was fitted into a turbine blade. Tests on individual blades fitted with an impact damper showed that the vibration energy of the blade was almost completely absorbed by the impact damper. The damping ratio of the damped blade was nearly two orders of magnitude greater than that of the blade without impact damper.

Impact dampers have also been widely used in metal cutting machines. The machining of metal is often accompanied by a vibration, usually known as "chatter", which is detrimental to the precision or smoothness of the machined surface. Erlikh [53] first fitted an impact damper inside a hollow boring bar to attenuate the vibration of the bar. The parameters of the impact damper, such as mass ratio and clearance, were found by trial and error. The control effect of the impact damper was reported as being significant.

Hanging-chain impact dampers [54] have been used on tall structures, such as masts and towers, to absorb wind-induced vibrations. Ogawa *et al.* [55] used a hybrid impact damper to reduce the wind-induced oscillations of a bridge pylon. The impact between the impact mass and the primary system was cushioned with neoprene rubber to prevent local damage.

Use of impact dampers in the above fields, such as mitigation of chatter vibration, still continues [56]. New fields of application, such as using impact dampers for control of dynamic drilling conditions [57], pile driving [58], percussive drilling [59] and ground moling [60] are being found.

### 1.7 Optimum design of impact damper

It is true that impact dampers have been applied to many dynamic engineering situations. However, they should perhaps be more popular considering that they are more effective than other vibration neutralizers [10]. There are, however, a number of obstacles to the widespread use of impact dampers in engineering applications. The performance of an impact damper, i.e. the vibration control effect of an impact damper, depends on many factors: the parameters of the impact damper itself, such as mass ratio and clearance; the dynamics of the primary structure to be controlled; the excitation, including its amplitude and frequency range (spectrum). Additionally, all these factors are interdependent. This makes the design of an impact damper theoretically very complicated and difficult. The lack of an easily applied and accurate optimal design method reduces the attraction of impact dampers and forms an obstacle to its widespread engineering application.

Despite the difficulty and complexity, efforts to develop a simple design method/procedure for an optimum impact damper have been ongoing. Warburton [14] studied the simplest case: a sinusoidally excited SDOF primary structure equipped with an impact damper, as shown in Figure 1.2. Making the assumption of two equispaced collisions every cycle of the periodic external force excitation, an analytical expression of the steady-state response was derived. By neglecting the damping of the primary system and looking only at the behaviour of the impact damper at resonance (letting the frequency ratio $r = \omega / \omega_1 = 1$) to simplify the analysis, a design relationship was derived as:

$$\frac{d}{x_{st}} = 1 + \frac{\pi^2}{4\mu} \tag{1.4}$$

where $x_{st} = F / k_1$, $d$ is the clearance and $\mu$ is the mass ratio.

This design relationship was confirmed by Sadek's experimental work [10] and by that of Dittrich [61].

For the same case, making the same assumptions and with the same intention to reduce resonant response but now taking the damping of the primary structure into consideration, Popplewell [62] provided a design relationship for the impact damper design as:

$$\frac{d}{x_{st}} = \frac{2\mu + \pi^2}{4\mu + 2\varsigma\pi(\frac{1 - c_r - 2\mu c_r}{1 + c_r})} \tag{1.5}$$

where $\varsigma$ is the damping ratio of the primary system and $c_r$ is coefficient of restitution.

Chatterjee [63] investigated the performance of an impact damper for controlling the vibration of a harmonically excited, hard Duffing's oscillator, as shown in Figure 1.11. A optimum design relationship based on the stable solution predicted by the harmonic balance method is given as:

$$\mu\Omega^2 d_0 = 1 \tag{1.6}$$

Here $\mu = \frac{m_1}{m}$, $\Omega = \frac{\omega}{\omega_0}$, $\omega_0 = \sqrt{(k_1 x_0^2 / m_1)}$, $x_0 = (F/k_1)^{1/3}$, $d_0 = \frac{d}{2x_0}$

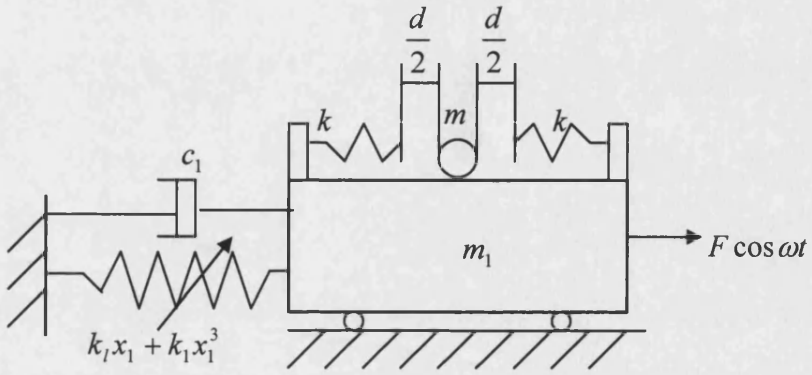


Figure 1.11: Duffing's oscillator equipped with impact damper

In this study the author modelled the elastic impacts with a linear spring $k$ and further modelled inelastic impact with a linear spring and viscous damping dashpot. However, the parameters of the spring appear to have been found by trial-and-error. The numerical simulation was carried out by arbitrarily supposing $k = 2000k_1$. In another later study Chatterjee [64] pointed out with a very high numerical value of $r_1$ ( of the order of $10^5$, where $r_1 = k/k_1$, a result close to that obtained by the impulse momentum model can be obtained for the case of collision between two hard metal objects. Again, it appears that the value of $k$ is derived by trial-and-error, fitting the simulation to the experimental data.

Despite the progress that has been made on the optimum design of an impact damper and the continuing efforts, it seems that there is still a long way to go on this rough road to achieve the goal of developing an easily applied and accurate design method. Considering the complexity of the problem itself, and taking into account issues such as

the complexity of the primary structure to be controlled (not just a SDOF system) and the complexity of the excitation that a real engineering structure could experience (not just a sinusoidal excitation), it seems that the prospect of developing an analytical design relationship for the optimum design of an impact damper is very difficult, if not impossible. However, to make the impact damper more greatly used in engineering practice, this obstacle must be cleared. One way to achieve this goal is via numerical simulation. Therefore, an efficient and reliable simulation of the interaction between an impact damper and the primary structure under control is vital. Efficient numerical simulation depends on the efficiency and reliability of the mathematical modelling, the numerical algorithm and the coding.

### 1.8 Remarks on the-state-of-the-art in control using impact dampers

The reviewed literature shows that the majority of work has been done on single unit impact dampers. The interaction of impact dampers and a SDOF primary system has been mainly studied, both theoretically and experimentally, although some work on the interaction of impact dampers with MDOF primary systems can be found. The excitation considered most often is sinusoidal excitation, although random excitation can be found in some work. In modelling and theoretical studies, the assumption that was first widely adopted was equispaced impacts when the primary system is subjected to sinusoidal excitation. Later work, especially experimental research, showed this assumption to be incorrect [24]. Another assumption, that steady state vibrations take place with two generally distributed impacts per loading cycle, occurring at each end stop, was widely adopted in theoretical analysis. It should be pointed out that this assumption may be reasonable for a SDOF primary system subjected to sinusoidal excitation, but with a MDOF primary system subjected to sinusoidal excitation, the assumption is not necessarily correct. This is borne out by the experimental observations described later in this dissertation. Furthermore, this assumption applied to a MDOF primary system subjected to random excitation is clearly invalid.

It should be pointed out that it is very difficult, if not impossible, to find an analytical solution of a vibro-impact system, although analytical solutions and some useful results have been derived for the simplest case of a sinusoidally excited SDOF primary system equipped with an impact damper. Even for this simple case, a number of assumptions must be employed to simplify the analysis. As has been pointed out, these assumptions

are invalid for most cases other than this special case and, hence, these solutions can not be applied to other cases. Therefore, numerical simulation becomes very important for the investigation of control using impact dampers.

Some numerical simulations of the interaction between an impact damper and a MDOF primary system subjected to random excitation have been done by using traditional numerical integration methods. Although the response of both the structure and the impact mass could be modelled analytically between impacts, numerical simulation seems more practical. The key for the modelling of the interaction of an impact damper with the primary system lies in the modelling of the impact process. Although the impulse momentum model has been employed for modelling the impact process in almost all cases, there are a number of issues with this model that can not be neglected. One issue is the timing of impacts. The timing must be calculated very accurately in order that errors do not accumulate. If even one impact is missed, which could easily happen if the timing is not accurate enough, this could lead to failure of the simulation. Therefore, an effective high precision numerical strategy is required. Another issue associated with this model is that it cannot be applied to the modelling of the impact process if the elastic deformation produced by impact or the contact time of impact can not be considered negligible.

Although the effect of parameter variation (clearance, coefficient of restitution, mass ratio) has been assessed, both analytically and experimentally, to a certain extent, especially for the case of SDOF primary systems under sinusoidal excitation, this has not been done with civil engineering structures in mind. Tests using actual earthquake records on MDOF primary systems will allow a more realistic assessment of the achievable damping response to be made.

### 1.9 Objective of research

Impact dampers are particularly attractive for structural dynamic control, especially for dynamic control of civil engineering structures, since they have the unique feature that they are synchronized to the frequency of vibration and so maximum reductions in dynamic response can be achieved over a wide range of frequencies. There is also no need for an external power source for its operation and therefore it can respond reliably during the lifespan of the structure. It can be used in both new buildings and existing buildings, acting against both earthquake and wind loading. It is easy to set, alter and

almost free of maintenance. However, there are less attractive features associated with impact dampers. They produce a high contact force and high accelerations that could have an effect upon the primary structure itself (possibly resulting in local damage or failure) and upon the contents and occupiers. Establishing methods of reducing impact accelerations to reasonable serviceability levels without compromising the damping effectiveness of the system is an important aspect that must be addressed if the system is to be suitable for civil engineering structures. The overall objective of the research presented in this thesis is to ascertain the effect of, and possible solutions to, the fundamental problems associated with impact dampers, especially examining those issues surrounding the application of impact dampers for use in civil engineering structures. The specific objectives relevant to this work were:

a) Experimental investigation into the interaction of impact dampers with primary structures, especially with MDOF primary structures, examining the performance of the impact damper, factors that affect its performance and examining problems associated with its engineering application.
b) Developing a numerical simulation of the interaction between an impact damper and a primary structure to provide a tool for performance prediction and design of impact dampers. This includes mathematical modelling and development of a suitable numerical algorithm, with emphasis on modelling the impact process.
c) Establishing improvements of impact dampers for structural control by devising new impact damper systems or improving the dynamics and parameters of conventional impact dampers, focussing on controlling the high contact force/accelerations of the impact damper and its performance optimisation.

### 1.10 Outline of thesis

**Chapter 2** discusses modelling of the vibro-impact system. The impulse momentum model for the modelling of the impact process, i.e. modelling of the interaction between an impact damper and a MDOF primary structure, is first presented. However, more emphasis is placed on the modelling of the impact process with a spring-damper model. A novel method is developed to determine the parameters of the spring-damper model based upon easily measured contact time and the coefficient of restitution, which makes the spring-damper model for impact no longer a conceptual model, but one with physical meaning and practical for modelling of engineering impact processes. The important feature of this model is that the contact time of impact is taken into

consideration quantitatively, and, therefore, the elastic deformation during impact can be included.

**Chapter 3** deals with numerical algorithms for solving the governing equations of vibro-impact systems numerically, since only for a few simple cases, can the governing equations be solved analytically (with the help of simplifying assumptions). A high precision direct (HPD) integration scheme is discussed. To overcome the limitation of linear loading on this scheme and make it suitable for transient dynamic loading, such as earthquake loading, load interpolation is introduced and a corresponding integration method is developed. To make the algorithm more efficient, the scheme is further modified to allow a variable time-step to be used. To meet the requirement of simulating the interaction of impact damper with a non-linear primary structure, the HPD scheme is further developed as a high precision direct integration scheme for non-linear systems (HPD-NL). Numerical examples and comparison with other numerical algorithms, such as Runge-Kutta method and Newmark method are given.

**Chapter 4** introduces the experimental system. To carry out experimental studies, two small-scale structures, a shaking table and the associated test apparatus have been constructed. Signal generation, data acquisition and signal processing software has been developed for the experimental system. To allow the shaking table to produce accurate movement, a Proportional-Integral-Derivative (PID) controller is developed and incorporated into the experimental system. The tracing ability and the robustness of the controller are demonstrated. The reliability and stability of the test system is also demonstrated.

**Chapter 5** presents the results of an experimental investigation on the effect of an impact damper for the vibration control of a MDOF primary structure under free and various forms of forced vibration. In particular, the effects of the system parameters, namely, mass ratio, excitation type and amplitude and clearance on the damping efficiency and system dynamics are investigated. Some results that have not been found in the studies on SDOF primary systems are observed. An insight into applying an impact damper for the vibration control of a MDOF primary system is offered. Also, clearly revealed by the experiments, is one of the main issues associated with the application of impact dampers in civil engineering, namely, the high accelerations occurring at the moment of collision.

**Chapter 6** suggests a new type of impact damper—a buffered impact damper (BID). The performance of BID is studied experimentally and compared with that of conventional impact damper. It is demonstrated that a BID can not only substantially reduce the contact force and associated high accelerations and noise generated by collision but also significantly enhance the vibration control effect, which makes it ideal for many engineering applications. Buffers of different materials and sizes are tested. The mechanism of the BID is explored. A procedure for the optimal design of the buffer is suggested, to allow practical engineering application.

**Chapter 7** compares the results of experiments with the results of numerical simulations. The numerical scheme based on the impulse momentum model of impact and that based on the spring–damper model of impact have been developed to numerically simulate the interaction of an impact damper with the primary structure. Simulation results obtained with both the impulse momentum model and the spring-damper model of impact are compared with corresponding experimental results. The advantage of the spring-damper model over the impulse momentum model is demonstrated. Parametric studies with numerical simulations are also performed and compared with the experimental results and previously published analytical and experimental results. The usefulness of the simulation as a predictive design tool for a vibro-impact system is demonstrated. The mathematical models and algorithms developed are tested and verified.

**Chapter 8** presents the results of preliminary experimental investigations of variations on the impact damper system: a hybrid pendulum impact damper (HPID) and a twin-unit impact damper (TUID). An initial insight into the benefits and application of HPID or TUID for vibration control of structure is offered.

**Chapter 9** provides a summary of the main achievements and conclusions of the research and gives some recommendations for further work. It concludes that impact dampers, especially impact dampers with buffers (BID), can be applied to engineering systems, including civil engineering structures, for dynamic control. Further research is required to develop an easily applied design procedure for the optimum design of impact dampers.

# Chapter 2

# Modelling of Structure Equipped with an Impact Damper

This chapter discusses the mathematical modelling of the interaction of an impact damper with a primary structure (the structure under control), subject to various forms of excitation. Emphasis is placed on the modelling of the impact process using a spring-damper model rather than an impulse momentum model. A novel method is developed to determine the parameters of this model. Based on the spring-damper model for the impact process, the interaction of the impact damper with a primary structure can be modelled using a consistent model before, during and after collision, unlike the case for other impact models.

## 2.1 Modelling with impulse momentum model (IMM) of impact

Modelling of a SDOF primary structure equipped with an impact damper has been extensively investigated by modelling the impact process with an impulse momentum model. The starting point for this chapter is, building upon this work, to model a MDOF primary structure equipped with an impact damper. The structure under investigation, the primary structure, is modelled as a n-DOF system, as shown schematically in Figure 2.1. $M_i$, $K_i$, $C_i$ represent respectively the mass, stiffness and damping of the $i^{th}$ storey of the primary system while the rigid mass $m$ is the impact damper mass. The impact damper is placed between stops on mass $M_n$ with total clearance $d=d_l+d_r$ .The analysis is based on the following assumptions:

(1) The primary system remains linear

(2) The collision is instantaneous: the duration of impact is infinitesimal

(3) Momentum is conserved (before and after a collision)

### 2.1.1 *Force excitation (e.g. wind load)*

The equations of motion of the n-degree-of-freedom primary system during the period between two collisions are given by:

$$\mathbf{M}\ddot{\mathbf{x}} + \mathbf{C}\dot{\mathbf{x}} + \mathbf{K}\mathbf{x} = \mathbf{f}(t) \qquad (2.1a)$$

Where **M, K, C** are mass, stiffness and damping matrices respectively. $\ddot{\mathbf{x}}, \dot{\mathbf{x}}$ and $\mathbf{x}$ are vectors of acceleration, velocity and displacement respectively. $\mathbf{f}(t)$ is the excitation

force vector. The impact damper experiences constant velocity motion between impacts, hence acceleration between impacts is zero, therefore:

$$m\ddot{x} = 0 \tag{2.1b}$$

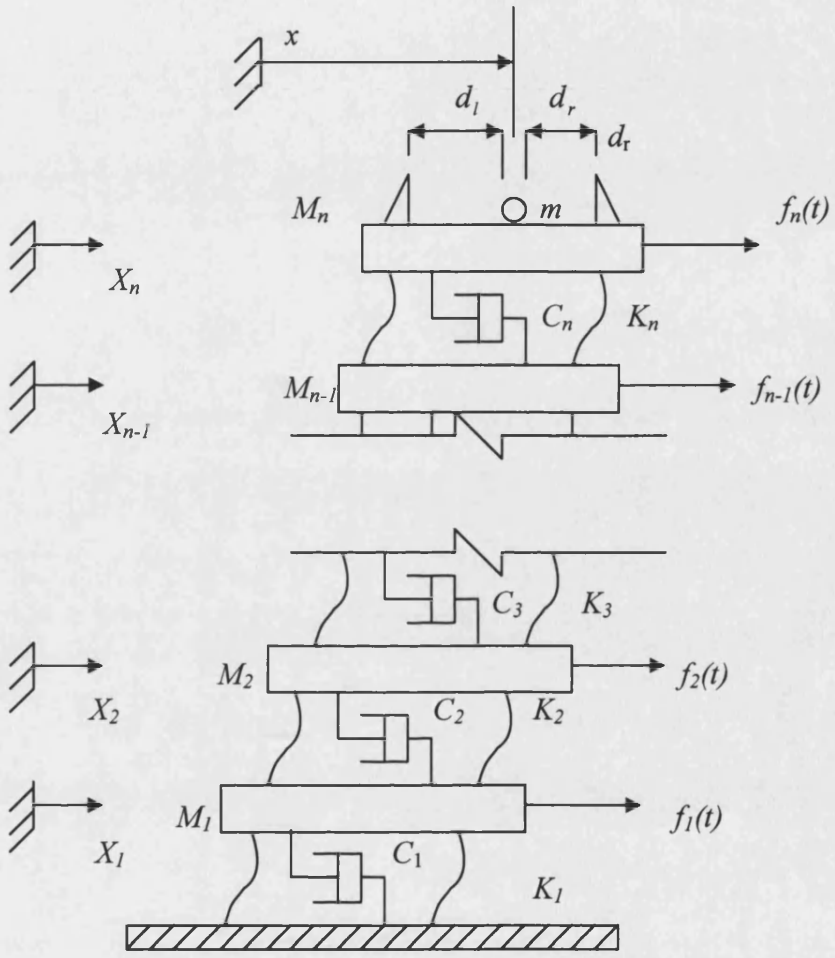


Figure 2.1: MDOF structure with impact damper—force excitation

Numerical integration of the equations of motion (2.1a) and (2.1b) can be carried out simultaneously until a contact between the stop and mass $m$ is established. A collision is assumed to take place when the difference between the two coordinates $X_n$ and $x$ is found to be smaller than some limiting value (taken as $d \times 10^{-6}$ in this model).

The assumption of instantaneous collision is adopted to implement transfer of momentum and energy dissipation. Each collision results in an incremental change in

the velocities of both the impact damper $m$ and the mass of the top storey, $M_n$, according to:

$$\dot{X}_n^{+} = \frac{1-\mu c_r}{1+\mu}\dot{X}_n^{-} + \frac{\mu(1+c_r)}{1+\mu}\dot{x}^{-} \tag{2.2a}$$

$$\dot{x}^{+} = \frac{1+c_r}{1+\mu}\dot{X}_n^{-} + \frac{\mu-c_r}{1+\mu}\dot{x}^{-} \tag{2.2b}$$

where $\mu = \frac{m}{M_n}$, is the mass ratio and $c_r$ is the coefficient of restitution. The superscripts – and + refer to the state of motion just before and immediately after a collision, respectively.

Equations (2.2a) and (2.2b) can be derived easily assuming conservation of linear momentum (before and after collision) where the coefficient of restitution is defined as:

$$c_r = -\frac{\dot{x}^{+} - \dot{X}_n^{+}}{\dot{x}^{-} - \dot{X}_n^{-}} \tag{2.3}$$

Consistent with the instantaneous collision assumption, the displacements of $m$ and $M_n$ remain unchanged immediately after the collision. After each collision, integration resumes with new initial conditions. The accurate timing of impacts becomes the central issue of simulation using this model.

### 2.1.2 *Base acceleration excitation (earthquake load)*

For base acceleration excitation, as experienced under seismic loading, the formulation of the equations of motion is slightly different. In this situation, between collisions, the equations of motion of a MDOF structure-impact damper system, as shown in Figure 3.2, have the vector matrix form:

$$\mathbf{M}\ddot{\mathbf{y}} + \mathbf{C}\dot{\mathbf{y}} + \mathbf{K}\mathbf{y} = -\mathbf{M}\{\mathbf{1}\}\ddot{X}_g \tag{2.4a}$$

$$m\ddot{y} = -m\ddot{X}_g \tag{2.4b}$$

where $\ddot{X}_g$ is the base acceleration and $\{\mathbf{1}\}$ is a vector of 1s. The vectors $\mathbf{y}$, $\dot{\mathbf{y}}$ and $\ddot{\mathbf{y}}$ are relative displacement, velocity and acceleration respectively.

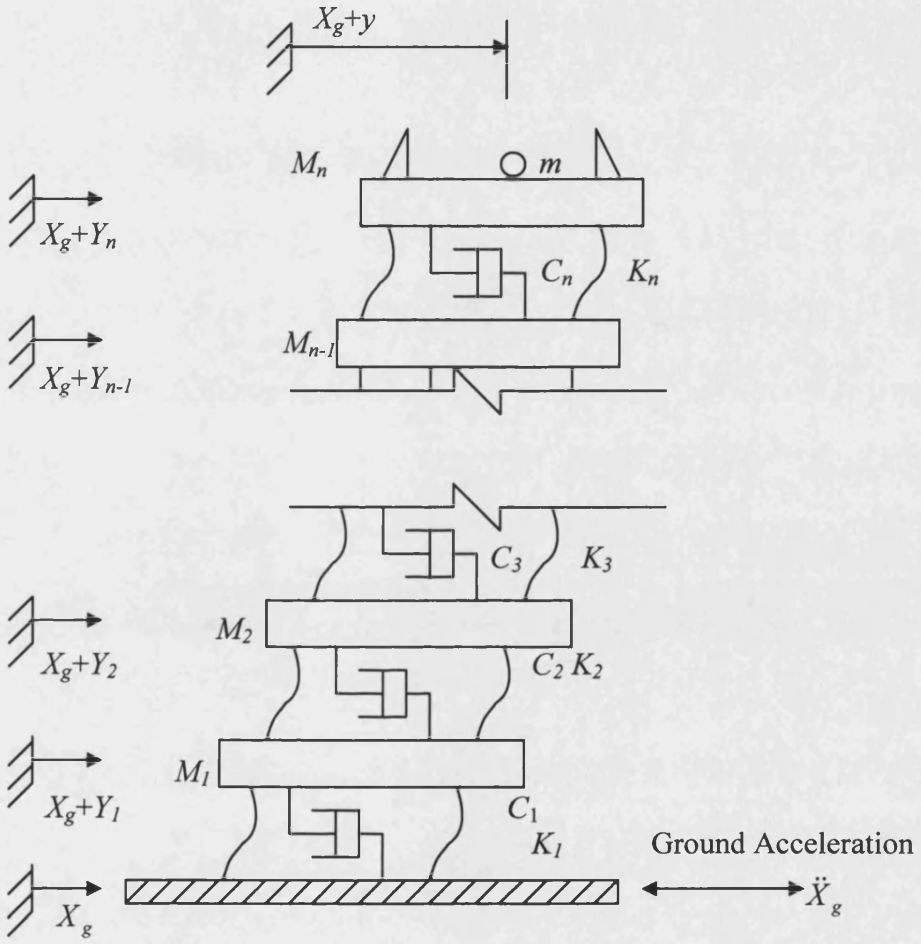


Figure 2.2: MDOF structure with impact damper—base excitation

For the numerical simulation of this case, the same strategy as adopted in 2.1.1 can be used.

## 2.2 Modelling with spring-damper model (SDM) of impact

The drawback of modelling the impacts with the impulse momentum model stems from the assumptions made. The instantaneous collision assumption on which it is based means that contact time (which could be very small for some collisions, such as that between two hard metal objects, but can never be zero) and the elastic deformation of the two masses during impact can not be taken into consideration. If the impact happens

not between two hard metal objects but, say, between a metal object and an object made of rubber, then even a reasonable approximation can not be expected from this model. In cases where the model can lead to a reasonable approximation, the numerical simulation faces the issue of accurate timing of impacts, since the governing equations given in 2.1 are valid only between impacts. In order to overcome these difficulties, a completely different approach to modelling impact is suggested using a spring-damper model of the impact surface. In the spring-damper model the impact is modelled as the compression of a spring that is between the two bodies and perpendicular to the plane of impact. The energy loss occurring during impact is modelled by a damper placed in parallel with the spring [31].

### 2.2.1 *SDOF primary structure under force excitation*

A SDOF system equipped with an impact damper is shown in Figure 2.3. The primary system is excited by external force $F$. Spring-damper pairs are placed between the moving damper mass and the stops to model the impact surface. The only assumption made in the following analysis is that the primary system is linear.

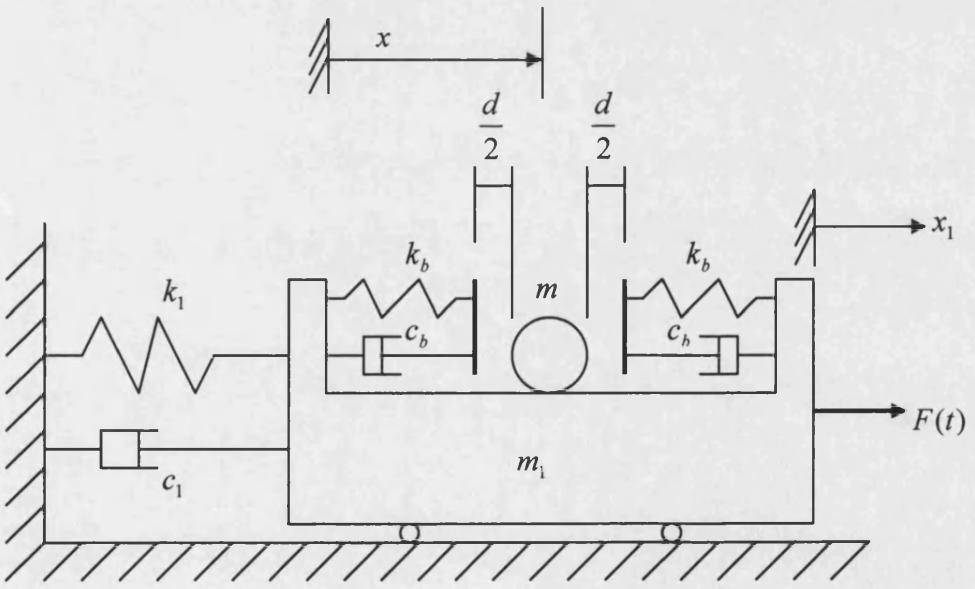


Figure 2.3: Forced excited SDOF system equipped with impact damper

The equations of motion for $m_1$ and $m$ are:

$$m_1\ddot{x}_1 + c_1\dot{x}_1 + k_1x_1 + c_b\dot{y}[U(y-\frac{d}{2}) + U(-y-\frac{d}{2})] + k_b[(y-\frac{d}{2})U(y-\frac{d}{2}) +$$

$$(y+\frac{d}{2})U(-y-\frac{d}{2})] = F(t) \qquad (2.5a)$$

and

$$m\ddot{y} + c_b\dot{y}[U(y-\frac{d}{2}) + U(-y-\frac{d}{2})] + k_b[(y-\frac{d}{2})U(y-\frac{d}{2}) +$$

$$(y+\frac{d}{2})U(-y-\frac{d}{2})] = m\ddot{x}_1 \qquad (2.5b)$$

where $y = x_1 - x$ (2.6)

and $U(\rho)$ is the Heaviside step function defined as:

$$U(\rho) = \begin{cases} 0 & \rho \le 0 \\ 1 & \rho > 0 \end{cases} \qquad (2.7)$$

Eq(2.5a) and Eq(2.5b) govern the motion of the primary structure $m_1$ and that of the damper mass $m$ respectively. They are valid before, during and after collision. Therefore, there is no need to discriminate motion between collisions or during the collision process, nor to accurately time collisions. It should be pointed out that Eq(2.5a) and Eq(2.5b) are non-linear, although the primary structure is assumed to be linear. The non-linearity is introduced through *d,* the clearance of the impact damper.

Note, that in the limiting case when $d = 0$, i.e. when mass $m$ is connected to the stops by the spring-damper pair, Eq(2.5a) and Eq(2.5b) reduce to:

$$m_1\ddot{x}_1 + c_1\dot{x}_1 + k_1x_1 + c_b\dot{y} + k_by = F(t) \qquad (2.8a)$$

$$m\ddot{y} + c_b\dot{y} + k_by = m\ddot{x}_1 \qquad (2.8b)$$

From Eq(2.6) the relative velocity and acceleration are given by

$$\left.\begin{aligned} \dot{y} &= \dot{x}_1 - \dot{x} \\ \ddot{y} &= \ddot{x}_1 - \ddot{x} \end{aligned}\right\} \qquad (2.9)$$

Substituting Eq(2.6) and Eq(2.9) into Eq(2.8a ) and Eq(2.8b) gives:

$$m_1\ddot{x}_1 + (c_1 + c_b)\dot{x}_1 + (k_1 + k_b)x_1 - c_b\dot{x} - k_b x = F(t) \tag{2.10a}$$

$$m\ddot{x} + c_b\dot{x} + k_b x - c_b\dot{x}_1 - k_b x_1 = 0 \tag{2.10b}$$

Putting Eq(2.10a) and Eq(2.10b) into matrix form gives:

$$\begin{bmatrix} m_1 & 0 \\ 0 & m \end{bmatrix}\begin{Bmatrix} \ddot{x}_1 \\ \ddot{x} \end{Bmatrix} + \begin{bmatrix} c_1 + c_b & -c_b \\ -c_b & c_b \end{bmatrix}\begin{Bmatrix} \dot{x}_1 \\ \dot{x} \end{Bmatrix} + \begin{bmatrix} k_1 + k_b & -k_b \\ -k_b & k_b \end{bmatrix}\begin{Bmatrix} x_1 \\ x \end{Bmatrix} = \begin{Bmatrix} F(t) \\ 0 \end{Bmatrix} \tag{2.11}$$

So Eq(2.5a) and Eq(2.5b), the governing equations of a vibro-impact damper system, reduce to those of a SDOF primary structure equipped with a linear dynamic vibration absorber (a spring-mass-damper) if *d*, the clearance of impact damper, is set to zero.

2.2.2 *SDOF primary structure under base acceleration excitation*

A SDOF primary structure equipped with an impact damper is shown by Figure 2.4. The primary structure is excited by the movement of the base. The equations of motion for $m_1$ and $m$ are:

$$m_1\ddot{x}_1 + c_1\dot{x}_1 + k_1 x + c_b\dot{y}[U(y - \frac{d}{2}) + U(-y - \frac{d}{2})] +$$
$$k_b[(y - \frac{d}{2})U(y - \frac{d}{2}) + (y + \frac{d}{2})U(-y - \frac{d}{2})] = -m_1\ddot{x}_g \tag{2.12a}$$

$$m\ddot{y} + c_b\dot{y}[U(y - \frac{d}{2}) + U(-y - \frac{d}{2})] + k_b[(y - \frac{d}{2})U(y - \frac{d}{2}) +$$

$$(y + \frac{d}{2})U(-y - \frac{d}{2})] = m(\ddot{x}_g + \ddot{x}_1) \tag{2.12b}$$

where $y = x_1 - x$ (2.13)

and $x_1$ and $x$ are the displacement of $m_1$ and $m$ relative to the base respectively.

When $d = 0$, i.e. when the damper mass is connected to the stops by the spring-damper pair, Eq(12a) and Eq(12b) reduce to:

$$\begin{bmatrix} m_1 & 0 \\ 0 & m \end{bmatrix}\begin{Bmatrix} \ddot{x}_1 \\ \ddot{x} \end{Bmatrix} + \begin{bmatrix} c_1 + c_b & -c_b \\ -c_b & c_b \end{bmatrix}\begin{Bmatrix} \dot{x}_1 \\ \dot{x} \end{Bmatrix} + \begin{bmatrix} k_1 + k_b & -k_b \\ -k_b & k_b \end{bmatrix}\begin{Bmatrix} x_1 \\ x \end{Bmatrix} = -\begin{Bmatrix} m_1 \\ m \end{Bmatrix}\ddot{x}_g \tag{2.14}$$

Eq (2.14) are exactly the governing equations of a SDOF structure equipped with a tuned mass damper undergoing base acceleration excitation.

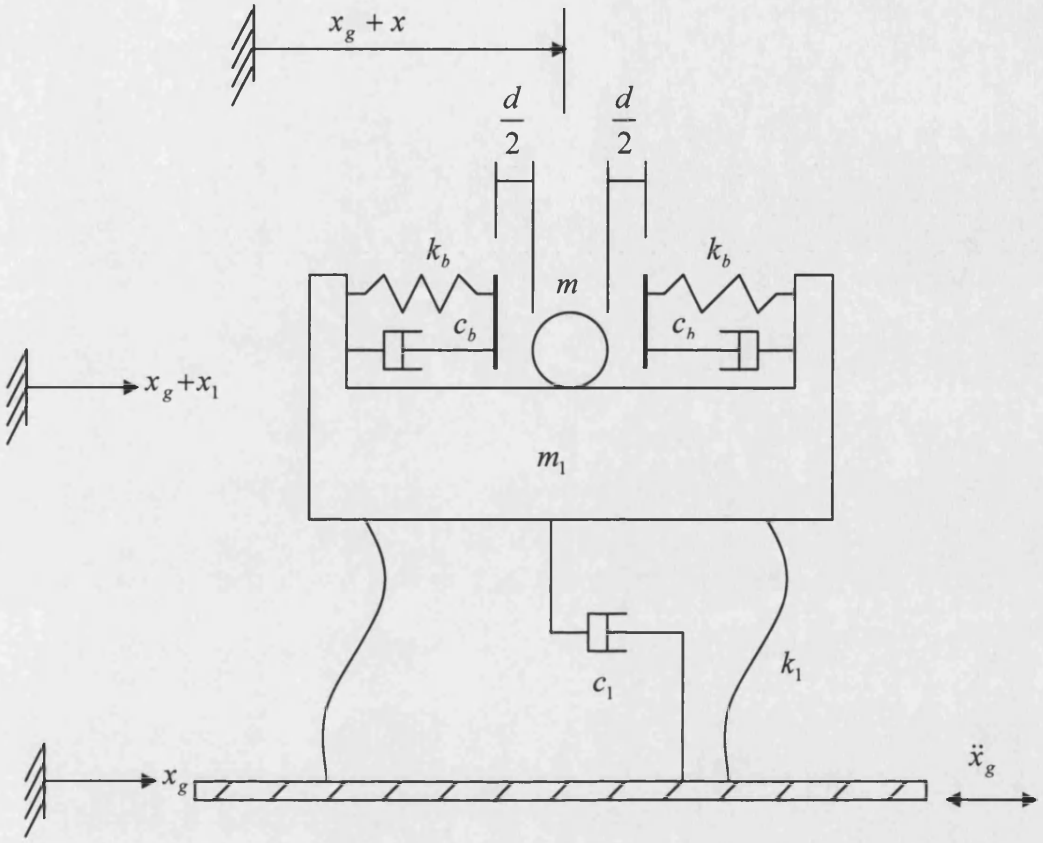


Figure 2.4: Base motion excited SDOF system equipped with impact damper

2.2.3 *MDOF primary structure under force excitation*

The same principles can be applied to a MDOF system. A MDOF primary system equipped with an impact damper is shown in Figure 2.5. The primary system is excited by forces as shown in the figure.

The governing equations of motion of the primary structure are:

$$m_1\ddot{x}_1 + (c_1 + c_2)\dot{x}_1 + (k_1 + k_2)x_1 - c_2\dot{x}_2 - k_2x_2 = f_1(t)$$

$$m_2\ddot{x}_2 + (c_2 + c_3)\dot{x}_2 + (k_2 + k_3)x_2 - c_2\dot{x}_1 - c_3\dot{x}_3 - k_2x_1 - k_3x_3 = f_2(t)$$

•

•

•

$$m_{n-1}\ddot{x}_{n-1} + (c_{n-1} + c_n)\dot{x}_{n-1} + (k_{n-1} + k_n)x_{n-1} - c_{n-1}\dot{x}_{n-2} - c_n\dot{x}_n - k_{n-1}x_{n-2} - k_nx_n = f_{n-1}(t)$$

$$m_n\ddot{x}_n + c_n\dot{x}_n + k_n x_n - c_n\dot{x}_{n-1} - k_n x_{n-1} + c_b\dot{y}[U(y-\frac{d}{2}) + U(-y-\frac{d}{2}) +$$

$$k_b[(y-\frac{d}{2})U(y-\frac{d}{2}) + (y+\frac{d}{2})U(-y-\frac{d}{2})] = f_n(t)$$

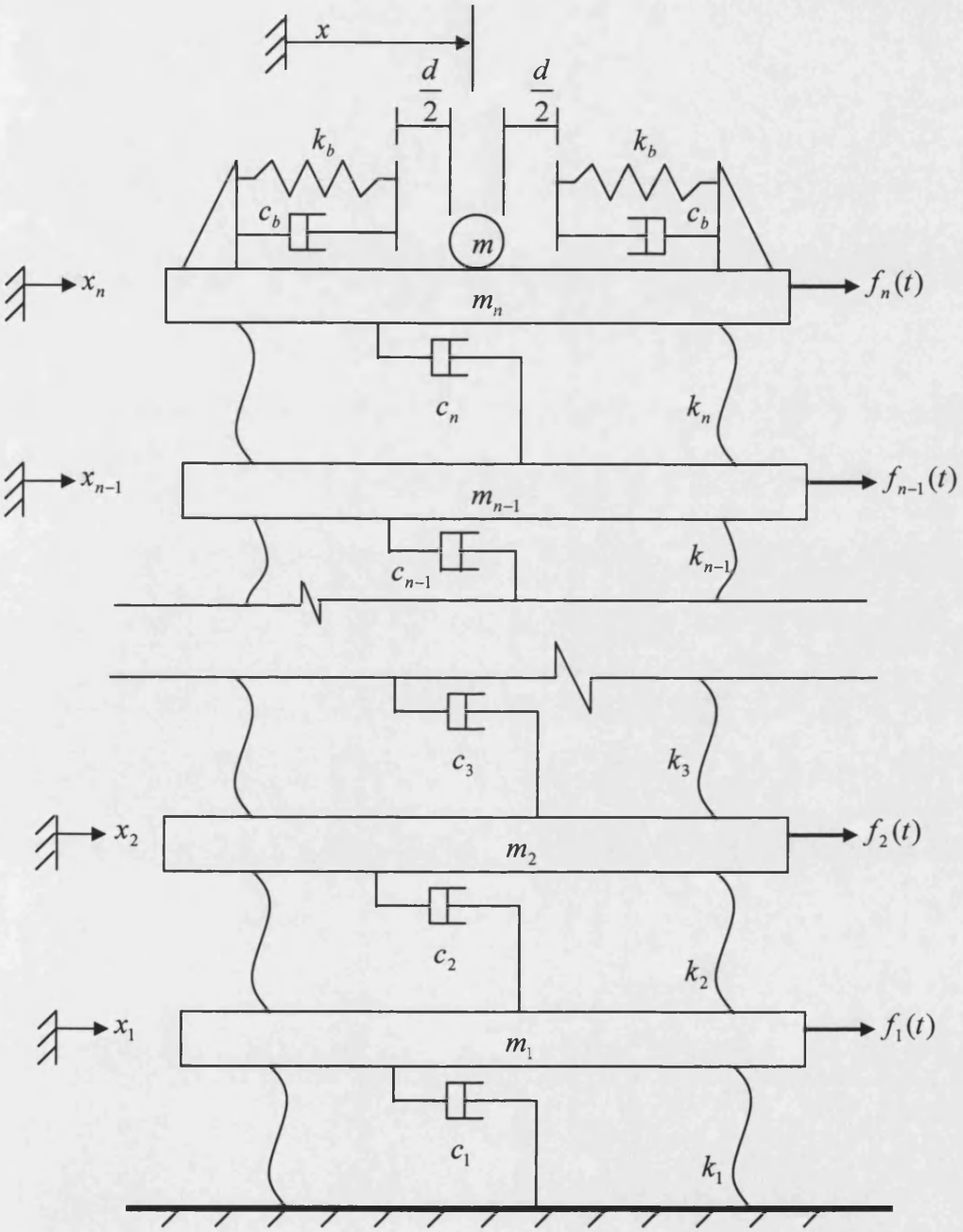


Figure 2.5: Force excited MDOF structure with impact damper

The governing equation of motion of the damper mass is:

$$m\ddot{y} + c_b\dot{y}[U(y-\frac{d}{2}) + U(-y-\frac{d}{2})] + k_b[(y-\frac{d}{2})U(y-\frac{d}{2}) + (y+\frac{d}{2})U(-y-\frac{d}{2})] = m\ddot{x}_n$$

Equations above can be written in a matrix form as:

$$\mathbf{M}\ddot{\mathbf{x}} + \mathbf{C}\dot{\mathbf{x}} + \mathbf{K}\mathbf{x} = \mathbf{f}(t) \tag{2.15}$$

and

$$m\ddot{y} + c_b\dot{y}\phi_2(y) + k_b\phi_1(y) = m\ddot{x}_n \tag{2.16}$$

Where

$$\mathbf{M} = \begin{bmatrix} m_1 & 0 & 0 & . & . & . & 0 \\ 0 & m_2 & 0 & . & . & . & 0 \\ . & & & & & & \\ . & & & & & & \\ . & & & & & & \\ 0 & 0 & . & . & . & 0 & m_n \end{bmatrix}$$

$$\mathbf{K} = \begin{bmatrix} k_1 + k_2 & -k_2 & 0 & . & . & . & 0 \\ -k_2 & k_2 + k_3 & -k_3 & . & . & . & 0 \\ . & & & & & & \\ . & & & & & & \\ 0 & 0 & . & . & -k_{n-1} & k_{n-1} + k_n & -k_n \\ 0 & 0 & . & . & . & -k_n & k_n + \varphi_1 \end{bmatrix}$$

$$\mathbf{C} = \begin{bmatrix} c_1 + c_2 & -c_2 & 0 & . & . & . & 0 \\ -c_2 & c_2 + c_3 & -c_3 & . & . & . & 0 \\ . & & & & & & \\ . & & & & & & \\ 0 & 0 & . & . & -c_{n-1} & c_{n-1} + c_n & -c_n \\ 0 & 0 & . & . & . & -c_n & c_n + \varphi_2 \end{bmatrix}$$

$$\mathbf{f}(t) = \{f_1(t) \quad f_2(t) \quad \ldots \quad f_n(t)\}^T$$

$$\varphi_1 = \frac{k_b}{x_n}[(y - \frac{d}{2})U(y - \frac{d}{2}) + (y + \frac{d}{2})U(-y - \frac{d}{2})] = \frac{k_b}{x_n}\phi_1(y)$$

$$\varphi_2 = \frac{c_b}{\dot{x}_n}\dot{y}[U(y-\frac{d}{2}) + U(-y-\frac{d}{2})] = \frac{c_b}{\dot{x}_n}\dot{y}\phi_2(y)$$

While $y = x_n - x$

and

$$\phi_1(y) = (y-\frac{d}{2})U(y-\frac{d}{2}) + (y+\frac{d}{2})U(-y-\frac{d}{2})$$

$$\phi_2(y) = U(y-\frac{d}{2}) + U(-y-\frac{d}{2})$$

2.2.4 *MDOF primary structure under base acceleration excitation*

A MDOF primary system equipped with an impact damper is shown in Figure 2.6. If the primary system is under base motion excitation, as shown in the figure, then the governing equations of motion of the primary structure are:

$$m_1\ddot{x}_1 + (c_1+c_2)\dot{x}_1 + (k_1+k_2)x_1 - c_2\dot{x}_2 - k_2x_2 = -m_1\ddot{x}_g$$

$$m_2\ddot{x}_2 + (c_2+c_3)\dot{x}_2 + (k_2+k_3)x_2 - c_2\dot{x}_1 - c_3\dot{x}_3 - k_2x_1 - k_3x_3 = -m_2\ddot{x}_g$$

•

•

•

$$m_{n-1}\ddot{x}_{n-1} + (c_{n-1}+c_n)\dot{x}_{n-1} + (k_{n-1}+k_n)x_{n-1} - c_{n-1}\dot{x}_{n-2} - c_n\dot{x}_n - k_{n-1}x_{n-2} - k_nx_n = -m_{n-1}\ddot{x}_g$$

$$m_n\ddot{x}_n + c_n\dot{x}_n + k_nx_n - c_n\dot{x}_{n-1} - k_nx_{n-1} + c_b\dot{y}[U(y-\frac{d}{2}) + U(-y-\frac{d}{2}) +$$

$$k_b[(y-\frac{d}{2})U(y-\frac{d}{2}) + (y+\frac{d}{2})U(-y-\frac{d}{2})] = -m_n\ddot{x}_g$$

The governing equation of motion of the damper mass is:

$$m\ddot{y} + c_b\dot{y}[U(y-\frac{d}{2}) + U(-y-\frac{d}{2})] + k_b[(y-\frac{d}{2})U(y-\frac{d}{2}) + (y+\frac{d}{2})U(-y-\frac{d}{2})] = m(\ddot{x}_n + \ddot{x}_g)$$

The above equations can be written in a concise matrix form as:

$$\mathbf{M}\ddot{\mathbf{X}} + \mathbf{C}\dot{\mathbf{X}} + \mathbf{K}\mathbf{X} = -\mathbf{M}\{\mathbf{1}\}\ddot{x}_g \tag{2.17}$$

$$m\ddot{y} + c_b\dot{y}\phi_2(y) + k_b\phi_1(y) = m(\ddot{x}_n + \ddot{x}_g) \tag{2.18}$$

where $x_i$ ($i$= 1,2,...$n$) is the displacement of $m_i$ relative to the base. Correspondingly, $\dot{x}_i$ and $\ddot{x}_i$ are the relative velocity and relative acceleration respectively and $\ddot{x}_g$ is the acceleration of the base. **M**, **K**, **C**, $\phi_1$ and $\phi_2$ are as defined in section 2.2.3, $y = x_n - x$ and $x$ is the displacement of the damper mass $m$ relative to the base.

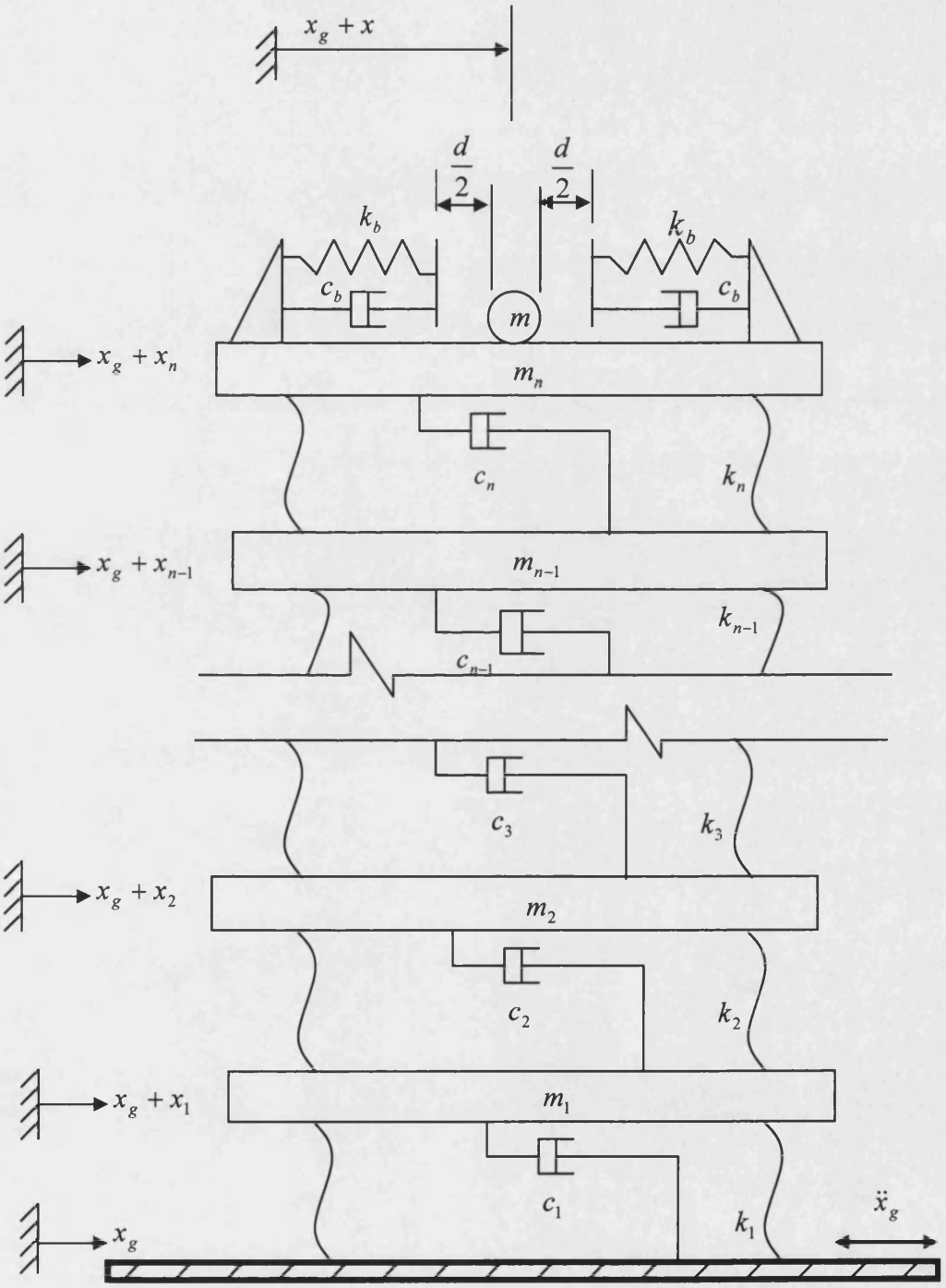


Figure 2.6: Base motion excited MDOF structure with impact damper

## 2.3 A Method for finding the parameters for spring-damper model of impact

The spring-damper model of impact employed in the modelling of the interaction of an impact damper with a primary structure, presented in 2.2, results from conceptual reasoning rather than the direct physical impact process. Unlike the impulse momentum model, which is based on assumptions such as instantaneous collision, there are no such limitations associated with the spring-damper model. It can produce accurate results given appropriate model parameters. Unfortunately, it is difficult to find the parameters of the model *a priori* [31] since they do not relate directly to the material properties. However, if the coefficient of restitution of impact and the contact time can be measured, the following method can be used to calculate the corresponding stiffness and damping terms $k_b$ and $c_b$.

During contact, the dynamics of two masses, $m_1$ and $m_2$, as shown in Figure 2.7, can be represented by the following differential equations:

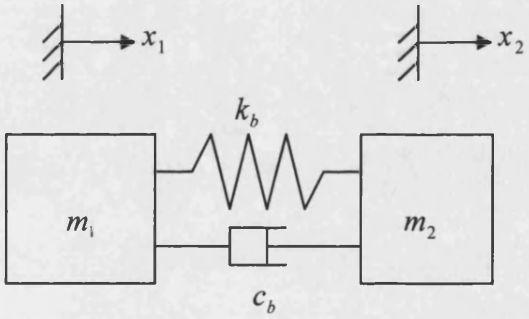


Figure 2.7: Model of an Impact Pair

$$m_2\ddot{x}_2 + c_b(\dot{x}_2 - \dot{x}_1) + k_b(x_2 - x_1) = 0 \tag{2.19}$$

$$m_1\ddot{x}_1 + c_b(\dot{x}_1 - \dot{x}_2) + k_b(x_1 - x_2) = 0 \tag{2.20}$$

Defining relative displacement between each mass as:

$$y = x_2 - x_1 \tag{2.21}$$

Eq(2.19) and Eq(2.20) become:

$$m_2\ddot{x}_2 + c_b\dot{y} + k_b y = 0 \tag{2.22}$$

$$m_1\ddot{x}_1 - c_b\dot{y} - k_b y = 0 \tag{2.23}$$

From Eq(2.22), Eq(2.23) and by defining a mass ratio:

$$\mu = \frac{m_2}{m_1} \tag{2.24}$$

the following can be derived:

$$\ddot{y} + \frac{c_b}{m_2}(1+\mu)\dot{y} + \frac{k_b}{m_2}(1+\mu)y = 0 \tag{2.25}$$

Letting:

$$\frac{k_b}{m_2}(1+\mu) = \omega_n^2 \tag{2.26}$$

$$\frac{c_b}{m_2}(1+\mu) = 2\zeta\omega_n \tag{2.27}$$

$\varsigma$ can be derived from Eq(2.26) and Eq(2.27) as:

$$\zeta = \frac{c_b\sqrt{1+\mu}}{2\sqrt{k_b m_2}} \tag{2.28}$$

Eq(2.25) can be written in the standard form of free vibration:

$$\ddot{y} + 2\zeta\omega_n\dot{y} + \omega_n y = 0 \tag{2.29}$$

At the initial moment of collision:

$$t = 0,\ y = 0, \text{ and } \dot{y} = \dot{y}_0 \tag{2.30}$$

where $\dot{y}_0$ represents the velocity of $m_2$ relative to $m_1$ at the initial moment of collision.

Corresponding to these initial conditions, the response can be obtained as:

$$y = \frac{\dot{y}_0}{\omega}e^{-\zeta\omega_n t}\sin\omega t \tag{2.31}$$

and

$$\dot{y} = \frac{\dot{y}_0}{\omega}e^{-\zeta\omega_n t}(\omega\cos\omega t - \zeta\omega_n\sin\omega t) \tag{2.32}$$

where $\omega = \omega_n\sqrt{1-\zeta^2}$

At the ending of the collision process:

$t = T_c$, $y = 0$, and $\dot{y} = -c_r\dot{y}_0$

where $c_r$ is coefficient of restitution of the collision and $T_c$ represents the duration of the collision, i.e. the contact time.

From Eq(2.31) and the condition $t = T_c$, $y = 0$, it can be found that:

$$\omega T_c = \pi \tag{2.33}$$

Making use of the condition that at $t = T_c$, $\dot{y} = -c_r\dot{y}_0$ and using Eq(2.33), Eq(2.32) results in the following form:

$$-c_r\dot{y}_0 = \frac{\dot{y}_0}{\omega}e^{-\zeta\omega_n T_c}(-\omega) = -\dot{y}_0 e^{-\zeta\omega_n T_c} \tag{2.34}$$

Noting that $\dot{y}_0 \neq 0$ (otherwise no collision will happen), the following is obtained:

$$\zeta\omega_n T_c = -ln(c_r) \tag{2.35}$$

From Eq(2.35) and the definition of $\zeta$, Eq(2.28), the parameter $c_b$ of the damper can be obtained as:

$$c_b = -\frac{2m_2 ln(c_r)}{(1+\mu)T_c} \tag{2.36}$$

Eq(2.33) can be rewritten as:

$$\omega = \omega_n\sqrt{1-\zeta^2} = \frac{\pi}{T_c} \tag{2.37}$$

or rearranging:

$$\zeta^2 = 1 - \left(\frac{\pi}{T_c}\right)^2 \frac{1}{\omega_n^2} \tag{2.38}$$

Substituting Eq(2.28) for $\zeta^2$ in Eq(2.38) results in:

$$1-\left(\frac{\pi}{T_c\omega_n}\right)^2=\frac{c_b^2(1+\mu)}{4k_bm_2} \tag{2.39}$$

Substituting Eq(2.26) for $\omega_n^2$ in Eq(2.39) and rearranging results:

$$4m_2k_b(1+\mu)=c_b^2(1+\mu)^2+4m_2^2\left(\frac{\pi}{T_c}\right)^2 \tag{2.40}$$

Finally, substituting Eq(2.36) for $c_b$ in Eq(2.40) and solving the obtained equation results in the following equation for the stiffness term, $k_b$:

$$k_b=\frac{m_2}{(1+\mu)T_c^2}(\pi^2+(ln(c_r))^2) \tag{2.41}$$

So, the parameters of the spring-damper model, $k_b$ and $c_b$, are obtained from Eq(2.36) and Eq(2.41). It can be seen that $k_b$ and $c_b$ depend on the damper mass $m_2$, mass ratio $\mu$, the coefficient of restitution $c_r$ and the contact time $T_c$, all of which can be measured experimentally.

It should be noted that the only assumption made in the derivation of Eq(2.36) and Eq(2.41) is that $k_b$ and $c_b$ remain constant during the process of collision. However, both the contact time $T_c$ and the coefficient of restitution $c_r$ could be affected by impact velocity $\dot{y}_0$ and therefore $k_b$ and $c_b$ may be dependent on impact velocity to some extent. This will be investigated experimentally in chapter 6.

# Chapter 3

# Direct Integration Scheme of Differential Equations

Introduction: In only a few of the simplest cases, such as a harmonically excited SDOF primary structure equipped with an impact damper, can an analytical solution of the governing equations be found. Even in these cases, assumptions must be introduced to simplify the analysis. For most cases, an analytical solution can not be found. This chapter discusses algorithms for solving the governing equations, developed in Chapter 2, numerically. A high precision direct (HPD) integration scheme is first discussed. To improve efficiency and reliability, further modifications to this scheme are made. A high precision direct integration scheme for non-linear systems is also developed.

## 3.1 Overview of direct integration methods for solving differential equations

The behaviour of systems in a given environment, such as the behaviour of structures during earthquakes, explosion and many other types of loading can be described mathematically. This process is called mathematical modelling. In many cases the mathematical model is a group of differential equations, which form the basis of numerical simulations of such behaviour. Computer simulations, which solve the governing differential equations numerically, are increasingly used in cases where an analytical solution is very difficult or impossible to obtain. Simulations are also employed to supplant tests in situations where they are either very expensive or impossible to conduct. Direct time integration schemes are the methods most commonly employed in solving the governing equations numerically.

Direct time integration schemes can be divided into implicit methods, that evaluate the derivatives using values at the end of the time step, such as, the Newmark method, Wilson $-\theta$ method and Houbolt method, and explicit methods that evaluate the derivatives using values at the beginning of the step, such as the central difference scheme. In the application of these methods, the time step size must be carefully selected, relative to the natural periods of the system and the variation of the loading, so as to ensure proper integration precision with reasonable computational effort. When explicit integration schemes are exploited, the time-step size must also be very strictly constrained by the shortest modal period of the discretized structure in order to achieve

integration stability. Hence, such direct integration analysis often requires very small time steps and therefore can be time consuming and numerically costly.

Zhong and Williams [65] proposed a special explicit integration scheme—the high precision direct (HPD) integration scheme, for which the time-step size is not constrained by any of the natural periods of the discretized structure. In this method, the time-step size is only restricted by the form of the loading, where the applied loading is simulated by a piece-wise linear approximation between time steps. To eliminate this restriction, Lin, Shen and Williams [66] developed the HPD-F method, by prior decomposition of the applied loading into Fourier components. To do this, the load must be given in an analytical function form and then expanded by Fourier transformation. Although the HPD-F method can sometimes produce better results, there is an inevitable additional computational effort needed by doing the Fourier decomposition and superposition. Moreover, in some cases, it cannot achieve more precise results than the standard HPD scheme.

## 3.2 High precision direct (HPD) integration scheme

The following provides a derivation of the HPD scheme based upon Zhong and Williams's work [65].

### 3.2.1. *Governing equation and its transformation*

A general second-order system of $n$ equations can be represented in matrix form by:

$$\mathbf{M}\ddot{\mathbf{x}} + \mathbf{C}\dot{\mathbf{x}} + \mathbf{K}\mathbf{x} = \mathbf{r}(t) \tag{3.1}$$

where **M, C, K** are $n \times n$ mass, damping and stiffness matrices respectively. The mass matrix **M** is symmetric and positive definite. The stiffness matrix **K** is symmetric and positive semi-definite and the damping matrix **C** is anti-symmetric. The vectors $\mathbf{x}, \dot{\mathbf{x}}, \ddot{\mathbf{x}}$ represent the displacement, velocity and acceleration of each d.o.f. respectively. The vector **r**(t) represents the external forcing function.

The initial conditions are:

$$\left.\begin{aligned} \mathbf{x}(0) &= \mathbf{x}_0 \\ \dot{\mathbf{x}}(0) &= \dot{\mathbf{x}}_0 \end{aligned}\right\} \tag{3.2}$$

Introducing a transform similar to that used in Hamiltonian systems:

$$\mathbf{p} = \mathbf{M}\dot{\mathbf{x}} + \tfrac{1}{2} \times \mathbf{C}\mathbf{x}$$

or

$$\dot{\mathbf{x}} = \mathbf{M}^{-1}\mathbf{p} - \tfrac{1}{2} \times \mathbf{M}^{-1}\mathbf{C}\mathbf{x} \tag{3.3}$$

allows Eq(3.1) to be rewritten as:

$$\dot{\mathbf{p}} = -(\mathbf{K} - \tfrac{1}{4} \times \mathbf{C}\mathbf{M}^{-1}\mathbf{C})\mathbf{x} - \tfrac{1}{2} \times \mathbf{C}\mathbf{M}^{-1}\mathbf{p} + \mathbf{r} \tag{3.4}$$

Eq(3.3) and Eq(3.4) can be written in the general form of a pair of first order equations:

$$\dot{\mathbf{x}} = \mathbf{A}\mathbf{x} + \mathbf{D}\mathbf{p} + \mathbf{0} \tag{3.5a}$$

$$\dot{\mathbf{p}} = \mathbf{B}\mathbf{x} + \mathbf{G}\mathbf{p} + \mathbf{r} \tag{3.5b}$$

where

$$\left.\begin{array}{c} \mathbf{A} = -\tfrac{1}{2} \times \mathbf{M}^{-1}\mathbf{C} \\ \mathbf{B} = \tfrac{1}{4} \times \mathbf{C}\mathbf{M}^{-1}\mathbf{C} - \mathbf{K},\ \mathbf{G} = -\tfrac{1}{2} \times \mathbf{C}\mathbf{M}^{-1} \\ \mathbf{D} = \mathbf{M}^{-1} \end{array}\right\} \tag{3.6}$$

Eq(3.5a) and Eq(3.5b) can be combined into the form:

$$\dot{\mathbf{u}} = \mathbf{H}\mathbf{u} + \mathbf{f} \tag{3.7}$$

where

$$\left.\begin{array}{c} \mathbf{u} = \{\mathbf{x}^T, \mathbf{p}^T\}^T, \mathbf{H} = \begin{bmatrix} \mathbf{A} & \mathbf{D} \\ \mathbf{B} & \mathbf{G} \end{bmatrix} \\ \mathbf{f} = \{\mathbf{0}^T, \mathbf{r}^T\}^T \end{array}\right\} \tag{3.8}$$

The solution of Eq(3.7) consists of the particular solution corresponding to **f** plus the complementary function solution of its homogeneous equation:

$$\dot{\mathbf{u}} = \mathbf{H}\mathbf{u} \tag{3.9}$$

If the system described by Eq(3.7) is time invariant, i.e., **H** is a constant matrix, the solution of Eq(3.9) can be expressed as:

$$\mathbf{u} = \exp(\mathbf{H} \cdot t)\mathbf{u}_0 \tag{3.10}$$

where $\mathbf{u}_0 = \mathbf{u}|_{t=0}$ (3.11)

Let the time step be represented by $\tau$ then,

$$\mathbf{u}(\tau) = \exp(\mathbf{H}\cdot\tau)\mathbf{u}_0 = \mathbf{T}\cdot\mathbf{u}_0 \tag{3.12}$$

where $\mathbf{T} = \exp(\mathbf{H}\cdot\tau)$ (3.13)

Now the problem turns to the calculation of the matrix **T**. If **T** can be calculated accurately, then the time integration can be carried out as:

$$\mathbf{u}_1 = \mathbf{T}\mathbf{u}_0; \mathbf{u}_2 = \mathbf{T}\mathbf{u}_1; ...; \mathbf{u}_k = \mathbf{T}\mathbf{u}_{k-1} \tag{3.14}$$

3.2.2. *Accurate calculation of matrix* **T** *and the solution of the homogeneous equation*

According to the properties of exponential functions, we can write Eq(3.13) as:

$$\mathbf{T} = \exp(\mathbf{H}\cdot\tau) = [\exp(\mathbf{H}\cdot\tau/m)]^m \tag{3.15}$$

Letting $m = 2^N$, for example taking $N$=20, then $m$=1048576. It should be noticed that time step $\tau$ itself is a small time interval so that $\Delta t = \tau/m$ must become a very small time span in relation to the smallest period of the structure. Therefore, using the first four terms of a binomial expansion, the exponential in Eq(3.15) can be approximated by:

$$\exp(\mathbf{H}\cdot\tau/m) = \exp(\mathbf{H}\cdot\Delta t) \approx \mathbf{I} + \mathbf{H}\cdot\Delta t + \tfrac{1}{2}\times(\mathbf{H}\cdot\Delta t)^2 + \tfrac{1}{6}\times(\mathbf{H}\cdot\Delta t)^3 + \tfrac{1}{24}\times(\mathbf{H}\cdot\Delta t)^4$$

$$= \mathbf{I} + \mathbf{T}_a \tag{3.16}$$

So, referring back to Eq(3.15)

$$\mathbf{T} = [\mathbf{I} + \mathbf{T}_a]^m = [\mathbf{I} + \mathbf{T}_a]^{2^N} = [\mathbf{I} + \mathbf{T}_a]^{2^{N-1}} \times [\mathbf{I} + \mathbf{T}_a]^{2^{N-1}} \tag{3.17}$$

$$[\mathbf{I} + \mathbf{T}_a]\times[\mathbf{I} + \mathbf{T}_a] = \mathbf{I} + 2\mathbf{T}_a + \mathbf{T}_a \times \mathbf{T}_a \tag{3.18}$$

It should be noticed that, compared with **I**, $\mathbf{T}_a$ is very small. When $\mathbf{T}_a$ is added to **I**, it becomes the tail part. The finite precision of a computer makes it quite possible that the function of $\mathbf{T}_a$ is completely lost, which may lead to loss of accuracy of the calculation. In order to prevent this, $\mathbf{T}_a$ is calculated and stored separately to **I**. $\mathbf{T}_a$ can be obtained by a loop in the computational code by referring to Eq(3.18), for *i=1* to *N*:

$$\mathbf{T}_{a,i} = 2\mathbf{T}_{a,i-1} + \mathbf{T}_{a,i-1} \times \mathbf{T}_{a,i-1} \tag{3.19}$$

where initially:

$$\mathbf{T}_{a,0} = \mathbf{H} \cdot \Delta t + \tfrac{1}{2} \times (\mathbf{H} \cdot \Delta t)^2 + \tfrac{1}{6} \times (\mathbf{H} \cdot \Delta t)^3 + \tfrac{1}{24} \times (\mathbf{H} \cdot \Delta t)^4 \tag{3.20}$$

Finally, at the end of the loop, **T** can be found as

$$\mathbf{T} = \mathbf{I} + \mathbf{T}_a \tag{3.21}$$

Thus the matrix **T** can be accurately obtained. Hence, the discrete step-by-step integration formula Eq(3.14) can be used to solve the homogeneous equation Eq(3.9). Bear in mind that the matrix **T** can be calculated in advance and need only be calculated once (assuming the system remains linear).

### 3.2.3. *Solution of non-homogeneous equations*

For the non-homogeneous Eq(3.7), using Zhong and Williams linear assumption during a time step $(t_k, t_{k+1})$, the non-homogeneous term **f** can be considered linear, i.e.,

$$\mathbf{f}(t) = \mathbf{r}_0 + \mathbf{r}_1 (t - t_k) \quad (t_k \le t \le t_{k+1}) \tag{3.22}$$

and $\mathbf{u} = \mathbf{u}_k$ when $t = t_k$

According to the principle of superposition and the theory of differential equations, the solution of Eq(3.7) can be expressed as:

$$\mathbf{u}(t) = \exp\left[\mathbf{H} \cdot (t - t_k)\right] \cdot \mathbf{u}_k + \int_{t_k}^{t} \exp\left[\mathbf{H}(t - \xi)\right] \mathbf{f}(\xi) d\xi \tag{3.23}$$

where $\xi$ is the integral variable for time. Letting $t = t_{k+1}$, noting that $t_{k+1} - t_k = \tau$, and carrying out the integration in Eq(3.23), the following is obtained:

$$\mathbf{u}_{k+1} = \mathbf{T}\left[\mathbf{u}_k + \mathbf{H}^{-1}(\mathbf{r}_0 + \mathbf{H}^{-1}\mathbf{r}_1)\right] - \mathbf{H}^{-1}\left[\mathbf{r}_0 + \mathbf{H}^{-1}\mathbf{r}_1 + \mathbf{r}_1 \tau\right] \tag{3.24}$$

This is the time integration formula for the non-homogeneous Eq(3.7).

### 3.2.4 *Comparison of HPD scheme with analytical solution.*

*Example 1.* To demonstrate the high accuracy characteristic of this time integration algorithm, the method is applied to a SDOF system, as shown in Figure 3.1, since the

analytical solution of a SDOF system for certain functions can be easily obtained and compared with the numerical results.

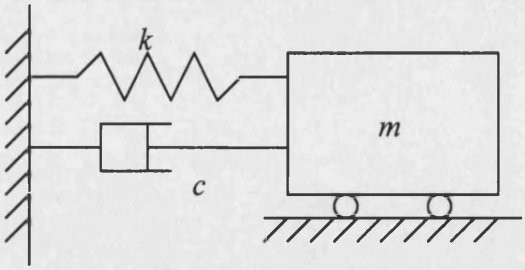


Figure 3.1: A SDOF system

If $k=400N/m$ *and* $m=1kg$ the period of free vibration without damping is approximately 0.3 seconds. The analytical [67] and numerical responses of the system to the initial conditions $x_0 = 0, \dot{x}_0 = 0.2\ m/s$ at different damping levels are shown in Figure 3.2. The time step taken in the time integration is 0.01 second. It can be seen that the numerical response and the analytical response match very well.

*Example 2*: Response of a SDOF system subject to an 'impact' load

The same system as shown in Figure 3.1 is taken, where $m$=8$kg$, $k$=32$N/m$, $c$=0 and $x_0 = \dot{x}_0 = 0$. The numerical and analytical [67] response of the system subject to the impact load represented by $f = 100e^{-5t}$, are shown in Figure 3.3. The time step taken in time integration is 0.01 seconds in order to accurately represent the load.

It can be seen that in both examples the numerical response matches the analytical solution well, although there is a discernable discrepancy, especially in the case of response to the impact load. It should, however, be pointed out that the high accuracy is not due to the very small time step, which is only necessary to describe the loading. This will be further demonstrated by the following examples.

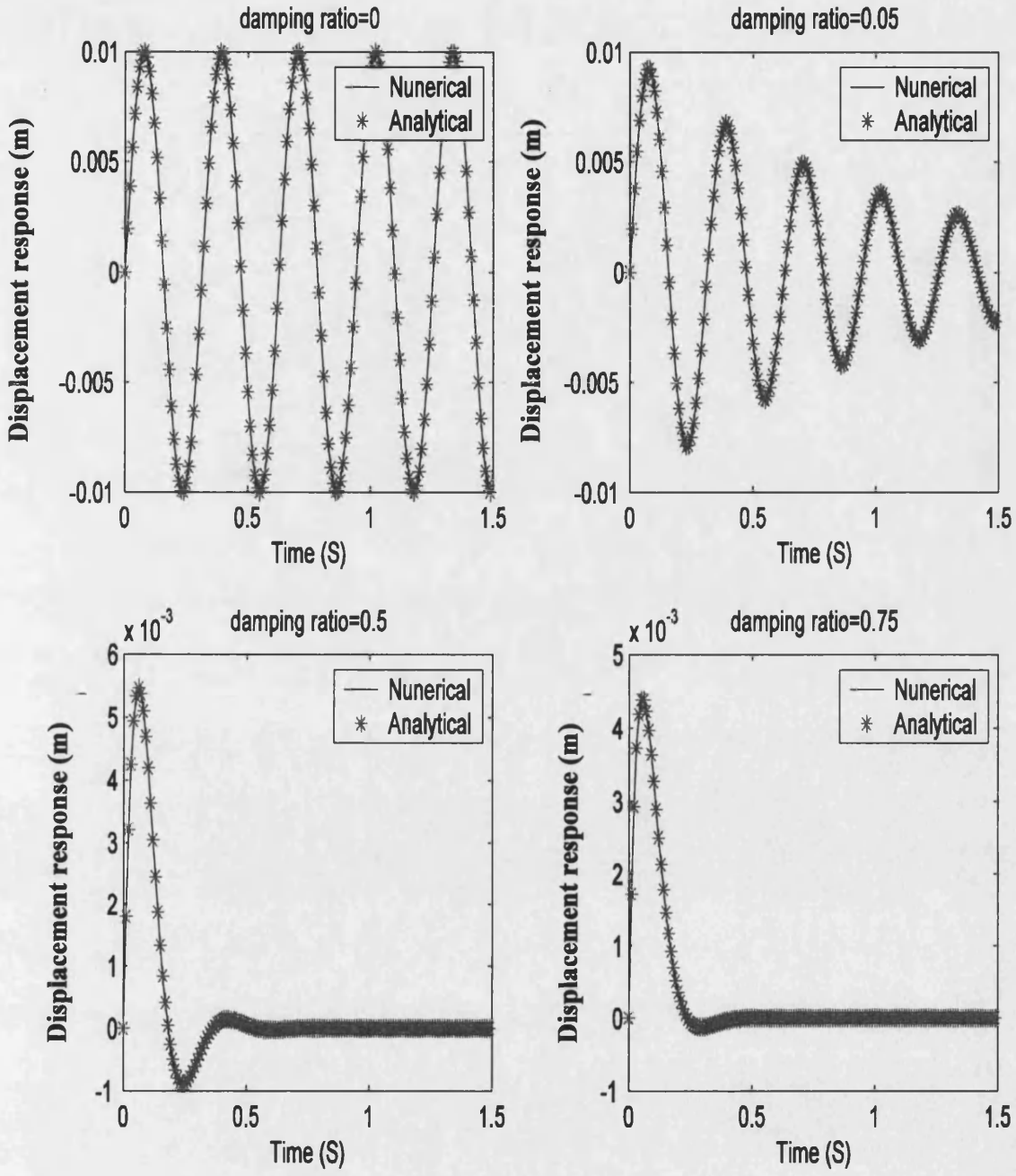


Figure 3.2: Comparison of numerical and analytical response to initial velocity

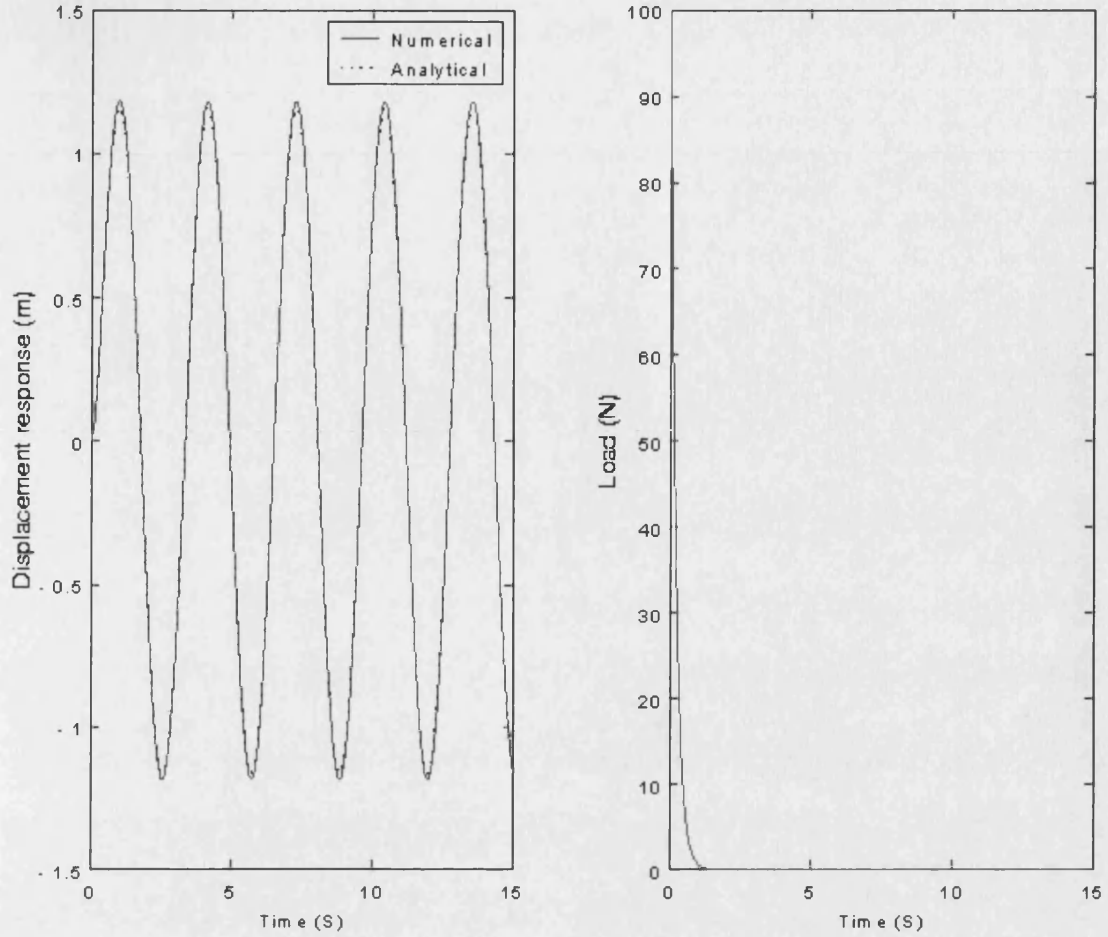


Figure 3.3: Comparison of numerical and analytical response to impact load

*Example 3:* Response of a MDOF system to free vibration

A five DOF system is shown in Figure 3.4., where $M_1=M_2=M_4=M_5=8kg$, $M_3=0.08kg$, $K_1=K_2=K_3=K_4=4N/m$, $C_3=0.1Ns/m$ and $C_4=2.0Ns/m$. The initial condition of the system is: $x_1 = 0, x_2 = 0.9m, x_3 = 10.0m, x_4 = 0, x_5 = -1m$; $\dot{x}_1 = \dot{x}_2 = \dot{x}_3 = \dot{x}_4 = \dot{x}_5 = 0$.

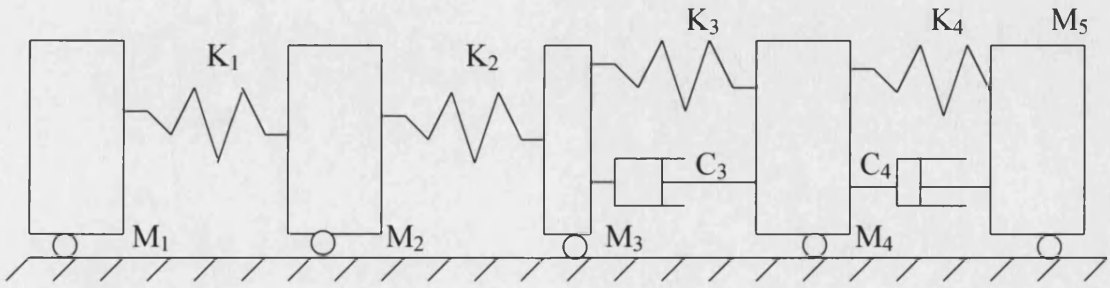


Figure 3.4: A five degrees of freedom system

The centre of the masses of the system, $\sum m_i x_i$, should remain unchanged. However, as mentioned at the beginning, in most numerical calculations algorithmic damping is introduced which will make this untrue after several time steps. An ideal time integration algorithm should not introduce damping nor be too sensitive to the size of time step. It is difficult to obtain an analytical solution of the system described above due to the existence of damping. However, the eigenvalues of the system can be obtained without damping as:

$$\omega_1^2 = 0, \omega_2^2 = 0.190983, \omega_3^2 = 0.9974857, \omega_4^2 = 1.309017, \omega_5^2 = 100.50251 (rad/s)^2$$

The period of the highest frequency of vibration is $T_h = 2\pi / 10.025 = 0.627(s)$. The accuracy of HPD method can be examined by comparing the results with time steps of $\tau = 0.1s$ and $\tau = 10s$ respectively. The numerical results are shown in Figure 3.5.

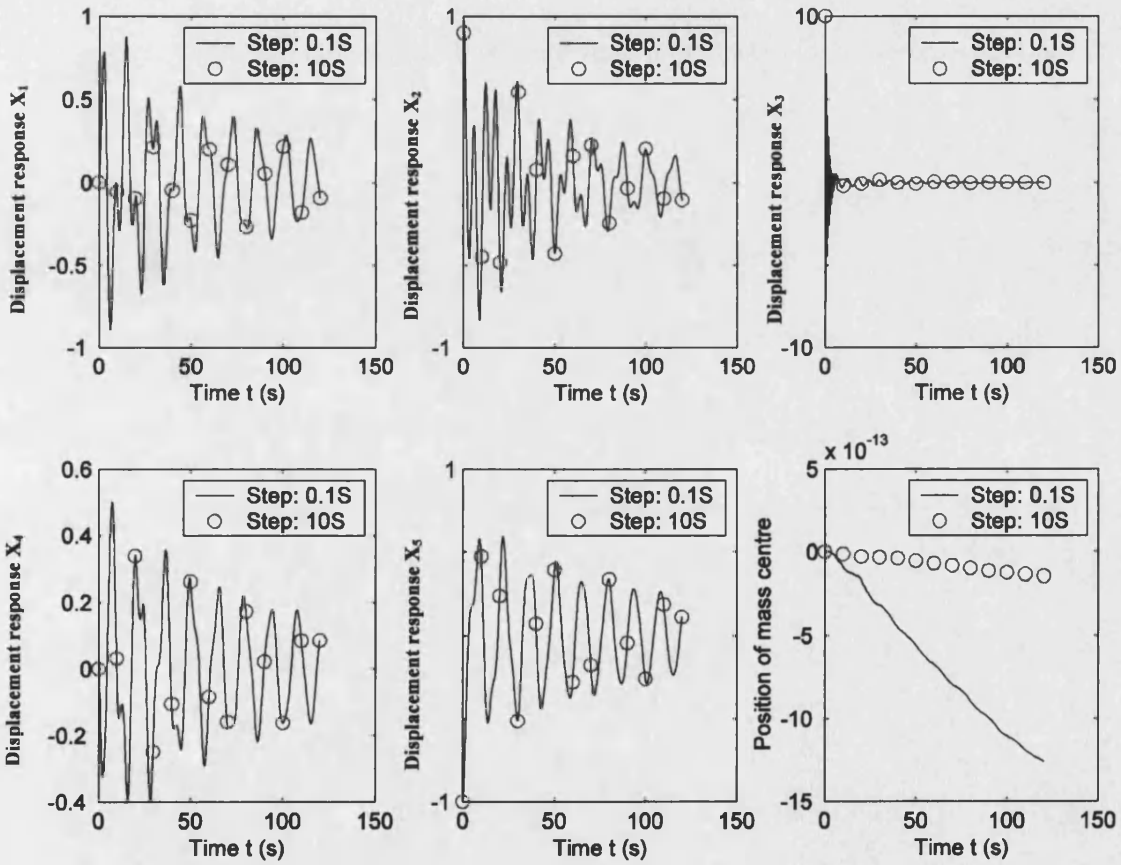


Figure 3.5: Numerical solution of displacement response with different time-step size in integration

From the results it can be seen that the size of time step does not affect the calculated results at the discrete points. Note that the scale of the centre of mass is of the order of $10^{-13}$ and therefore the mass centre, ( $\sum m_i x_i$ ) is approximately zero, as expected.

*Example 4.* Response of a MDOF system to an impulse load

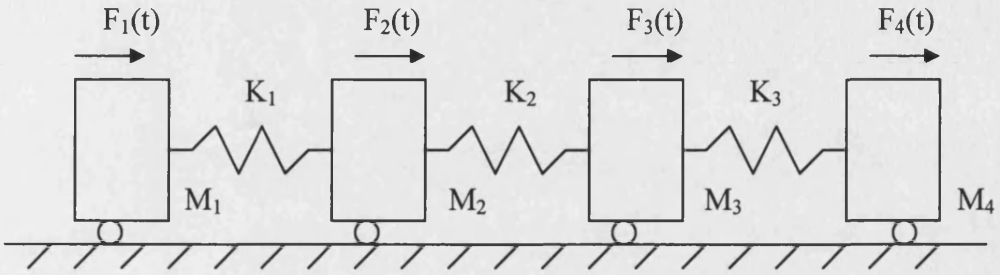


Figure 3.6: A MDOF system subject to impulse load

A MDOF system is shown in Figure 3.6. where $M_1=M_2=M_3=M_4=1\ kg$ , $K_1=K_2=K_3=K_4=1$ N/m; $F_1(t)=\delta(t)$, $F_2(t)=F_3(t)=0$, $F_4(t)=-\delta(t)$. where $\delta(t)$ is the Dirac delta function. The numerical and analytical responses of the system are shown in Figure 3.7. The time step taken is 0.05 seconds. Again, it can be seen that the numerical result matches the analytical response very well.

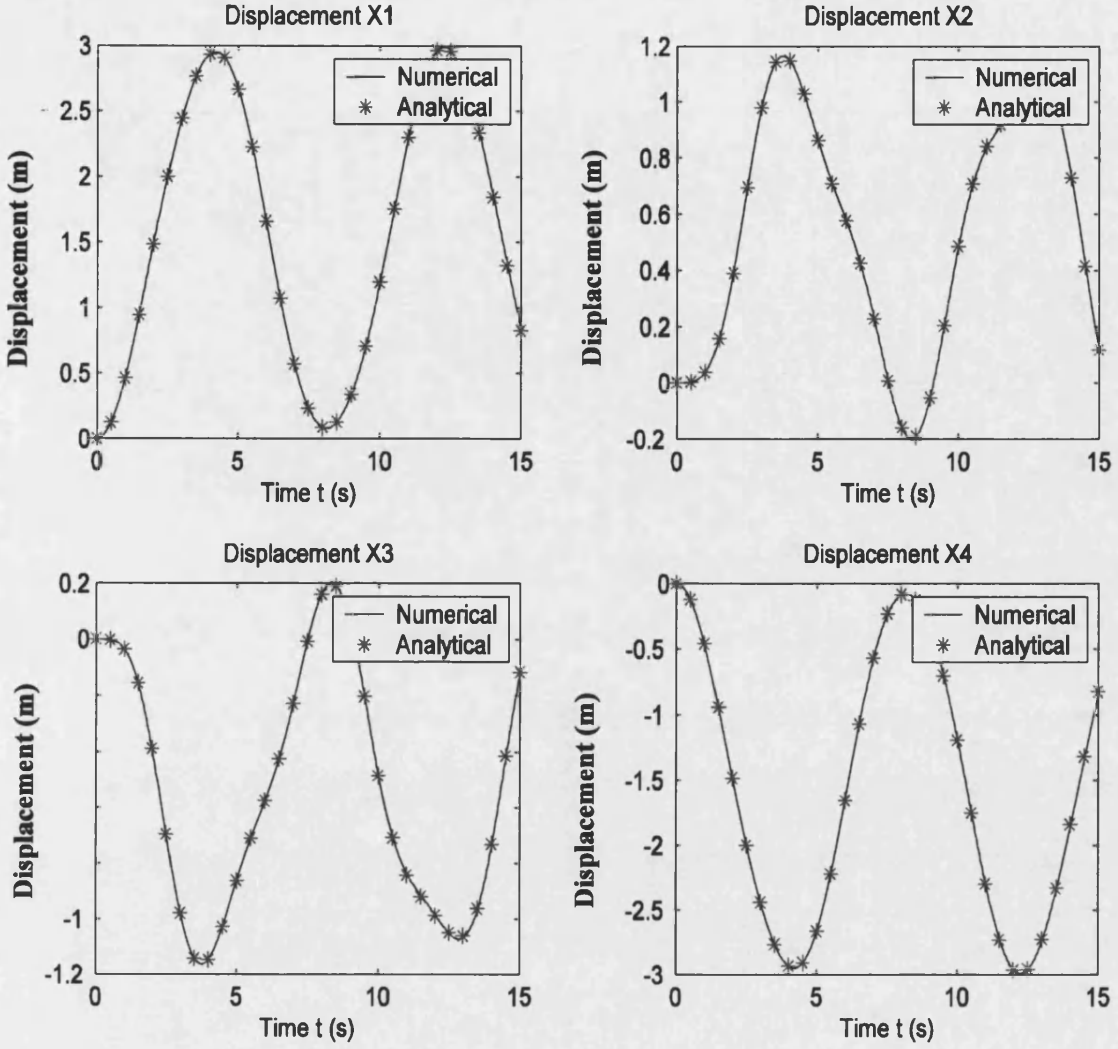


Figure 3.7: Numerical and analytical response of a MDOF system to impact load

### 3.3 Variable time-step scheme

From the numerical examples given above, it can be seen that for free vibration analysis, the HPD method can obtain accurate results, even with a large time step. However, for response of structure subject to an impact load the time step taken needs to be small enough to accurately represent the loading. This is because the HPD scheme assumes that the load during a time step changes linearly. In the calculation of the response of a structure subject to an impact load, it should be noted that the duration of the impact load is very short. Moreover the matrix **T**, which plays a key role in the HPD scheme, need only be generated once for a given step size since it does not depend on the form of the loading. Considering these points, the HPD method can be extended by

taking different time-step sizes during and after the impact load. During the impact load, a small time step is taken to ensure that the quickly varying load is simulated properly. After the impact, a much bigger step size can be taken to reduce computational cost whilst maintaining accuracy of response. By this extension, the HPD scheme becomes more efficient with no loss of accuracy when calculating the response of structures subject to impact load.

For the numerical simulation of the structure-impact damper system, a two time-step integration scheme is considered. After each integration step, the left clearance $d_l$ and the right clearance $d_r$ between the impact mass and the stops can be calculated from the newly obtained displacements. According to these results, the state of the system can be evaluated. If it is close to a collision, for example, if $d_l - d < 0.02d$, a small time step $\tau_s$ is taken, otherwise, a larger time step $\tau_l$ can be used.

Based on the HPD scheme as described in section 3.2, the variable time step, or two-time-step integration scheme can be developed as follows:

(1) According to the characteristic of the problem to be solved, choose a small time step $\tau_s$ and larger time step $\tau_l$.

(2) Using the same method and strategy as that employed in the constant time step scheme in section 3.2, calculate the matrix $\mathbf{T}$ corresponding to $\tau_s$ and $\tau_l$, i.e. $\mathbf{T}_s$ and $\mathbf{T}_l$.

(3) In the process of integration, while the small time step is used replace $\mathbf{T}$ with $\mathbf{T}_s$ and while a larger time step is applicable use $\mathbf{T}_l$.

To check how the variable time step high precision direct integration scheme works, the numerical example of Example 2 in section 3.2 is examined using this scheme. The small time step $\tau_s$ =*0.001*s is used during the application of the load (about *0.5* second), while a larger time step, $\tau_l$ = *0.6*s, is taken following the load application. The analytical results at the corresponding times are also calculated. The results, shown in Figure 3.8, demonstrate that the numerical result matches the analytical result very well (the maximum error being *0.8%*). Also, since after the *0.5* seconds of the load duration a much larger time step is used (*600* times $\tau_s$), the numerical simulation is much more computationally efficient whilst retaining accuracy.

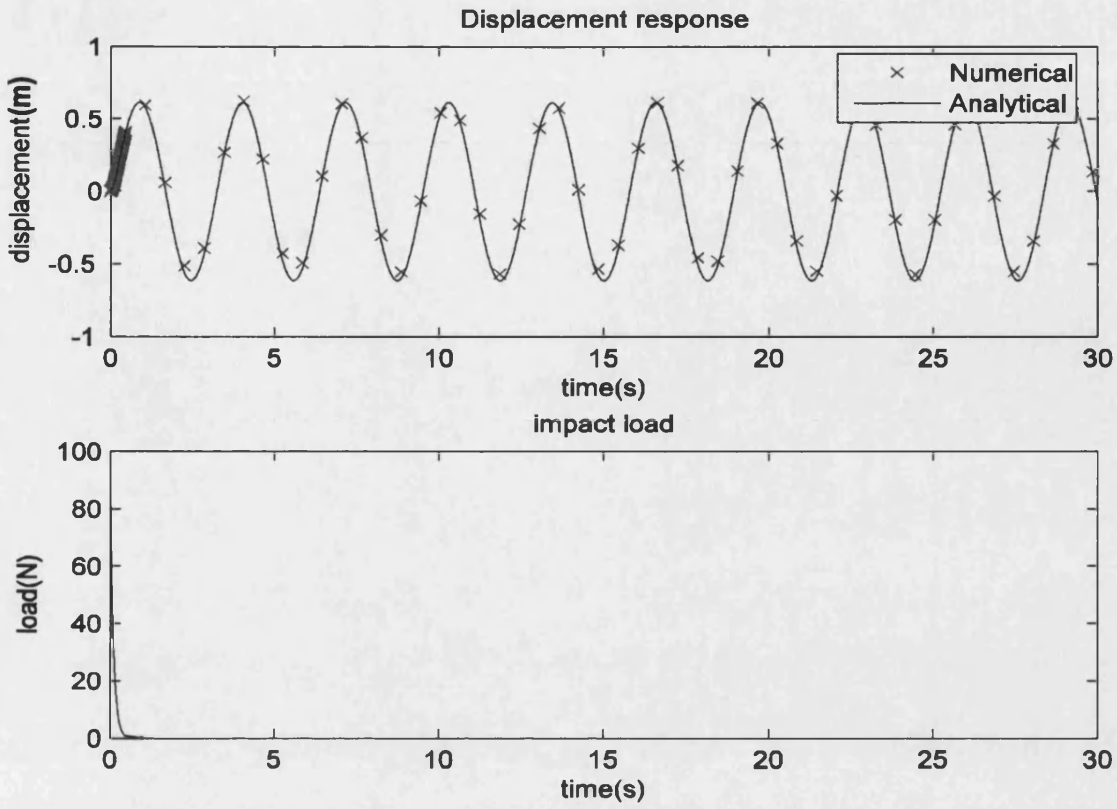


Figure 3.8: Response calculated by variable time step scheme vs. analytical result

### 3.4 HPD scheme with cubic interpolation of load

The time-step size in the HPD scheme is only restricted by the form of the loading since the applied loading is approximated by a straight line between time steps. Thus, if the load varies rapidly the time steps must be small in order to accurately represent the loading and, hence, the structural response. To eliminate this problem, Lin et al. [66] developed the HPD-F method, by prior decomposition of the applied loading between time steps into Fourier components. For this to be possible, the load must be given in an analytical form and then expanded as a Fourier series. With this additional computational effort and that needed to superpose the response of the structure to each component of the Fourier series, the HPD-F method can usually produce more accurate results than the standard HPD scheme. The HPD-F method overcomes the limitations of the HPD scheme but the computational efficiency of the algorithm is greatly reduced and there is a need for the loading to be described analytically.

By giving up the assumption of linear loading between time steps of the HPD method and instead approximating the transient dynamic loading within each time step using

cubic interpolation, the HPD method is further developed to provide accurate representation of rapidly time varying loading whilst allowing the use of relatively large time-steps to maintain computational efficiency. For the convenience of description, the original HPD method is indicated by the name HPD-L (implying a Linear approximation of the load between time steps), the HPD method using Fourier decomposition of the load by HPD-F, and that using the cubic approximation of the loading, suggested by the author, by HPD-C.

### 3.4.1 *Cubic interpolation of loading* (HPD-C)

The forcing function within a time step can be approximated by making use of the values of the load $\mathbf{f}$ at several points within a time step $(t_k, t_{k+1})$, i.e. $\mathbf{f}(t_k + \Delta t_i)$, $(\Delta t_i < \tau)$ and interpolating the load within the time step, for example, by using Lagrange cubic interpolation:

$$\mathbf{f}(t) = \mathbf{l}_0 + \mathbf{l}_1(t - t_k) + \mathbf{l}_2(t - t_k)^2 + \mathbf{l}_3(t - t_k)^3 \tag{3.29}$$

Where

$$\left.\begin{aligned} \mathbf{l}_0 &= \mathbf{f}(t_k) \\ \mathbf{l}_1 &= [-11\mathbf{f}(t_k) + 18\mathbf{f}(t_k + \tau/3) - 9\mathbf{f}(t_k + 2\tau/3) + 2\mathbf{f}(t_{k+1})]/(2\tau) \\ \mathbf{l}_2 &= 9[2\mathbf{f}(t_k) - 5\mathbf{f}(t_k + \tau/3) + 4\mathbf{f}(t_k + 2\tau/3) - \mathbf{f}(t_{k+1})]/(2\tau^2) \\ \mathbf{l}_3 &= 9[-\mathbf{f}(t_k) + 3\mathbf{f}(t_k + \tau/3) - 3\mathbf{f}(t_k + 2\tau/3) + \mathbf{f}(t_{k+1})]/(2\tau^3) \end{aligned}\right\} \tag{3.30}$$

Substituting Eq(3.29) into Eq(3.23) and carrying out the integration (letting $t = t_{k+1}$ and noting that $t_{k+1} - t_k = \tau$) gives:

$$\mathbf{u}_{k+1} = \mathbf{T}\{\mathbf{u}_k + \mathbf{H}^{-1}[\mathbf{l}_0 + \mathbf{H}^{-1}(\mathbf{l}_1 + \mathbf{H}^{-1}(2\mathbf{l}_2 + 6\mathbf{H}^{-1}\mathbf{l}_3))]\} - \mathbf{H}^{-1}\{\mathbf{l}_0 + \mathbf{l}_1\tau + \mathbf{l}_2\tau^2 + \mathbf{l}_3\tau^3 +$$

$$\mathbf{H}^{-1}[\mathbf{l}_1 + 2\mathbf{l}_2\tau + 3\mathbf{l}_3\tau^2 + \mathbf{H}^{-1}(2\mathbf{l}_2 + 6\mathbf{l}_3\tau + 6\mathbf{H}^{-1}\mathbf{l}_3)]\} \tag{3.31}$$

This is the time integration formula of the HPD-C scheme. The computational efficiency of the scheme is better than the HPD-F method and only slightly lower than that of the HPD-L method. However, considering that for same accuracy it can use a much bigger time step than the HPD-L method, it becomes more efficient.

### *3.4.2 Numerical examples*

The following examples demonstrate the accuracy and efficiency of the proposed HPD-C scheme compared with the HPD-L scheme and the standard Newmark and fourth order Runge-Kutta methods.

*Example 1*: The equation of motion of an undamped SDOF system and its initial conditions are:

$$\left.\begin{aligned} &\ddot{x} + 400x = f(t) \\ &x(0) = 0,\ \dot{x}(0) = 0 \\ &f(t) = 100e^{-5t} \end{aligned}\right\} \tag{3.32}$$

The natural frequency of the system is 20 rad/s and the corresponding period of vibration is 0.314 seconds. The analytical solution of Eq(3.32) is:

$$x = \frac{4}{17}(0.25\sin(20t) - \cos(20t) + e^{-5t}) \tag{3.33}$$

The displacement responses at times $t$ = 0.2, 2.0 and 10.0 seconds are computed with the HPD-L method, Newmark method, fourth order Runge-Kutta method and HPD-C scheme using various time-step sizes. The results are listed in Table 3.1. Also listed in Table 3.1 are the analytical results given by Eq(3.33) for comparison.

It can be seen from Table 3.1 that for each time-step size the precision of the HPD-C method is the highest. With very small time steps the fourth order Runge-Kutta, HPD-L and HPD-C methods all produce satisfactory results. However, as the time-step becomes bigger the Runge-Kutta method rapidly loses precision and ultimately becomes unstable. Compared with the Runge-Kutta method, the HPD-L method behaves better in this respect while the HPD-C method is the best. Compared with the HPD-L method the HPD-C method can use a much bigger time-step (greater than the natural period of the system) whilst maintaining a good level of accuracy. It can also be seen that the computational effort required for the HPD-C method is only slightly greater than that for the HPD-L method (around 25% greater) for a given time step, yet

the accuracy is an order of magnitude greater. It should be noted that the Runge-Kutta Method is twice as efficient as the HPD method and would therefore be more appropriate in situations where a very small time-step is required. The Newmark method has very poor accuracy for the commonly chosen values of $\beta$ and $\gamma$, although better accuracy might be achieved with different values.

Table 3.1: Comparison of time integration schemes

| Scheme | Time-step $\tau$ | Response at moment $t$ (s) | | | Max. err. (%) | CPU Time (s) |
|---|---|---|---|---|---|---|
| | | 0.2 | 2.0 | 10.0 | | |
| Analytical | | 0.19584057 | 0.20076747 | -0.16600282 | | |
| HPD-L | 0.001 | 0.19584098 | 0.20076789 | -0.16600317 | 0.0002 | 32 |
| | 0.01 | 0.19588143 | 0.20080930 | -0.16603740 | 0.0200 | 1.2 |
| | 0.1 | 0.20056148 | 0.20500044 | -0.16940022 | 2.0500 | 0.12 |
| | 1.0 | | 0.16473847 | -0.12277846 | 26.4000 | 0.04 |
| Kutta4 | 0.001 | 0.19584057 | 0.20076746 | -0.16600278 | 0.0000 | 17 |
| | 0.01 | 0.19585081 | 0.20067793 | -0.16546407 | 0.0032 | 0.8 |
| | 0.1 | 0.13559611 | 0.00068026 | 0.00000000 | 100.0000 | 0.1 |
| | 1.0 | | 10418569.3 | infinite | $\infty$ | 0.02 |
| Newmark ($\beta = 0.5$, $\gamma = 0.25$) | 0.001 | 0.19586958 | 0.20058581 | -0.16482032 | 0.7100 | 17 |
| | 0.01 | 0.19871467 | 0.18101670 | -0.02206499 | 86.7100 | 0.7 |
| | 0.1 | 0.32261760 | -0.2358417 | -0.23585236 | | 0.07 |
| | 1.0 | | -0.2376445 | 0.07926076 | | 0.02 |
| HPD-C | 0.001 | 0.19584057 | 0.20076747 | 0-.16600282 | 0.0000 | 40 |
| | 0.01 | 0.19584057 | 0.20076747 | -0.16600282 | 0.0000 | 1.6 |
| | 0.1 | 0.19584212 | 0.20076894 | -0.16600402 | 0.0007 | 0.8 |
| | 1.0 | | 0.19549907 | -0.15900593 | 4.2100 | 0.06 |

*Example 2*: The equation of motion of a damped SDOF system and its initial conditions are:

$$\left.\begin{aligned} &\ddot{x} + 0.1\dot{x} + x = f(t) \\ &x(0) = 0, \dot{x}(0) = 0 \end{aligned}\right\} \tag{3.34}$$

$f(t)$ is a bi-linear (triangular) loading:

$$f(t) = \begin{cases} 2.0t & 0 \le t \le 0.5 \\ 2.0(1.0 - t) & 0.5 \le t \le 1.0 \end{cases} \tag{3.35}$$

The natural period of the system is 6.28 seconds. The displacement response at times $t$ = *0.25, 0.5, 0.75* and *1.0* second are calculated using an analytical solution and the HPD-L, HPD-C, HPD-F, Runge-Kutta and Newmark methods. The results are listed in Table 3.2. It can be seen that in this case both the HPD-L and HPD-C methods produce equally accurate results even with large time steps since the loading varies linearly and, thus, the linear loading assumption of the HPD-L method is accurate. Similarly, the HPD-F produces equally good results but only with a substantial number of terms in the Fourier expansion of the loading and thus a substantially greater computational effort. The Runge-Kutta and Newmark methods produce significantly less accurate results even with relatively small time steps.

*Example 3*: In this example, the same SDOF system as Example 2 is used but replacing the loading with:

$$f(t) = \sin(\pi t) + 0.1\sin(20\pi t) \tag{3.36}$$

The displacement responses computed with the HPD-L and HPD-C methods with time steps of both *0.006* and *0.6* are shown in Figure 3.9. It can be seen from Figure 3.9 that for the small time step the results appear to be the same. However for the much larger time step (approximately $1/10^{th}$ of the natural period of the structure) the HPD-C method still produces accurate results whilst the HPD-L method results in significant error.

Table 3.2: Displacement response of SDOF system subject bi-linear loading

| Scheme | Time-step $\tau$ | Response at moment $t$ (s) | | | | Max err (%) |
|---|---|---|---|---|---|---|
| | | 0.25 | 0.5 | 0.75 | 1.0 | |
| Analytical | | 0.00515983 | 0.04064179 | 0.12390102 | 0.22813456 | 0 |
| HPD-L | 0.125 | 0.00515983 | 0.04064179 | 0.12390102 | 0.22813456 | 0.0000 |
| | 0.25 | 0.00515983 | 0.04064179 | 0.12390102 | 0.22813456 | 0.0000 |
| | 0.5 | | 0.04064179 | | 0.22813456 | 0.0000 |
| HPD-C | 0.125 | 0.00515983 | 0.04064179 | 0.12390102 | 0.22813456 | 0.0000 |
| | 0.25 | 0.00515983 | 0.04064179 | 0.12390102 | 0.22813456 | 0.0000 |
| | 0.5 | | 0.04064179 | | 0.22813456 | 0.0000 |
| Newmark ($\beta = 0.5$, $\gamma = 0.25$) | 1/512 | 0.00515998 | 0.04064210 | 0.12390100 | 0.22813400 | 0.003 |
| | 0.125 | 0.00537355 | 0.04172409 | 0.12398514 | 0.22720582 | 0.4100 |
| | 0.25 | 0.00759878 | 0.04494600 | 0.12424550 | 0.22445897 | 1.6100 |
| Kutta4 | 0.125 | 0.00516079 | 0.04064349 | 0.12390116 | 0.22813310 | 0.0006 |
| | 0.25 | 0.00517578 | 0.04067081 | 0.12390576 | 0.22811340 | 0.0090 |
| | 0.5 | | 0.04114583 | | 0.22787795 | 0.1100 |
| HPD-F | | | | | | |
| $q$=2 | 0.25 | 0.00471647 | 0.04010810 | 0.12281800 | 0.22689200 | 8.6270 |
| $q$=50 | 0.25 | 0.00515983 | 0.04064179 | 0.12390102 | 0.22813456 | 0.0000 |

*Example 4*: A three-storey shear structure is shown in Figure 3.10, where $M_1=M_2=M_3=500$kNs$^2$/m, $K_1=1.26\times10^8$N/m, $K_2=8.41\times10^7$N/m, $K_3=4.20\times10^7$N/m; $C_1=4.2657\times10^5$Ns/m, $C_2=2.8438\times10^5$Ns/m, $C_3=1.4219\times10^5$Ns/m. The displacement response of each storey of the building subject to an exponentially decaying dynamic loading $f(t) = 2000e^{-25t}$ acting on the top storey, is computed with the HPD-L, HPD-C,

fourth order Runge-Kutta and Newmark methods using time-steps of *0.01* seconds and *0.1* seconds. The results for the third storey are given in Figure 3.11.

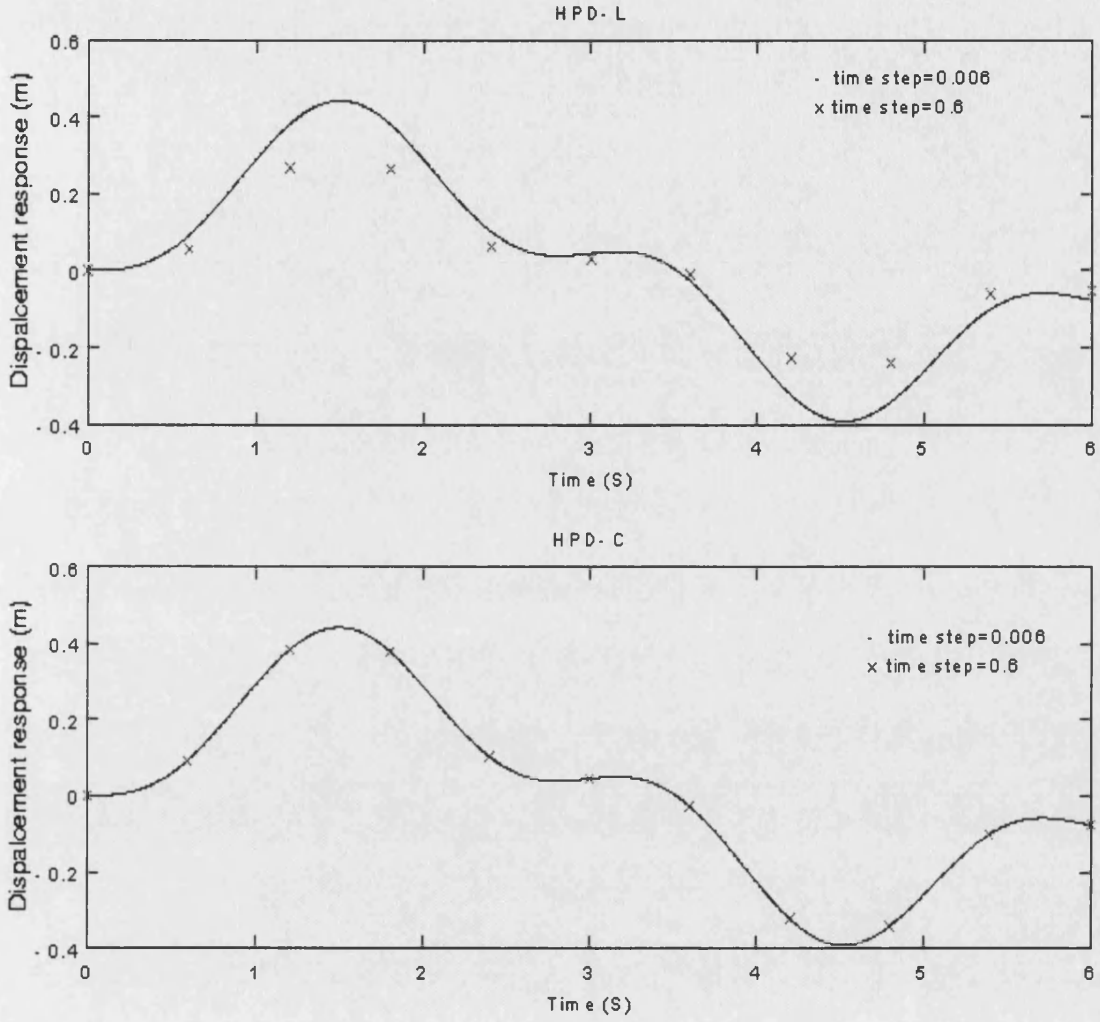


Figure 3.9: Numerical results of HPD-L and HPD-C with a small and large time step

It can be seen from these figures that when the time step is *0.01* seconds there is no obvious difference between the results given by these four methods. However, when the time step is increased to *0.1* seconds the error for both the Newmark method and the HPD-L method becomes significant. If the time step size is increased to *0.2* seconds (the figures are not included here for space saving), the Runge-Kutta method becomes unstable, the Newmark method produces a very serious error and the HPD-L method produces a significant error. The HPD-C method, however, still produces accurate results with no obvious difference between the response given by a time-step of *0.01* seconds or *0.2* seconds.

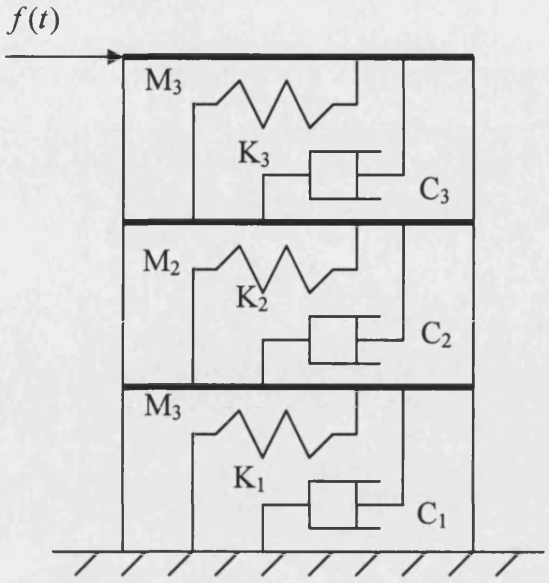


Figure 3.10: A three-storey building subject to impact loading

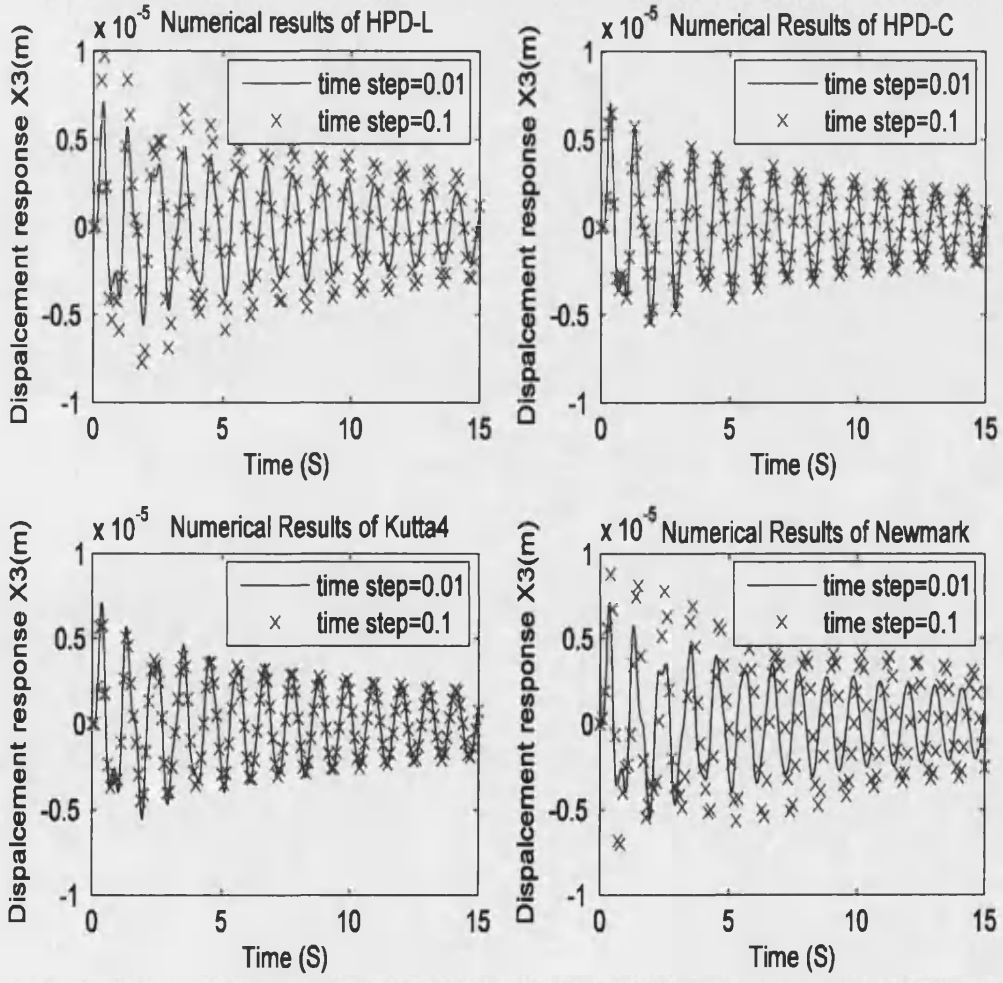


Figure 3.11: Response of the 3rd storey obtained by different numerical schemes

## 3.5 High precision direct integration scheme for non-linear system (HPD-NL)

### *3.5.1 HPD-NL scheme*

The algorithms discussed previously are all for linear systems. In the governing equations Eq(3.7), **H** is assumed to be constant, not time varying, and **f** is assumed to be only dependent on time *t*, not on the displacement or velocity of the system itself. However, **M**, **K** and/or **C** could vary both with time t and with **u** (i.e. the displacement and/or velocity of the system). In these cases, **H** is no longer constant, but varies with time and/or **u**, i.e. **H**(t, **u**). In practice, the forcing function **f** could be depend on **u** as well, i.e. **f**(t, **u**). Moreover, as pointed in Chapter 2, when the spring-damper model is employed in the modelling of a structure equipped with an impact damper, the governing equations are non-linear, even though the primary structure is linear. In such cases, the numerical schemes discussed earlier are not directly applicable. However, it is possible to modify the HPD scheme to make it applicable to non-linear systems.
An alternative form of system matrix **H** is introduced as:

$$\overline{\mathbf{H}} = \begin{bmatrix} \mathbf{0} & \mathbf{I} \\ \mathbf{B} & \mathbf{G} \end{bmatrix} \tag{3.37}$$

where

$$\mathbf{B} = -\mathbf{M}^{-1}\mathbf{K}, \mathbf{G} = -\mathbf{M}^{-1}\mathbf{C}$$

Eq(3.7) can now be written in the following form:

$$\dot{\mathbf{u}} = \overline{\mathbf{H}}\mathbf{u} + \bar{\mathbf{f}} \tag{3.38}$$

in which

$$\mathbf{u} = \left\{\mathbf{x}^T \quad \dot{\mathbf{x}}^T\right\}^T, \ \bar{\mathbf{f}} = \left\{\mathbf{0}^T \quad (\mathbf{M}^{-1}\mathbf{r})^T\right\}^T \tag{3.39}$$

The first row of Eq(3.38) simply gives the identity $\dot{\mathbf{x}} = \dot{\mathbf{x}}$ whilst the second row gives Eq(3.1), premultiplied by $\mathbf{M}^{-1}$. Compared with the system matrix given in Eq(3.8), forming $\overline{\mathbf{H}}$ on a computer becomes easier. More importantly, the null submatrix **0** and the unit submatrix **I** in the new system matrix $\overline{\mathbf{H}}$ make the manipulation and computation associated with system matrix much easier and more efficient.

As pointed out, for non-linear and/or time variant systems, the matrix $\overline{\mathbf{H}}$ is not constant but a function of time *t* and/or **u**, a vector composed of the displacement and velocity vectors of the system known as the state vector of the system.

Supposing that $\overline{\mathbf{H}}$ can be expressed as:

$$\overline{\mathbf{H}}(t,\mathbf{u}) = \mathbf{H} + \mathbf{H}_1(t,\mathbf{u}) \tag{3.40}$$

In Eq(3.40), $\mathbf{H}$ is constant matrix, and $\mathbf{H}_1(t,\mathbf{u})$ is a variable matrix depending on time $t$ and state vector $\mathbf{u}$.

Substituting Eq(3.40) into Eq(3.38) gives:

$$\dot{\mathbf{u}} = \overline{\mathbf{H}}\mathbf{u} + \bar{\mathbf{f}} = \mathbf{H}\mathbf{u} + \mathbf{H}_1(t,\mathbf{u})\mathbf{u} + \bar{\mathbf{f}} = \mathbf{H}\mathbf{u} + \mathbf{f}(t,\mathbf{u}) \tag{3.41}$$

where:

$$\mathbf{f}(t,\mathbf{u}) = \bar{\mathbf{f}} + \mathbf{H}_1(t,\mathbf{u})\mathbf{u} \tag{3.42}$$

The solution of Eq(3.41) is:

$$\mathbf{u}(t) = \exp[\mathbf{H}\cdot(t-t_k)]\cdot\mathbf{u}_k + \int_{t_k}^{t}\exp[\mathbf{H}(t-\xi)]\,\mathbf{f}(\xi,\mathbf{u}(\xi))d\xi \tag{3.43}$$

The first term in Eq(3.43) can be obtained accurately with the HPD method as discussed earlier. The key to solving Eq(3.43) lies in the second term, the integral. To carry out the integration requires calculating values of $\mathbf{f}(t,\mathbf{u}(t))$ at several points within a time step $(t_k,t_{k+1})$, i.e. $\mathbf{f}(t_k+\Delta t_i,\mathbf{u}(t_k+\Delta t_i))$, $(\Delta t_i<\tau)$ and interpolating the load within the time step by using, for instance, Lagrange cubic interpolation:

$$\mathbf{f}(t,\mathbf{u}(t)) = \mathbf{l}_0 + \mathbf{l}_1(t-t_k) + \mathbf{l}_2(t-t_k)^2 + \mathbf{l}_3(t-t_k)^3 \tag{3.44}$$

where:

$$\left.\begin{aligned}
\mathbf{l}_0 &= \mathbf{f}(t_k,\mathbf{u}(t_k)) \\
\mathbf{l}_1 &= [-11\mathbf{f}(t_k,\mathbf{u}(t_k)) + 18\mathbf{f}(t_k+\tau/3,\mathbf{u}(t_k+\tau/3)) - 9\mathbf{f}(t_k+2\tau/3,\mathbf{u}(t_k+2\tau/3)) \\
&\quad + 2\mathbf{f}(t_{k+1},\mathbf{u}(t_{k+1}))]/(2\tau) \\
\mathbf{l}_2 &= 9[2\mathbf{f}(t_k,\mathbf{u}(t_k)) - 5\mathbf{f}(t_k+\tau/3,\mathbf{u}(t_k+\tau/3)) + 4\mathbf{f}(t_k+2\tau/3,\mathbf{u}(t_k+2\tau/3)) \\
&\quad - \mathbf{f}(t_{k+1},\mathbf{u}(t_{k+1}))]/(2\tau^2) \\
\mathbf{l}_3 &= 9[-\mathbf{f}(t_k,\mathbf{u}(t_k)) + 3\mathbf{f}(t_k+\tau/3,\mathbf{u}(t_k+\tau/3)) - 3\mathbf{f}(t_k+2\tau/3,\mathbf{u}(t_k+2\tau/3)) \\
&\quad + \mathbf{f}(t_{k+1},\mathbf{u}(t_{k+1}))]/(2\tau^3)
\end{aligned}\right\} \tag{3.45}$$

It should be noted that $\mathbf{u}(t_k + \tau/3)$, $\mathbf{u}(t_k + 2\tau/3)$ and $\mathbf{u}(t_{k+1}) = \mathbf{u}(t_k + \tau)$ are unknown. They can be predicted by a method given by Bathe [68]:

$$\left.\begin{aligned} \bar{\mathbf{x}}_i &= \mathbf{x}_k + \dot{\mathbf{x}}_k t_i + (2\ddot{\mathbf{x}}_k + \ddot{\mathbf{x}}_i^e)t_i^2/6 \\ \bar{\dot{\mathbf{x}}}_i &= \dot{\mathbf{x}}_k + (2\ddot{\mathbf{x}}_k + \ddot{\mathbf{x}}_i^e)t_i/3 \end{aligned}\right\} \quad (t_i = i\tau/3, i = 1,2,3) \tag{3.46}$$

where $\ddot{\mathbf{x}}_i^e$ can be obtained by substituting

$$\left.\begin{aligned} \mathbf{x}_i^e &= \mathbf{x}_k + \dot{\mathbf{x}}_k t_i + 0.5\ddot{\mathbf{x}}_k t_i^2 \\ \dot{\mathbf{x}}_i^e &= \dot{\mathbf{x}}_k + \ddot{\mathbf{x}}_k t_i \end{aligned}\right\} \quad (i=1, 2, 3) \tag{3.47}$$

into the original governing equations.

Substituting Eq(3.44) into Eq(3.43), letting $t = t_{k+1}$ and carrying out the integration results in:

$$\begin{aligned} \mathbf{u}_{k+1} = \mathbf{T}\{\mathbf{u}_k + \mathbf{H}^{-1}[\mathbf{l}_0 + \mathbf{H}^{-1}(\mathbf{l}_1 + \mathbf{H}^{-1}(2\mathbf{l}_2 + 6\mathbf{H}^{-1}\mathbf{l}_3))]\} - \mathbf{H}^{-1}\{\mathbf{l}_0 + \mathbf{l}_1\tau + \mathbf{l}_2\tau^2 + \mathbf{l}_3\tau^3 + \\ \mathbf{H}^{-1}[\mathbf{l}_1 + 2\mathbf{l}_2\tau + 3\mathbf{l}_3\tau^2 + \mathbf{H}^{-1}(2\mathbf{l}_2 + 6\mathbf{l}_3\tau + 6\mathbf{H}^{-1}\mathbf{l}_3)]\} \end{aligned} \tag{3.48}$$

*3.5.2 Examples of the HPD-NL method*

*Example 1*: A SDOF rigid pendulum as described by Bornemann *et al.*[69] is shown in Figure 3.12. The angle, $\theta$, between the pendulum and the vertical direction, is the only d.o.f of the system, while $l$ is a constant length and $m$ is a point mass at the tip of the pendulum. The gravity field is defined in the negative $y$ direction by the constant acceleration $g$. No external or damping forces are applied.

The equation of motion of the pendulum is:

$$ml\ddot{\theta} + mg\sin\theta = 0 \tag{3.49}$$

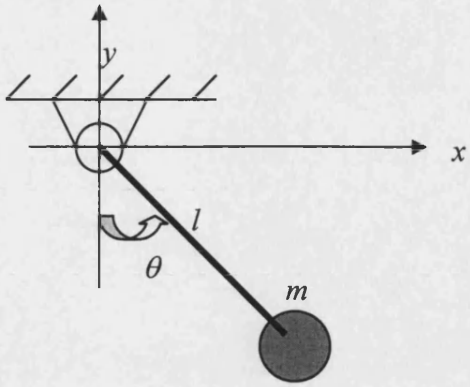


Figure 3.12: 1-DOF pendulum

The parameters are taken as: $l = 1m$ and $m = 1kg$. The initial conditions are $\theta_0 = -\pi$, $\dot{\theta}_0 = 10^{-3} s^{-1}$. The pendulum rotates continuously anticlockwise due to the initial angular velocity under the effect of gravity $g = 9.8\ m/s^2$ with constant total energy. The period of the system is $T \approx 6.47s$.

The pendulum equation Eq(3.49) is integrated from *t=0*s to *t=350*s using different time-steps. Both the $4^{th}$ order Runge-Kutta and the HPD-NL integration schemes are employed. The results are shown in Figure 3.13. When the time-step is $\tau = 0.001$ s, i.e. roughly *6500* steps per period, both the HPD-NL and Kutta 4 schemes work well and the results match very well. However, if the time step is increased to $\tau = 0.01$ s, i.e. about *650* steps per period, as Bornemann *et al.* [69] demonstrated, the algorithmic damping of the Kutta 4 scheme leads to a qualitative change in the result at $t \approx 190$ s. The pendulum oscillates rather than rotating in the subsequent integration. Therefore, as Bornemann *et al.* [69] pointed out, caution must be used when integrating even very simple non-linear systems with the popular fourth order Runge-Kutta explicit algorithm. From Figure 3.13, it can be seen that if the time step is further increased to $\tau = 0.05$ s, i.e. about *130* steps per period, errors occur soon after the start of the integration. In contrast, the HPD-NL scheme can still produce an accurate result even with a time step of $\tau = 0.05$ s. In other words, to produce a result with approximately same accuracy, the Kutta 4 method needs to calculate 350000 steps while the HPD-NL scheme need only

calculate 7000 steps. Moreover, with a large time-step, the Kutta 4 method may lead to a result that is completely wrong, not just inaccurate.

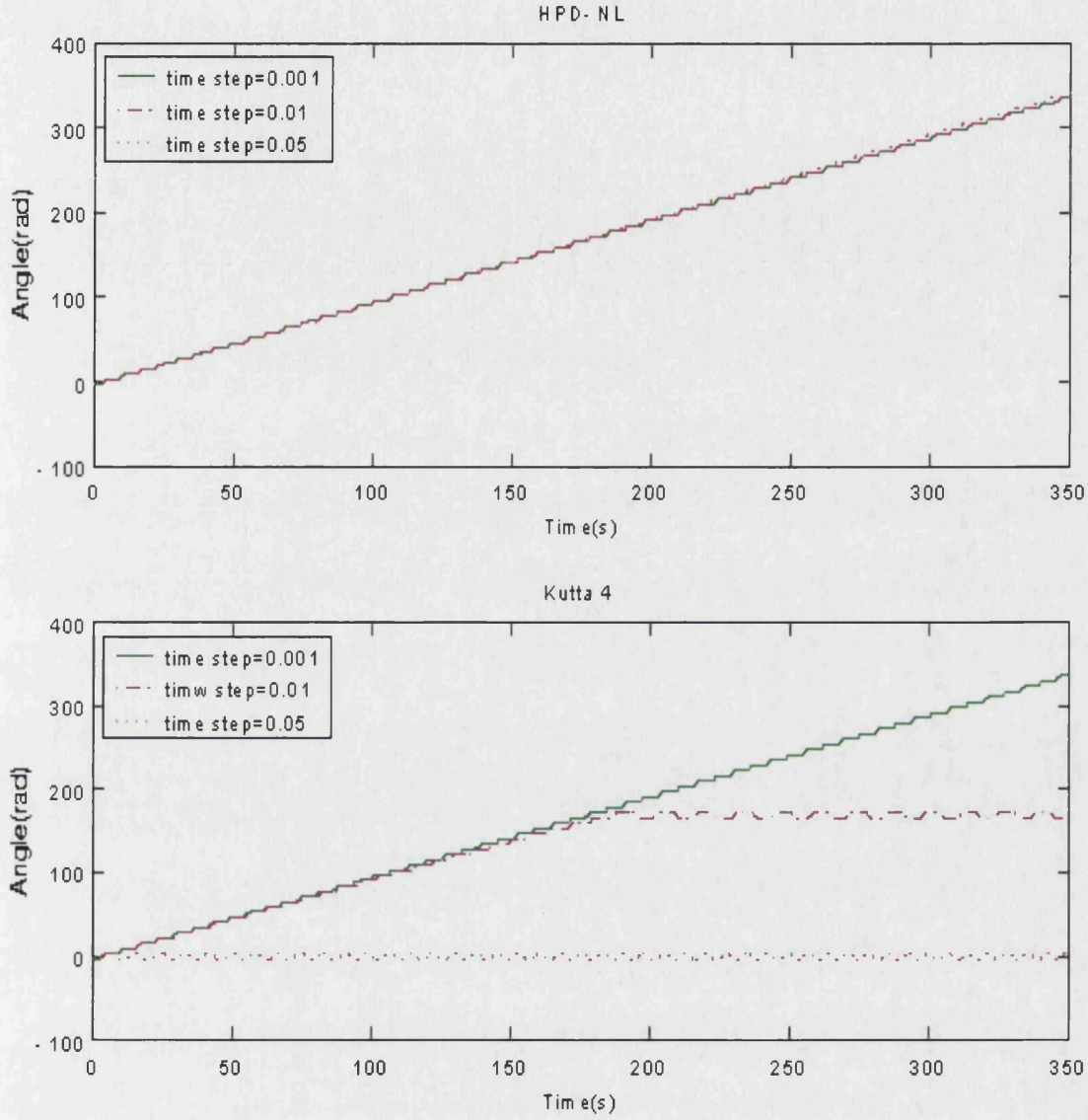


Figure 3.13: Angle versus time with different time steps

*Example 2*: A SDOF system with a hardening spring [70] can be described by:

$$\ddot{x} + 100x(1 + 10x^2) = 0 \tag{3.50}$$

The initial conditions are set at: $x_0 = 1.5$, $\dot{x}_0 = 0$.

Integration of Eq(3.50) from $t$=0s to $t$=15s was carried out with both the HPD-NL and Kutta 4 schemes respectively. The results are shown in Figures 3.14 and Figure 3.15.

From either the calculated time history responses shown in Figure 3.14 or the phase portraits shown in Figure 3.15, the good performance of HPD-NL is easily to observe, with little difference in response even for a relative large time step, in contrast with the results obtained by the Kutta 4 method.

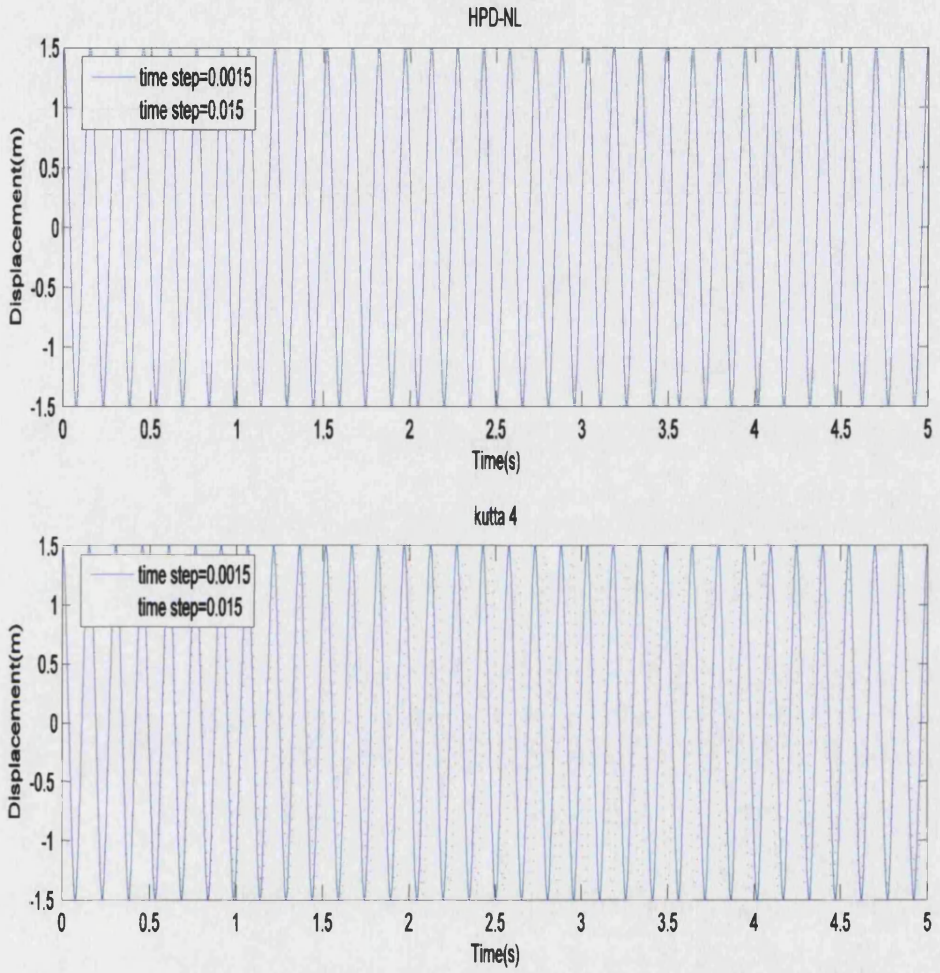


Figure 3.14: Displacement responses obtained by the HPD-NL and Kutta 4 integration schemes for different time-steps

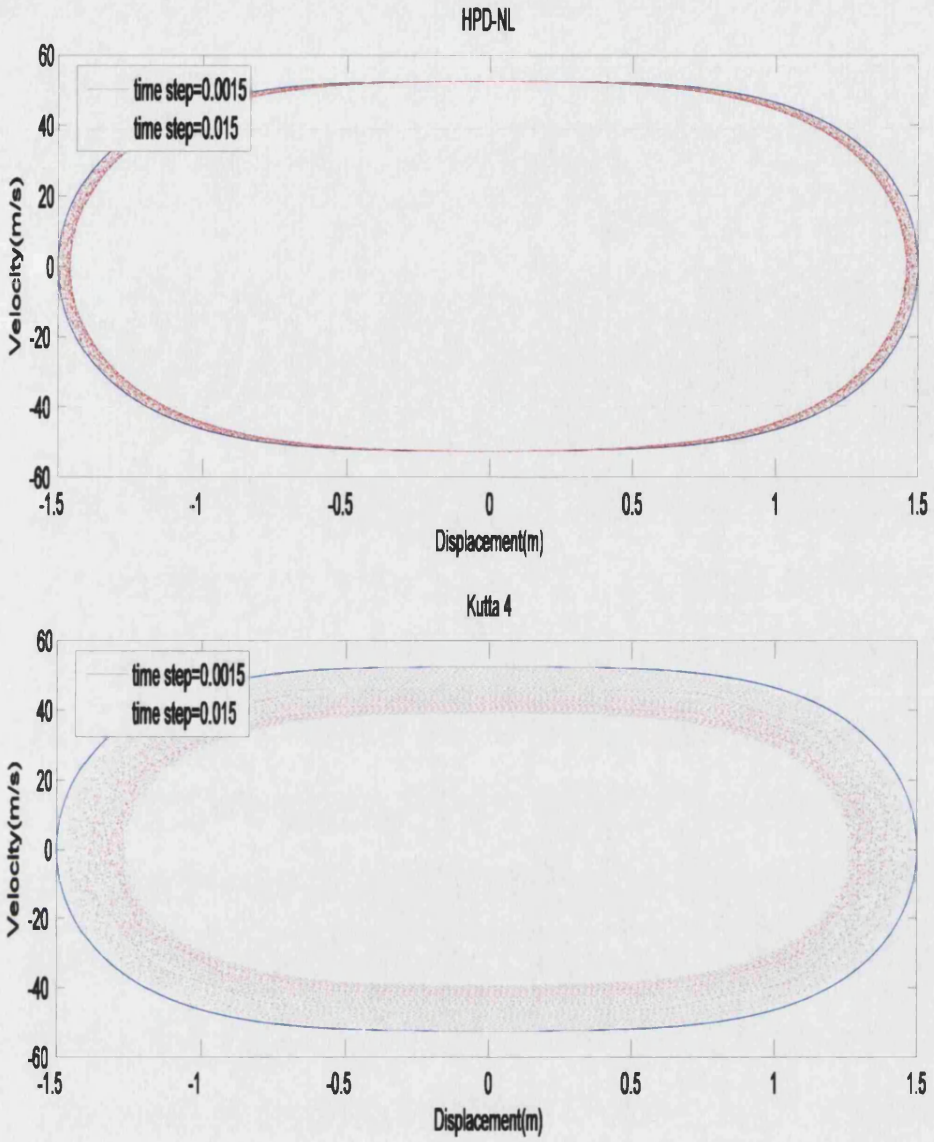


Figure 3.15: Phase portraits obtained by the HPD-NL and Kutta 4 integration schemes for different time-steps

*Example 3*: A 2-DOF system, a SDOF system equipped with a pendulum damper, is shown in Figure 3.16. The governing equations of the system are:

$$(M+m)\ddot{x} + c\dot{x} + kx + m\rho\ddot{\theta}\cos\theta - m\rho\dot{\theta}^2\sin\theta = F(t) \tag{3.51a}$$

and

$$\frac{7}{5}\rho\ddot{\theta} + g\sin\theta + \ddot{x}\cos\theta = 0 \tag{3.51b}$$

where $\rho = R - r$, and $r$ is the radius of the rolling ball.

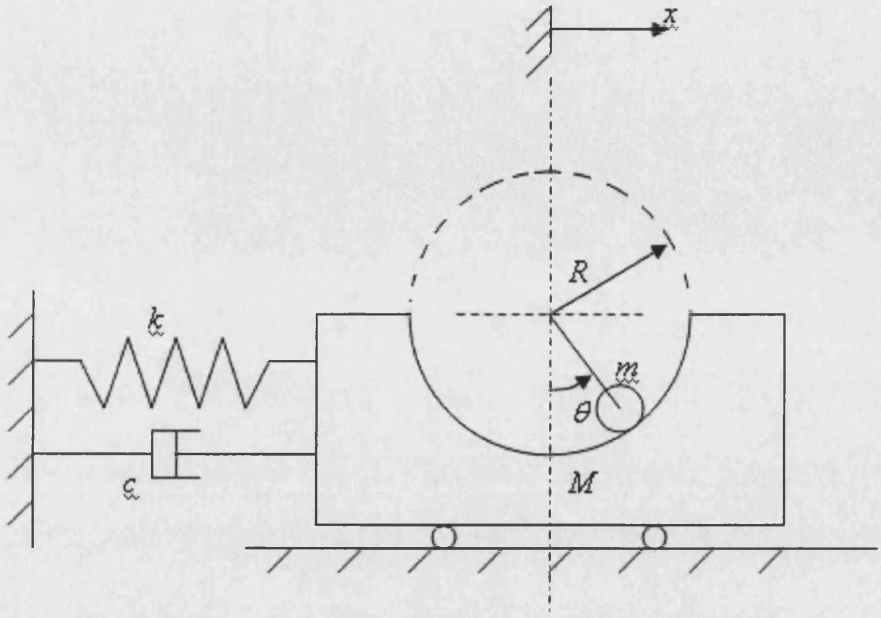


Figure 3.16: Spherical pendulum damper

Setting $M$=1kg, $k$=4N/s, $c$=0.08Ns/m and $m$=0.05kg, the natural frequency of the primary system is $\omega_1 = \sqrt{\frac{k}{M}}$ =2 rad/s. The applied excitation is $F(t) = 0.5\cos 2t$, i.e., the excitation frequency is applied at the natural frequency of the primary structure. The frequency of the pendulum damper, $\omega_2 = \sqrt{\frac{5g}{7\rho}}$, is the tuned frequency. The HPD-NL scheme is applied to integrate the non-linear governing equations of this 2-DOF system when the damper is tuned to $\omega_2 = 1.41 rad/s$ and $\omega_2 = 2 rad/s$ respectively. The time step taken in the integration is 0.01s. The results are shown in Figure 3.17. The results compare very well with the integration carried out with the Runge-Kutta method with a smaller time step of 0.0005, although these results are not presented for clarity. From Figure 3.17, it can be seen that when the tuned frequency equals the excitation frequency, the response of the primary system is mitigated effectively, as would be expected.

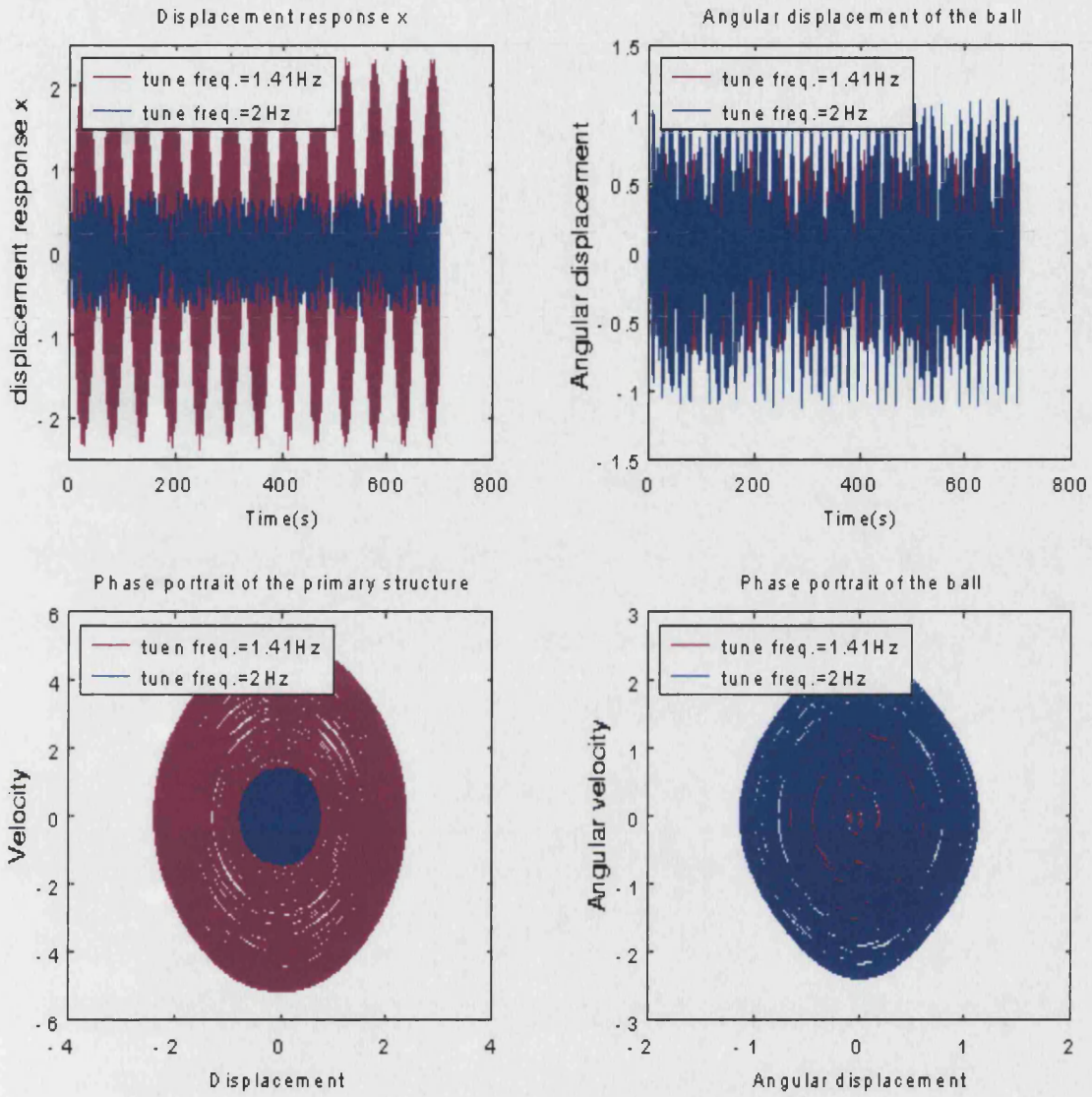


Figure 3.17: Responses of 2-DOF non-linear system obtained by HPD-NL scheme

# Chapter 4

# Experimental System

Introduction: In order to evaluate the effectiveness of impact dampers for structural dynamic control and to check the numerical simulation, two small-scale structures, a shaking table and the associated test apparatus have been constructed. Signal generation and data acquisition software has been developed for the experimental system. Signal processing software has also been developed for analysing the results. To allow the shaking table to produce accurate movement, a PID controller is developed and incorporated into the experimental system. The good tracing ability and the robustness of the controller are demonstrated.

## 4.1 Experimental structures

A three-storey shear frame, represented in Figure 4.1, was chosen as an experimental structure to be controlled, i.e. the primary structure. The test frame is composed of two sets of flexible columns made from steel strips with a $40 \times 1mm$ cross-section and three beams made of aluminium alloy with a $40 \times 30mm$ cross section. The beams are fixed to the columns by bolts. The whole frame is fixed to a unidirectional shaking table that is driven by an electro-dynamic shaker to allow base excitation to be applied.

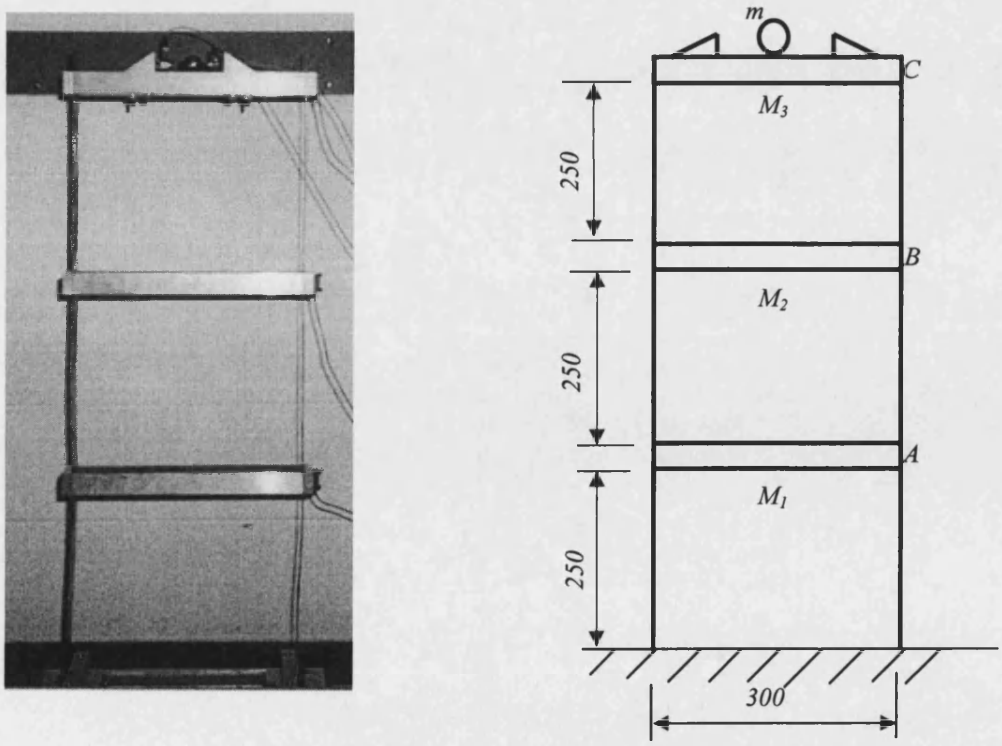


Figure 4.1: Three-storey test structure

Two triangular shaped aluminium brackets are mounted on the top storey of the structure to acts as motion-limiting stops for the impact mass. The clearance between the stop brackets is adjustable. The impact mass is a steel ball which rolls in a groove cut into the top beam.

As shown in Figure 4.2, a second test structure was constructed in order to represent a SDOF primary structure. The structure is composed of two sets of flexible columns made from steel strips with a $40 \times 1\,mm$ cross section and a single beam that is made from aluminium alloy with a $40 \times 30\,mm$ cross section.

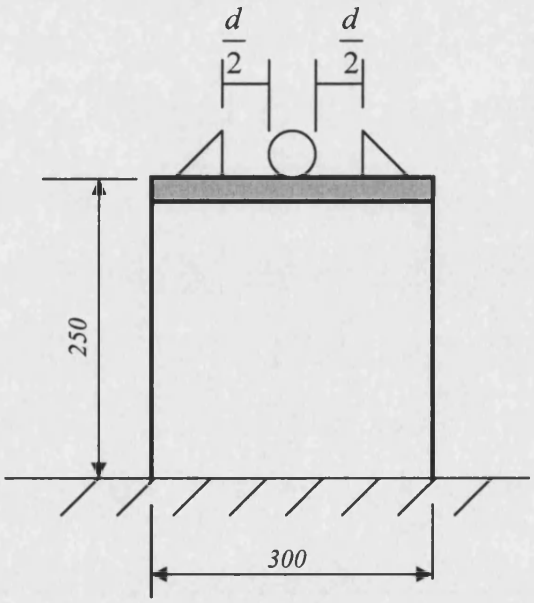


Figure 4.2: SDOF Experimental model

**4.2 Experimental set-up**

The full experimental set-up is shown in Figure 4.3 and diagrammatically in Figure 4.4. A personal computer with an analogue-digital/digital-analogue (AD/DA) board works as a controller to generate and control the excitation signal to the shaker, and allow data acquisition. All these functions were obtained by software developed specially for this project.

The computer outputs a signal to an APS Dynamics Model 114-EP power amplifier, which in turn drives an APS Dynamics Model 113 electro-dynamic shaker. The shaker is attached to shaking table via a thin rod. The shaking table rests on the linear bearings

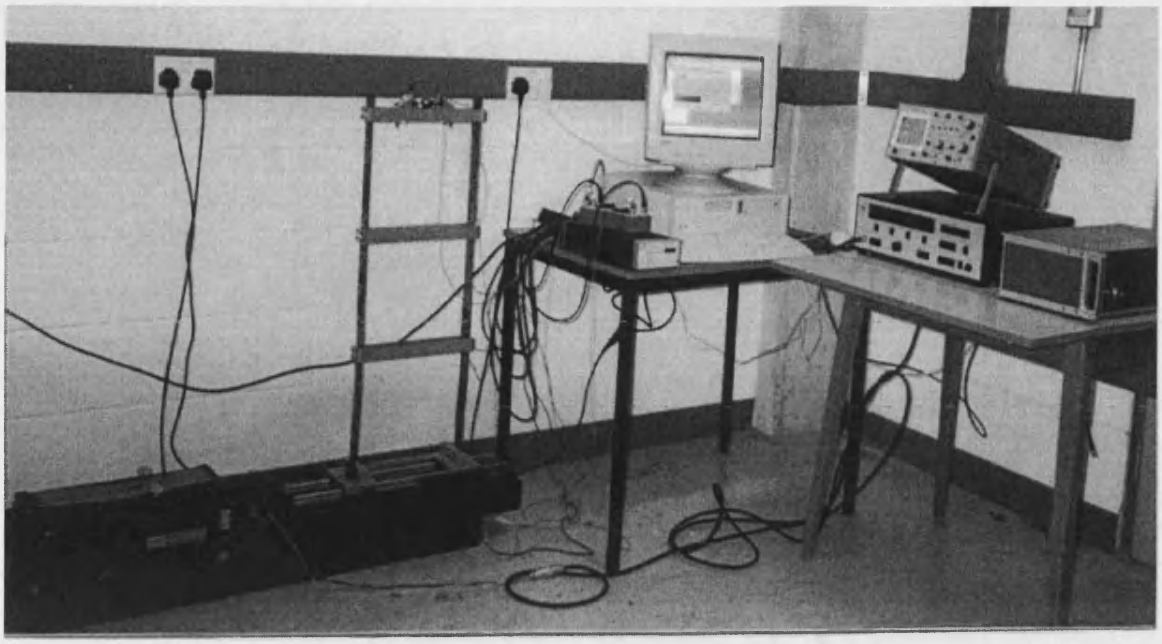

Figure 4.3: Photo of the experimental set-up

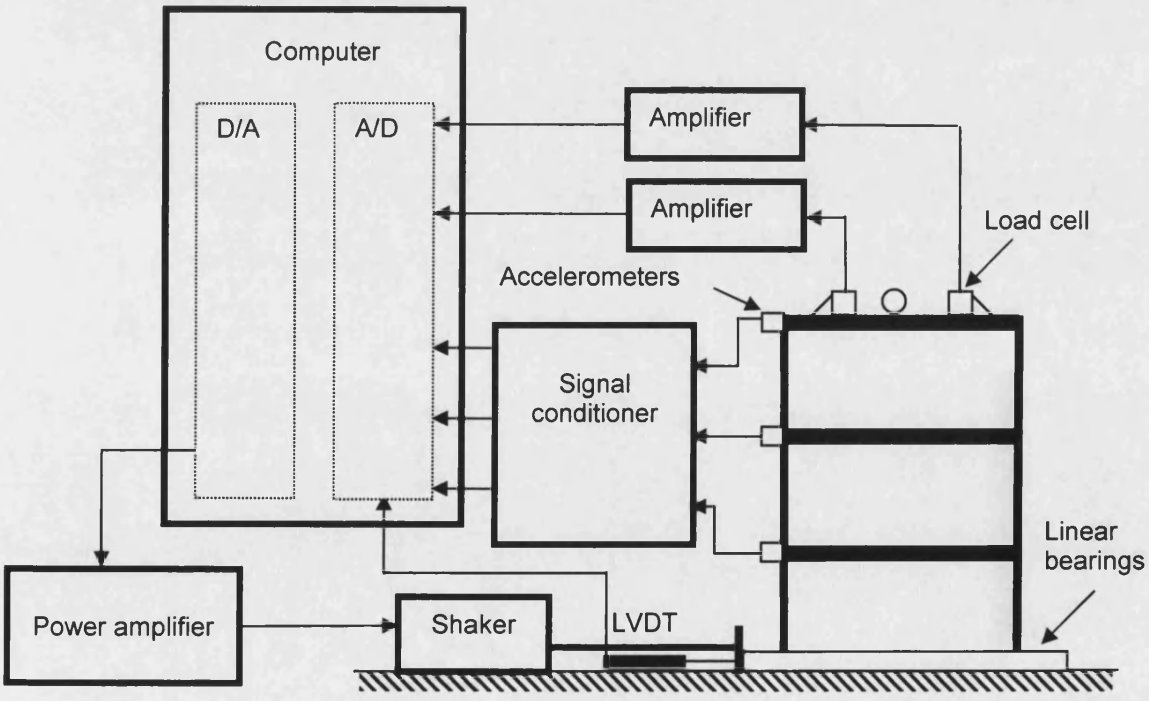


Figure 4.4: Experimental set-up

fixed to a heavy bracket on the floor. ENDEVCO Model 7596-30 variable capacitance accelerometers (capable of measuring to DC levels with a high shock limit and high sensitivity) were fixed at each floor level of the structure. Response signals from accelerometers were sent to a Model 136 EVDEVCO DC differential voltage amplifier. Additionally, a displacement transducer was fixed to the shaking table to measure the displacement response of the shaking table. Both of the motion limiting stops were equipped with PCB M208C02 force transducers that were used with PCB Model 480C02 sensor signal conditioners to gain an initial understanding of the impact forces. The acceleration, displacement and force measurements could be sent to the computer via the analogue/digital board.

## 4.3 Shaking table control with a PID controller

### *4.3.1 Why a controller is needed*

Shaking tables have been widely recognised as a fundamental tool in the examination of the dynamic behaviour of civil engineering structures subject to earthquakes. They have also become essential in order to improve modelling techniques, as well as to verify new mitigation strategies. To examine the dynamic behaviour of structures subject to earthquakes, the shaking table should be able to accurately simulate earthquake motion. In order to reproduce a desired acceleration or displacement record, two approaches can be used. In the first approach, the characteristics of a dynamic signal with a proper spectrum are produced. The second approach attempts to reproduce the signal in the time domain. For historical earthquake record reproduction, the latter approach must be employed.

After the experimental system was developed, an initial trial test was carried out with the Northridge earthquake record (Newhall record, X direction displacement). The performance of the shaking table is shown in Figure 4.5. From Figure 4.5, it can be seen that the measured displacement, which is produced by the shaking table, is obviously different from the desired reference displacement.

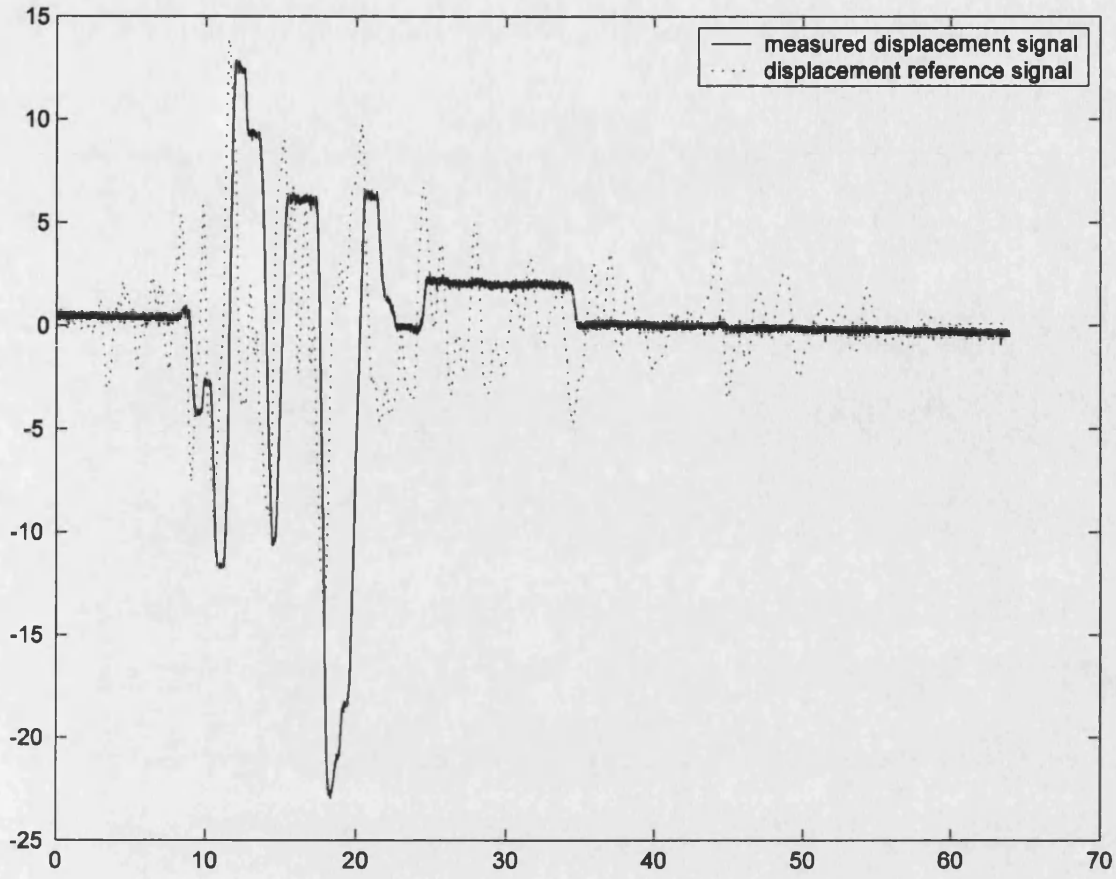


Figure 4.5: Reference and measured displacements of the shaking table

There are a number of reasons for the poor representation, such as bearing friction and non-linear effects in the electromagnetic devices of the shaker. Moreover, there is always an unwanted interaction between the test structure and the shaking table assembly. The output (acceleration or displacement) of the shaking table is altered, often decreased, at frequencies close to the natural frequencies of the structural model. As a consequence, the actual displacement signal measured during the experiment does not match the reference signal and the earthquake can not be reproduced. To improve the performance of the shaking table, or the experimental set-up to be exact, closed-loop control of the motion of the shaking table is required.

### *4.3.2 Overview of the control strategy of shaking table*

Various methods have been considered to control the motion of a shaking table. The control methods can be divided into two categories: closed-loop control methods and

open-loop control methods. For open-loop control methods, the entire command signal is determined (based on experiments) prior to testing. However, closed-loop control methods are much more popular than open-loop control methods for their high efficiency and versatility. Closed-loop systems use feedback of the table motion to alter the command signal whilst the test is in progress.

Several closed-loop control methods have been developed for shaker systems [71][72]. However, the procedures reported in the literature can not easily be implemented in the existing small-scale shaking table system. Some control methods developed for small-scale shaking tables [73] require accurate identification of the dynamic properties of the structural model, which is impractical for a general purpose shaking table set-up because the dynamics of different test structures are quite different. A feasible approach to tackle this problem might be the application of an adaptive control strategy as proposed in [71]. Another approach [74] is to separate the shaking table and test structure and develop a robust control strategy, such as sliding mode control.

A very efficient and simple control strategy that has been widely used in industrial process control is Proportional-Integral-Derivative (PID) control. The design of a PID controller can be carried out without the need for a mathematical model of the plant, which is ideal for the control of a general purpose-shaking table and, thus, has been chosen for the experimental system.

### *4.3.3 PID controller design*

Figure 4.6 is a schematic that shows how a PID controller works.

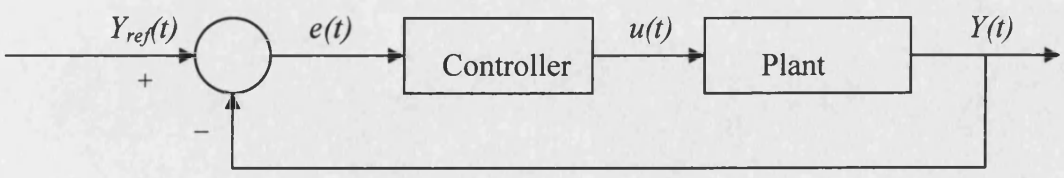


Figure 4.6: Schematic of PID Controller

In the schematic, the plant represents the system to be controlled. Here it is the shaking table and test specimen. The controller provides the input to the plant to control the

overall system behaviour. The variable *e(t)* represents the tracking error, the difference between the desired input value $Y_{ref}$ and the actual output $Y$. In the project, the control target is to make the shaking table reproduce an earthquake record. The actual output $Y$ is the measured displacement of the shaking table. If the shaking table is well controlled, $Y$ will match the earthquake record (displacement) $Y_{ref}$, i.e. if

$$e(t) = Y(t) - Y_{ref}(t) = 0 \tag{4.1}$$

the shaking table reproduces the earthquake accurately.

After calibration of the system, using the given earthquake displacement record, we can form the desired input $Y_{ref}$. It is obvious that if there is no controller, the desired input value $Y_{ref}$ can not produce an expected output $Y$ because of friction and non-linearity of the system, which makes the output highly frequency dependent. In other words, the response of the shaking table—the measured actual displacement $Y$ of the shaking table is not equal to the earthquake displacement record, i.e.

$$e(t) = Y(t) - Y_{ref}(t) \neq 0 \tag{4.2}$$

The error signal $e(t)$ is sent to the PID controller. The controller computes both the derivative and the integral of this error signal and forms an input signal $u(t)$, which equals the proportional gain $K_p$ times the magnitude of the error plus the integral gain $K_i$ times the integral of the error plus the derivative gain $K_d$ times the derivative of the error.

$$u(t) = K_p e(t) + K_i \int_0^T e(t)dt + K_d \frac{de(t)}{dt} \tag{4.3}$$

This signal $u$ is sent to the shaking table, and the new output $Y$ *is* obtained. The new output $Y$ is sent back to find the new error signal $e$. The process begins again, rapidly reducing the error.

To design a digital PID controller, the analogue operations of integration and derivation are substituted as follows:

$$\int_0^T e(t)dt = T_s \sum_{i=1}^{k} e_i \tag{4.4}$$

$$\frac{de(t)}{dt} = \frac{\Delta e_k}{T_s} = \frac{e_k - e_{k-1}}{T_s} \tag{4.5}$$

where $T_s$ is the period of sampling.

The discrete form of the controller equation is:

$$u_k = K_p e_k + K_i (T_s \sum_{i=1}^{k} e_i) + K_d (\frac{e_k - e_{k-1}}{T_s}) \tag{4.6}$$

Generally speaking, a proportional controller will have the effect of reducing the rising time and will reduce, but never eliminate, the steady-state error. An integral controller will have the effect of eliminating the steady-state error, but it may make the transient response worse. A derivative controller will have the effect of increasing the stability of the system, reducing the overshooting, and improving the transient response.

To make the shaking table applicable for various test structures, the PID controller should be made robust. To achieve this, the gains of the PID controller, $K_p$ (proportional gain), $K_i$ (integral gain) and $K_d$ (derivative gain) are designed to be adjustable in a range of *1* to *100.* It should be noticed that $K_p$, $K_i$ and $K_d$ are independent of each other.

For a given system (test structure + shaking table), without knowledge of the dynamics of the system, the PID controller can be adjusted and set up to obtain a desired response following the steps below:

1. Obtain an open-loop response and determine what needs to be improved.
2. Add proportional control to improve the rising time. The proportional gain $K_p$ can be obtained by Ziegler-Nichols method[75]:

Let $K_d = K_i = 0$, increase $K_p$ slowly until oscillation occurs in the system. The corresponding proportional gain is denoted by $K_m$ and frequency of oscillation $\omega_m$. The proportional gain is then taken as: $K_p = 0.6K_m$

3. Add a derivative controller to improve the overshooting using the expression:

$$K_d = \frac{K_p \pi}{4\omega_m}$$

4. Add an integral controller to eliminate the steady-state error using:

$$K_i = \frac{K_p \omega_m}{\pi}$$

5. Taking the values of gains as starting points, adjust $K_p, K_i$ and $K_d$ until a desired overall response is obtained.

Although all the three controllers (proportional, derivative and integral) can be included in the controller, it is often not necessary (or desirable) to implement all three. For example, if a proportional controller gives a good enough response, it is not necessary to implement a derivative controller and an integral controller into the system (the corresponding gains can be set to zero)

The PID controller was implemented using a software development program called Test Point (see the Appendix) and incorporated into the experimental system. The interface of the experimental system is shown in Figure 4.7

The gains $K_p, K_i$ and $K_d$ can be adjusted with the corresponding slider on the control panel. The tracking performance can be observed as a time history on the panel denoted Graph 1.

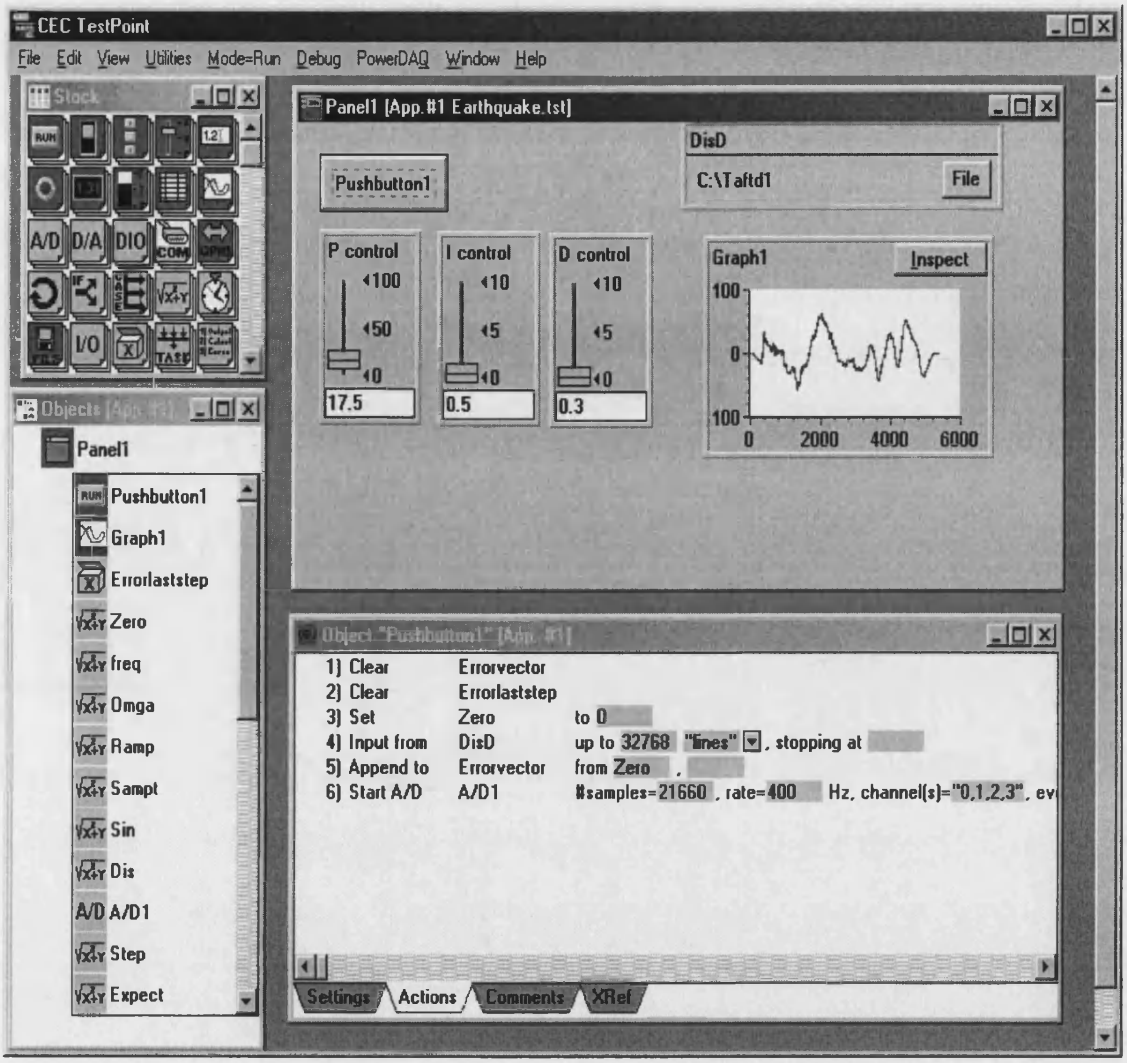


Figure 4.7: Control Panel designed for the experimental system

### *4.3.4 Results and Improvements*

The improved experimental set-up is tested for a typical laboratory experiment where the subject of the investigation is the three-storey shear frame structure. As shown in Figure 4.1, accelerometers positioned on each storey measure the absolute acceleration of the test structure. A displacement sensor located on the base measures the displacement of the shaking table, the ground excitation. This is used to feedback the response, $Y$, to the controller.

The improved experimental set-up is checked with different earthquake records. Its performance is compared with the original open-loop experimental set-up. First, the structure is excited with the Northridge earthquake record (displacement). The

measured displacement responses of the shaking table, with both controlled and uncontrolled experimental set-up, are shown in Figure 4.8.

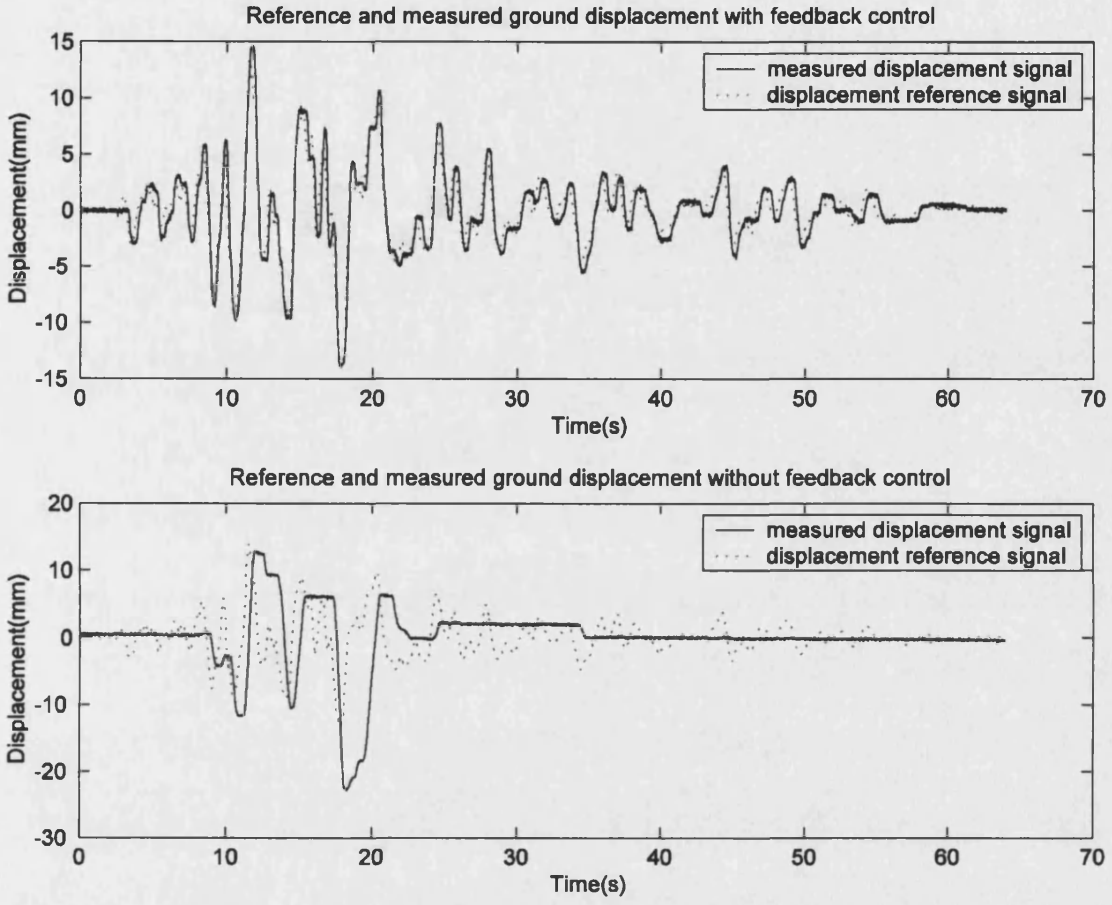


Figure 4.8: Reference and measured ground displacements (Northridge) —with and without controller

Secondly, the experimental set-up is checked with the Kobe earthquake record (JMA station, East-West). The tracking performance of both the improved experimental set-up and that of the original experimental set-up are given in Figure 4.9.

Thirdly, the El Centro earthquake record is applied. The tracking performance of both the improved experimental set-up and that of the original experimental set-up are shown in Figure 4.10.

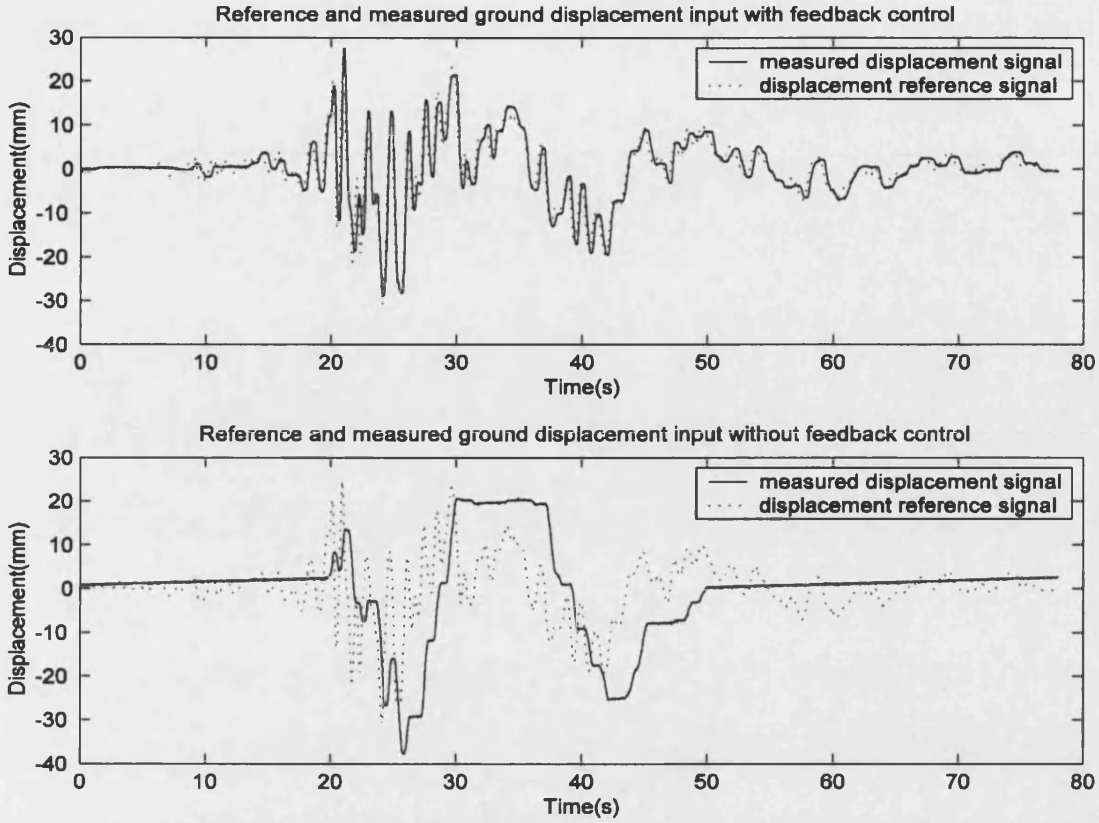


Figure 4.9: Reference and measured ground displacements (Kobe)

—with and without controller

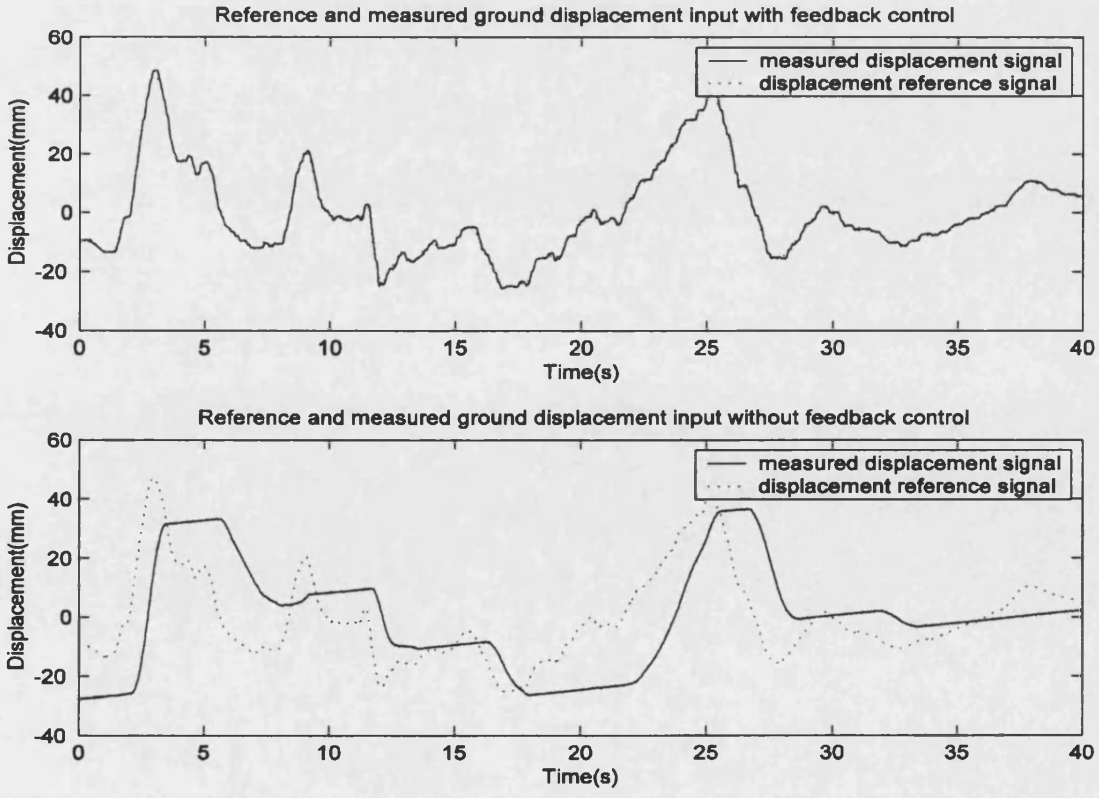


Figure 4.10: Reference and measured ground displacements (El Centro)

—with and without controller

Finally, the Taft earthquake record is employed. The tracking performance of both the improved experimental set-up and that of the original experimental set-up are shown in Figure 4.11.

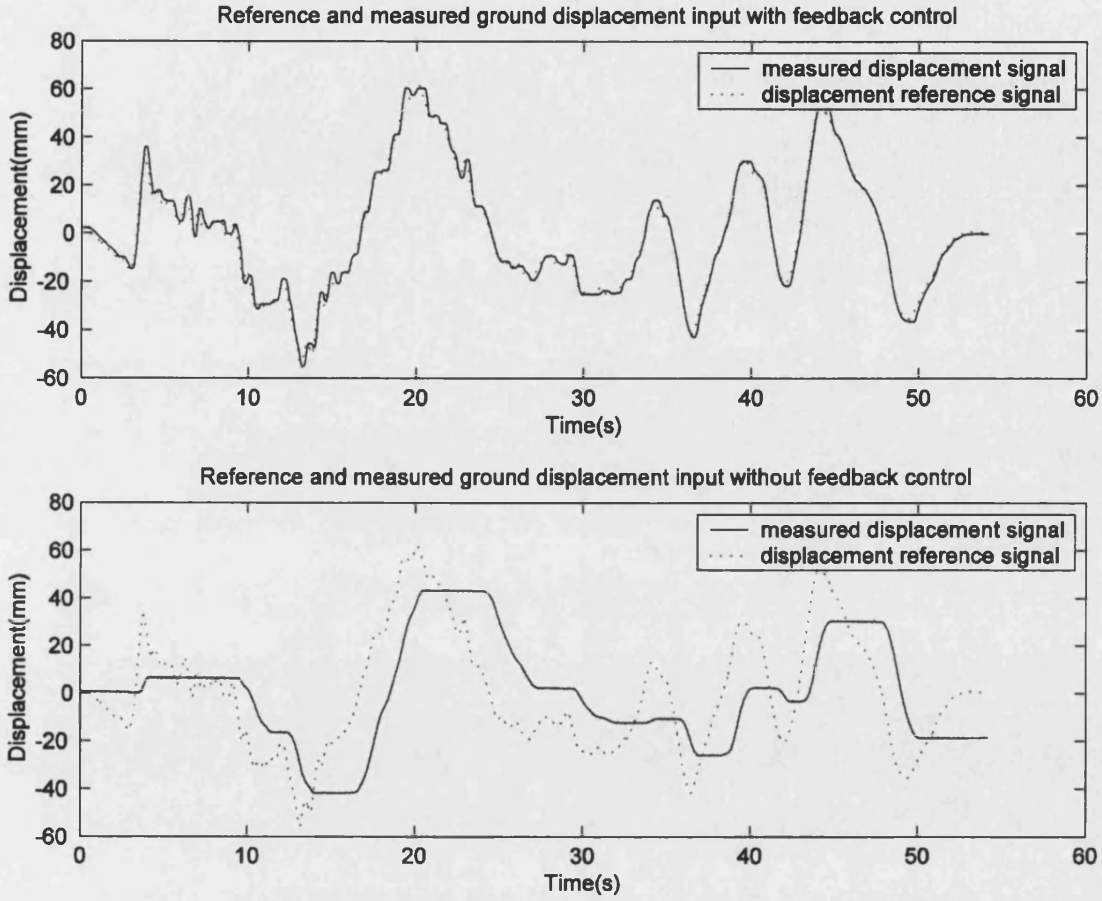


Figure 4.11: Reference and measured ground displacements (Taft)
—with and without controller

From Figures 4.8, 4.9, 4.10 and 4.11 it can be seen that the tracking performance of the controlled experimental set-up is much better than that of the uncontrolled system. Indeed, the tracking performance of the original experimental set-up is so poor that the shaking table can not reproduce a representative earthquake record.

To check if the improved experimental set-up can be used as a general-purpose system, i.e. it can be used for various test structures of quite different dynamic properties, experiments were also performed with the SDOF test structure, as shown in Figure 4.2. Figure 4.12 shows the tracking performance of controlled closed-loop set-up with four different earthquakes: Kobe, Taft, El Centro and Northridge. It can be seen that the

controlled set-up works well with this test model. Therefore, the PID controller can be used as a general purpose controller within the experimental set-up to investigate the performance of various test structures under various types of excitation.

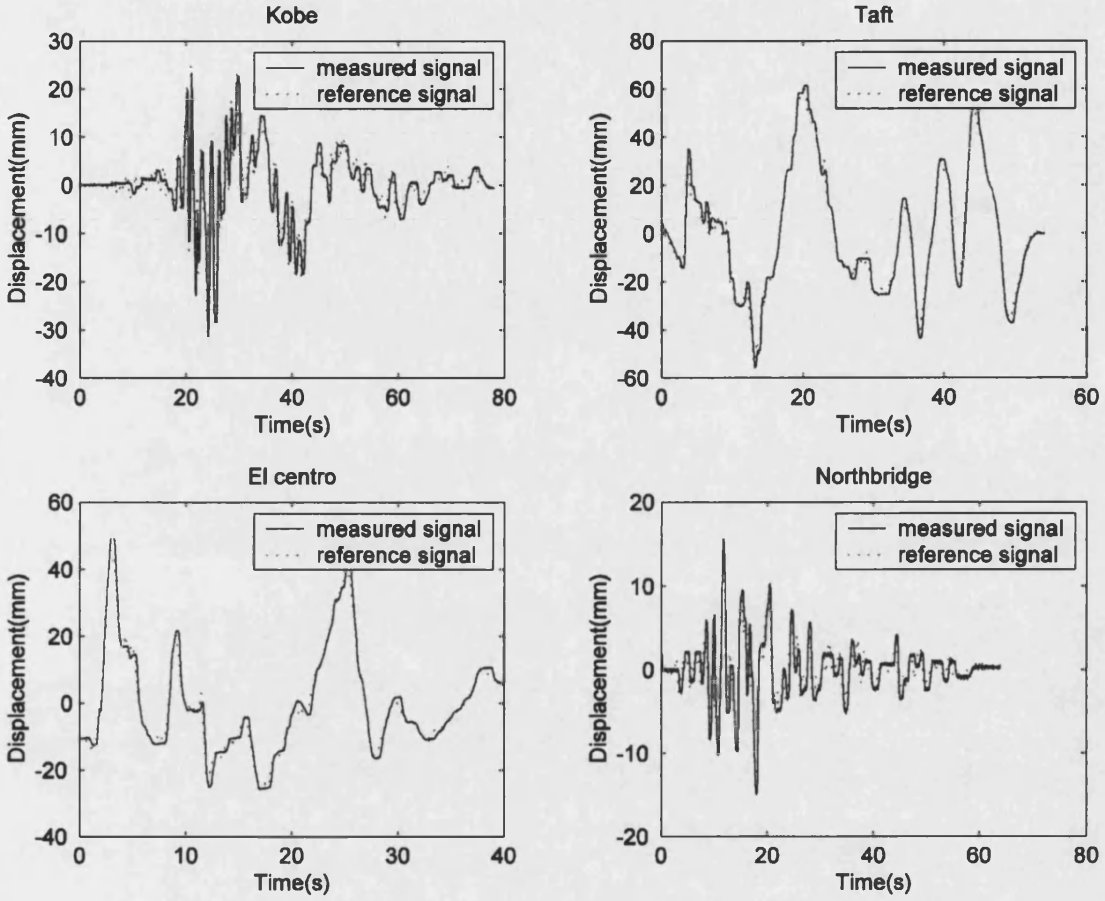


Figure 4.12: Tracking performance of the controlled experimental set-up for a SDOF test structure

*4.3.5 Remarks on the experimental set-up with a PID controller*

Although difficult to achieve, accurate base motion is essential for a shaking table to simulate an earthquake, thus forming the basis of reliable and accurate testing of structural models used for prediction of the behaviour of real structures under earthquake loading. A PID controller guarantees high robustness and easy implementation into the shaking table set-up. The controller does not need the accurate mathematical model or even the dynamics of the actual system to work satisfactorily. Experiments with different test structures and different excitations (earthquake records)

have been conducted. The results show that significant improvements over the original set-up (without controller) can be achieved. Also demonstrated are the high robustness, simple implementation and satisfying performance of the controller. The reliability and stability of the test system is also demonstrated.

# Chapter 5

## Experiments on the Effect of Impact Damper on a MDOF System

Introduction: With the closed-loop controlled experimental set-up, experimental investigations on the interaction of an impact damper with a structure were carried out. The interaction of an impact damper with a SDOF primary structure has been investigated experimentally for a number of years. Although a limited number of experiments were carried out for further understanding of the interaction of an impact damper with a SDOF primary structure, for space saving, the results are not presented here. However, there are very few investigations into the behaviour of impact dampers on MDOF structures. Presented here are the results of experimental investigations on the effect of an impact damper on a MDOF primary system under free and various forms of forced vibration. In particular, the effects of the system parameters, namely, mass ratio, excitation and clearance, on damping efficiency and system dynamics are investigated. Some results that have not been found in the study of the interaction of an impact damper with a SDOF primary system are observed. An insight into applying an impact damper for the vibration control of a MDOF primary system is offered. Also clearly revealed by the experiments is one of the main issues associated with the application of impact dampers in civil engineering, namely, the high accelerations occurring at the moment of collision.

### 5.1 Experimental structure and experimental set-up

The three-storey shear frame, described in section 4.1, was chosen as the experimental structure to be controlled (i.e. the primary system) due to its dynamic simplicity and widely spaced natural frequencies. Referring to Figure 5.1, the total clearance between the impact mass and the stops is $d = d_1 + d_2$. The parameters of the primary structure and impact damper system are given in Tables 5.1 and 5.2 respectively. The mass ratio, in this instance, is defined as the ratio of the damper mass $m$ to the mass of the top storey, $M_3$, not the total mass of the primary structure.

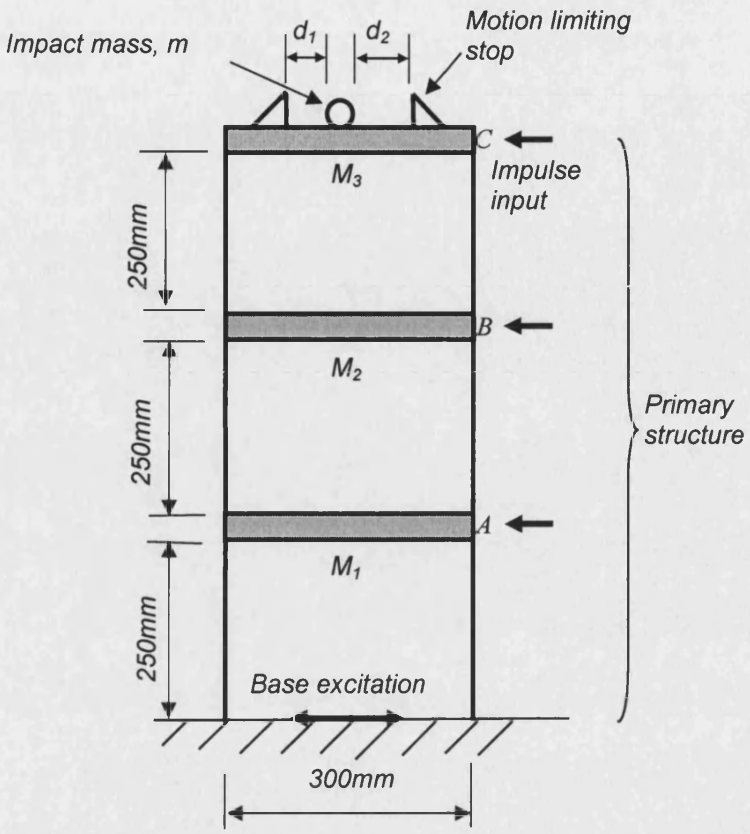


Figure 5.1: Experimental structure

Table 5.1: Parameters of the primary structure

| *Mass of each floor* | *Natural frequencies* |
|---|---|
| $M_1 = 1.105kg$<br>$M_2 = 1.105kg$<br>$M_3 = 1.350kg$ | $f_1 = 1.7685\ Hz$<br>$f_2 = 5.2185\ Hz$<br>$f_3 = 7.7210\ Hz$ |

Table 5.2: Parameters of the impact mass

| *Impact mass size* | *Mass, m* | *Mass ratio* |
|---|---|---|
| Small ball,<br>25 mm diameter | $m = 0.068kg$ | $\mu = \frac{m}{M_3} = 0.05$ |
| Medium ball,<br>30 mm diameter | $m = 0.11kg$ | $\mu = \frac{m}{M_3} = 0.082$ |
| Large ball,<br>40 mm diameter | $m = 0.26kg$ | $\mu = \frac{m}{M_3} = 0.194$ |

The complete experimental set-up is shown in the diagram of Figure 4.4. The closed-loop PID controlled set-up is employed to ensure the correct motion of the shaker is achieved.

## 5.2 Experimental procedure

Both free vibration and forced vibration tests were carried out. Free-vibration experiments were performed by striking the primary structure with a pendulum hammer released from a predetermined distance, providing an impulse input. The base of the structure, connected to the shaking table was fixed rigidly to the static base. This type of excitation reliably produces a consistent and repeatable transient disturbance capable of exciting all frequencies of the structure. The response of each storey of the structure was measured using the accelerometers. This procedure was repeated both with and without the presence of an impact damper mass for each case investigated.

The forced vibration experiments were carried out in three groups, namely, sinusoidal dwell, sinusoidal sweep and random/earthquake excitation experiments. For the dwell experiments, the base of the structure was excited at a constant frequency and amplitude. For the sine sweep experiments, a sweep rate of *0.1Hz* per second was used over the range *0.5* to *10Hz*, covering the full range of natural frequencies of the structure.

## 5.3 Experimental results

### *5.3.1Free vibration*

#### *5.3.1.1 location of excitation input*

In order to examine the effect of excitation input location, the primary structure was excited by striking with the pendulum at *A*, *B* or *C* (as indicated in Figure 5.1). Care was taken to avoid multiple strikes. During the experiments the shaking table was fixed to a static base. The mass ratio used in the experiments is $\mu = 0.082$ (i.e. the medium sized ball-bearing was used) and the clearance was kept at $d = 20\ mm$ in each case.

The acceleration time history of each storey, shown in Figures 5.2, 5.3 and 5.4, and the corresponding power spectral density (PSD) of the acceleration responses, shown in Figures 5.5, 5.6 and 5.7, relate to the excitation force acting at positions *A, B* and *C* respectively. In all cases, the dotted line represents the uncontrolled vibration and the

solid line, the response when the impact damper is used. There is a clear controlling effect of the impact damper for each storey at each mode of vibration regardless of the location of the excitation force. In all cases, at the 3rd storey, large accelerations are evident initially as the impact mass collides with the stops. The impacts rapidly reduce the response of the structure at all floor levels. Once motion of the 3rd storey is insufficient for impacts to occur (which depends upon the distance between stops, amplitude of motion and the velocity of the impact mass), the structure oscillates freely, with only internal damping of the structure itself causing the response to decay. Without the damper, there is no initial rapid reduction in response and the oscillations decay exponentially over a longer period of time, as shown by the dashed line.

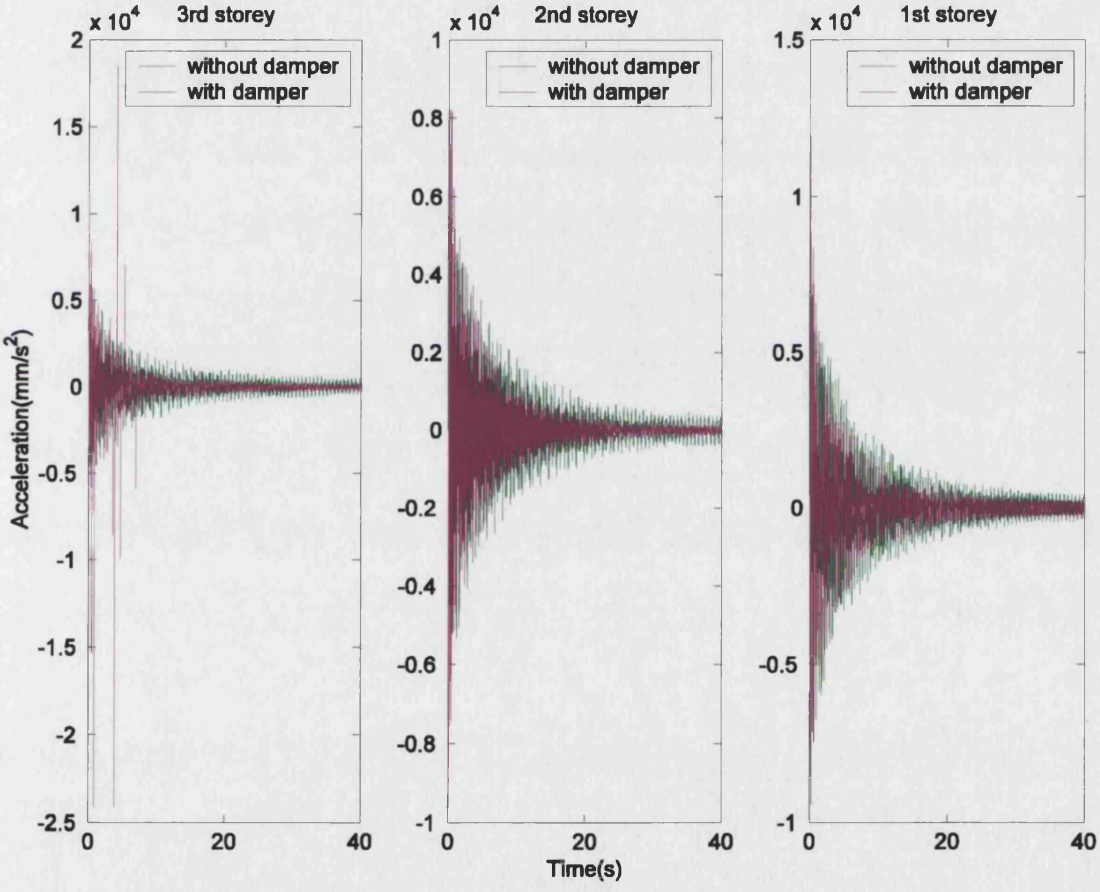


Figure 5.2: Histories of acceleration response (excitation at A)
—without and with impact damper

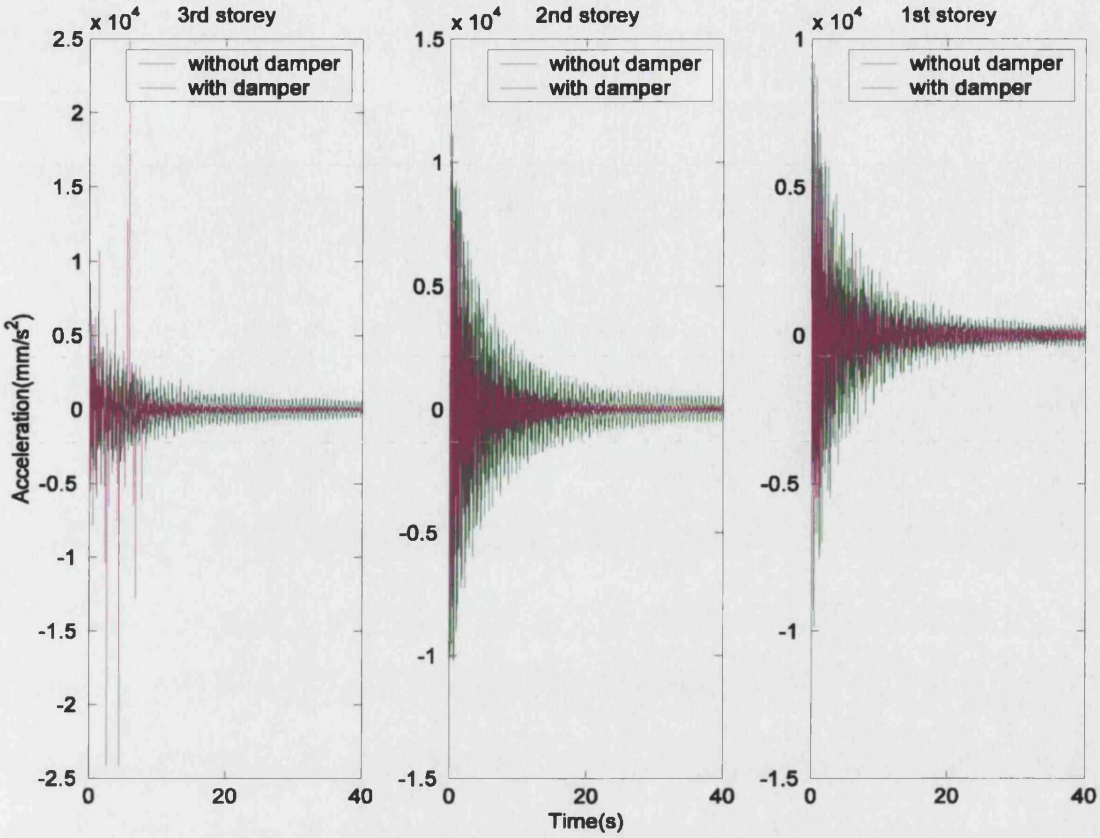


Figure 5.3: Histories of acceleration response (excitation at B)

—without and with impact damper

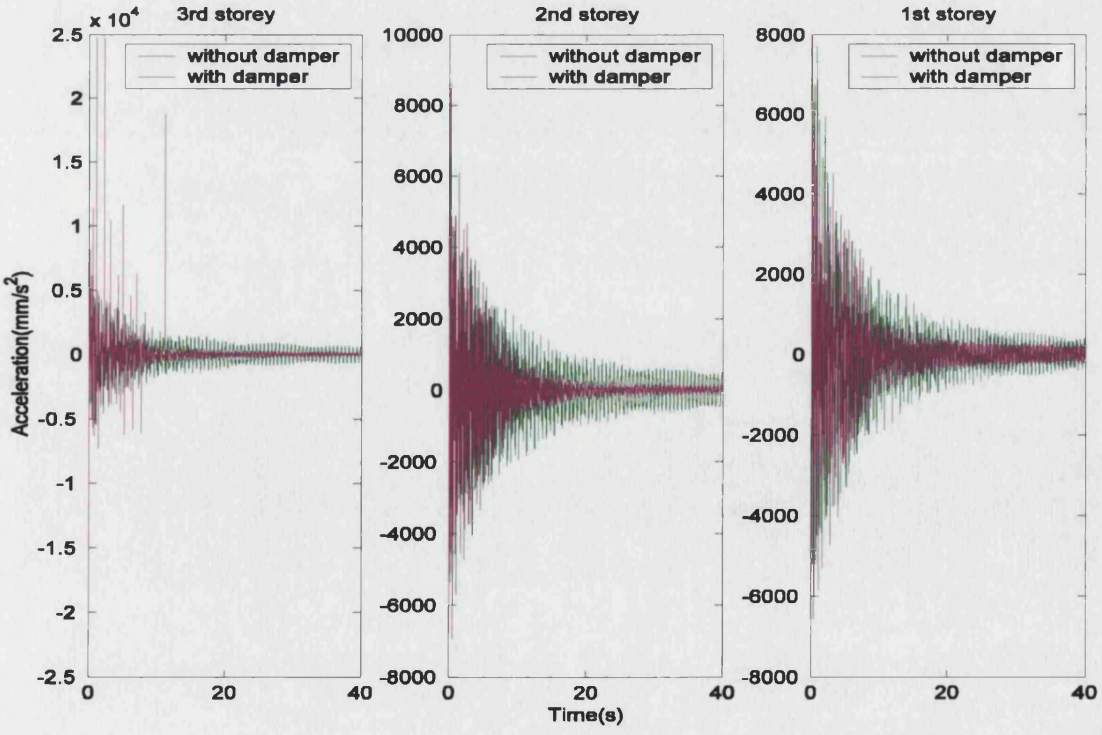


Figure 5.4: Histories of acceleration response (excitation at C)

—without and with impact damper

It can be observed in Figure 5.2, that when the excitation is at *A* (i.e. the first storey), there is initially (for the first couple of seconds) no reduction in amplitude of oscillations. The impact damper, located on the third storey, takes longer to establish effective collision, due to initially smaller amplitude motions at this storey, compared with the cases of excitation higher up the structure, at *B* or *C*. However, this does not mean impact damper shows no control effect in this case, only that there is a delay in commencement of control. Once momentum is imparted to the impact mass, the response is rapidly controlled. When the excitation is at *B* or *C*, Figures 5.3 and 5.4 respectively, the oscillations can be observed to reduce immediately from the start of excitation, indication immediate contact between the impact mass and the stops. It should also be noted that the accelerations of the third storey, where the impact damper is located, are very high at the moments of collision, although these high accelerations are not evident in the response of the other storeys. This should be taken into consideration when applying impact dampers to practical situations.

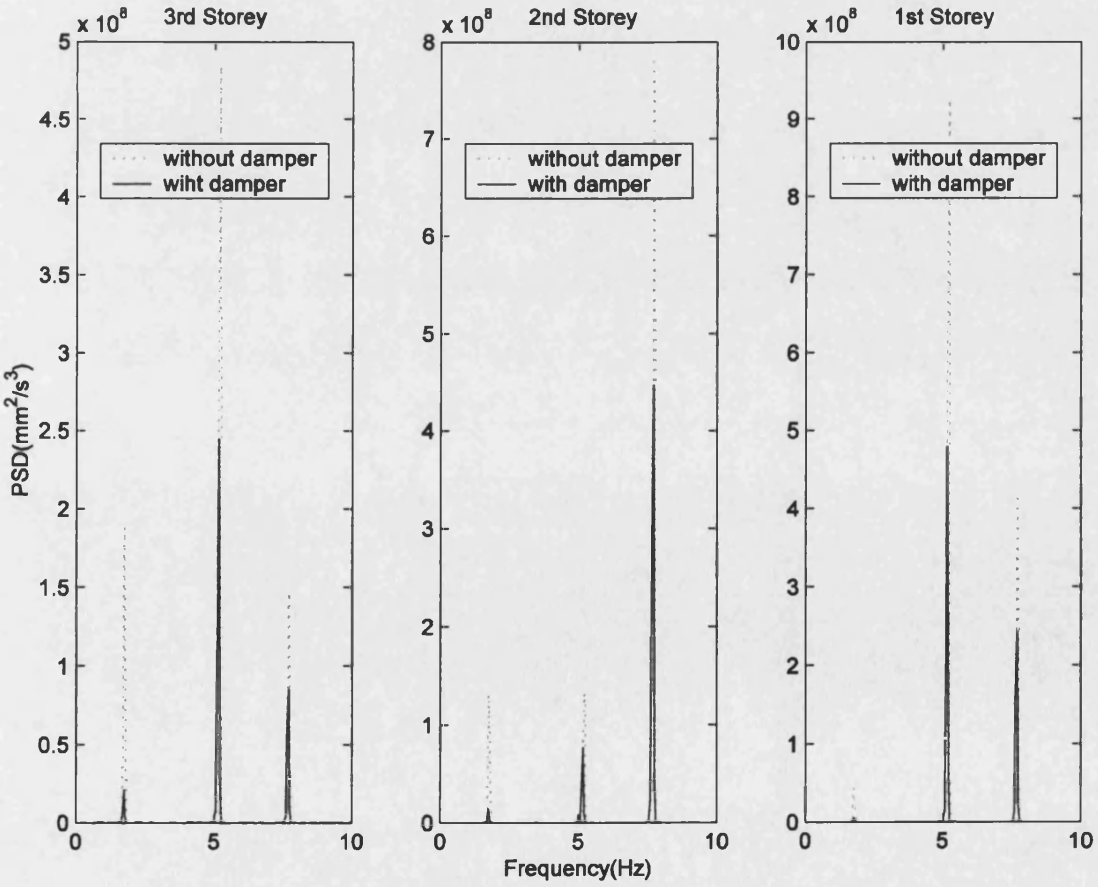


Figure 5.5: PSD of acceleration response (excitation at A)
—without and with impact damper

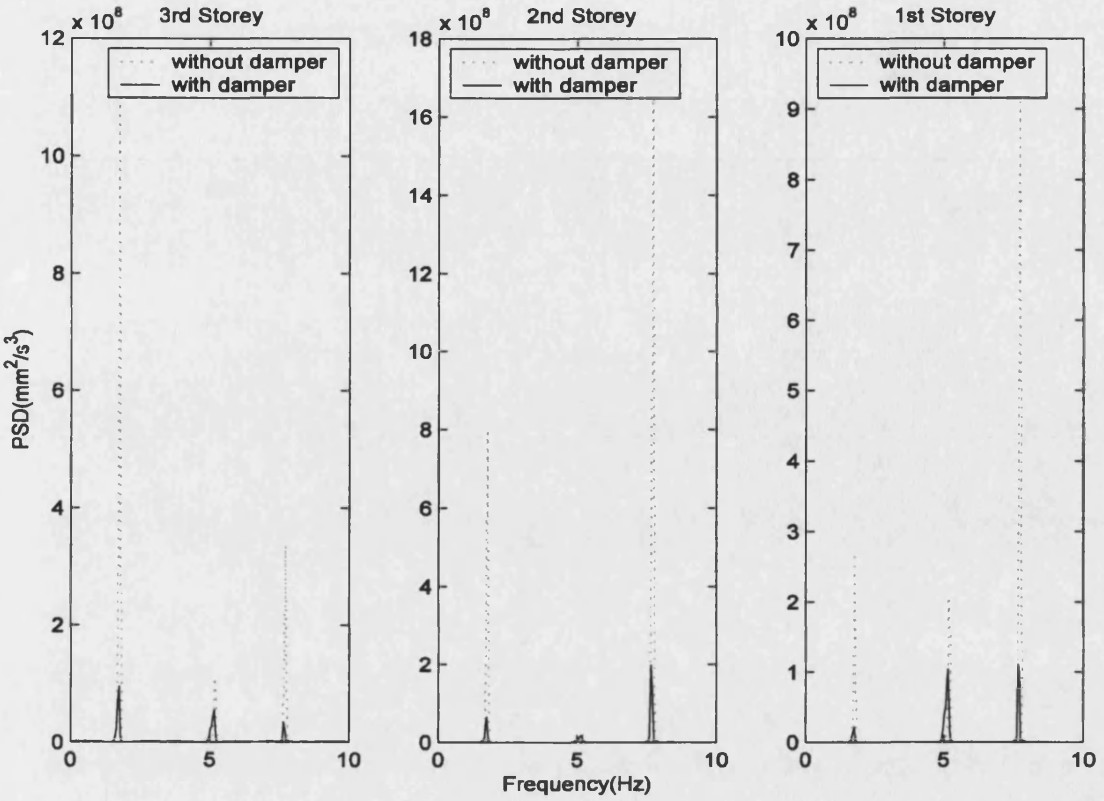


Figure 5.6: PSD of acceleration response (excitation at B)

—without and with impact damper

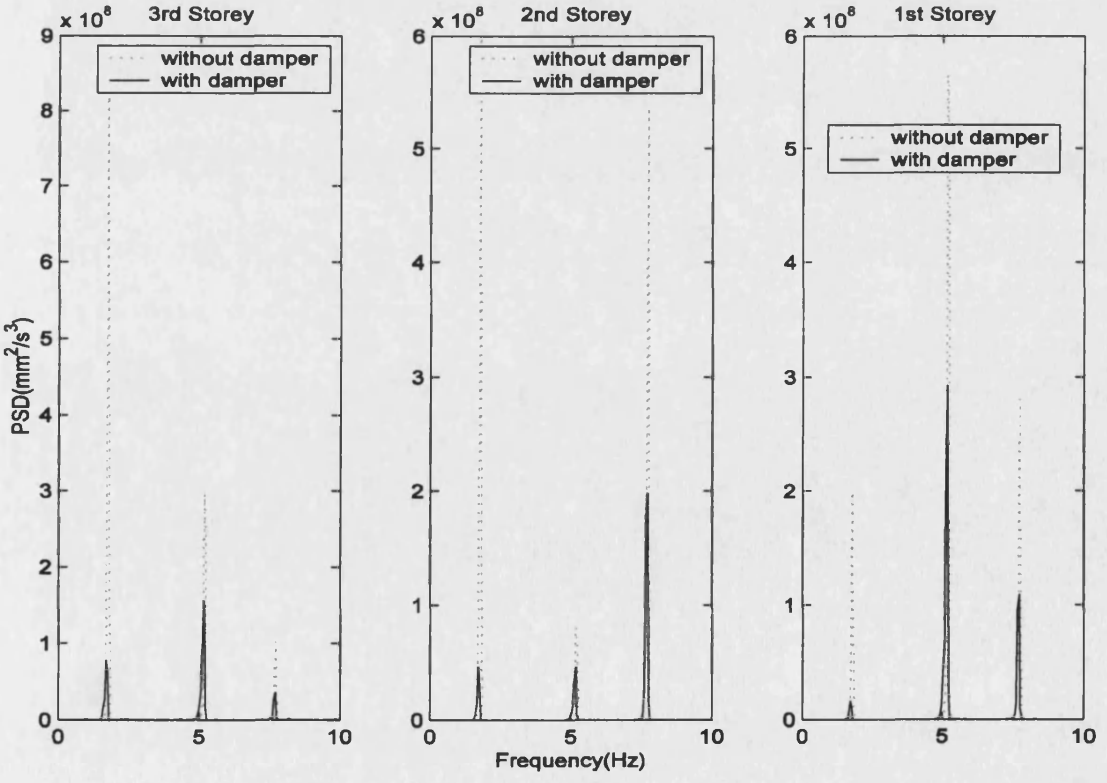


Figure 5.7: PSD of acceleration response (excitation at C)

—without and with impact damper

From Figures 5.5, 5.6 and 5.7, it can be seen that in all cases, the first mode is effectively controlled by the impact damper regardless of whether the excitation is at *A*, *B* or *C* while the control effect upon the higher modes is more clearly affected by location of excitation. In particular, comparing Figures 5.5 and 5.6, it can be observed that better control of the third mode of each storey occurs when excitation is at *B* rather than at *A*.

It can also be observed, as one might expect, that certain modes are excited more depending on where the structure is excited, leading to a more obvious control effect where the response of the mode is greatly excited. The second mode is a clear example of this, being greatly excited when the input is at 1st floor level (Figure 5.5), and reasonably well controlled by the damper, whilst being excited very little when the input is at 2nd floor level (Figure 5.6), due to this being the approximate location of an anti-node of the second mode shape (however, even for this small degree of excitation, a similar degree of control is demonstrated).

*5.3.1.2 mass ratio*

The effect of mass ratio on control effect was studied with a constant total clearance of *15* mm between the impact mass and the stops. Three different mass ratios of $\mu = 0.05$, *0.082* and *0.193* were tested and the response compared to that without the impact damper. Figure 5.8 shows the comparison between the PSDs of the acceleration response of the structure without the impact damper mass (shown by the dotted line) and the controlled responses with the three different mass ratio impact masses. The excitation is applied at 1st storey level. It can be seen that, in all cases each mode at each storey is effectively controlled when an impact damper is in operation. To more clearly show the effect of the different mass ratios, Figure 5.8 is re-plotted by focussing in on each natural frequency, as shown in Figure 5.9. Examining the response of the first mode for each storey, it is evident that a higher mass ratio results in better control, as one might expect. This is consistent with the findings of the analytical investigations of Bapat and Sankar [76] and the experimental results of Ekwaro-Osire and Desen [46] when studying the interaction of impact dampers with a SDOF primary system. A similar trend is revealed for the second mode, i.e. the higher mass ratio results in better control. It should be noted, however, that the level of control does not increase in direct proportion to the increase in size of impact mass, i.e. a doubling in size of impact mass

does not necessarily result in a doubling of control effect. More significantly, for the third mode the highest mass ratio results in the worst control effect over all storeys (although it is recognised that the overall control effect on this mode for all mass ratios is not as great as for the other two modes).

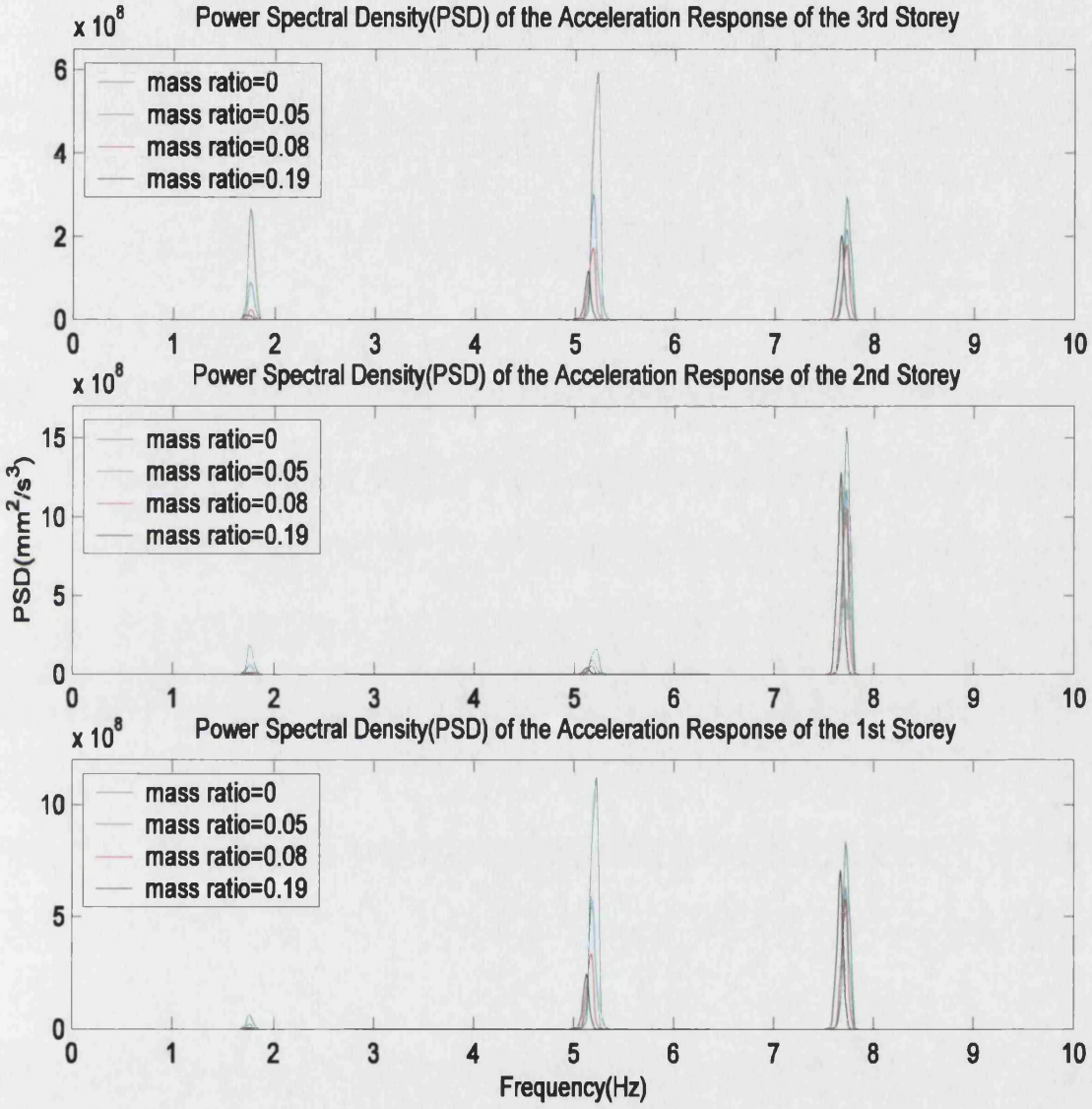


Figure 5.8: Effect of mass ratio (excitation at A)—free vibration

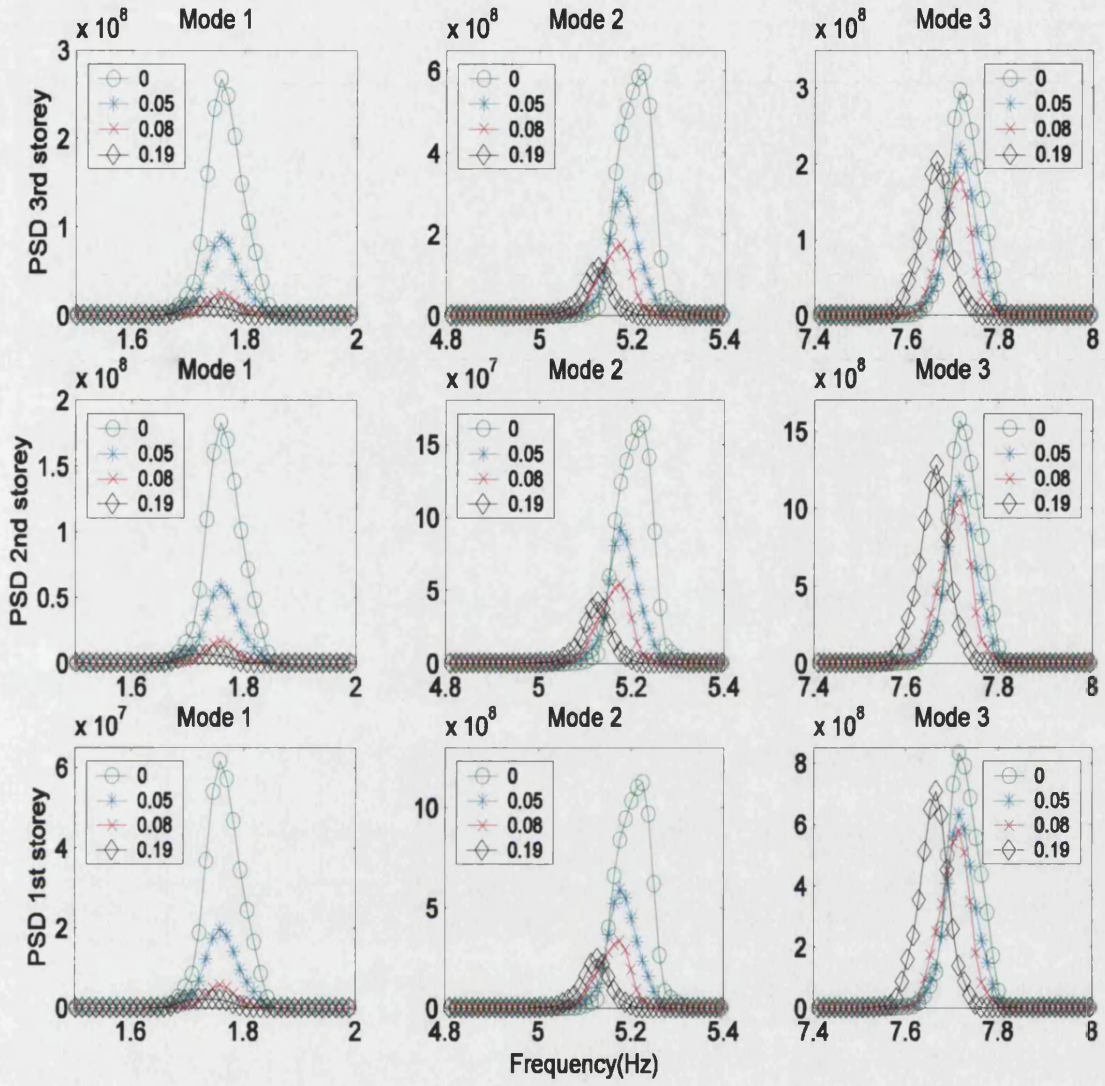


Figure 5.9: Effect of mass ratio (excitation at A)—free vibration

The results when the excitation is applied at B and C (the 2nd and 3rd stories) are shown in Figures 5.10, and 5.11 respectively. All the results confirm that a progressively higher mass ratio results in progressively better control of the first mode but demonstrate graphically that a higher mass ratio does *not* automatically lead to better control of higher modes. Indeed, Figure 5.10 shows that for the second mode the smallest mass ratio appears to provide greatest control, whilst the largest mass ratio results in the worst control effect and, indeed, makes the response worse in some instances (it is, however, recognised that the PSD of the response for the second mode is an order of magnitude smaller than for the other two modes). Similarly for the third

mode it can be seen that the control effect for the medium mass ratio, $\mu = 0.082$, is better than that of both the largest and smallest mass ratio.

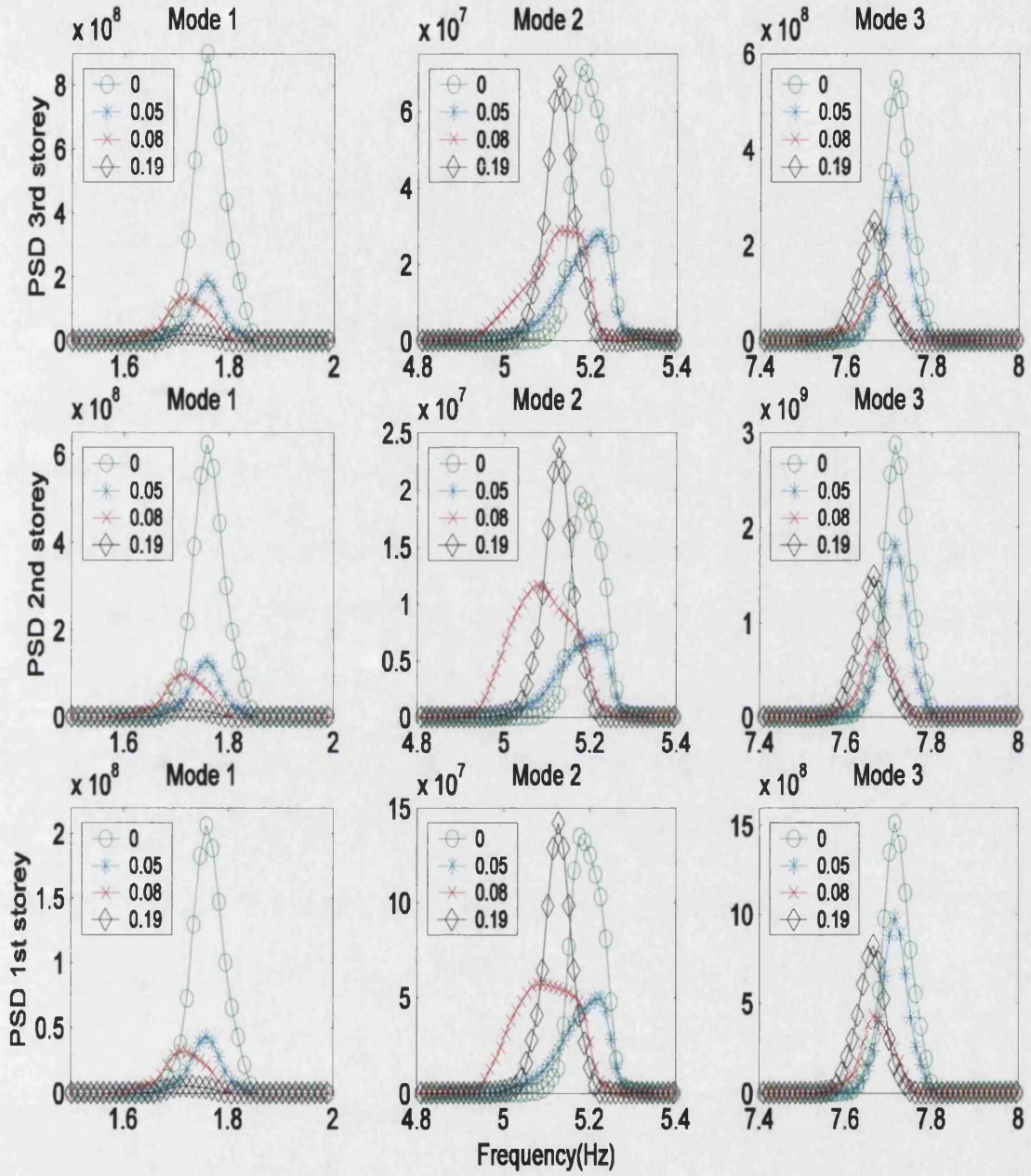


Figure 5.10: Effect of mass ratio (excitation at B)—free vibration

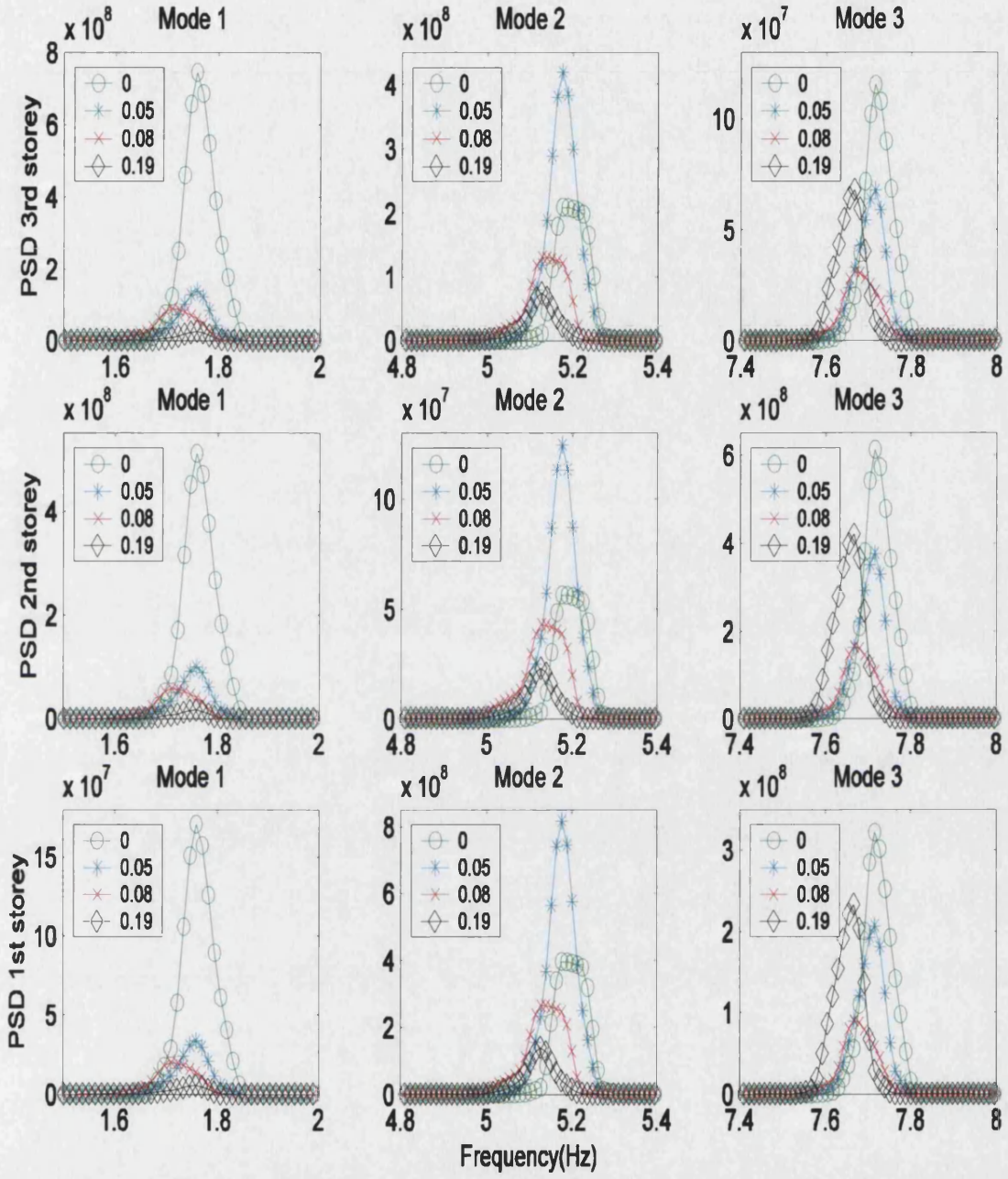


Figure 5.11: Effect of mass ratio (excitation at C)—free vibration

Compared with the case of an impact damper applied to a SDOF primary system, the effect of mass ratio on a MDOF primary system, where higher modes must also be controlled, is not so straightforward. In this situation a higher mass ratio does not necessarily lead to better control, except for the first mode and, even in this case, the

degree of control is not directly related to the mass ratio. It is necessary to take into account excitation position, strength, and frequency range when choosing a mass ratio.

*5.3.1.3. clearance*

To study the effect of clearance between the impact mass and the stops upon the control effect, a series of clearances *d=0, 5, 10, 15, 20, 25, 30, 35, 40, 45, 50, 60, 70, 80, 105* mm were investigated. Free vibration tests were carried for each clearance, and compared to the response without an impact damper. Peak values of the PSD of the acceleration response for each mode were obtained in each case. All the experiments were carried out with mass ratio $\mu = 0.082$ and excitation at *B* (level 2). The results, shown in Figure 5.12, are given as a ratio between the peak value of the PSD at the natural frequency of interest when with the impact damper, *P*, and the corresponding peak value when without the impact damper, $P_0$. Therefore, a ratio of less than one shows some control effect, whilst a ratio greater than 1 indicates a detrimental effect.

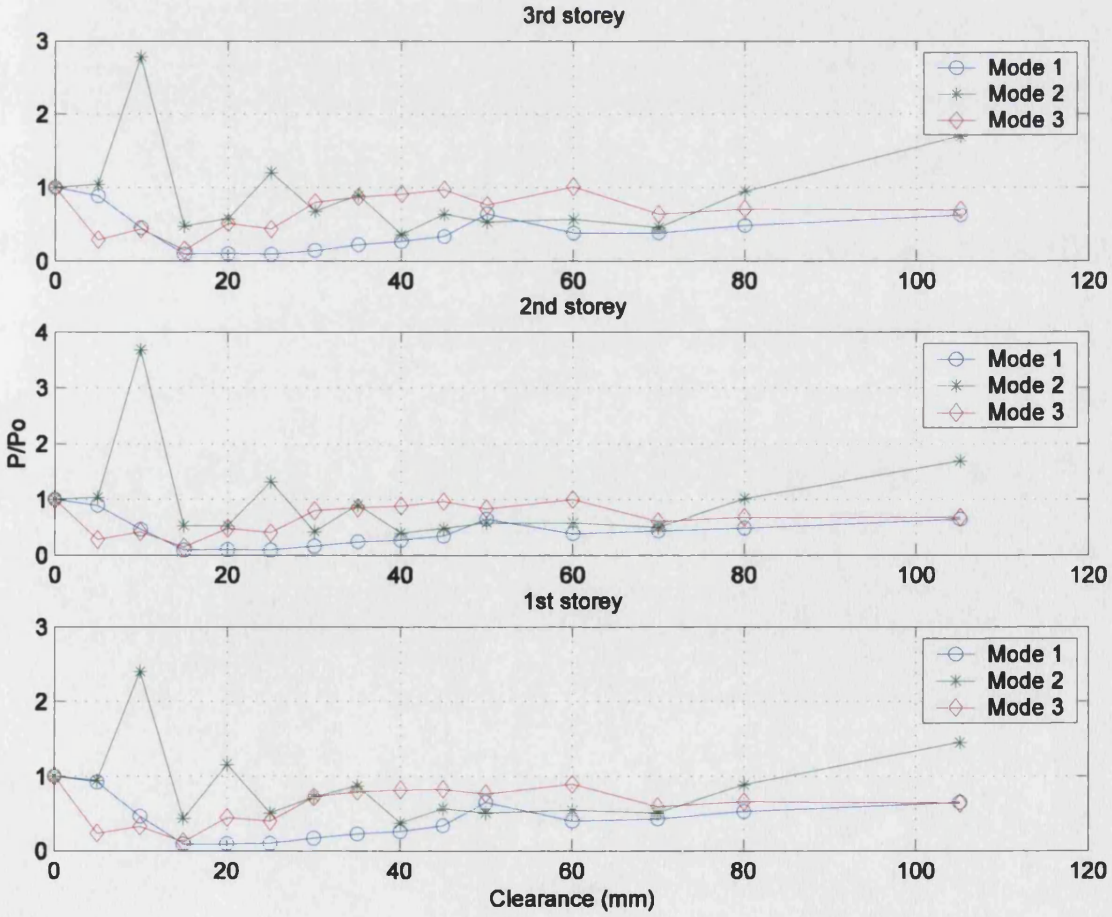


Figure 5.12: Effect of clearance—free vibration

Figure 5.12 reveals that the first mode of each storey can, to varying degrees, be effectively controlled over the full range of clearances. However, for low and high clearance values, the second mode could be not controlled and in a number of instances made the response worse. For the third mode, in the mid range of clearances, very little control effect was produced, although in no instance was the response made worse. It appears that, for the structure as tested, a clearance of about 15mm produced optimum control for all three modes, although it should be noted that the control effect for clearances either side of this (10 and 20 mm) was significantly worse, demonstrating the sensitivity of response to clearance. It should also be noted that the data points presented in Figure 5.12 are connected by lines only for the purposes of clarity, it is not suggested that the response ratio for a clearance lying between two data points necessarily lies on, or close to, the line.

Ekwaro-Osire and Desen [46] concluded that, for the case of a SDOF system, the control effect increases as the clearance increases, up until a point where impacts no longer occur. The same conclusions cannot be made for the case of a MDOF system. For the first mode, this appears to be the case up to the optimal clearance of 15mm although there is still a significant control effect on this mode for even quite large clearances. However, the response of the other two modes to changes in clearance is a lot less predictable.

*5.3.1.4 intensity of excitation*

The final set of free vibration tests examines the effect of the intensity of the excitation force on the degree of control effect. For these tests, the mass ratio $\mu = 0.082$, the clearance $d=15$ *mm* with the excitation force applied at the 3$^{rd}$ storey level. The excitation force was progressively increased by dropping the pendulum hammer from increasingly greater distances, although the actual resulting impulse force was not measured. Figures 5.13(a), (b) and (c) respectively, show the PSD of the acceleration records for each storey as the amplitude of the impulse input force is increased. It can be seen that the increase in intensity of excitation makes little difference to the control effect upon the first mode of each storey. However, there is a marked difference of the control effect on the higher modes. The general trend is for higher intensity excitation to result in better control. This is due to greater movement of the top storey for all

modes resulting in more impacts and, thus greater control. However, it can be noted, looking at 5.13(b) and 5.13(c) that for both the second and third mode there reaches a point where the control effect no longer increases significantly (and in some cases decreases) as the intensity of loading increases.

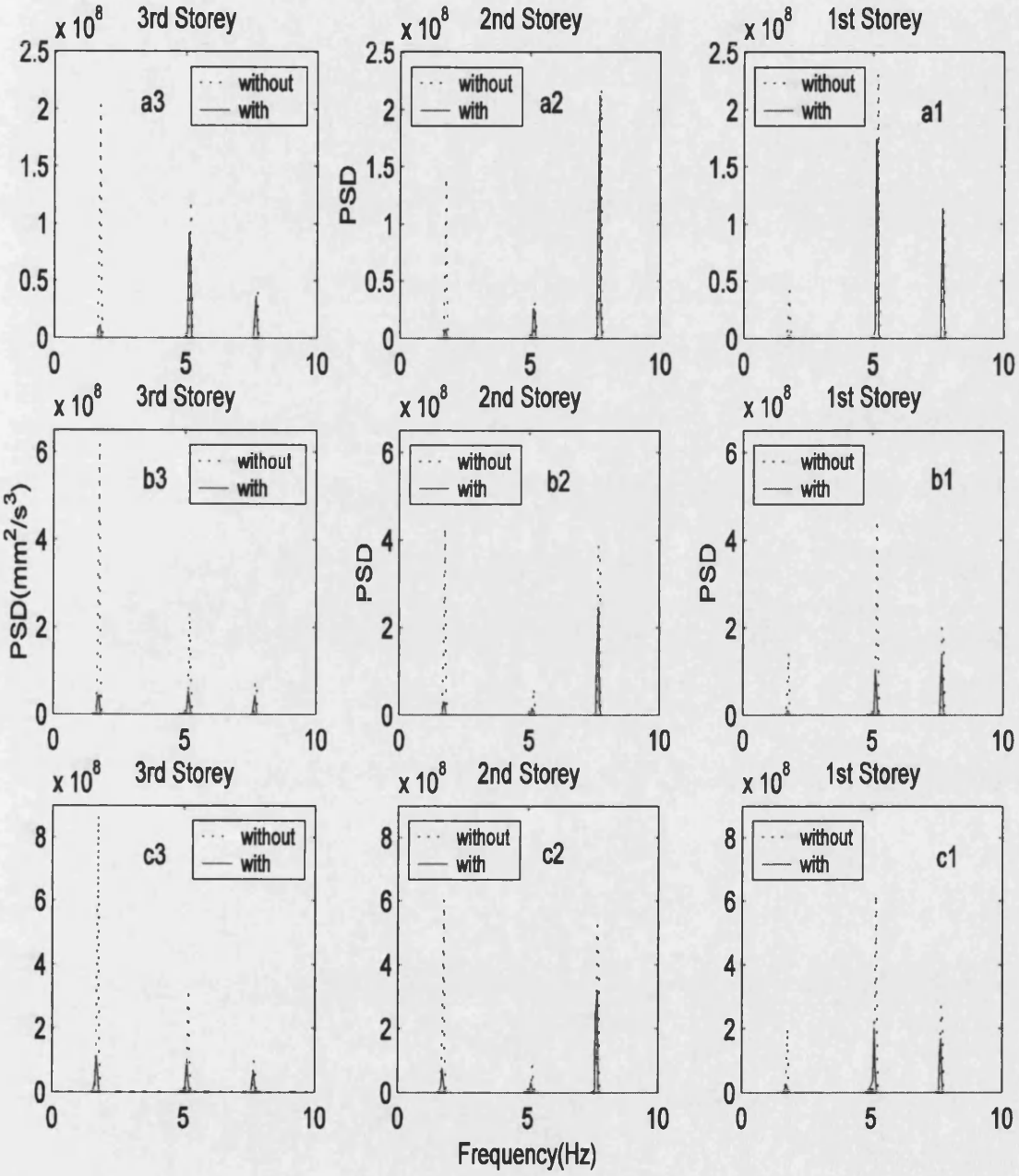


Figure 5.13: Effect of intensity of excitation—free vibration

*5.3.2 Forced vibrations*

*5.3.2.1 mass ratio—sinusoidal excitation*

For forced-vibration experiments, the movement of the shaking table on which the test structure was fixed provides excitation for the primary structure. First, dwell experiments were carried out. Figure 5.14 shows the effect of mass ratio under excitation $Y = A\sin(2\pi f t)$. Here $A=7mm$, $f=2Hz$ and the clearance taken in the experiments is $d=20mm$. It can be observed, from Figure 5.14, that under such an excitation a larger mass ratio results in a better control result. This is true for each storey. The influence of mass ratio on control effect is more obvious for the third storey, on which the impact damper is located, than for the first storey.

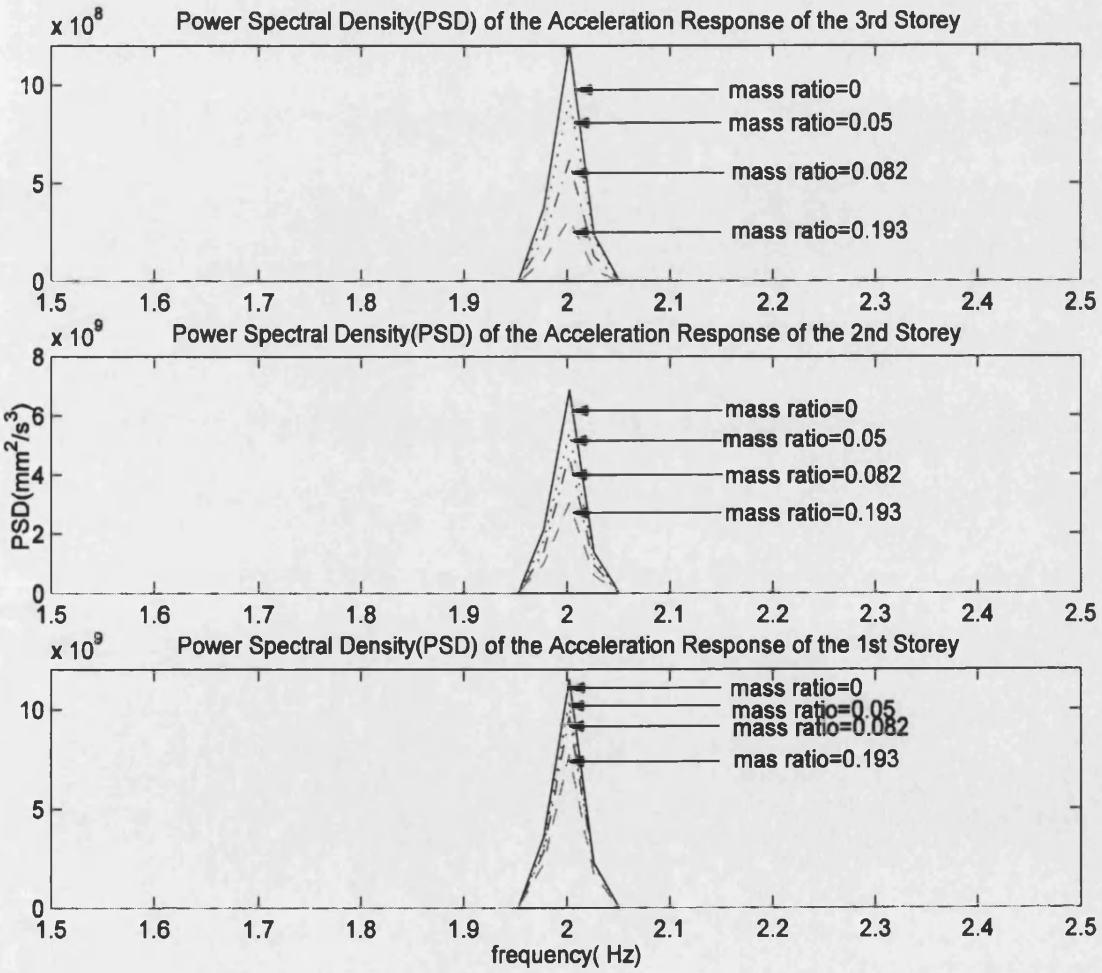


Figure 5.14 Effect of mass ratio-sinusoidal excitation

*5.3.2.2 clearance—sinusoidal excitation*

Figure 5.15 shows the effect of clearance under sinusoidal excitation: $Y=Asin(2\pi f t)$, $A=7mm$, $f=2Hz$. The mass ratio in the experiments is $\mu=0.082$. *Pa* is the peak value of the power spectral density of acceleration response when the impact damper is in operation while *Pa0* is that when the impact damper is not in operation. It can be seen that an impact damper shows control effect over a large clearance range in the case of sinusoidal excitation.

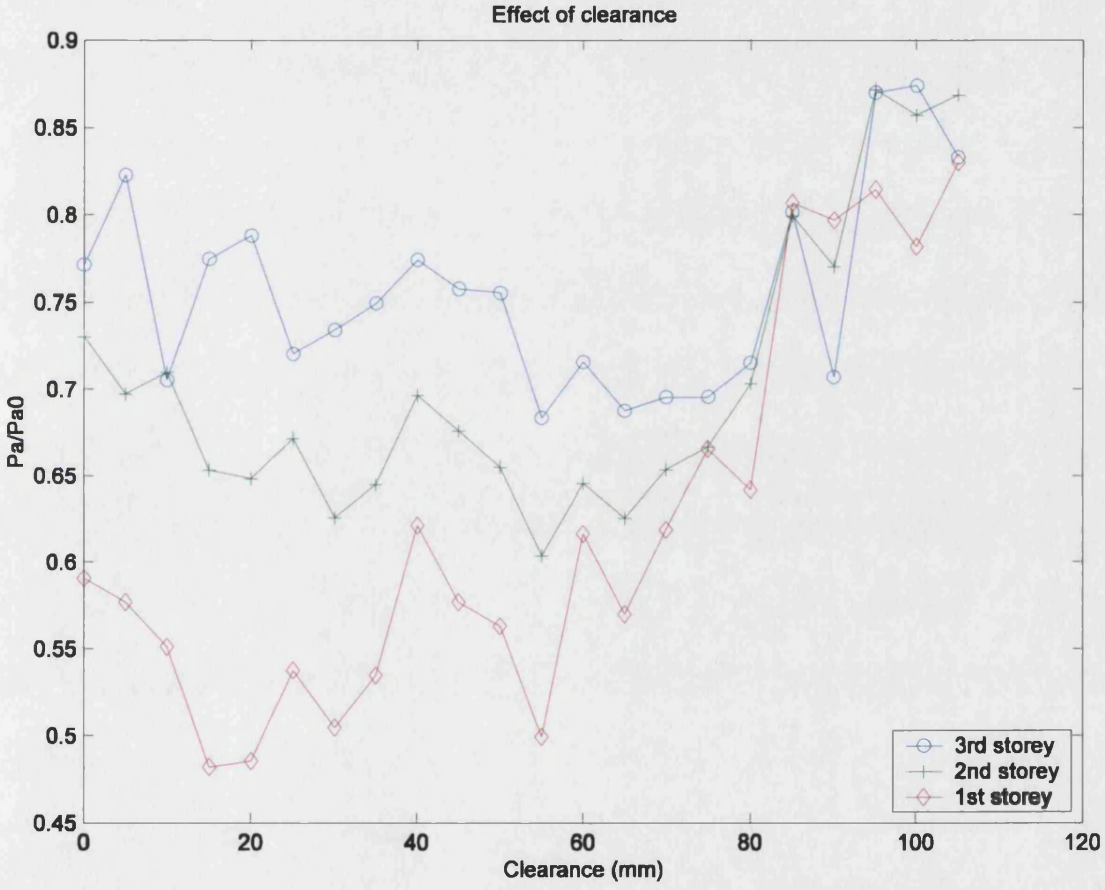


Figure 5.15: Effect of clearance—sinusoidal excitation

*5.3.2.3 excitation intensity—sinusoidal excitation*

Figure 5.16 shows the effect of excitation intensity. In this group of experiments the excitation frequency is $f=2$ *Hz*, mass ratio $\mu=0.082$ and clearance $d=55mm$. The amplitude of excitation is set at $A=2.5$ *mm*, *5 mm*, *7.5 mm* and *10 mm* respectively. It can be seen that the control effect increases as the intensity of excitation increases at

first. However, after the excitation intensity reaches a certain level, the control effect decreases.

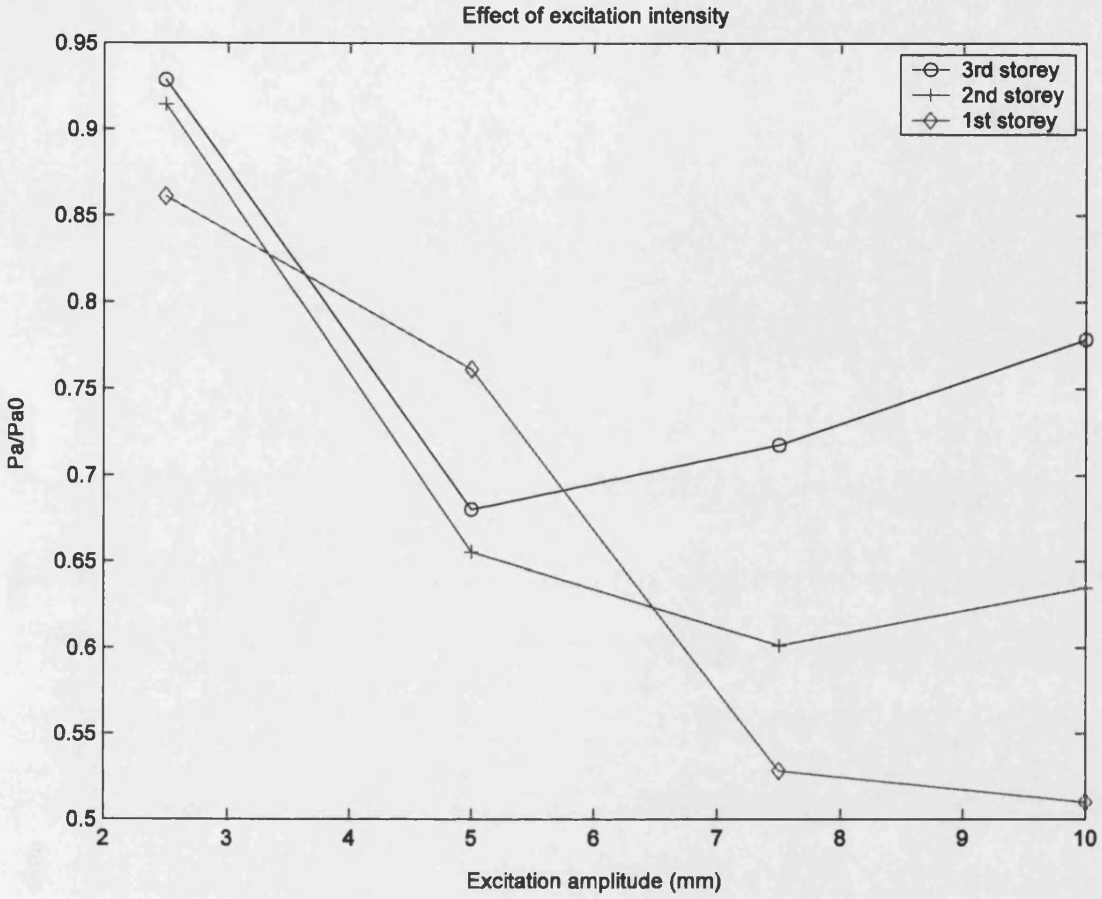


Figure 5.16: Effect of excitation intensity-- sinusoidal excitation

It should be noted in the above sinusoidal dwell tests that the frequency of excitation does not correspond to, or excite, a natural frequency of the structure and therefore represents control of an already low response.

*5.3.2.4 excitation frequency—sinusoidal excitation*

To study the effect of excitation frequency on the vibration control effect of impact damper, experiments are carried out at a series of sine dwell excitation frequencies either side of the first natural frequency, $f_1=1.7685$ *Hz*, i.e. taking $f=0.2f_1$, $0.4f_1$, $0.6f_1$, $0.8f_1, f_1, 1.2f_1, 1.4f_1, 1.6f_1, 1.8f_1, 2.0f_1$. For the tests, the amplitude of the base excitation was 5 mm, the mass ratio $\mu = 0.082$, and the clearance $d=12$ *mm*. The ratio of peak values of the PSD of the acceleration response at the excitation frequency when with

and without the impact damper was obtained. The results are shown in Figure 5.17. It can be seen that for the first and second storeys the impact damper shows some degree of control effect for $0.95 \leq r \leq 2$ and, for $0.95 \leq r \leq 1.5$ for the third storey, where $r$ *is* frequency ratio (the ratio of excitation frequency to the first natural frequency of the structure).

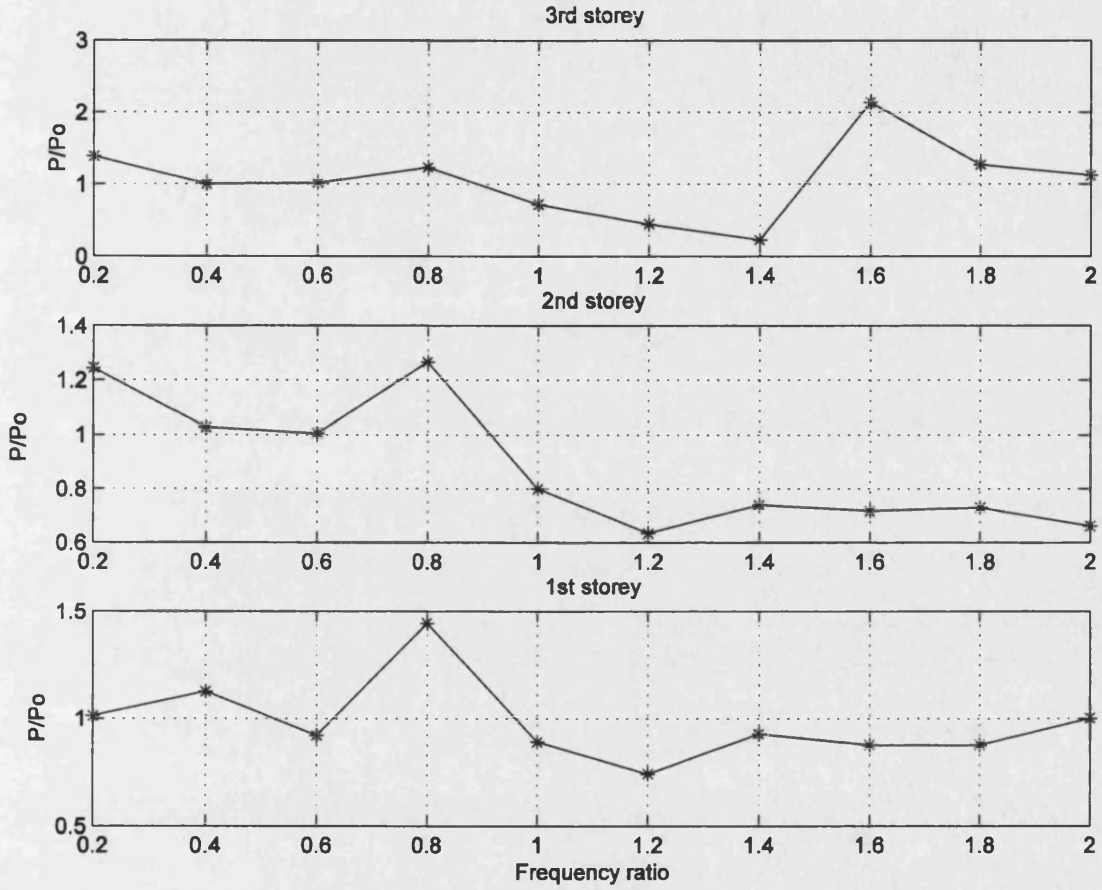


Figure 5.17: Effect of excitation frequency—sinusoidal excitation

The results seem to suggest that for excitation below the natural frequency, the response can become worse, but for frequencies immediately above the natural frequency the response is improved. This is quite different from the results observed in the study of SDOF primary systems controlled by impact dampers (Ekwaro-Osire and Desen, 2001 [46]). In the case of an impact damper-SDOF primary system, with a similar mass ratio $\mu = 0.096$, the amplitude ratio (the ratio of the amplitude of the response with and without the impact damper) becomes larger than *1* when $r \geq 1.025$, i.e. for excitation frequencies immediately above the natural frequency. Moreover, in the case of an impact damper-SDOF primary system, the control is found to be best around $r=1$.

However, Figure 5.17 clearly shows that for the case of impact damper-MDOF primary system the highest degree of damping occurred around $r=1.2$ for the 1st and 2nd storey and at around $r=1.4$ for the 3rd storey.

*5.3.2.5 mass ratio—sinusoidal sweep excitation*

The effect of mass ratio was also studied by sinusoidal sweep excitation experiments. The results are shown in Figure 5.18. The clearance used in the experiments was $d=20$ *mm*. Figure 5.18 reveals again that for the first mode a higher mass ratio leads to a progressively better control result whereas this is not necessarily the case for the higher modes. It is evident that none of the masses effectively control the highest mode (this is most likely due to the rather low amplitude of excitation used for this mode, preventing significant impacts from occurring), and the largest mass ratio actually makes the response worse. Similarly, the response of the second mode is controlled most effectively by the medium sized mass, rather than the largest impact mass.

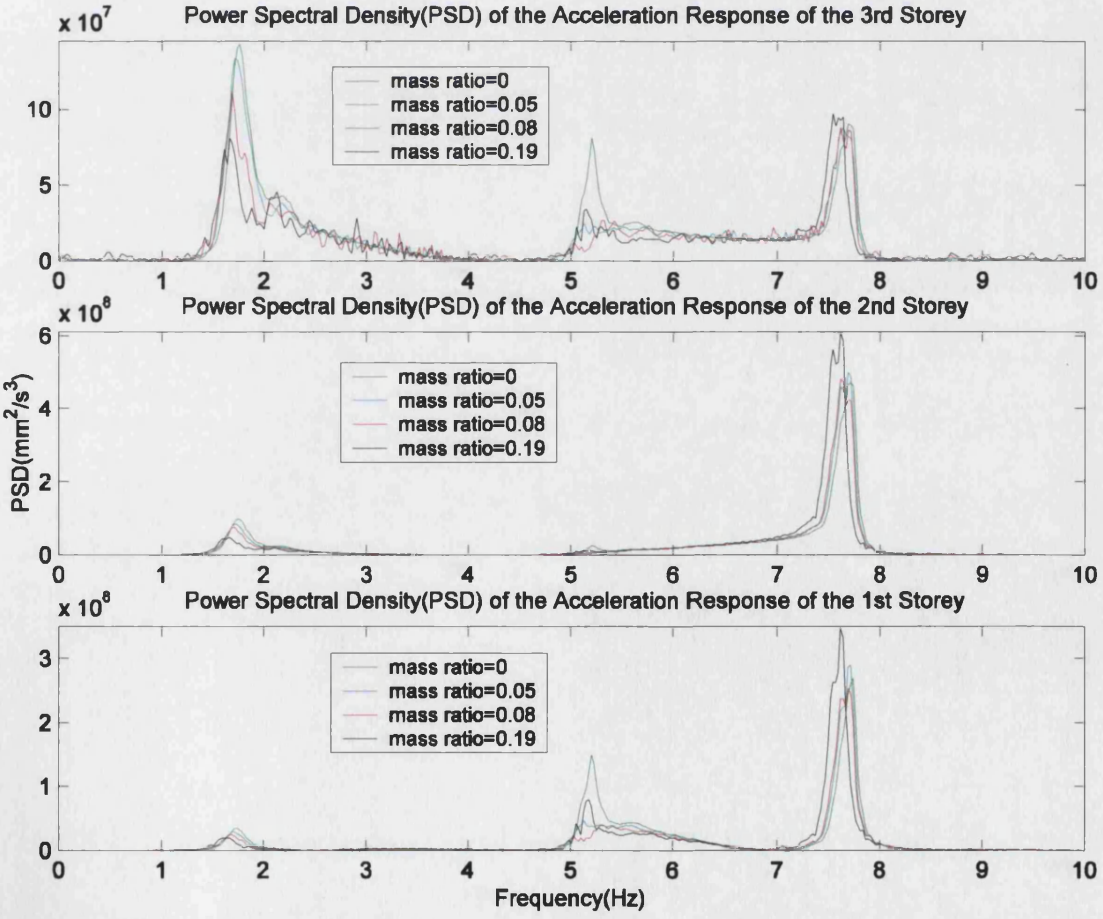


Figure 5.18: Effect of mass ratio—sinusoidal sweep excitation

*5.3.2.6 clearance—sinusoidal sweep excitation*

The effect of clearance is also studied under sinusoidal sweep excitation. The results of the ratio of the controlled and uncontrolled response against clearance are shown in Figure 5.19. The experiments were carried out with a mass ratio of $\mu = 0.082$. From Figure 5.19 it can be seen that the first mode of each storey can be controlled to a varying degree, over the whole clearance range tested. However, the response of the second mode can be made worse for a range of clearances between 30 and 45 mm whilst the response of the third mode for all storeys can only be controlled for a clearance of about 10 mm (which is not necessarily an optimum clearance for the other modes). Incidentally, the figure also reveals why the control effect on the third mode, as shown in Figure 5.18, is not significant, since these tests were performed using a clearance of 20 mm.

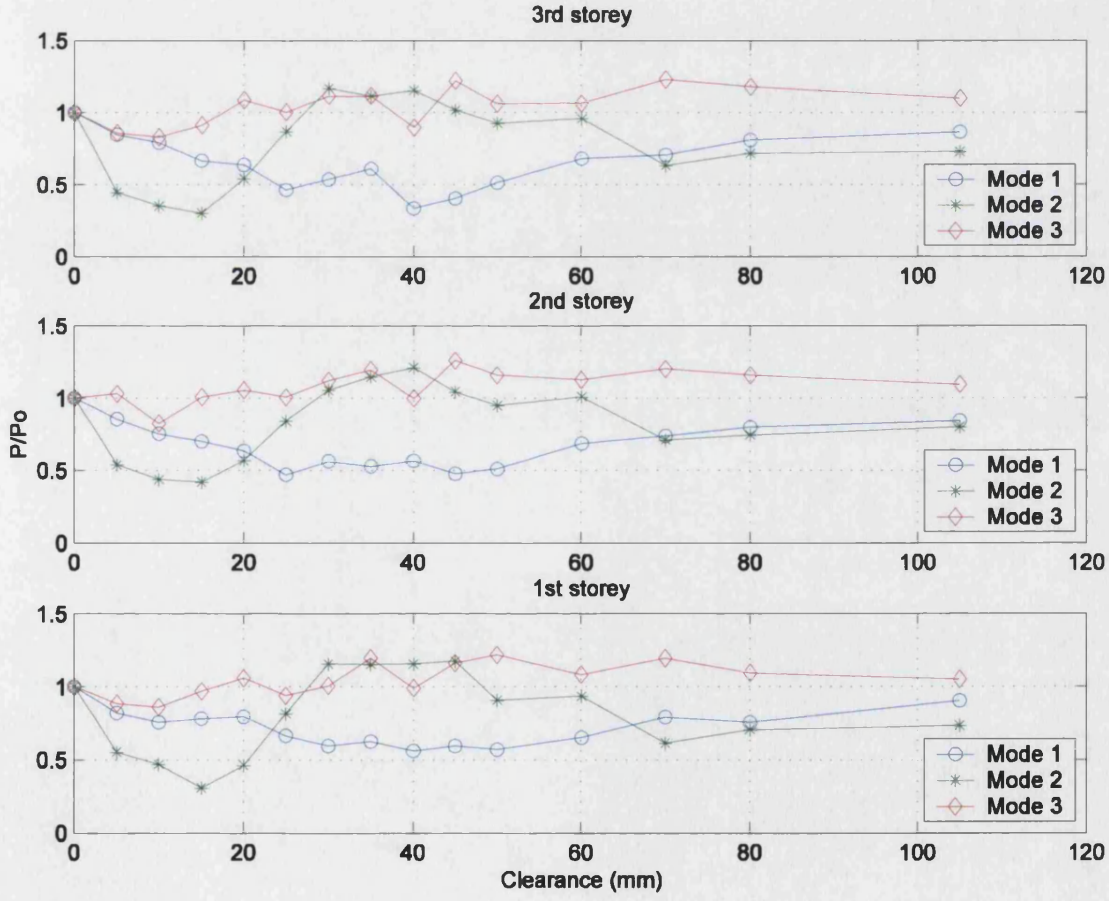


Figure 5.19: Effect of clearance—sinusoidal sweep excitation

*5.3.2.6 random base excitation—band limited white noise*

Further tests have been performed using random base excitation with a band-limited frequency content between 0 and 15 Hz. The mass ratio taken in the tests is $\mu = 0.082$ and the clearance $d=20mm$. PSDs of each storey, without and with an impact damper, are presented in Figure 5.20. Figure 5.21 is Figure 5.20 re-plotted by zooming in on each natural frequency. It is clear that the impact damper can achieve significant control of each mode of each storey, although, a differing degree of control is evident. The first mode is most effectively controlled.

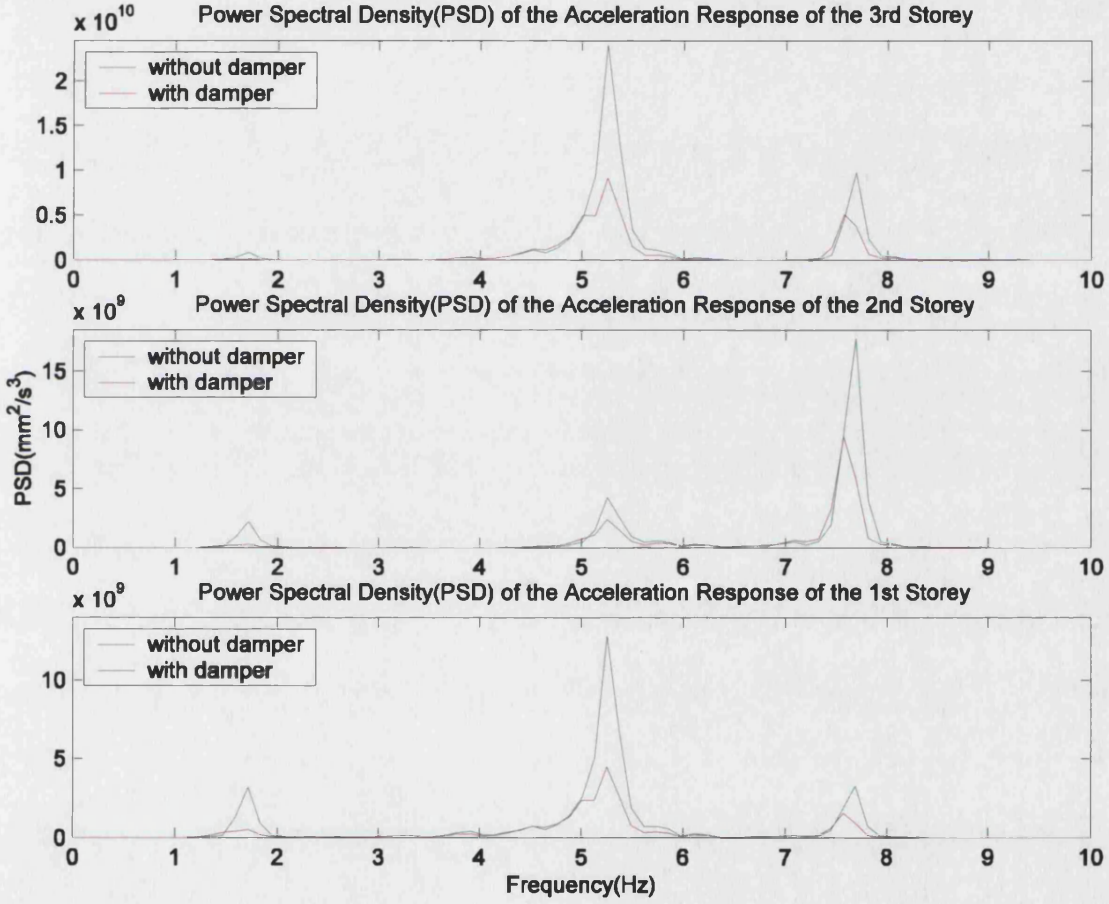


Figure 5.20: PSDs under random excitation—without and with impact damper

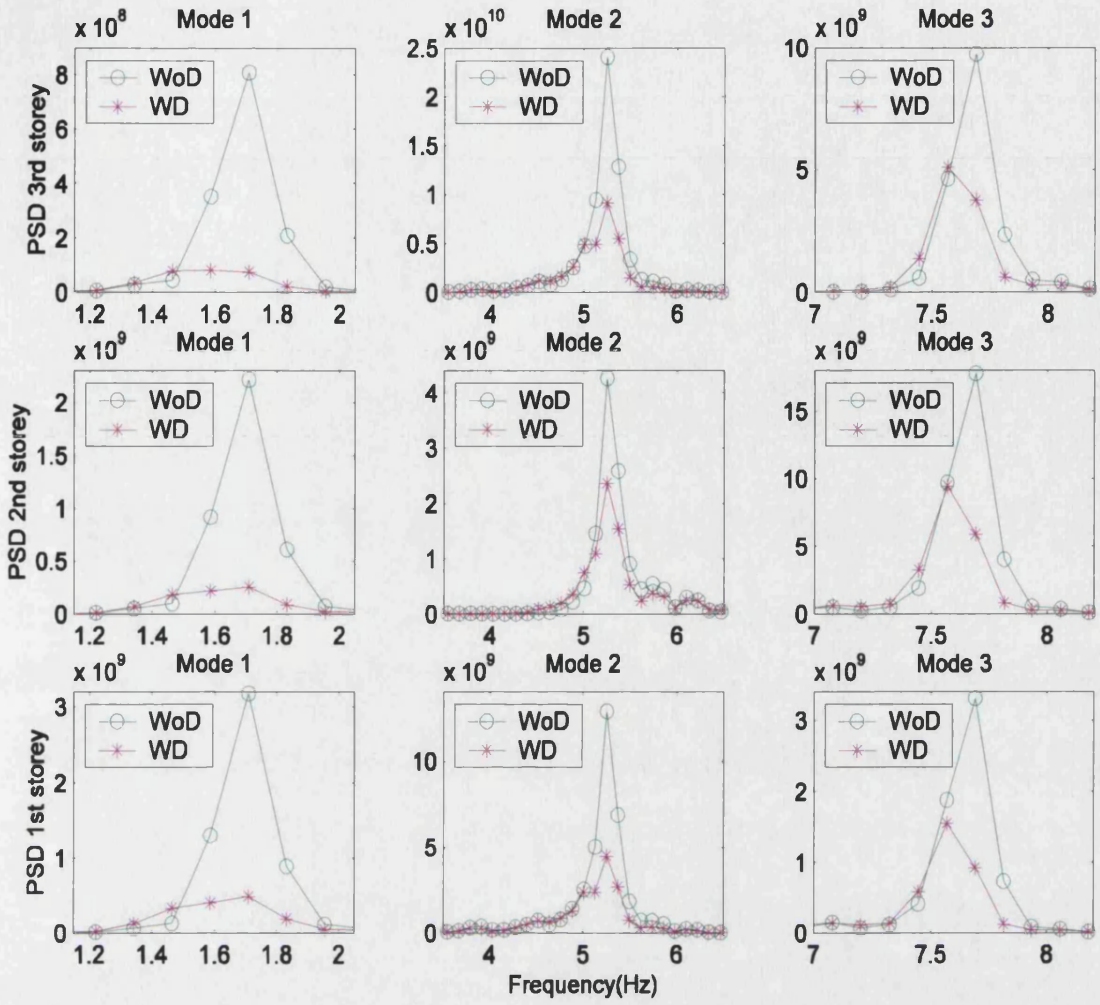


Figure 5.21: PSDs (zoomed in on natural frequency) under random excitation (band-limited white noise)—without (WoD) and with impact damper (WD)

*5.3.2.7 Kobe earthquake record*

Tests using the Kobe earthquake record were also performed. The mass ratio taken in the tests is $\mu = 0.082$ and the clearance $d$=15$mm$. PSDs of each storey, without and with an impact damper, are presented in Figure 5.22. It can be seen that both the first and second modes are significantly excited under this loading. However, the impact damper results in obvious control for all the excited modes.

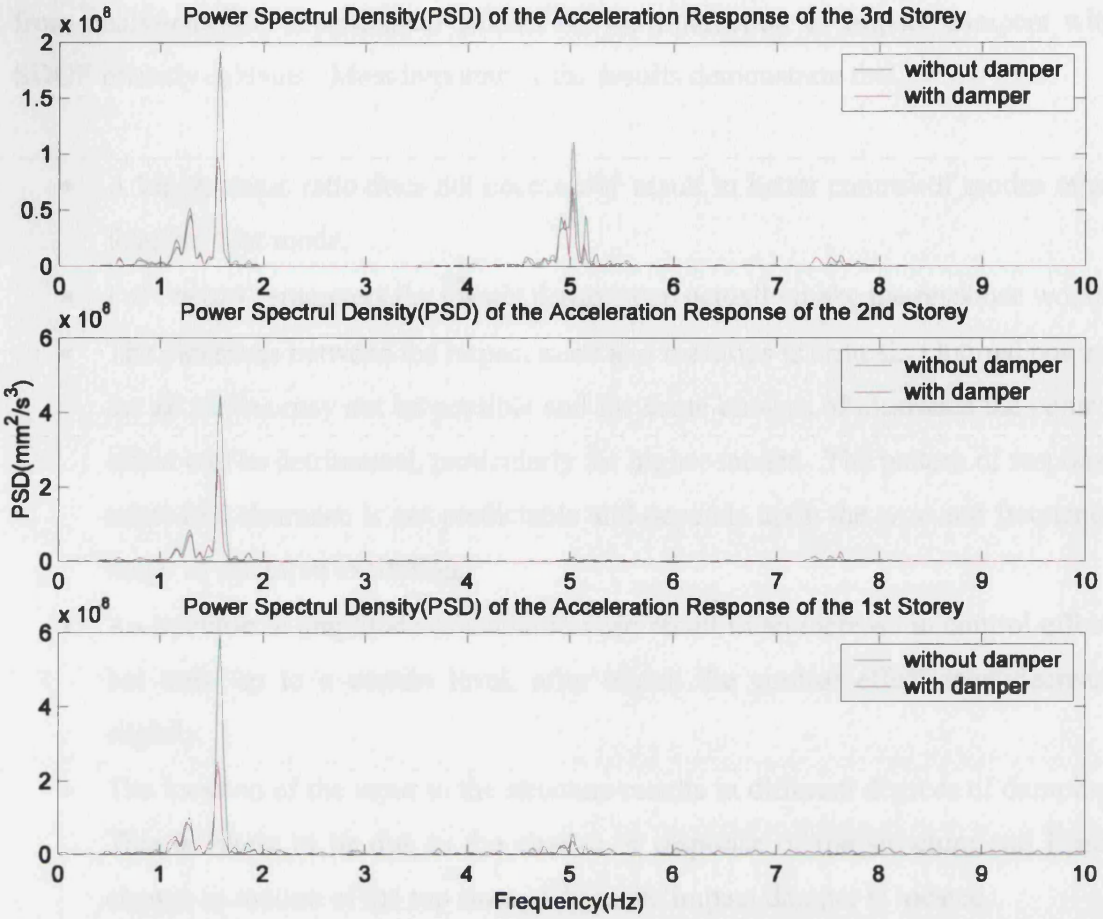


Figure 5.22: PSDs under Kobe earthquake excitation
—without and with impact damper

## 5.4 Comments of impact damper for dynamics control of MDOF structure

The behaviour of impact dampers to control SDOF systems has been investigated by a number of researchers. However, little has been done on controlling MDOF systems, despite the fact that control over a large frequency range is possible, using a mass comparable in size to that of a tuned-mass-damper. This chapter has presented experimental observations which give an insight into the behaviour of impact dampers for the vibration control of a MDOF primary system. It has been demonstrated that with a properly designed impact damper it is possible to control all modes of a MDOF primary system to a certain extent. However, the experiments have also revealed that the performance of an impact damper is closely related to the response of the primary system, the location and amplitude of the excitation force and the mass and clearance parameters of the impact damper itself. Many of the results contradict those derived

from analytical and experimental studies on the interaction of impact dampers with SDOF primary systems. Most importantly the results demonstrate that:

- A higher mass ratio does not necessarily result in better control of modes other than the first mode.
- For certain parameters the impact damper can actually make the response worse.
- The clearance between the impact mass and the stops is critical. Optimal control for all modes may not be possible and for some choices of clearance the control effect can be detrimental, particularly for higher modes. The pattern of response related to clearance is not predictable and depends upon the type and frequency range of the input excitation.
- An increase in amplitude of excitation can result in an increase in control effect, but only up to a certain level, after which the control effect may decrease slightly.
- The location of the input to the structure results in different degrees of damping. This is likely to be due to the change in response of the structure and hence change in motion of the top storey where the impact damper is located.

What becomes clear from these tests is that the general behaviour of MDOF structures controlled using impact dampers is rather unpredictable. General trends defining the size of impact mass and clearance do not appear to exist except, perhaps, when examining the response of the fundamental mode. It is likely, therefore, that in-situ tuning of an impact damper would be required to extract optimal performance from it, in much the same way as optimisation of the damping of a tuned-mass-damper can only be performed once installed. However, the ability to simulate the response of the complete impact damper/MDOF system before construction would be a useful tool. This would allow the behaviour of the system, under various damper parameters, to be predicted at a preliminary stage without the need for testing the actual system.

To conclude this chapter, one thing worth remembering is that experiments have clearly revealed that with an impact damper very high accelerations can occur at the moment of collision, as shown in Figure 5.2, 5.3, 5.4, for example. This is an important issue and it must be addressed if impact dampers are to be used in general engineering applications. This is the subject of the next chapter.

# Chapter 6

# Buffered Impact Damper

Introduction: To reduce the contact force and the corresponding high accelerations and noise level associated with a conventional rigid impact damper, a new type of impact damper—a buffered impact damper (BID) is proposed. The performance of a BID is studied experimentally and compared with that of a conventional rigid impact damper. The BID can not only significantly reduce the contact force, peak value of acceleration and noise generated by collisions but actually enhances the vibration control effect, which makes it ideal for general engineering applications. Buffers of different materials and sizes are tested and the mechanism of the BID is explored. To simplify use in engineering practice, a procedure for optimum buffer design is suggested.

## 6.1 From conventional rigid impact damper to buffered impact damper

An impact damper is normally a rigid slug that moves freely within the boundaries formed by stops attached to the primary system. The effectiveness of impact dampers for structural dynamic control has been experimentally demonstrated in Chapter 5. However, there are a number of issues which prevent more widespread use of impact dampers, particularly in civil engineering. One such obstacle is the high level of acceleration, as illustrated in Figure 6.1, caused by collision of the rigid mass with the rigid stops attached to the structure, together with the corresponding high noise level, particularly when collisions occur between hard metal objects. From Figure 6.1, it can be seen that the high accelerations occur not only on the third storey where the impact damper is located, but also at the other storeys. Additionally, the large contact force at impact, as shown in Figure 6.2, may cause local damage to the structure of the mass or the stops. If the structure under control is a building, then the high accelerations and noise will cause discomfort to the building's occupants. Another obstacle to more widespread use is that the performance of an impact damper is particularly sensitive to system parameters and type of loading as illustrated in Chapter 5. The performance can drop off significantly if the parameters are not optimised for a particular excitation type.

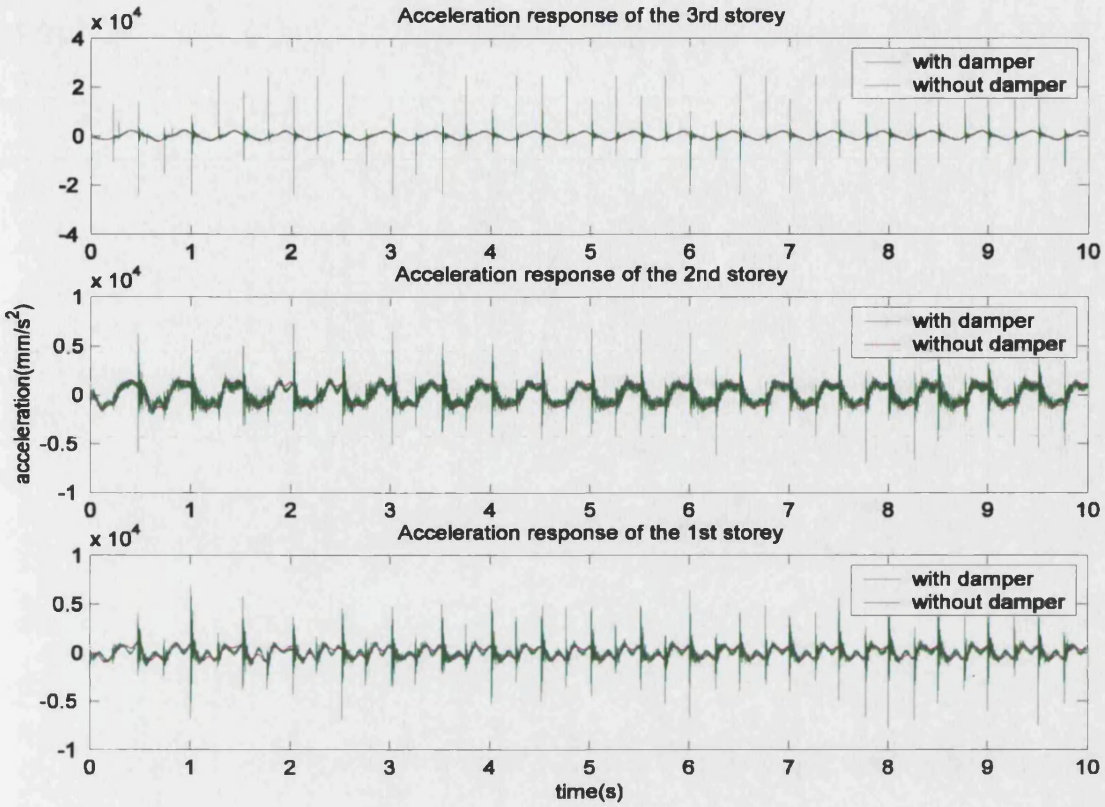


Figure 6.1: Acceleration responses of the primary structure under base sinusoidal excitation using conventional impact damper

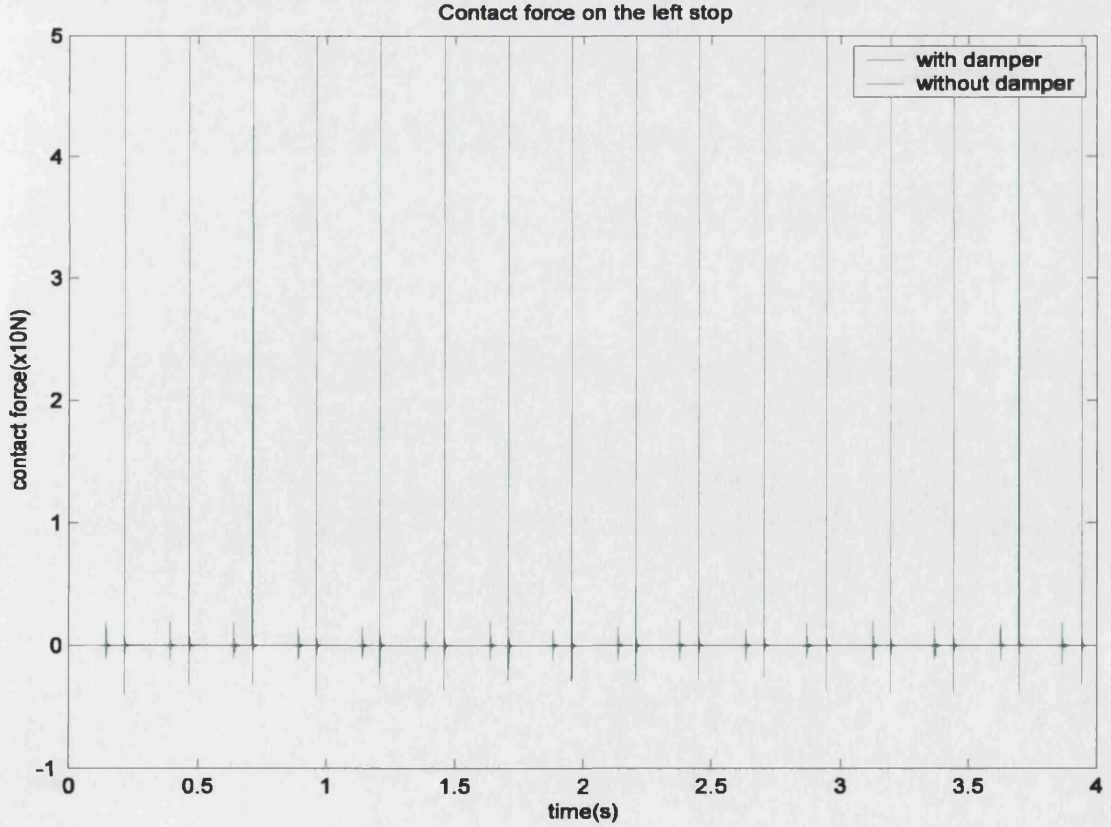


Figure 6.2: Contact force of conventional rigid impact damper

As mentioned in the literature review, attempts have been made to decrease the contact force and the corresponding high noise level, by introducing the idea of multi-unit impact dampers where a single mass is replaced by a number of smaller masses resulting in smaller contact forces for each mass, but with a similar overall effect as a single large mass [77][78]. A particular form of multi-unit impact damper is a bean-bag damper [49]. This consists of a bag filled with small, spherical lead shot. The resilience stems from the flexibility of the bag which can be modified by adjusting the bag's tightness. The performance of a bean-bag impact damper has been studied for controlling a SDOF structure under sinusoidal excitation. The investigation showed that the bean bag impact damper is not only a better attenuator of the resonant displacement of a lightly damped system but the contact force and the noise generated by collisions are also reduced. This investigation also revealed that the performance of the bean-bag impact damper is significantly affected by the tightness of the bag, since it is one of the main factors governing the contact characteristics. As it was pointed out, the contact force is the key to the control effect and in turn the key to the design of such a impact damper. Unfortunately, the contact forces cannot be predicted or simulated easily because they evolve over time and change non-linearly with the level of the external excitation force. This may prove to be an obstacle to the application of this kind of impact damper. Moreover, further investigations are necessary to ascertain the response of structures under other forms of excitation, such as random excitation.

Another similar system, called a particle, or granular impact damper, has been developed [50] with the same aim of reducing or eliminating the acceleration and noise problems associated with a rigid impact damper. This consists of a bed filled with granular materials which is fixed to the primary structure. The performance of a particle impact damper on a SDOF primary structure under random excitation has been investigated [79]. The influence of particle size, container dimensions, mass ratio and intensity of excitation were investigated experimentally. One problem with this kind of impact damper is that its performance is significantly influenced by the intensity of the excitation. When the excitation is not intense enough, the control effect of this kind of impact damper is poor since the particles are not mobilised. The level of damping of particle impact dampers has also been shown to depend upon the geometry of the device [52]. It should be noted that, in this case damping occurs primarily from friction between the particles rather than through impacts and, therefore, is not a true impact damper. Another problem posed by particle impact dampers is precise modelling of the

dynamic system. This, like the bean-bag impact damper, is difficult to resolve satisfactorily, although an attempt has been made to capture the physics of the main energy dissipation mechanisms [80].

With the same aim in mind, i.e. reducing or eliminating the problems of a rigid slug impact damper, a new kind of impact damper—a buffered impact damper, is proposed by introducing a flexible buffer zone between the moving damper mass and the stops fixed to the primary system. This cushions the impact, thus reducing contact force, whilst increasing contact time. The advantage of this system over bean-bag or particle impact dampers is that it has the potential for simple modelling of the system dynamics, as discussed in Chapter 2. Experimental investigations into the performance of the buffered impact damper are carried out and compared with that of a rigid impact damper. Not only are the effects of clearance investigated, but also excitation type, frequency and amplitude, size of damper mass and buffer stiffness.

## 6.2 Experimental investigation on the contact characteristics of collision

### *6.2.1 Measuring of coefficient of restitution*

As described in Chapter 2, section 2.3, the contact surface can be modelled as a spring and damper pair, provided that the coefficient of restitution and contact time can be established. The following looks at finding these properties for a series of buffers used in this investigation.

The coefficient of restitution between two objects can be found by a drop test, as sketched in Figure 6.3. Dropping the ball (the impact mass) from a set height $h_1$, the bounce height $h_2$ can be measured, in this case, using a high-speed video camera. The impact velocity $v_1$ and the rebound velocity $v_2$ can be calculated from $h_1$ and $h_2$. Then the coefficient of restitution, $c_r$, can be calculated as:

$$c_r = \frac{v_2}{v_1} = \sqrt{\frac{h_2}{h_1}} \tag{6.1}$$

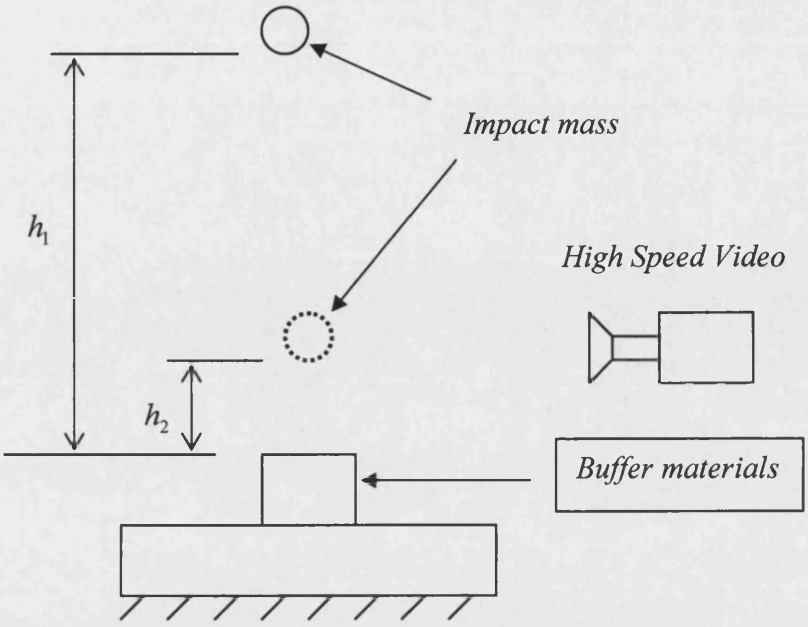


Figure 6.3: Drop test for the measurement of coefficient of restitution

The measured coefficients of restitution for collision between a steel ball and buffers of increasing stiffness are presented in Table 6.1. It should be noted that the coefficient of restitution does not relate to the stiffness of the materials, but to the inherent damping and plastic deformation of the material. Buffer 1 is the buffer employed in the following experiments. It is made from a sponge packing material and has the lowest stiffness of all the buffers investigated.

Table 6.1: Coefficient of restitution for collision bodies of different materials

| Body1 | Body 2 | Coefficient of restitution |
|---|---|---|
| steel ball | buffer 1(sponge) | 0.61 |
| steel ball | buffer 2(soft rubber) | 0.44 |
| steel ball | buffer 3(hard rubber) | 0.53 |
| steel ball | buffer 4(plastic) | 0.49 |
| steel ball | buffer 5(hard plastic) | 0.72 |
| steel ball | steel | 0.46 |

It should be pointed out that the coefficient of restitution is typically dependent upon the impact velocity. As the impact velocity increases, the coefficient of restitution may reduce, since the impact behaviour involves some plastic deformation. However, it can be taken as approximately constant if the impact velocity lies within a limited range.

### *6.2.2 Contact time of impact*

To investigate the effect of impact velocity on the contact time of impact, both drop tests and in-situ tests were carried out. For the drop tests, a load cell is mounted between the buffer onto which the impact mass will be dropped and the rigid base. For the in-situ tests, the load cell is mounted between the stop and the buffer of the impact damper. Thus, the force-time history of each impact can be obtained and the contact time of impact can be deduced.

For drop tests, the impact velocity can be calculated from the drop height. The results of the drop tests are shown in Table 6.2 and as a bar chart in Figure 6.4. For the in-situ tests, i.e. tests on an actual test structure, the primary structure is excited by 1Hz and 7Hz base sinusoidal excitation respectively. The impact velocity when the primary structure is excited by 1Hz sinusoidal excitation is significantly lower than that of 7Hz sinusoidal excitation, although measurement of the impact velocity was not possible. The results are shown in Figure 6.5 and 6.6 for impact between two steel objects and impact between the steel damper mass and buffer 1.

From both the drop tests and in-situ tests, it can be seen that there is little variation in contact time of collision within the impact velocity range tested and the results of the two tests are in broad agreement for each material tested. This has also been confirmed by tests on the impact between a steel object and the other buffer materials (test results are not presented here to save space). To simplify the modelling, the effect of impact velocity on contact time is neglected in this study, since there is little significant variation within the range tested (even though contact force varies considerably with velocity as one would expect). Therefore, an average contact time is used, i.e. the contact time of a collision between two steel objects is taken as *0.0003* seconds and that between steel and buffer 1 is taken as *0.022* seconds.

Table 6.2: Contact Time of different impact velocity

| Height (m) | Velocity (m/s) | Contact Time (s) steel--steel | Contact Time (s) steel—buffer 1 |
|---|---|---|---|
| 0.001 | 0.1400 | 0.00035 | 0.025 |
| 0.003 | 0.2425 | 0.0003 | 0.0229 |
| 0.005 | 0.3130 | 0.0003 | 0.0224 |
| 0.007 | 0.3704 | 0.0003 | 0.0210 |
| 0.01 | 0.4427 | 0.00025 | 0.0202 |
| 0.012 | 0.4850 | 0.00025 | 0.0206 |
| 0.015 | 0.5422 | 0.00025 | 0.0205 |
| 0.017 | 0.5772 | 0.0003 | 0.0206 |
| 0.020 | 0.6261 | 0.0003 | 0.0183 |
| 0.025 | 0.7000 | 0.0003 | 0.0212 |
| 0.030 | 0.7668 | 0.00025 | 0.0220 |
| 0.035 | 0.8283 | 0.0003 | 0.0216 |
| 0.040 | 0.8845 | 0.00025 | 0.0209 |
| 0.050 | 0.9899 | 0.0002 | 0.0208 |
| 0.060 | 1.0844 | 0.00022 | 0.0222 |

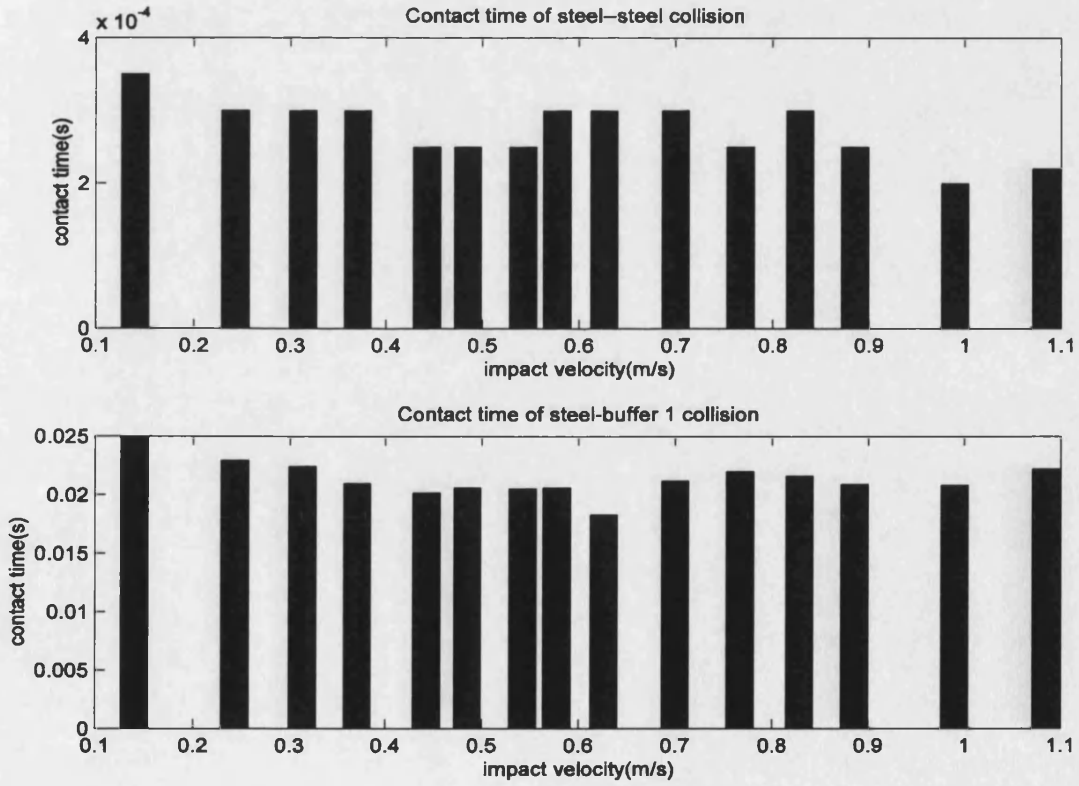


Figure 6.4: Effect of impact velocity on contact time

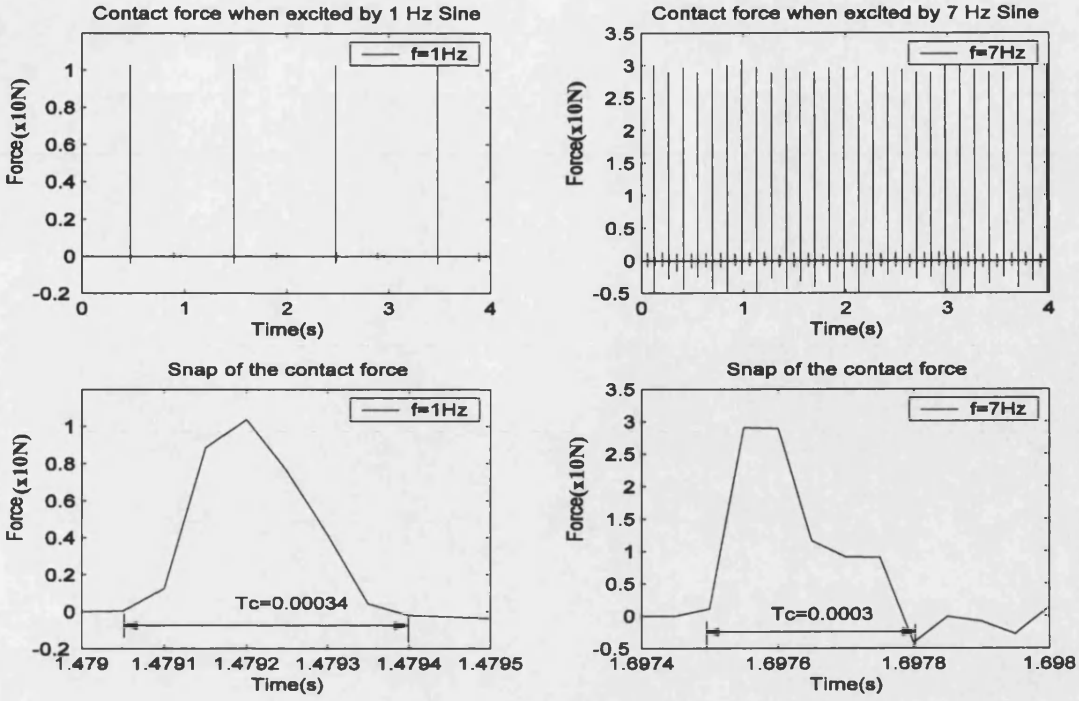


Figure 6.5: Contact times at different excitation frequencies

--impact between steel—steel

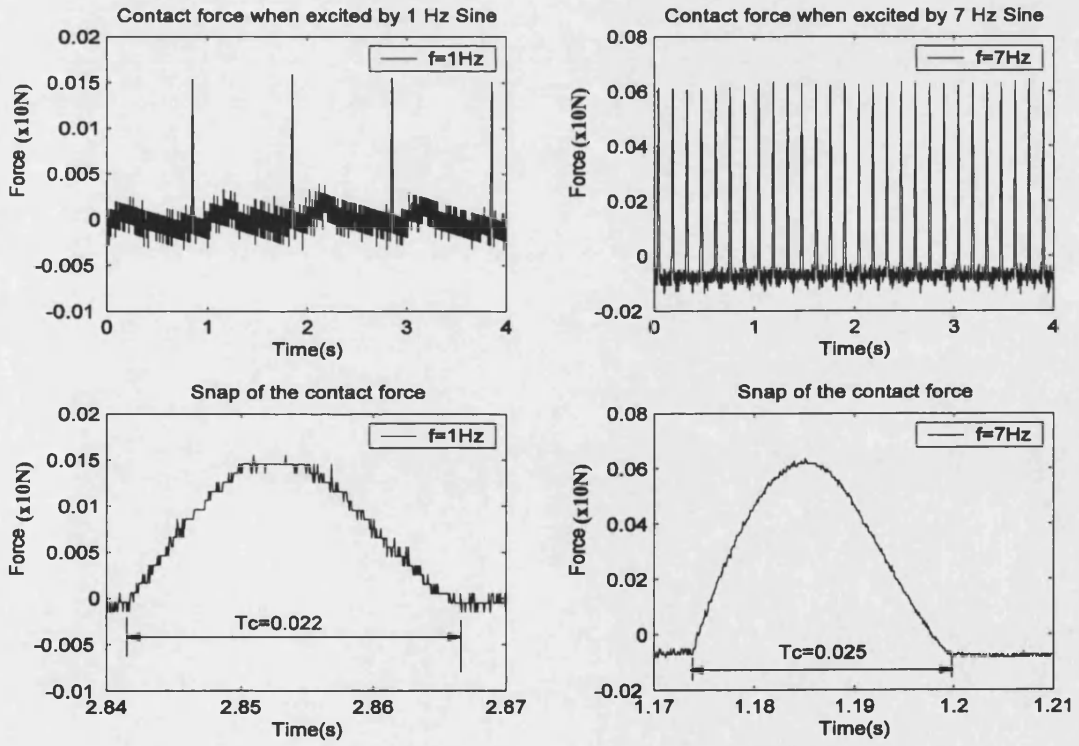


Figure 6.6: Contact times at different excitation frequencies

--impact between metal—buffer 1

Comparing Figure 6.5 and 6.6, it can be seen that the contact force between steel damper mass and buffer 1 is two orders of magnitude smaller than that between two steel objects. However, it should also be noted that the contact time of collision between a metal object and buffer 1 is also two orders of magnitude longer than that between two steel objects. This is investigated further in section 6.3.4.

## 6.3 Experimental investigation on a SDOF primary structure equipped with an impact damper—with and without buffer

### *6.3.1 Experimental structure and set-up*

To examine the performance of a buffered impact damper, an experimental structure, described in section 4.1, illustrated in Figure 6.7, was built to simulate a SDOF linear oscillator, forming the primary system to be controlled. The natural frequency of the primary structure is $f_n$ = 4.0283Hz.

The impact mass itself is a steel ball which runs in a groove along the beam. Two triangular shaped brackets are mounted on top of the beam to act as motion limiting stops for the free-moving impact mass. The buffer is fixed by adhesive to the stops and can be easily removed and changed. The clearance between the buffers, $d = d_1 + d_2$, is adjustable. The response of the structure is measured using an accelerometer fixed to the end of the beam. The base excitation is also measured using an accelerometer. Impacts between the stops and the impact mass are measured using force transducers fixed between the stops and the buffers. The complete experimental set-up is shown diagrammatically in Figure 6.8.

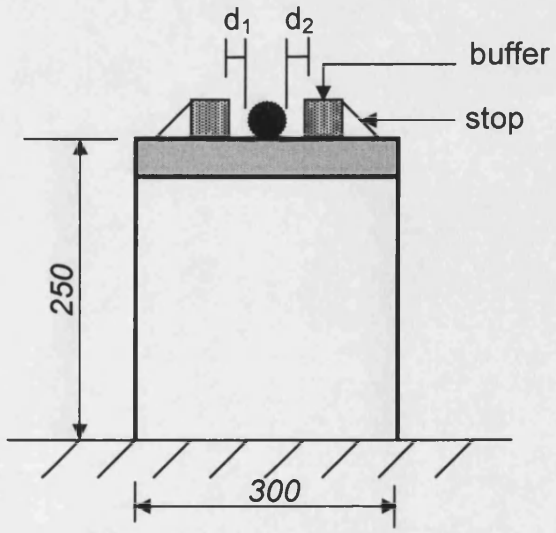


Figure 6.7: Experimental model—SDOF structure

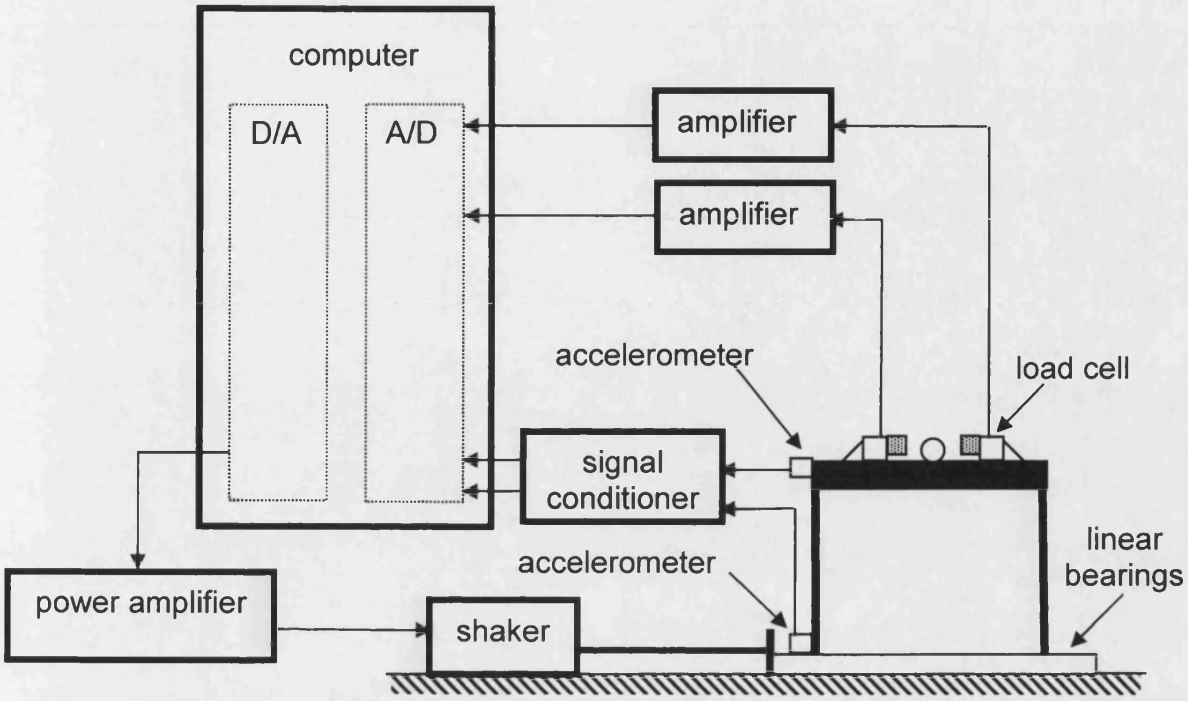


Figure 6.8: Experimental set-up

*6.3.2 Experimental procedure*

Free-vibration experiments were carried out by initially exciting the primary structure in two different ways. The first is by applying an initial displacement, $x_0$, to the structure and then releasing it. The second is by releasing a pendulum from a predetermined distance to strike the primary structure and, hence, give it an initial velocity, $v_0$. During the free-vibration experiments the shaking table was fixed to a stationary base. Both of these two simple excitation methods have been found to be reliable in producing a consistent and repeatable transient disturbance.

Forced-vibration experiments were also carried out using both sinusoidal dwell and random excitation. The test structure was excited through movement of the shaking table on which the test structure was fixed. The free and forced excitations described above were repeated for the structure without an impact damper, with a conventional rigid impact damper and with a buffered impact damper.

*6.3.3 Results and comparison*

*6.3.3.1 free vibrations*

For free-vibration experiments, the primary structure is excited by setting it to an initial displacement of $x_0$ = 10 mm and then releasing. The mass ratio (i.e. the ratio of the mass of the impact mass to the mass of the primary structure) is taken as $\mu$ = 0.082 and the clearance (defined as the diameter of the impact mass subtracted from the distance between the stops or buffers, or, referring to Figure 6.7, $d = d_1+d_2$) taken is $d$ = 15mm (less than twice the initial displacement as suggested by Chen and Wang, [81]) for both the conventional rigid impact damper and the buffered impact damper. Figure 6.9 shows the power spectral density (PSD) of the acceleration response of the primary structure when without an impact damper, with the conventional rigid impact damper and with the buffered impact damper. It can be seen that both the rigid and buffered impact dampers provide a high level of attenuation, with the buffered impact damper resulting in better control compared to the conventional rigid impact damper. Figure 6.10 shows the time history of the acceleration responses. Very high acceleration peaks are seen to occur for the rigid impact damper at the moment of each collision with the stops whereas, for the buffered impact damper, the accelerations remain small and at a lower level than the acceleration response without an impact damper. It was also evident that the large acceleration caused by a large, short-duration impact force resulted in a high level of noise. It can also be seen from Figure 6.10 that the buffered impact damper reduces the acceleration response more quickly than the rigid impact damper.

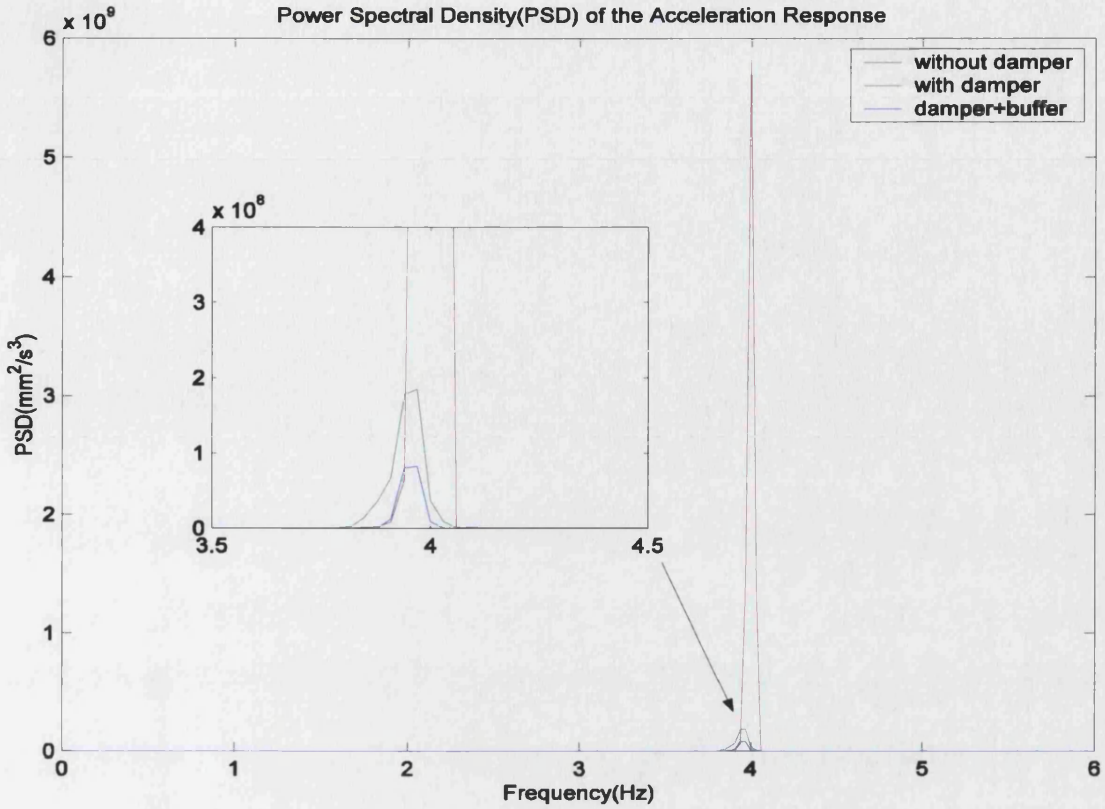


Figure 6.9: Power spectral density of acceleration response—initial displacement excitation

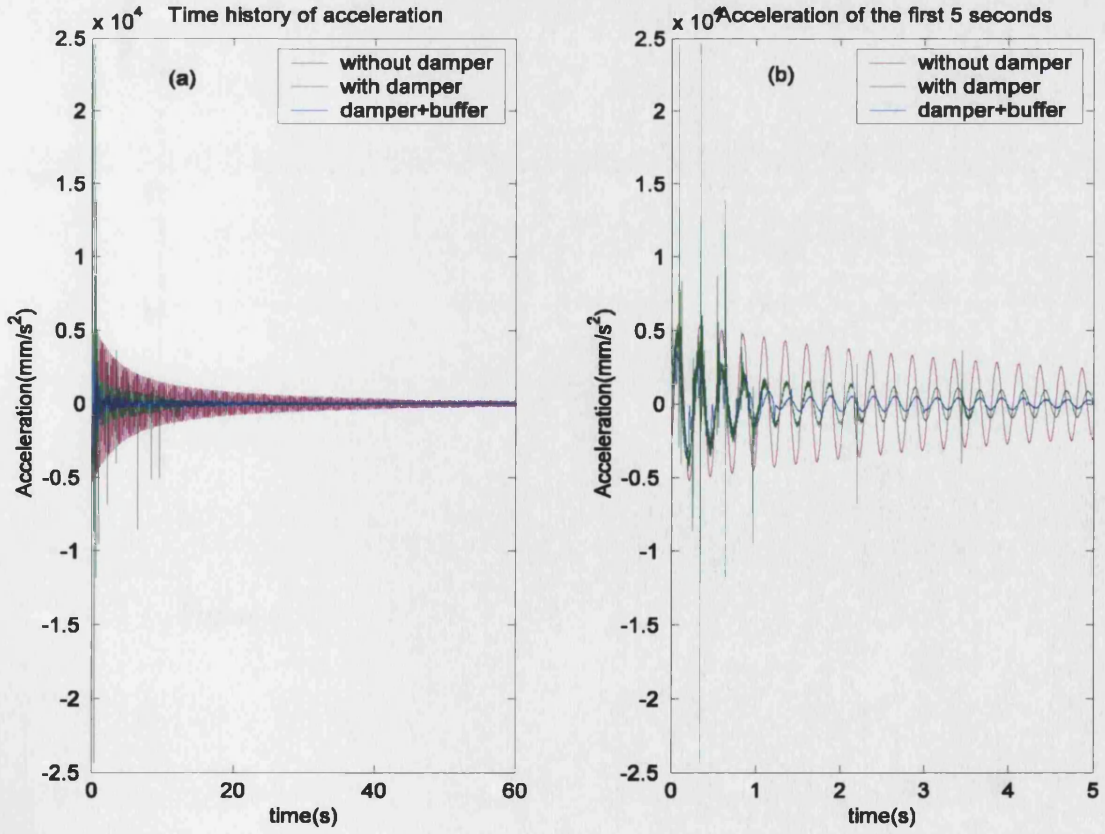


Figure 6.10: Time history of acceleration—initial displacement excitation

Similar results are obtained when the structure is excited by an initial velocity (by release of a pendulum from a predetermined distance and striking the primary structure), as presented in Figures 6.11 and 6.12. Figure 6.11 shows the comparison between the PSDs of the acceleration response when without an impact damper, with a conventional rigid impact damper and with a buffered impact damper. Figure 6.12 shows the corresponding time histories of the acceleration responses. The same conclusions can be reached, i.e. the buffered impact damper reduces the response most effectively with no peaks in acceleration or related noise at the moment of impact.

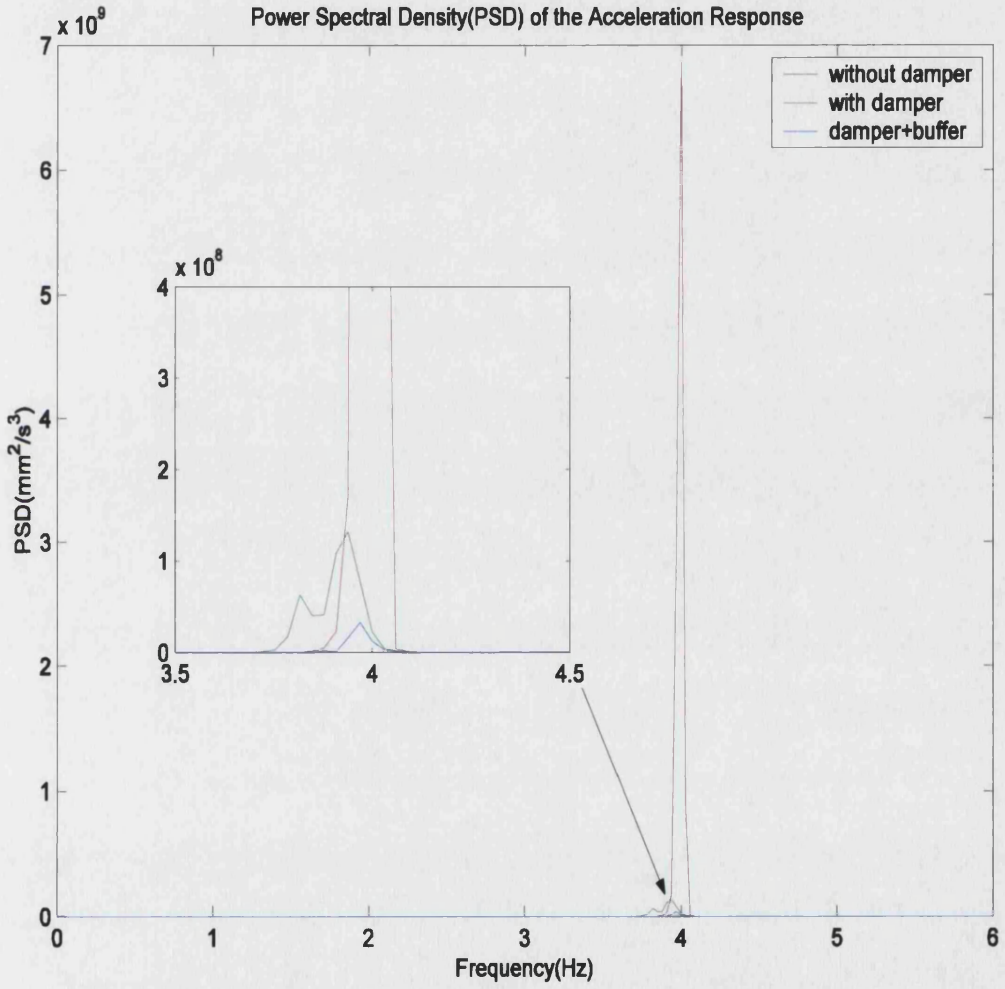


Figure 6.11: Power spectral density of acceleration response

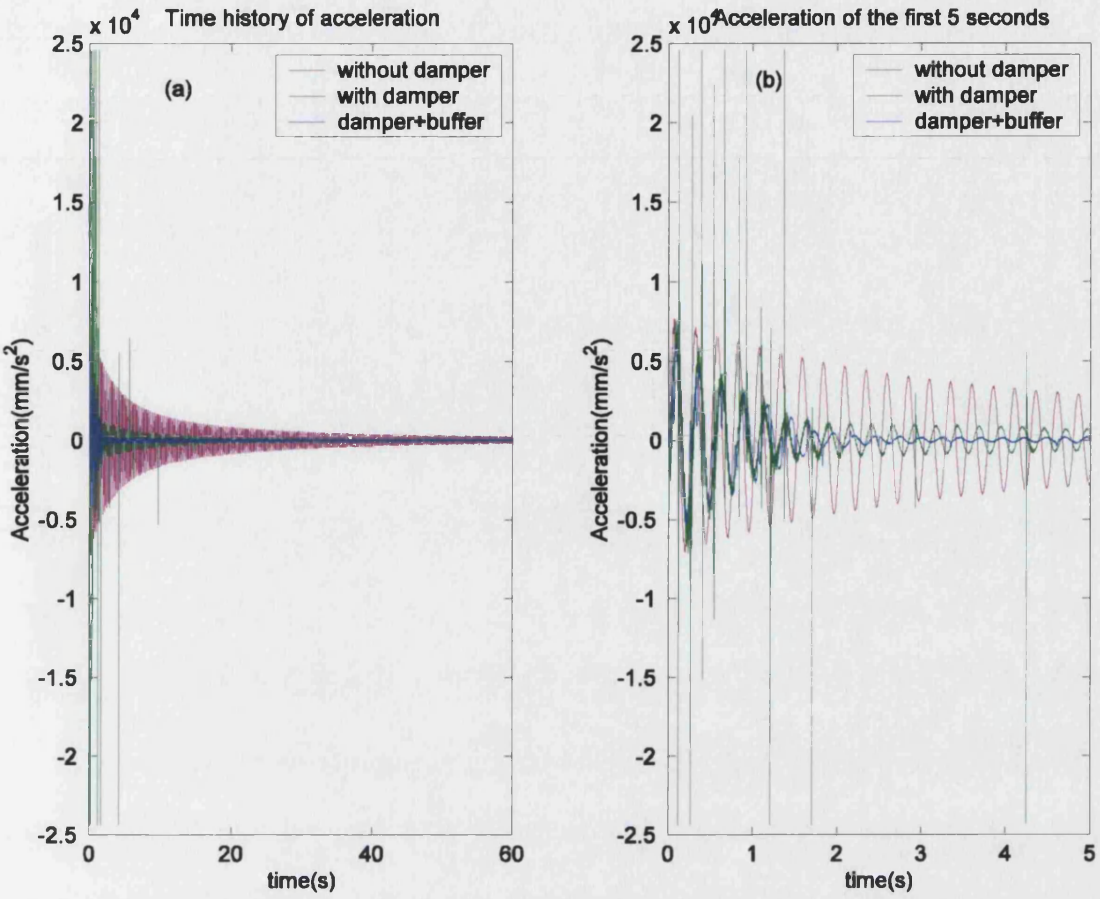


Figure 6.12: Time history of acceleration --initial velocity excitation

The effect of mass ratio was investigated by means of initial velocity excitation. In this case the clearance chosen was $d$ = 20mm and the three mass ratios investigated were $\mu$ = 0.19, $\mu$ = 0.082 and $\mu$ = 0.05. The results, shown in Figure 6.13, demonstrate that the buffered impact damper controlled the structure better than the rigid impact damper for all three mass ratios tried. Moreover, the difference between the response with the rigid impact damper and the buffered impact damper becomes more significant as the mass ratio becomes smaller. This makes the buffered impact damper even more attractive for use in practice since it is desirable for the impact mass to be as small as possible.

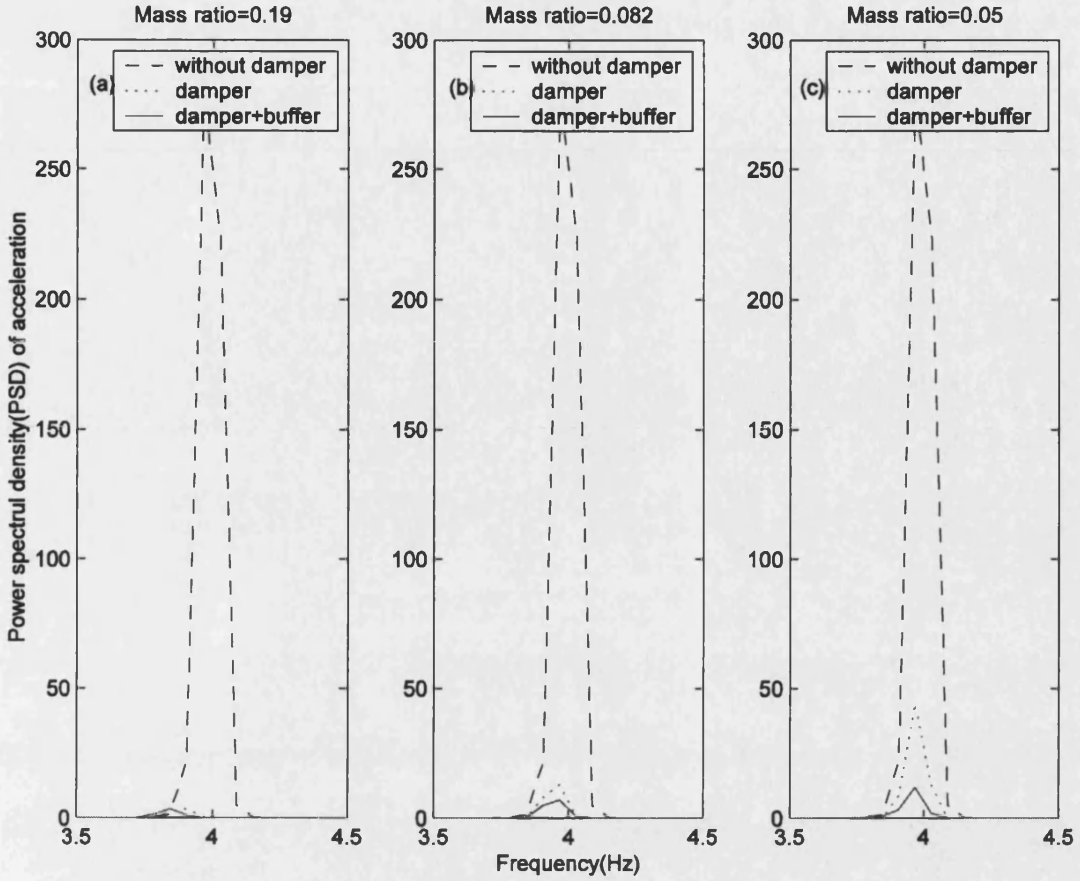


Figure 6.13: Performance at different mass ratio

Finally, the effect of intensity of excitation was investigated with a mass ratio of $\mu = 0.05$ and a clearance of $d = 20mm$. The results, shown in Figure 6.14, are in the order of increasing intensity of excitation (although the actual excitation force was not measured). It can be seen that for the buffered impact damper, the PSD is brought down to approximately the same level irrespective of the intensity of excitation, and in all cases results in a significantly smaller response than the rigid impact damper.

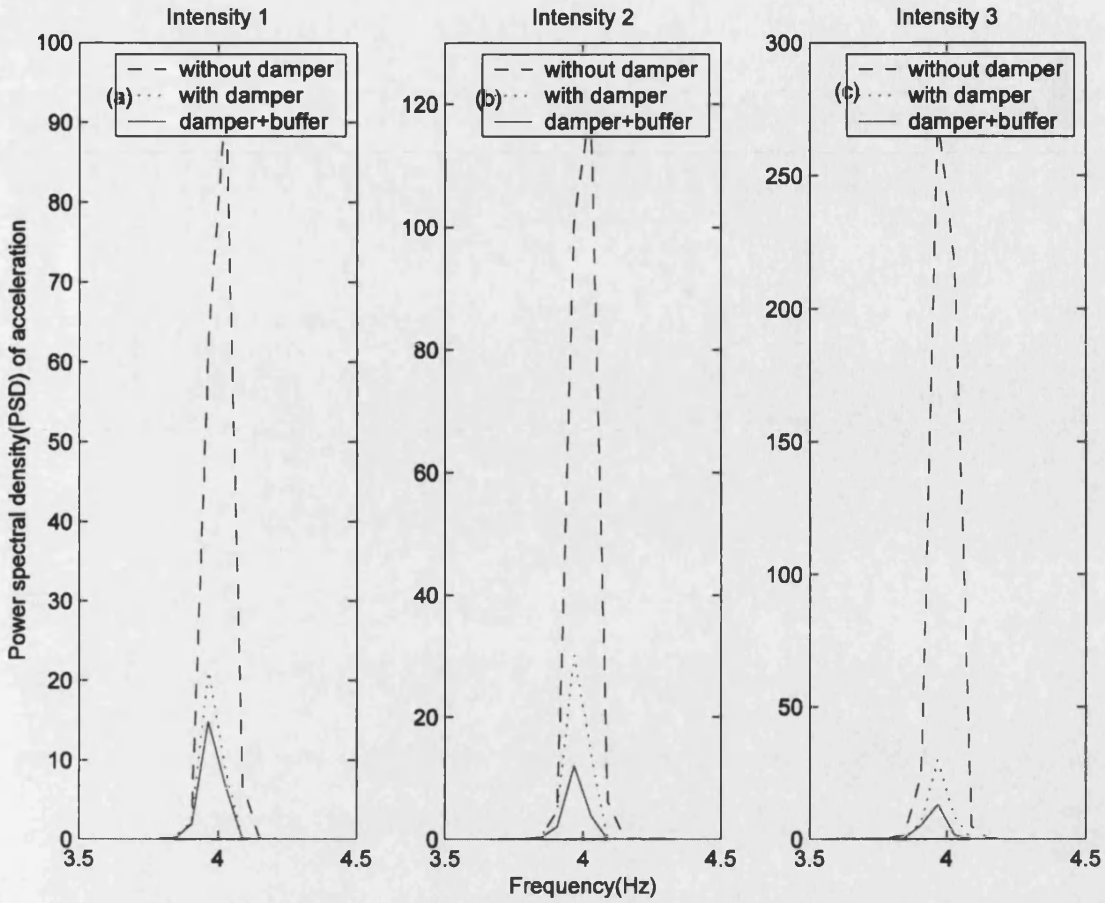


Figure 6.14: Performance at different excitation intensities

*6.3.3.2 forced vibrations*

First, dwell sinusoidal excitation experiments were carried out. Figure 6.15(a) and 6.15(b) show the results when excited with a *4.0283Hz* sinusoidal excitation (i.e., at the natural frequency of the structure). The mass ratio and clearance taken in this case are $\mu$*=0.082* and *d=20mm* respectively. From Figure 6.15(a) it can be seen that the control effect of the buffered impact damper is better than that of the conventional rigid impact damper. Moreover, as shown in Figure 6.15(b), the acceleration with the buffered impact damper is much smaller than that with the conventional impact damper, and even smaller than that without impact damper. The peak acceleration, of course, reflects the magnitude of the collision force so that the far quieter operation of the new impact damper should not be surprising.

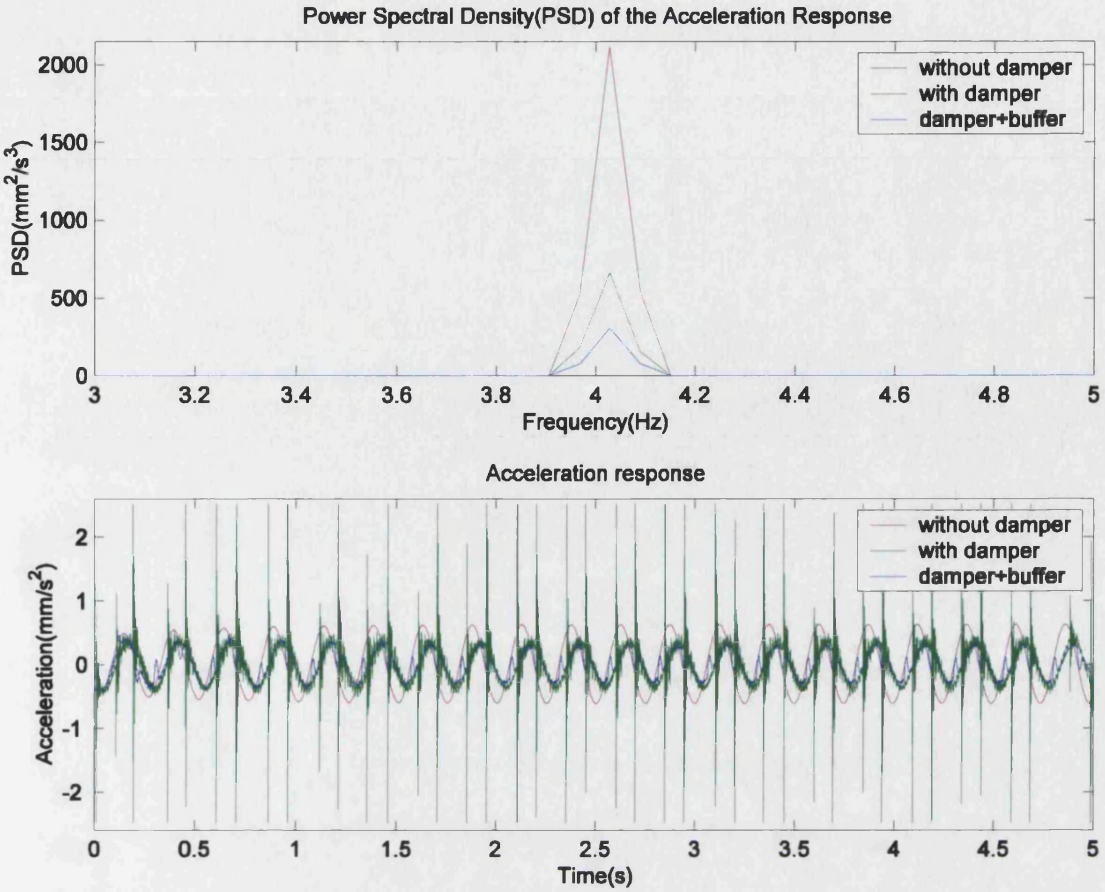


Figure 6.15: Performance under sinusoidal excitation

The effect of intensity of excitation under a *4.0283*Hz sinusoidal excitation is presented in Figure 6.16(a), 6.16(b) and 6.16(c), in the order of increasing amplitude of excitation. The mass ratio taken in this case is $\mu$*=0.082* and the clearance is *d=15mm.* It is clear that at different levels of excitation the buffered impact damper always results in a better control result than conventional impact damper.

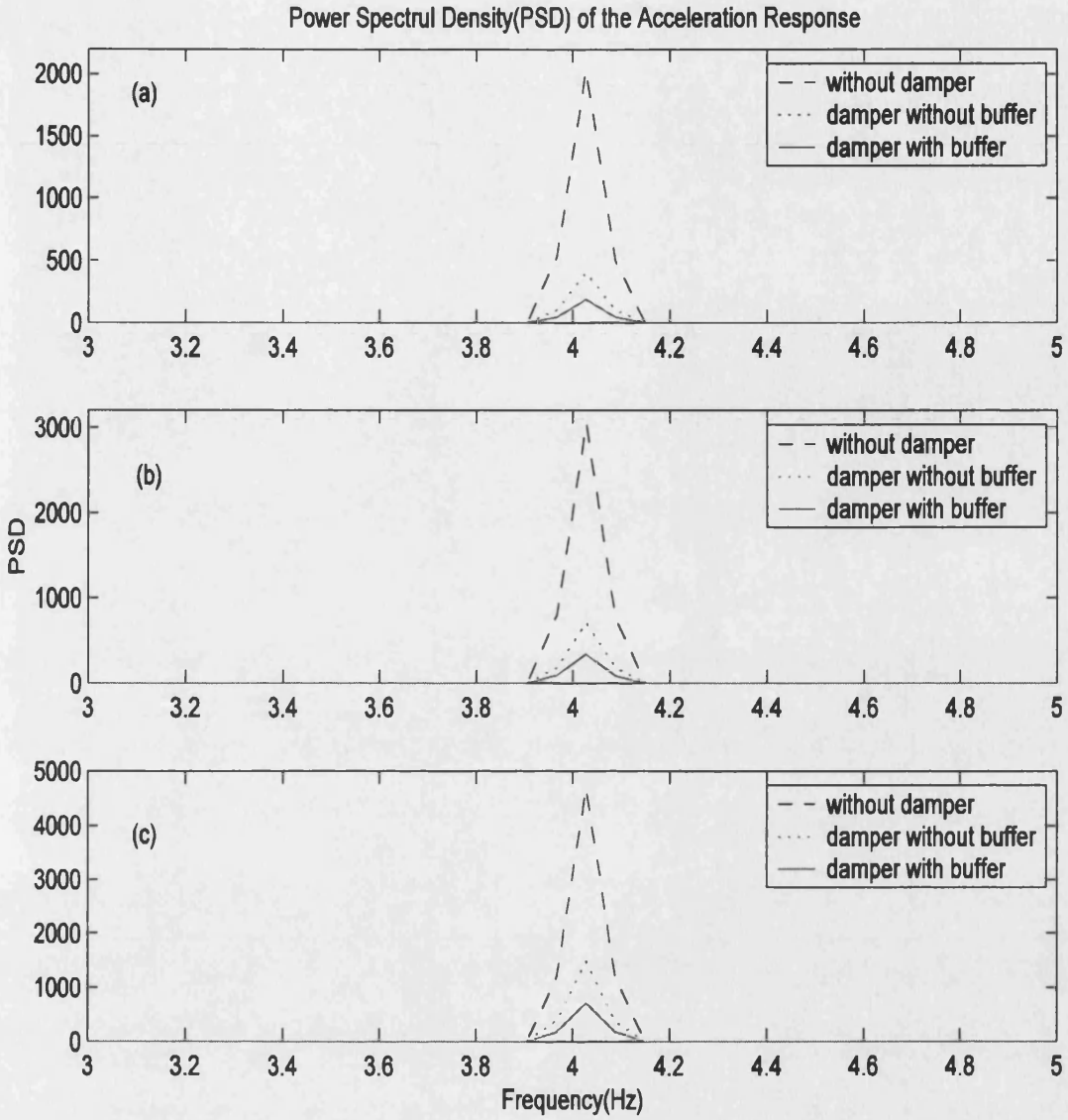


Figure 6.16: Performance under sinusoidal excitation with different intensity

Figure 6.17 shows the effect of mass ratio under a *4.0283*Hz sinusoidal excitation. The clearance taken in this case is *d=15mm.* It can be found that for all the three mass ratios the control result of the buffered impact damper is better than that of the conventional impact damper, although the difference when the mass ratio is $\mu$*=0.05* is small.

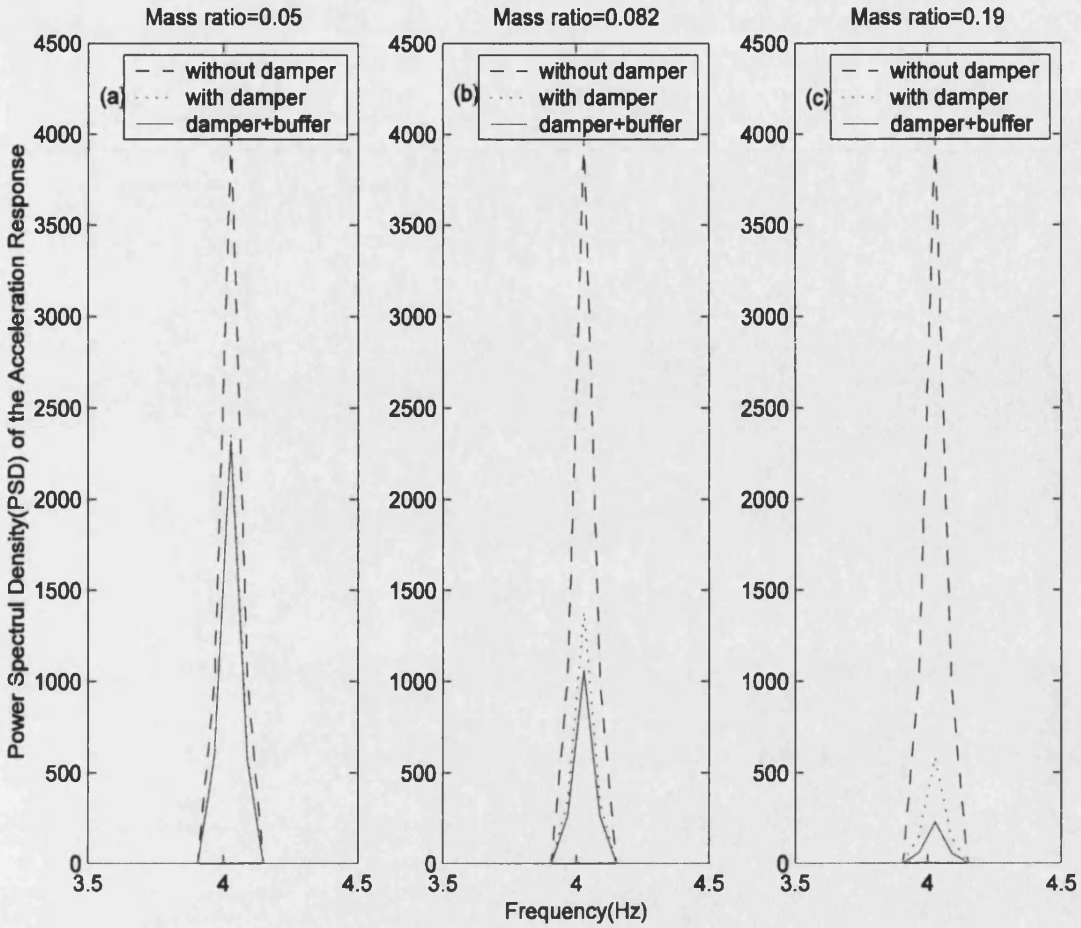


Figure 6.17: Performance under sinusoidal excitation
--with different mass ratios of damper

By applying sinusoidal excitation at frequencies above and below the natural frequency of the structure, the effect of excitation frequency was investigated. The mass ratio was chosen to be $\mu = 0.082$ and clearance $d = 20mm$. The results are shown in Figure 6.18(a) and 6.18(b) where frequency ratio, $r$, is defined as the ratio of excitation frequency, $f$, to that of the natural frequency of the primary structure, $f_n$, i.e. $r = f / f_n$, and $P/P_0$ represents the ratio of $P$, the peak value of the PSD of acceleration with an impact damper, to $P_0$, the peak value of the PSD of acceleration of the structure without an impact damper. Hence, a PSD ratio of less than 1 represents a control effect, whilst a ratio greater than 1 represents a detrimental effect. It can be seen that when the frequency ratio is less than $0.9$ both the buffered impact damper and conventional impact damper result in an increased response of the primary system with the buffered impact damper increasing the response of the primary system more than the conventional impact damper. When the frequency ratio is between $0.9$ and $0.95$ the control effect of the buffered impact damper and that of the rigid impact damper is

almost identical. However, when the frequency ratio is between *0.95 and 1.25* the control effect of buffered impact damper is significantly better than that of conventional impact damper. It should be noted that for the lightly damped structure under investigation, the response of the structure, whether controlled or not, is relatively small outside the range $0.95 > f/f_n > 1.05$, as can be seen in Figure 6.18(b) and therefore the effect of the damper increasing the response for $f/f_n < 0.9$ is not of major concern in this example. The overall response at these frequencies is still less than, or equal to, the controlled response when excited at the resonant frequency.

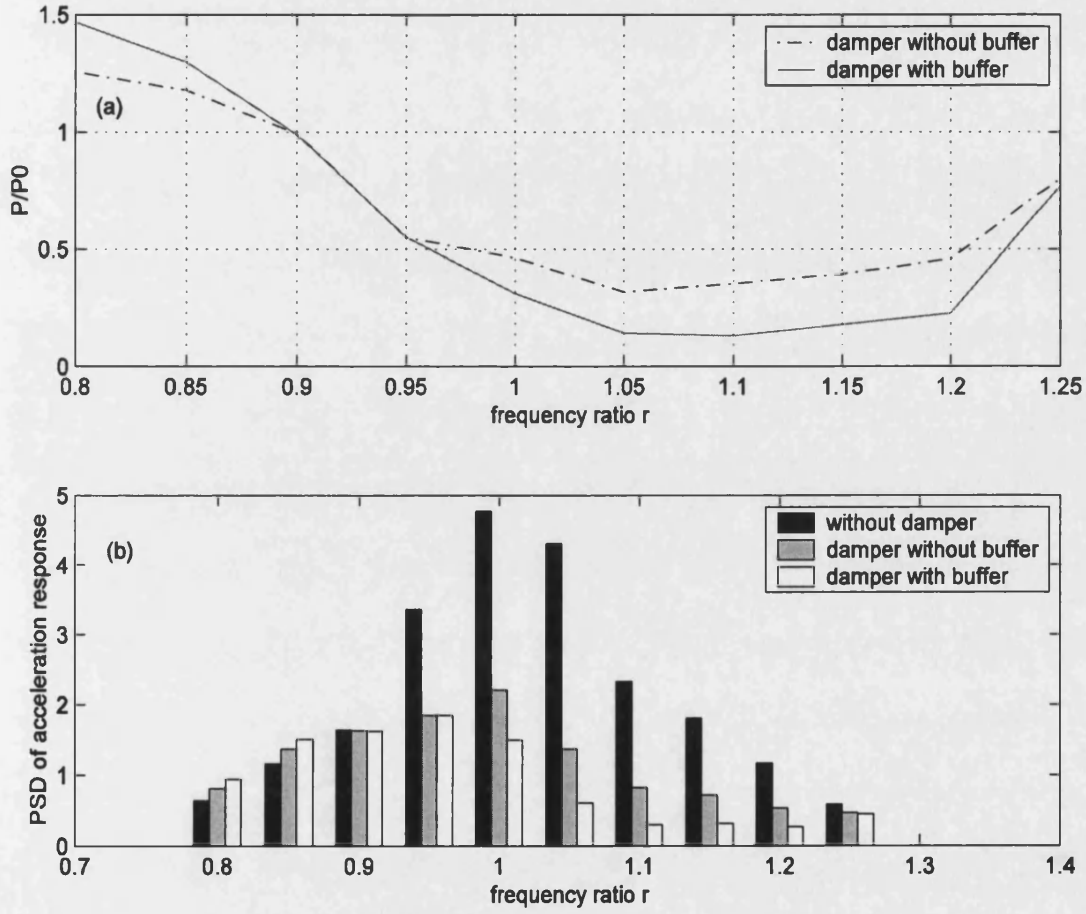


Figure 6.18: Effect of excitation frequency on performance

In general, a structure will be excited over a wide frequency range, rather than at a specific frequency. Therefore, further tests have been performed using random base excitation with band-limited frequency content between *0* and *10Hz*. Figures 6.19(a), 6.19(b) and 6.19(c) show comparisons between the PSDs of the acceleration response of the primary structure when without an impact damper, with a conventional impact damper and with a buffered impact damper for three different mass ratios. The clearance

taken in this case is $d$ = 20mm. It can be seen that for both the buffered and rigid impact damper, a higher mass ratio results in better control. However, the buffered impact damper produces better control than the conventional rigid impact damper in all cases except at some frequencies below the natural frequency as expected from the previously described tests. This is similar to the results seen in Figure 6.13 for free vibration.

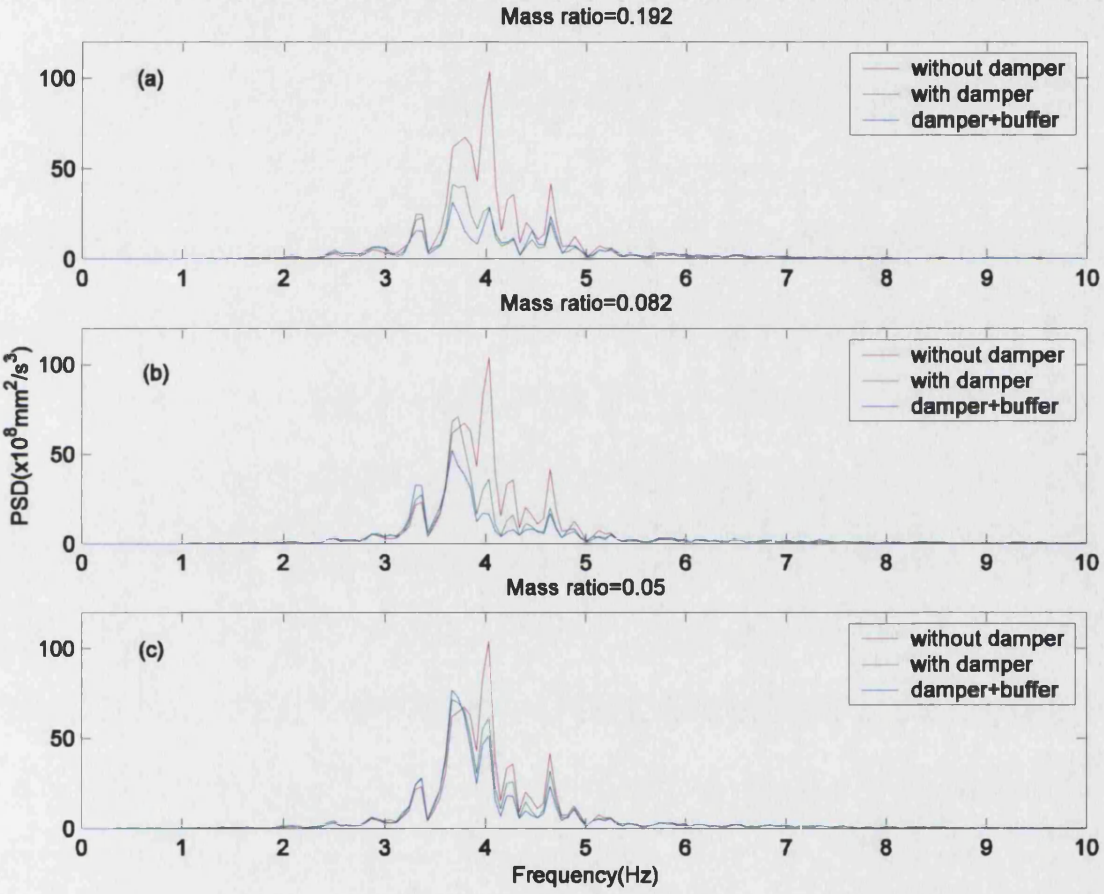


Figure 6.19: Performances under random excitation

Figure 6.20(a) shows a typical time history of the acceleration response for a given random excitation input. The graph shows a comparison between the response of the primary structure without a damper, with a conventional rigid impact damper of mass ratio $\mu = 0.05$ and with a buffered impact damper of mass ratio $\mu = 0.192$. It can be seen that even though the mass ratio of the buffered impact damper is almost four times that of conventional impact damper, the peak accelerations are much smaller and, as expected, smaller than without an impact damper. Figure 6.20(b) shows the

corresponding measured contact force between the mass and the stops for the rigid impact damper and the buffered impact damper. It can be seen that the contact force of the buffered impact damper is also much smaller than that of the conventional rigid impact damper, even though the mass ratio of the former is much larger. However, it can also clearly be seen that the contact time of each collision is much longer for the buffered impact damper.

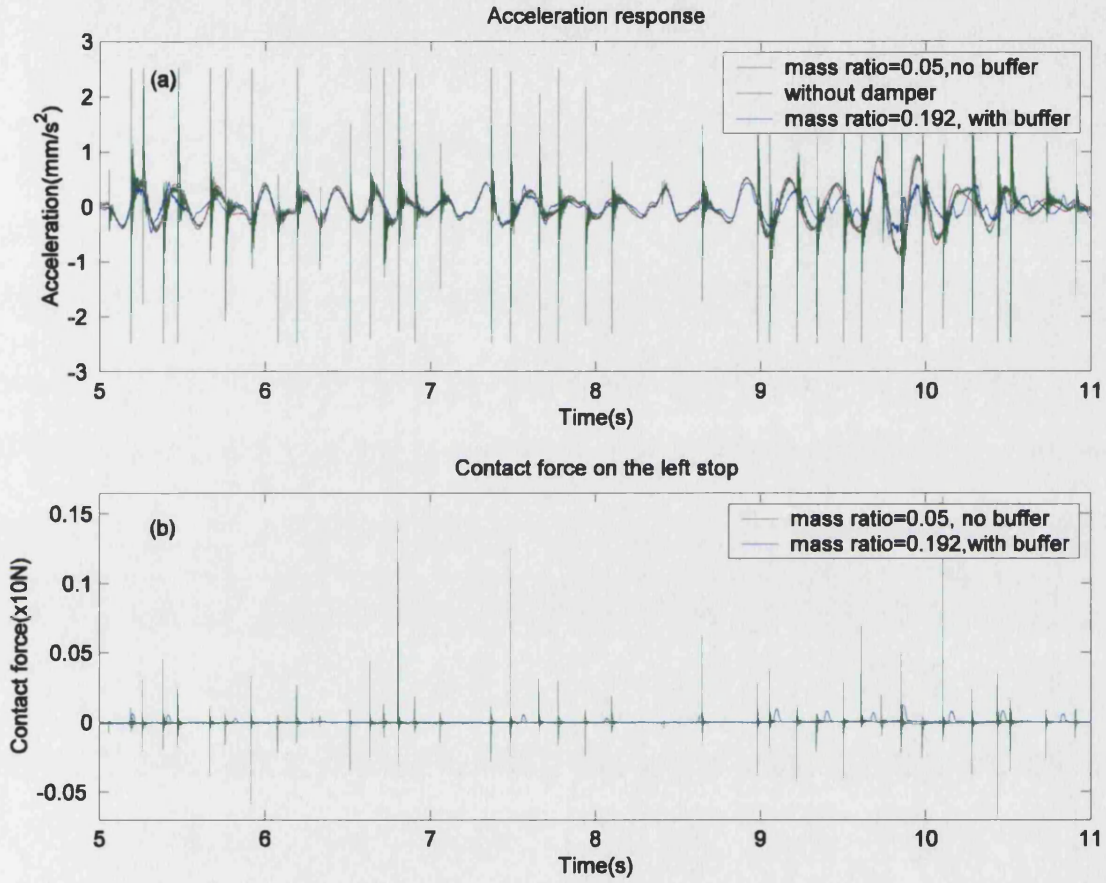


Figure 6.20: Acceleration and contact force under random excitation

The effect of clearance under random excitation is shown in Figures 6.21(a) and 6.21(b) where $A_0$ is the integral of the PSD of the acceleration response of the primary structure without an impact damper while $A$ is the integral of the PSD of the acceleration response of the structure with either a rigid or buffered impact damper (the integral of the PSD was used since, as can be seen from Figure 6.19, the response of the structure is significant over a wide frequency range rather than concentrated at the natural frequency, so the integral provides a better indication of the degree of control over the whole frequency range than the peak value would). In this case the mass ratio used is $\mu$

$= 0.082$. It can be seen that over the whole range of clearances $0 < d < 55mm$, the control effect of buffered impact damper is always better than that of conventional impact damper with the difference more significant when the clearance is small $(d \leq 35mm)$.

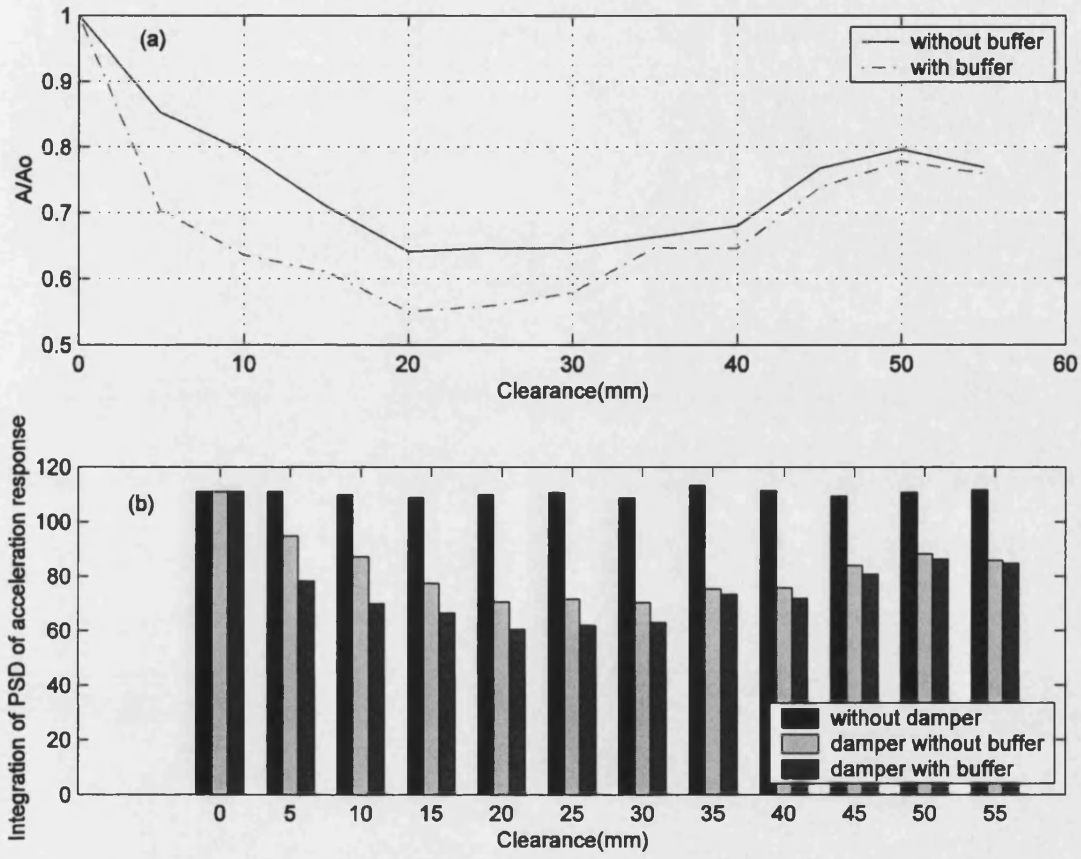


Figure 6.21: Effect of clearance---random excitation

Finally, the effect of the intensity of random excitation on control effect is investigated. Figures 6.22(a), 6.22(b) and 6.22(c) present a comparison of the PSDs of the response in order of increasing excitation intensity. The mass ratio and clearance taken in this case are $\mu = 0.082$ and $d = 20mm$ respectively. It can be seen that at different levels of excitation the control effect of the buffered impact damper is always better than that of the conventional rigid impact damper at the resonant frequency although in some cases it is slightly worse at frequencies below the natural frequency. This confirms the findings indicated by Figure 6.18.

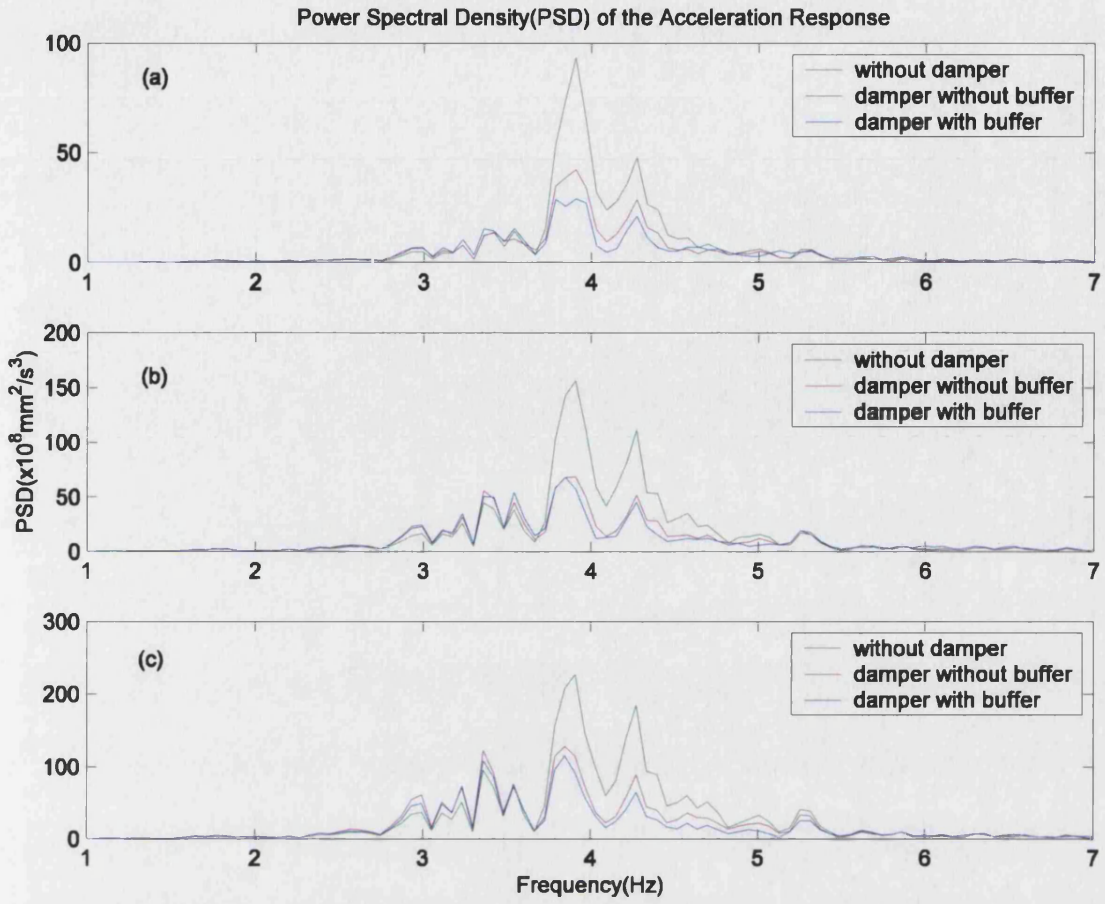


Figure 6.22: Effect of excitation intensity—random excitation

From the experimental investigations above, the following points can be drawn:

- The introduction of a buffer can significantly change the contact characteristics of collision of an impact damper, such as significantly reducing of the contact force and increasing the contact time
- A buffered impact damper can eliminate the inherent disadvantage of a conventional impact damper, i.e. high contact force and associated high accelerations and noise caused by collision, and significantly enhance vibration control effect meanwhile.
- A buffered impact damper can achieve better control than a conventional impact damper; However, in cases where the control effect of a conventional impact damper is detrimental, the control effect of a buffered impact damper can be more detrimental, as in the case of the frequency ratio $r < 0.9$.
- The buffered impact damper is less sensitive to variations in excitation type and the clearance and mass parameters of the damper itself. It also results in quicker

attenuation in the free vibration response. The features of the buffered impact damper make it not only attractive but also practical for engineering application.

### *6.3.4 Buffer and contact characteristics*

The experimental results presented in section 6.3.3 demonstrate that the buffered impact damper is more effective in vibration attenuation than a conventional rigid impact damper. Additionally, the peak accelerations (and hence the collision force and noise) of the primary structure equipped with a buffered impact damper are much smaller than with a conventional rigid impact damper.

The excellent performance of the buffered impact damper arises from the buffer itself. The characteristics of the contact force during impacts are altered by the introduction of the buffer. To understand this behaviour, further buffers of different materials (as described in Table 6.1) are investigated and compared with the behaviour with no buffer, i.e. the conventional rigid impact damper. For these tests, a sinusoidal dwell excitation was provided to the base of the structure at a frequency of *4.0283*Hz. The mass ratio and clearance used are $\mu = 0.082$ and $d = 20mm$ respectively. Figure 6.23 shows the PSDs of the acceleration response of the primary structure when without a damper, with the conventional rigid impact damper and with a series of buffered impact dampers. Buffers 1 to 4 are progressively stiffer materials. The rigid impact damper can be thought of as a limiting upper bound case for the buffered impact dampers. It can be seen that with buffer *1*, the least stiff buffer, the control effect is best whilst with buffer *4* the control effect is only slightly better than for the rigid impact damper. However, all give a significant level of control over the case with no impact damper.

Figures 6.24(a), 6.24(b), 6.24(c) and 6.24(d) give the time history of the acceleration response of the primary structure with buffers *1*, *2*, *3* and *4* respectively. For comparison, the responses with the conventional rigid impact damper and without a damper are also presented. Acceleration spikes can be seen in the sinusoidal acceleration which corresponds to collisions between the impact mass and the stops. These spikes get progressively larger as the stiffness of the buffer material is increased. However, it can be seen that of the four buffers, only in the case of buffer *4* are the accelerations of the primary structure bigger than that without a damper. The accelerations for the case with the rigid impact damper are significantly greater at the moment of impact than for the uncontrolled case.

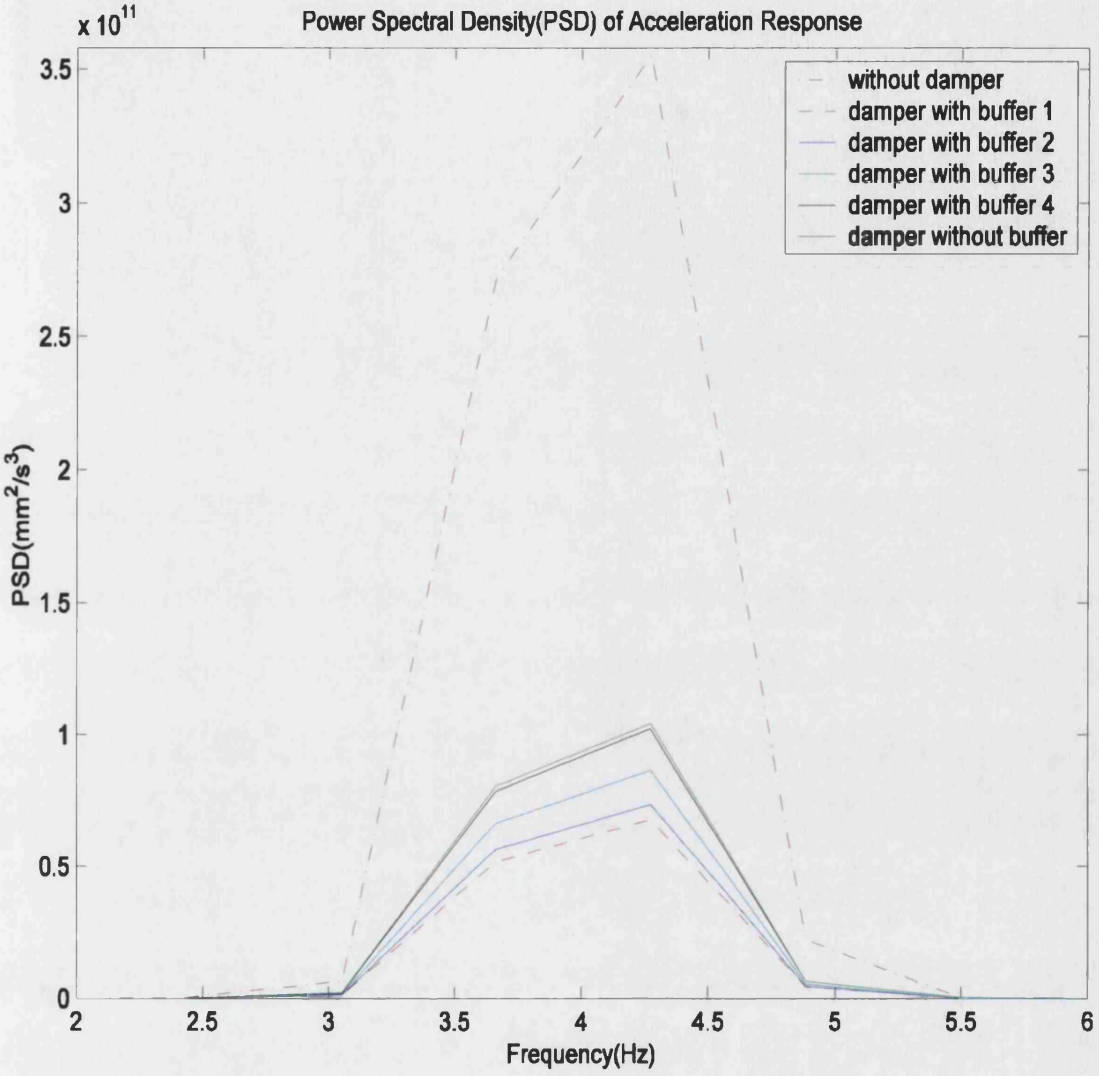


Figure 6.23: Performance of BID with different buffers

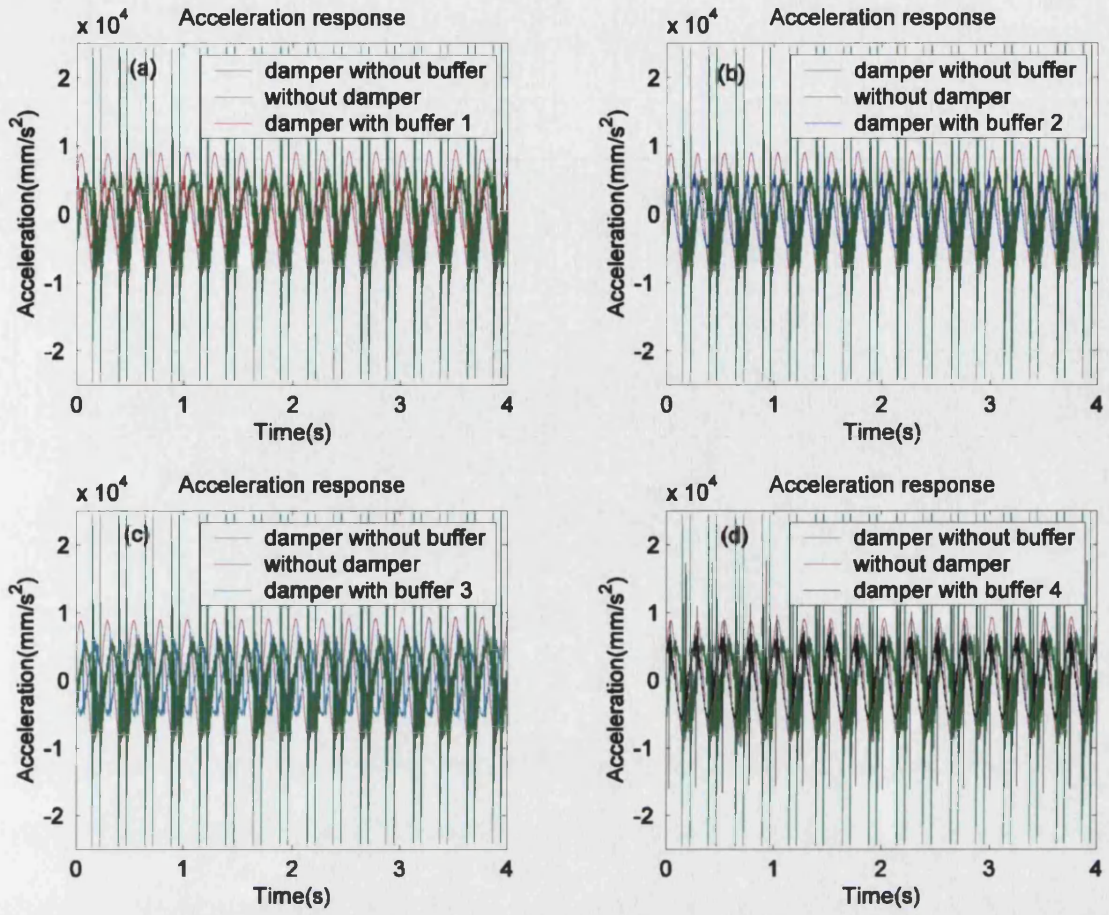


Figure 6.24: Effect of buffer on acceleration

Figure 6.25(a1) to (e1) show the contact force measured with buffers *1* to *4* and without a buffer (the rigid impact damper). Figure 6.25(a2) to (e2) focuses in on a single impact for the five cases. It is clear that as the stiffness of the buffer decreases, so the collision force decreases (note that both the time and force scales are different for each plot). The force in the case of buffer *1* is two orders of magnitude smaller than for the rigid impact damper. However, the contact time, which is defined as the time duration while the impact mass stays in contact with the stop, increases as the buffer stiffness decreases. As already mentioned, the contact time for the conventional rigid impact damper is about *0.0003* seconds, while for buffers *1* to *4* the contact times are about *0.0255*, *0.019, 0.004* and *0.003* seconds respectively. Hence, the contact time for buffer *1* is two orders of magnitude greater than for the rigid impact damper.

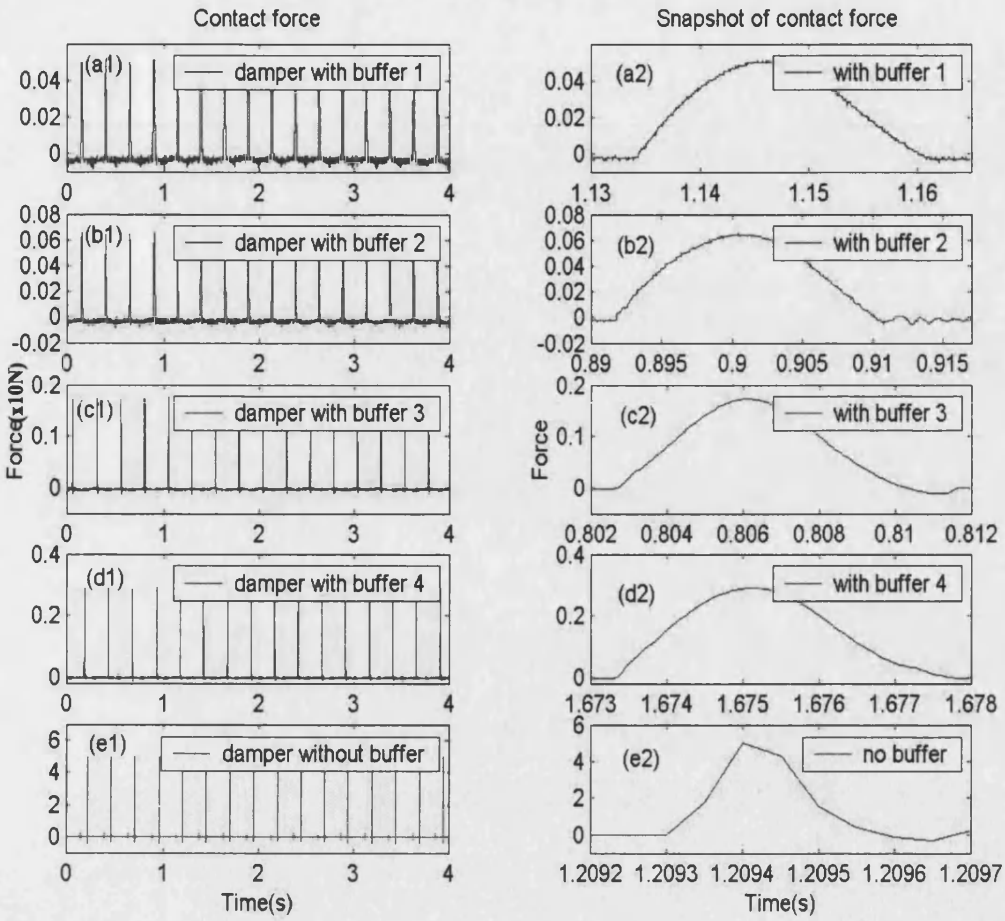


Figure 6.25: Contact forces and contact times of different buffers

The vibration control effect of an impact damper comes from collisions of the impact mass with the stops, resulting in exchange of momentum. For a single collision, the impulse momentum relationship is given by:

$$I = M(V^+ - V^-) = \int_0^{T_c} f_c(t)\,dt \tag{6.1}$$

Here $M$ is the mass of the primary structure and $V^+$ and $V^-$ represent the velocity of the primary structure immediately before and after the collision respectively. $T_c$ and $f_c(t)$ represent contact time and contact force respectively. The effect of a collision upon the structure depends upon the impulse, $I$. This, in turn, depends not only upon the contact force, but, importantly, also on the contact time. According to Hertzian impact theory [32], for an elastic collision the contact time $T_c$ is proportional to $(X_1 + X_2)^{2/5}$ where $X_1$ and $X_2$ are elastic coefficients for the two bodies (i.e. the impact damper mass and the

stop). The elastic coefficient of a buffered stop, say $X_2$, is much higher than that of an unbuffered steel stop. Therefore, unsurprisingly, there is an increase in contact time by the addition of a buffer and hence a corresponding reduction in contact force resulting in lower accelerations and reduced damage during impacts.

To make further comparison, Figure 6.26 shows the ratio of the impulse momentum of one collision (obtained by numerical integration), where $I_0$ is without a buffer and $I$ is with a buffer, and the ratio of the control effect, where $A_0$ is the integral of the PSD of the acceleration response of the primary structure with the rigid impact damper and $A$ is with a buffered damper. It can be seen that the impulse momentum ratios get progressively higher as the buffer stiffness decreases, resulting in better control effect (i.e. lower $A/A_0$ ratios).

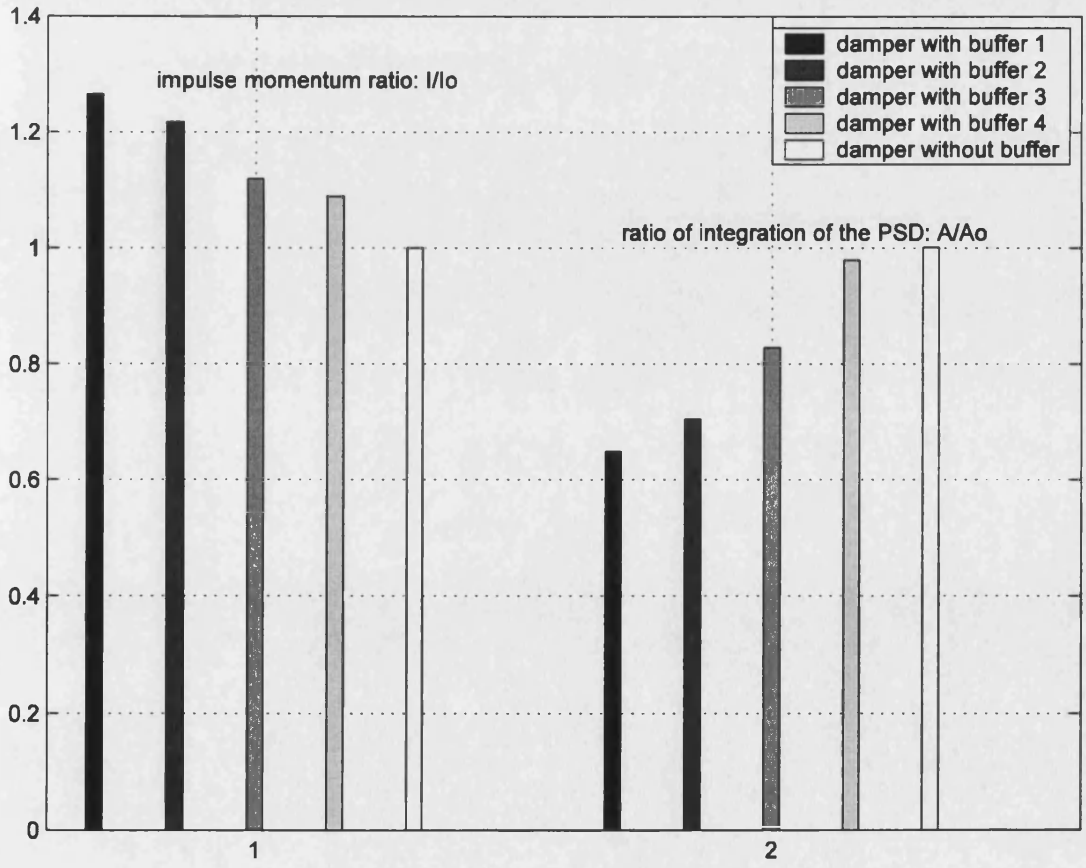


Figure 6.26: Impulse momentum ratio and corresponding control effect

The improved performance of a buffered impact damper (i.e. the high $I/I_0$ ratio) possibly stems from the elastic deformation of the buffer. This can be seen by examining the coefficient of restitution, $c_r$, defined as:

$$c_r = \frac{v^- - V^-}{V^+ - v^+} \tag{6.2}$$

where $v^+$ and $v^-$ are the velocities of the impact mass immediately before and after impact respectively. A coefficient of restitution of 1.0 represents perfectly elastic collision with no damping occurring by the impact process itself. At the other extreme, a coefficient of restitution of zero represents a perfectly plastic collision where all energy is dissipated in the form of plastic deformation (and only a single impact would occur). Chatterjee *et al.* [64] found that, in the case of an impact damper for control of a forced oscillator, the value of coefficient of restitution should be as high as possible to achieve a maximum attenuation. Experimental measurements show that, for the system under investigation, the coefficient of restitution for impact between a steel ball and buffer *1* is *0.61* while the coefficient of restitution for impact between a steel ball and the unbuffered steel stop is *0.46.* Therefore, significant plastic deformation occurs during impact of the unbuffered damper (as one might expect for metal on metal impact) whilst impact with the buffered damper is more elastic in nature. Whilst it might be thought desirable that energy is dissipated during the impact itself, it is more important that the impact mass has a high velocity following impact. This means that more kinetic energy is transferred from the structure to the impact mass (and, thus, the dynamic response of the structure is reduced) and also results in a high impulse being imparted at the next impact. The impulse of the impact of the damper mass can be defined according to the following equation:

$$I = m(v^+ - v^-) \tag{6.3}$$

where $m$ is the mass of the damper mass. The impulse defined in equation (6.3) is equivalent to impulse defined in equation (6.1). Assuming $v^+$ and $V^+$ act in the opposite sense before collision and $v^-$ and $V^-$ act in the same sense following collision (i.e. the impact mass starts moving in the same direction as the structure) then it follows that if

$v^-$ remains high following collision then, equating equations (6.1) and (6.3), $V^-$ must become correspondingly smaller.

If significant energy is absorbed during the impact (i.e. if the coefficient of restitution is small) then the post impact velocity is small and the subsequent impulse will be smaller and less kinetic energy is transferred to the impact mass. The more elastic contact of the buffered damper provides a higher coefficient of restitution and therefore higher post impact velocity of the impact mass, greater impulse and lowers the velocity of the structure more efficiently at each collision.

Preliminary investigations into the contact characteristics show that the impulse and duration of a collision, rather than the contact force itself, are the important factors in the design and behaviour of such a damper. A higher coefficient of restitution, given by an elastic buffered damper results in higher impulse and increased transfer of kinetic energy from the structure to the damper mass. However, since collision duration is also important, a simple coefficient of restitution model is not suitable for modelling such impact behaviour. Rather, a spring-damper model of the buffer is more appropriate, provided that the stiffness and damping characteristics can be defined, as described in section 2.3.

## 6.4 Experimental investigation on a MDOF primary structure equipped with an impact damper—with and without a buffer

Note: To save space, only some of the results of experiments on the MDOF primary structure are presented. The test structure is the same as that shown in Figure 5.1 except that buffers are added to the stops for the buffered impact damper. The experimental procedures are similar to those described in section 5.4 and 6.3.

### *6.4.1 Free vibration*

#### 6.4.1.1 *initial velocity excitation on the first storey*

The mass ratio taken in this investigation case is $\mu = 0.082$ and the clearance taken is $d = 10mm$, for both the conventional rigid impact damper and the buffered impact damper (BID). Excitation is exerted by striking the structure at A, the first storey of the primary structure (as shown in Figure 5.1). Figure 6.27 gives the acceleration response of each

storey without an impact damper, with a conventional impact damper and with the BID. From Figure 6.27 it can be seen that at the moments of collision when the conventional impact damper is in operation, high accelerations occur not only at the third storey, where the impact damper is located, but also, to a lesser extent, at the other storeys. When the BID is in operation, for the third storey, the peak acceleration occurring at the moments of collision is at about the same level as when there is no impact damper at all.

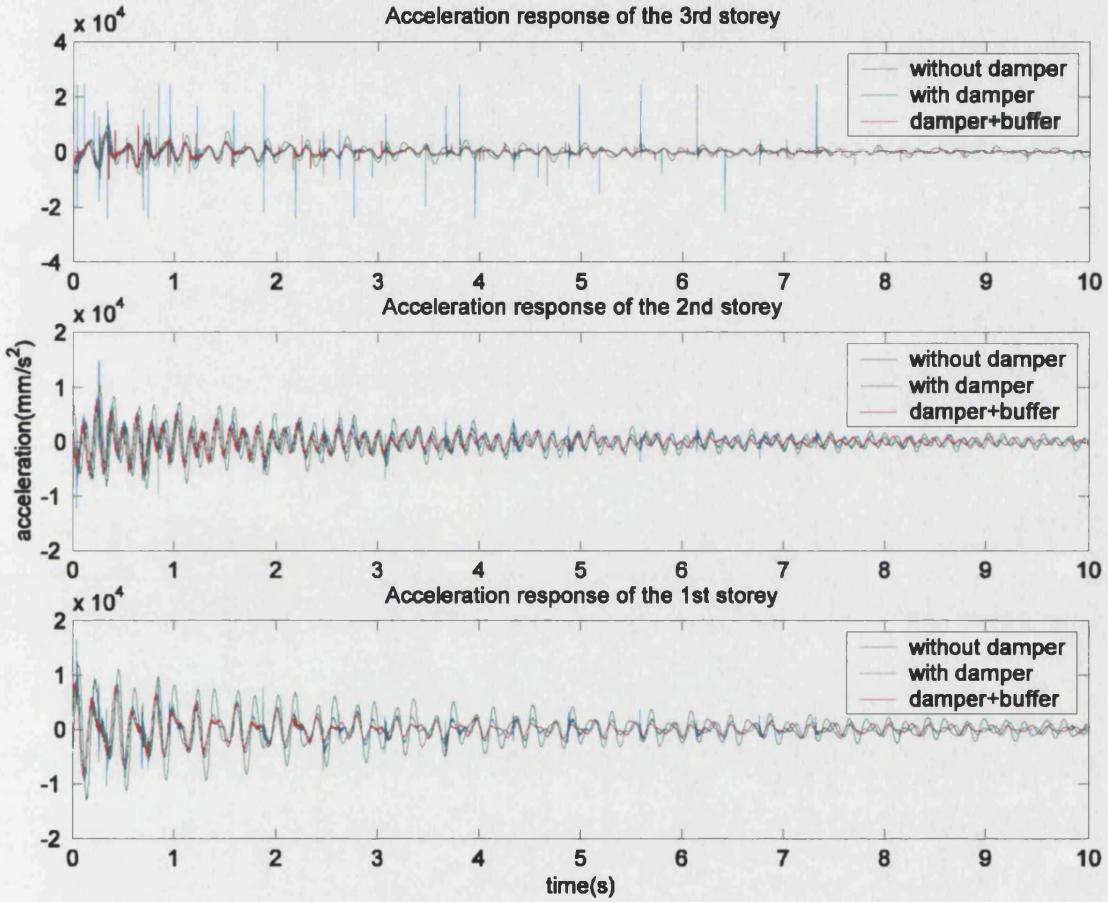


Figure 6.27: Acceleration response of each storey

Figure 6.28 shows the corresponding power spectral densities. To show the effect of a BID more clearly and compare it with that of the conventional impact damper, Figure 6.28 is re-plotted by zooming in on each natural frequency, as shown in Figure 6.29. From Figure 6.29 it can be seen that the BID results in significant control of each mode for each storey. For the first mode, the control effect of BID is slightly better than that of the conventional impact damper. For the second mode, the control effect of BID and that of the conventional impact damper are almost identical. However, the BID shows significant control effect on the third mode of each storey while the conventional impact

damper results in no control effect and actually makes things slightly worse, which is consistent with the experimental results presented in Chapter 5.

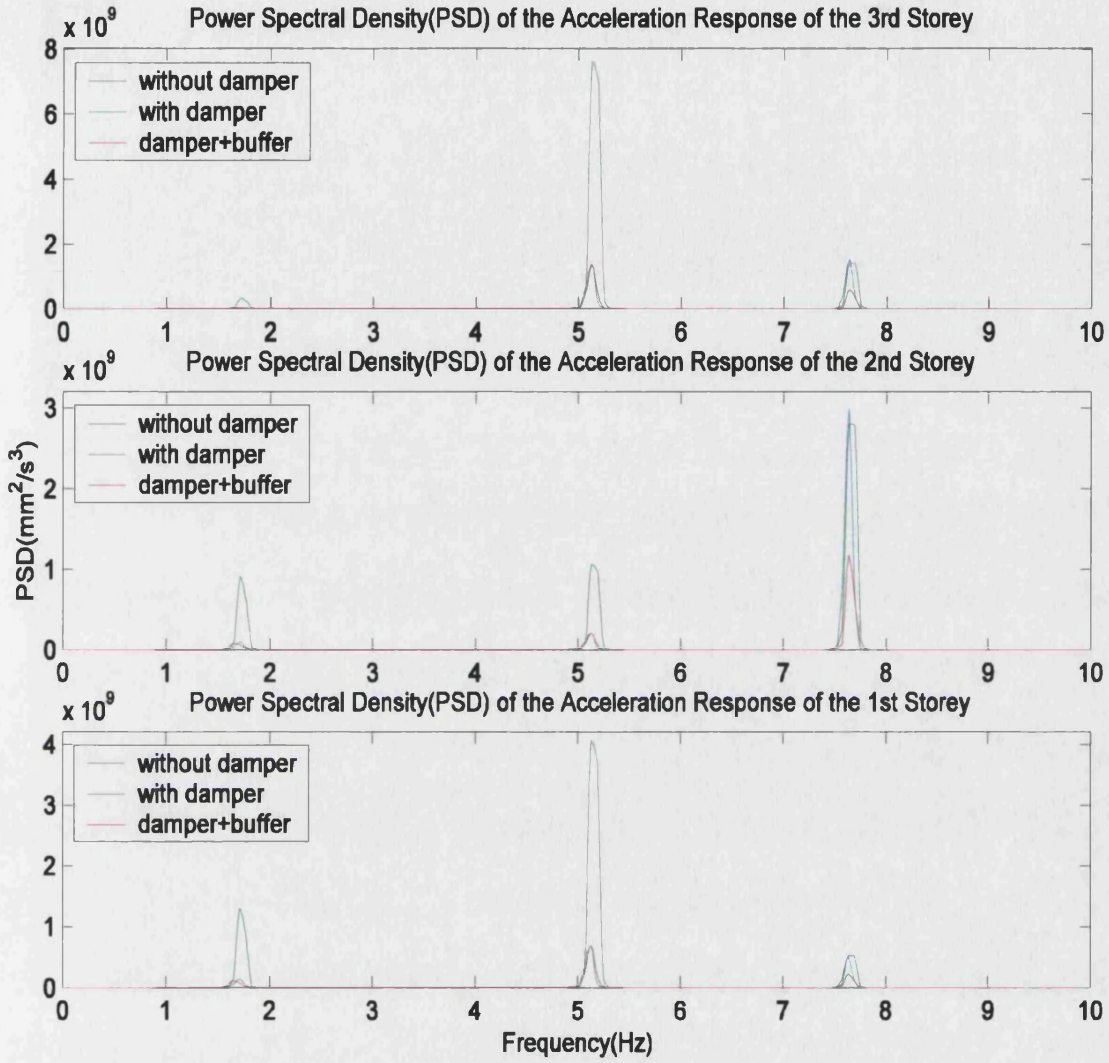


Figure 6.28: Power spectral density of the primary structure

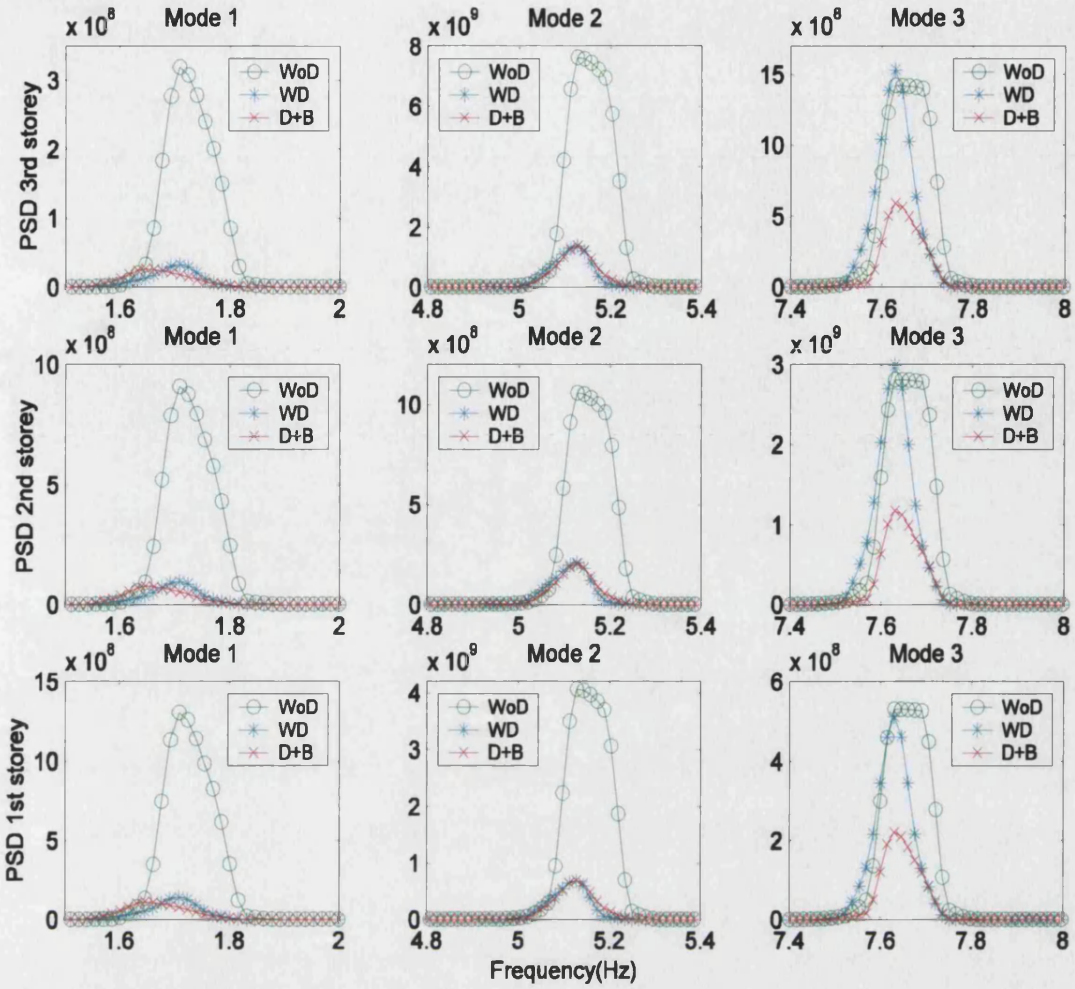


WoD: without damper; WD: with conventional impact damper; D+B: with BID

Figure 6.29: Power spectral density of the primary structure—zoomed in

6.4.1.2 *initial velocity excitation on the third storey*

The mass ratio taken in this investigation case is $\mu=0.082$ and the clearance taken is $d=20mm$, for both the conventional rigid impact damper and the buffered impact damper. This time excitation is exerted by striking the structure at $C$, the third storey of the primary structure. Figure 6.30 shows the power spectral density of the acceleration response of the primary structure. Figure 6.31 is Figure 6.30 re-plotted by zooming in on each natural frequency. It can be seen that for the first mode both the conventional impact damper and the BID result in significant control effect, with the control effect of the conventional impact damper slightly better than that of the BID. For the second and third modes, the conventional impact damper shows little control effect, while the BID shows significant control effect. This is the case for each storey.

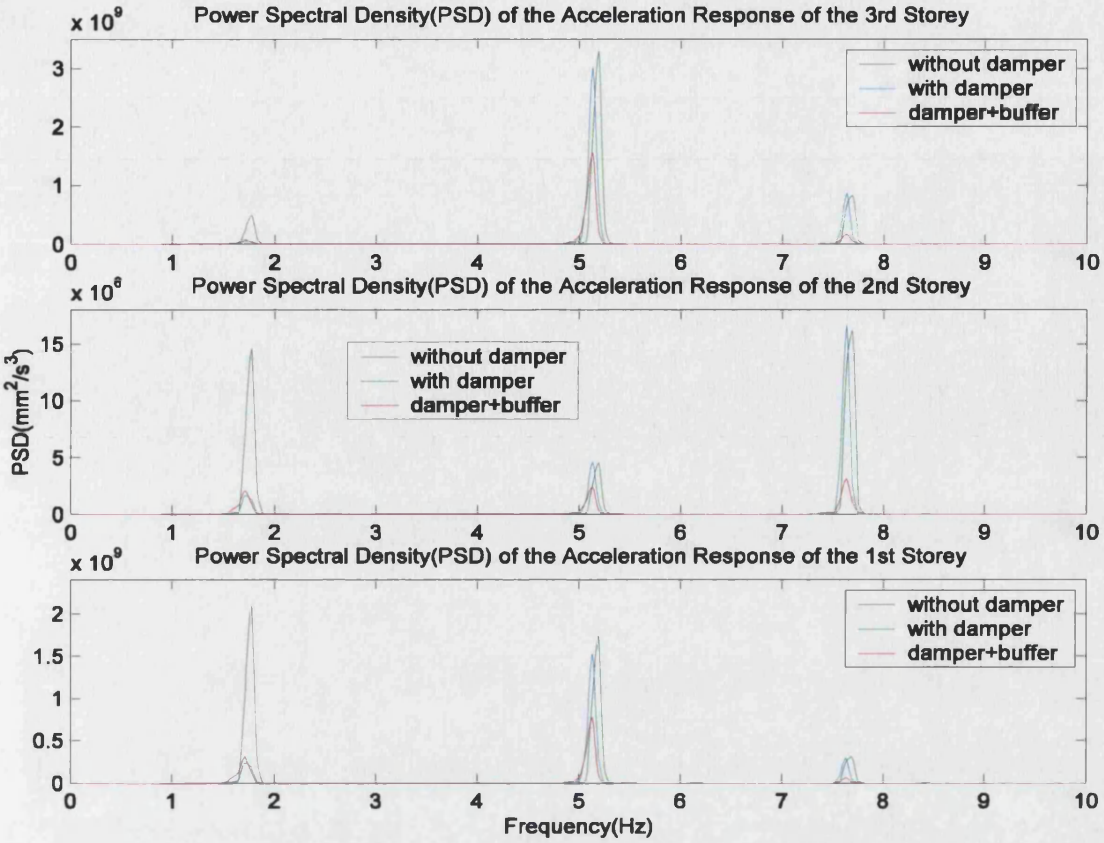


Figure 6.30: Power spectral density of the primary structure

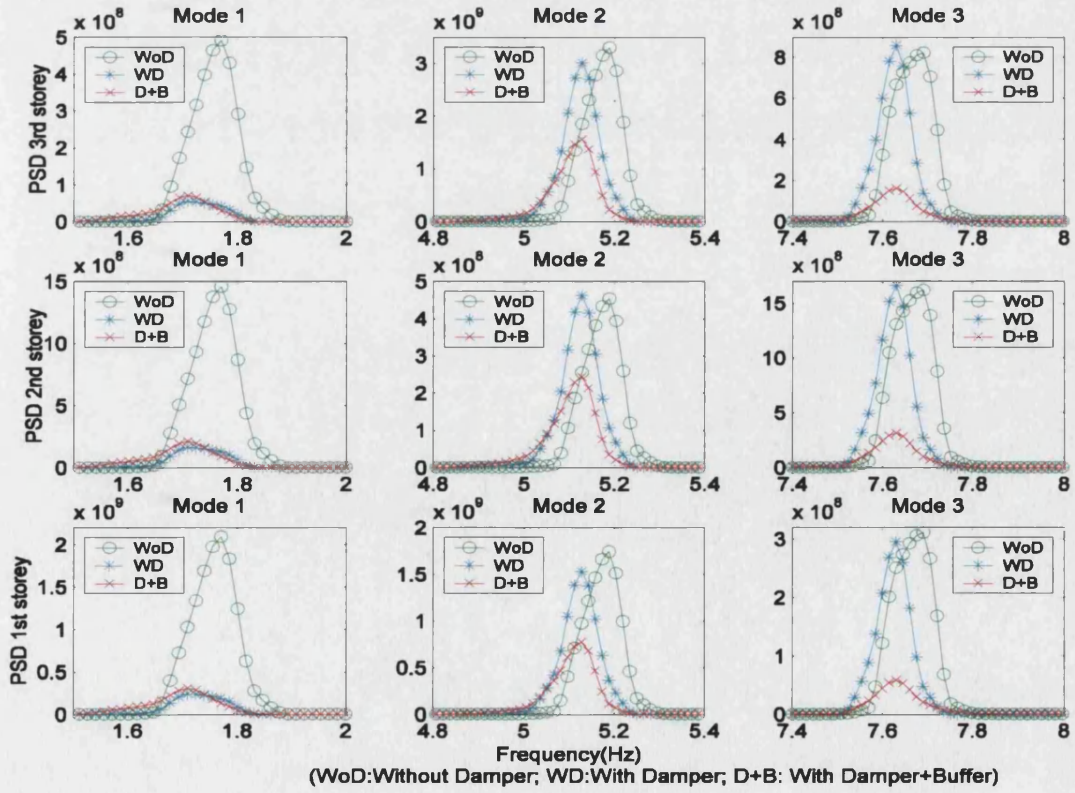


Figure 6.31: Power spectral density of the primary structure—zoomed in

6.4.1.3 *effect of excitation intensity*

To investigate the performance of a BID under different excitation intensities and compare it with that of a conventional impact damper, a further set of tests were carried out. For these tests, the mass ratio $\mu=0.082$ and the clearance taken is $d=15mm$ with the excitation force applied at the first storey. For each test, the excitation force was increased by releasing the pendulum hammer from an increasingly greater distance. Figures 6.32(a), (b) and (c) show the PSD of the acceleration records for each storey as the amplitude of the impulse input force is increased. The following points can be drawn from these Figures:

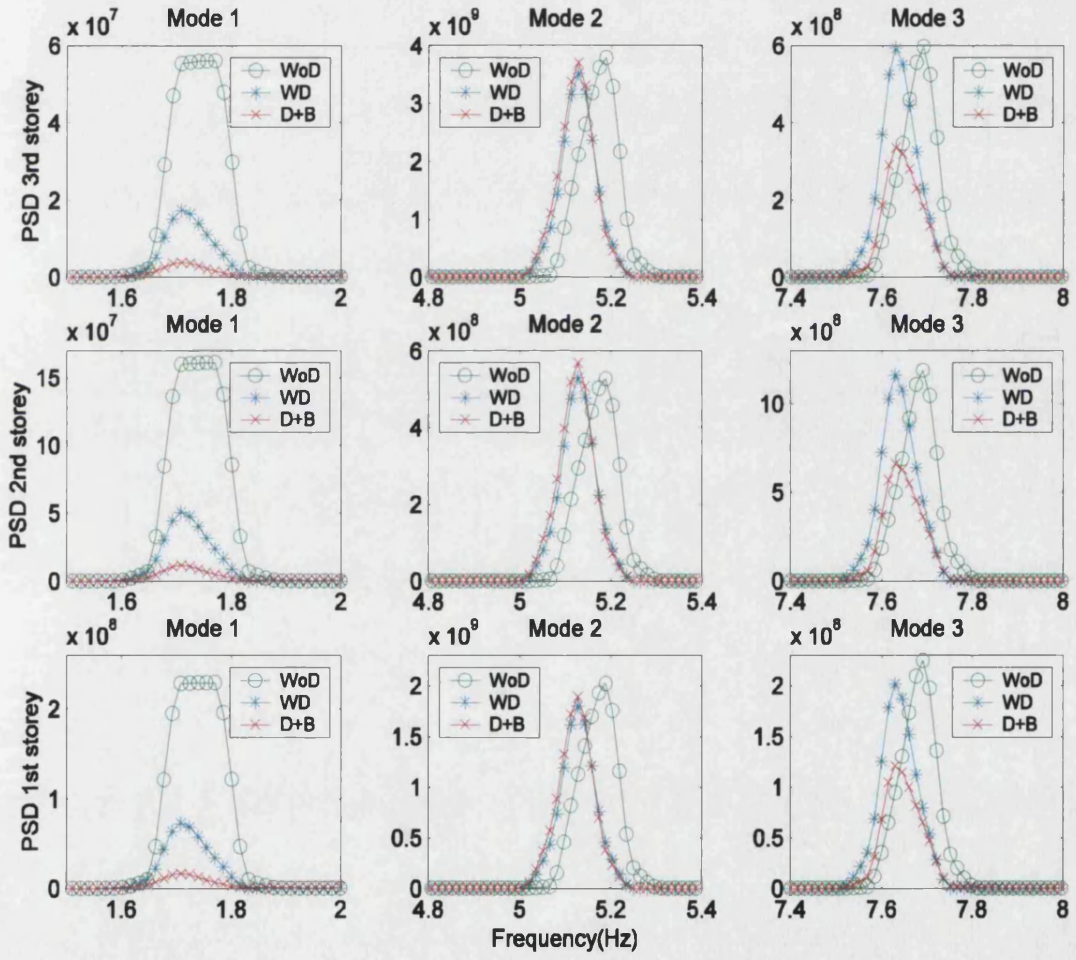


Figure 6.32(a): Power spectral density of acceleration responses—weak excitation

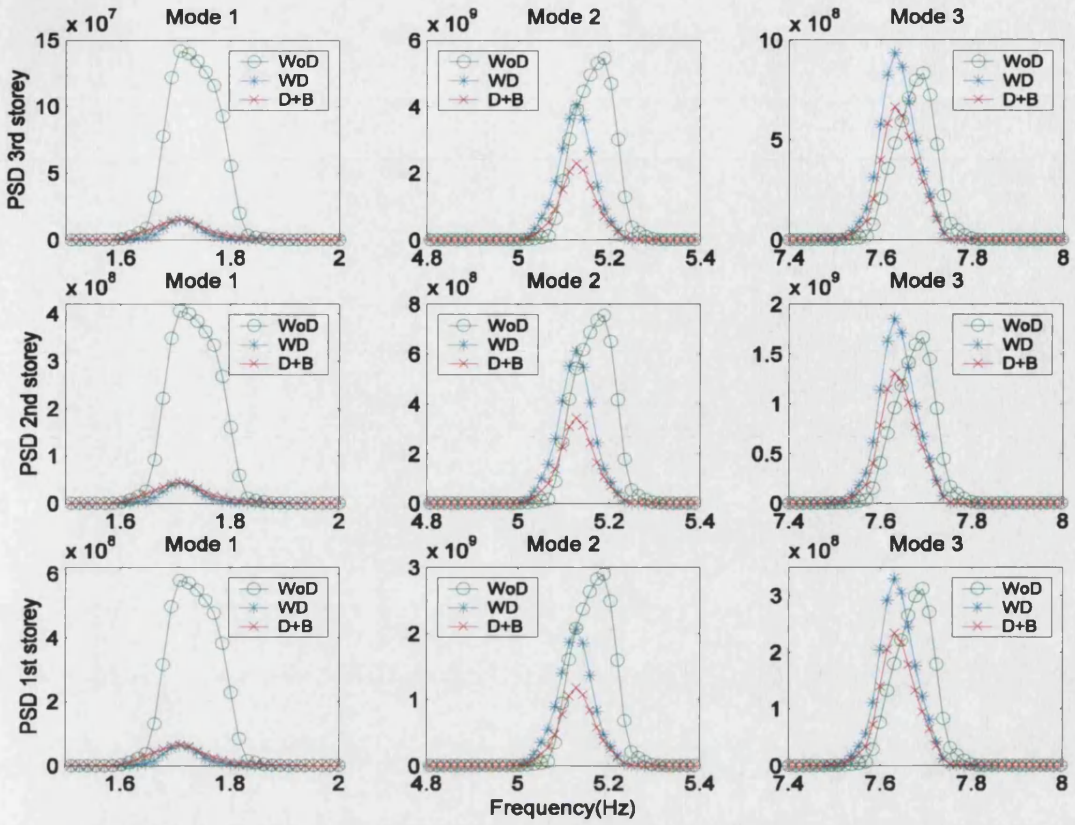


Figure 6.32 (b): Power spectral density of acceleration responses—medium excitation

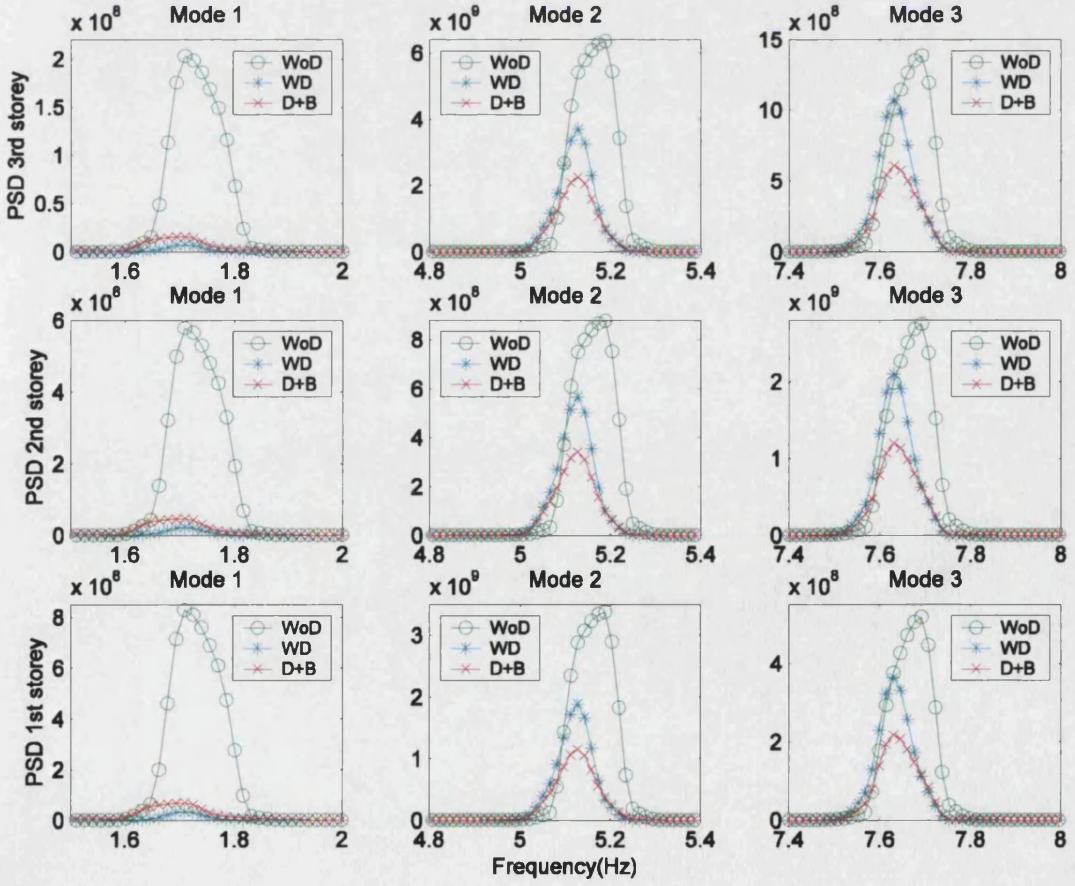


Figure 6.32(c): Power spectral density of acceleration responses—strong excitation

- For all the three excitation levels, both the conventional impact damper and the BID result in significant control of the first mode of each storey
- Compared with the conventional impact damper, the BID results in better control of the second and third modes of each storey for almost all cases (in the case of 'weak excitation', the control effect on the second mode is negligible for both the conventional impact damper and the BID)
- In the case of 'strong excitation', both the conventional impact damper and the BID show significant control of each mode of each storey, while the control effect of the BID over the second and third modes of each storey is significantly better than that of the conventional impact damper. In this case, the control effect of the BID over the first mode is slightly worse than that of the conventional impact damper, although the control effect from both is significant.

#### 6.4.1.4 *effect of clearance*

To study the effect of clearance between the impact mass and the stops upon the control effect, a series of clearances $d$=*0, 5, 10, 15, 20, 25, 30, 35, 40, 45, 50*mm were investigated. Free vibration tests were carried for each clearance, without a damper, with a conventional impact damper and with the BID. Peak values of the PSD of the acceleration response for each mode were obtained in each case. All the experiments were carried out with $\mu = 0.082$, and excitation was applied at $A$ (the first storey). The results, shown in Figure 6.33, are given as a ratio between the peak value of the PSD at the natural frequency of interest with the impact damper (conventional or BID), $P$, and the corresponding peak value without the impact damper, $P_0$. Therefore, a ratio of less than one shows some control effect, whilst a ratio greater than 1 shows a detrimental effect. It can be seen that

- for the third mode the BID results in better control than the conventional impact damper over most of the clearance range tested.
- the control effect of the BID upon the second mode is better than that of the conventional impact damper when clearance is $d < 30$mm.
- for the first mode, the control effect of the conventional impact damper is slightly better than that of the BID when the clearance is $d <$ 25mm. For a greater clearance, the control effect of the BID is better than that of the conventional impact damper.

- control of the first mode can be achieved over a large range of clearances, whilst control of higher modes requires smaller clearance.
- for the third mode, the conventional impact damper results in no control effect or makes the response worse if clearance $d>17mm$. Taking control effect of each mode into consideration, it seem that a clearance in the range $5mm<d<20mm$ results in good control, with $d=10mm$ as an optimum.

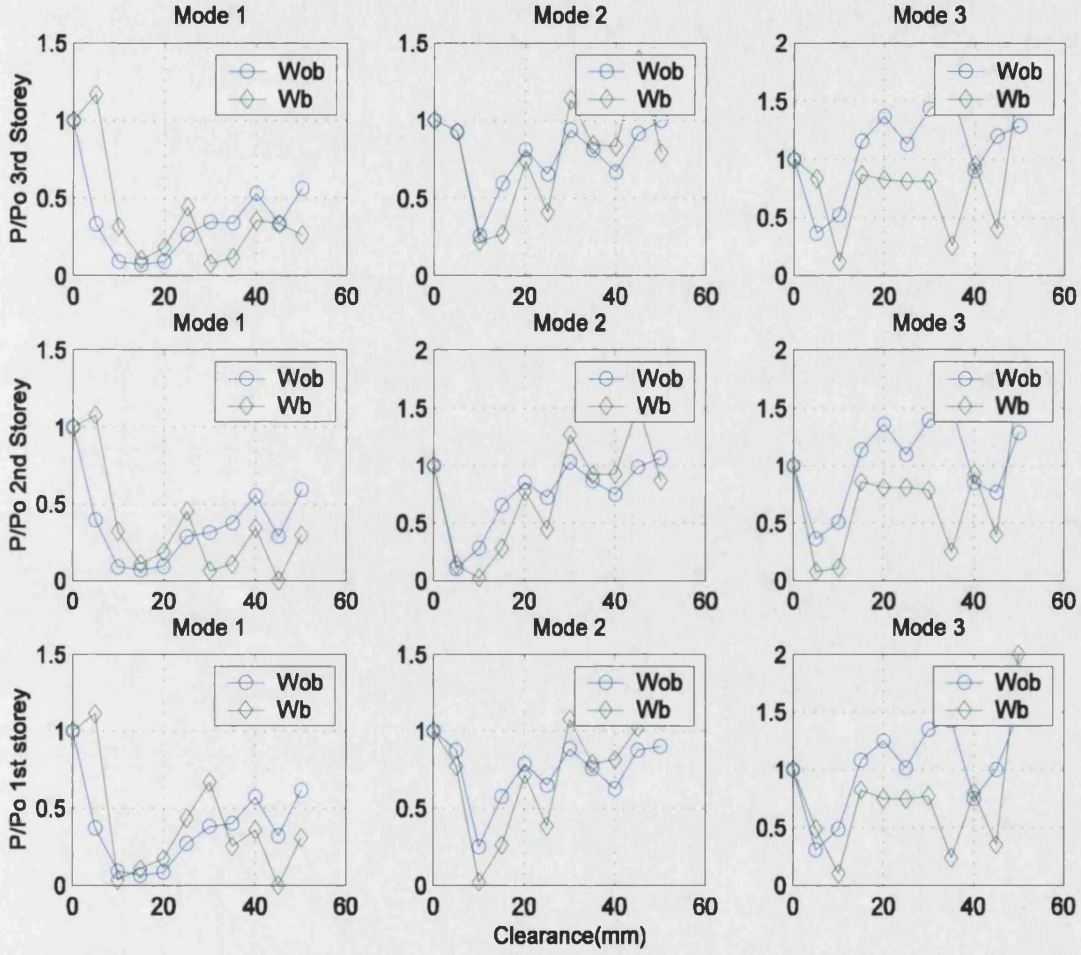


Figure 6.33: Effect of clearance—without buffer (Wob) and with buffer (Wb)

*6.4.2 Forced vibration*

*6.4.2.1 effect of excitation frequency*

To study the effect of excitation frequency on the vibration control effect of an impact damper, experiments were carried out at a series of sine dwell excitation frequencies either side of the first frequency, $f_1=1.7685$ *Hz*, i.e. taking $f=0.6f_1$, $0.8f_1$, $0.9f_1$, $f_1$, $1.2f_1$,

$1.4f_1, 1.6f_1, 1.8f_1$. For the tests, the excitation amplitude was $A$=5 mm, the mass ratio $\mu$ = *0.082*, and the clearance *d=12 mm*. The ratio of the peak value of the PSD of the acceleration response at the excitation frequency without the impact damper, with the conventional impact damper and with the BID is shown in Figure 6.34. It can be seen that the buffer does not make much difference until frequency ratio $r \geq 1$, at which point both the conventional impact damper and the BID start to show a control effect. This is similar to what was observed for a SDOF system. However, over the frequency range where the conventional impact damper shows a control effect, the BID, in general, shows a better control effect.

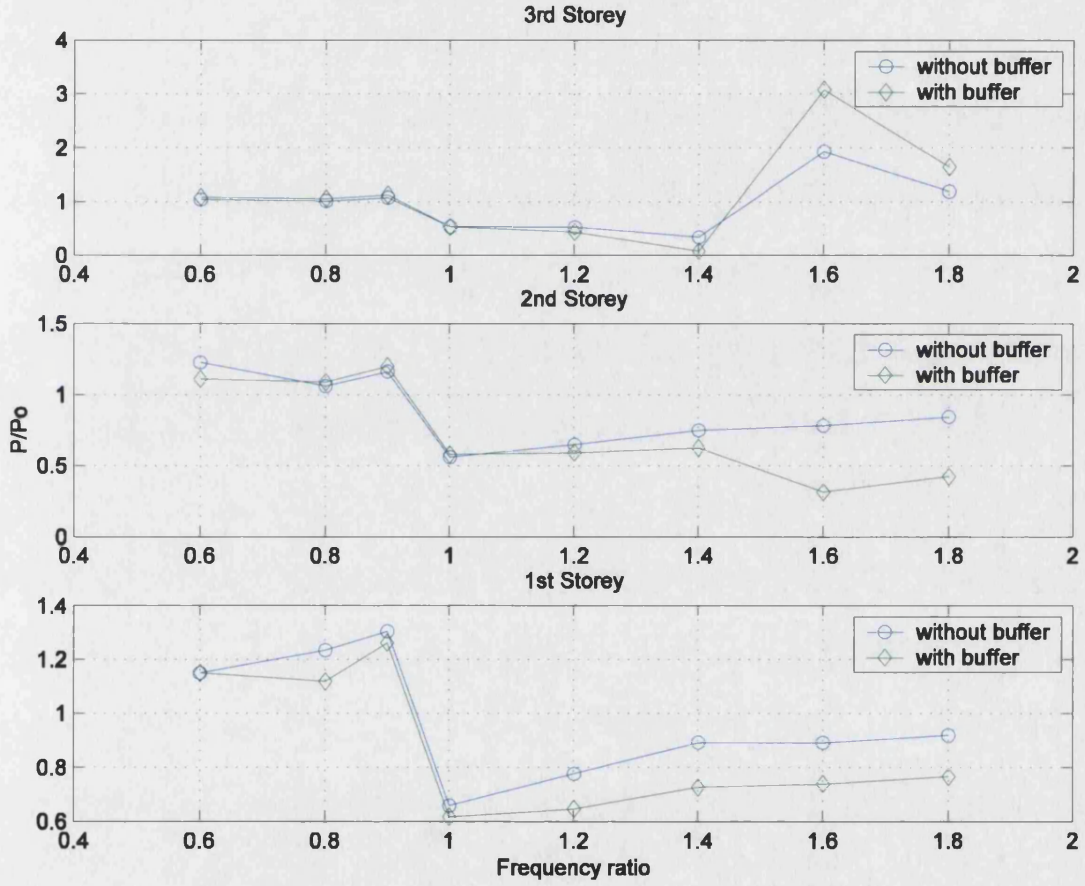


Figure 6.34: Effect of excitation frequency

*6.4.2.2 band limited white noise base excitation*

Further tests have been performed using random base excitation with a band-limited frequency content between *0* and *15 Hz* (to encompass the natural frequencies of the structure). The mass ratio taken in this set of tests is $\mu$=*0.082* and the clearance is *d*

=*20mm*. The accelerations of each storey are shown in Figure 6.35. The figure shows that when the conventional impact damper is in operation, high accelerations occur at the moments of collision not just on the third storey but also at other storeys. However, this does not occur when the BID is in operation. When the BID is in operation, the acceleration always remains smaller than that without impact damper, as shown more clearly in Figure 6.36. Figure 6.37 shows the power spectral density of the acceleration response of each storey. Figure 6.38 is Figure 6.37 re-plotted by zooming in on each natural frequency. It is clear that both the conventional impact damper and the BID result in significant control of each mode of each storey. The control effect of the BID over the second and third modes is better than that of the conventional impact damper, but for the first mode the control effect of the conventional impact damper is slightly better.

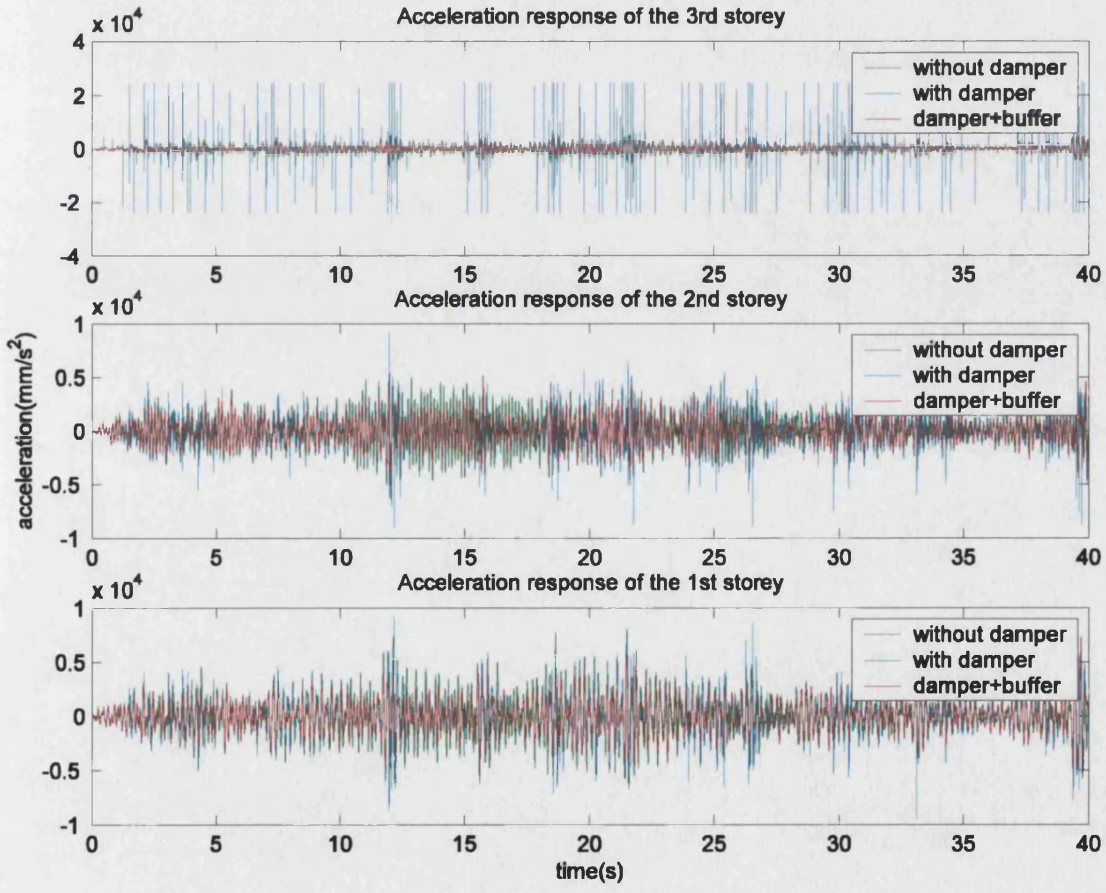


Figure 6.35: Acceleration responses of each storey

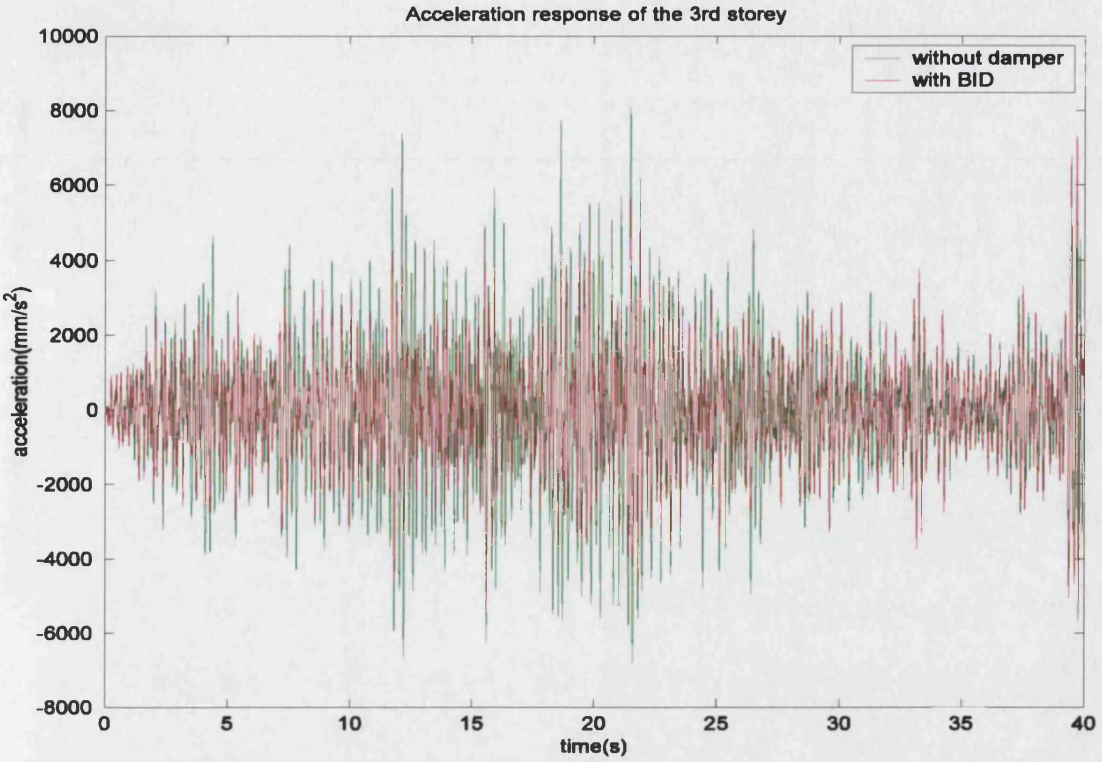


Figure 6.36: Acceleration responses of the third storey
—without damper and with BID

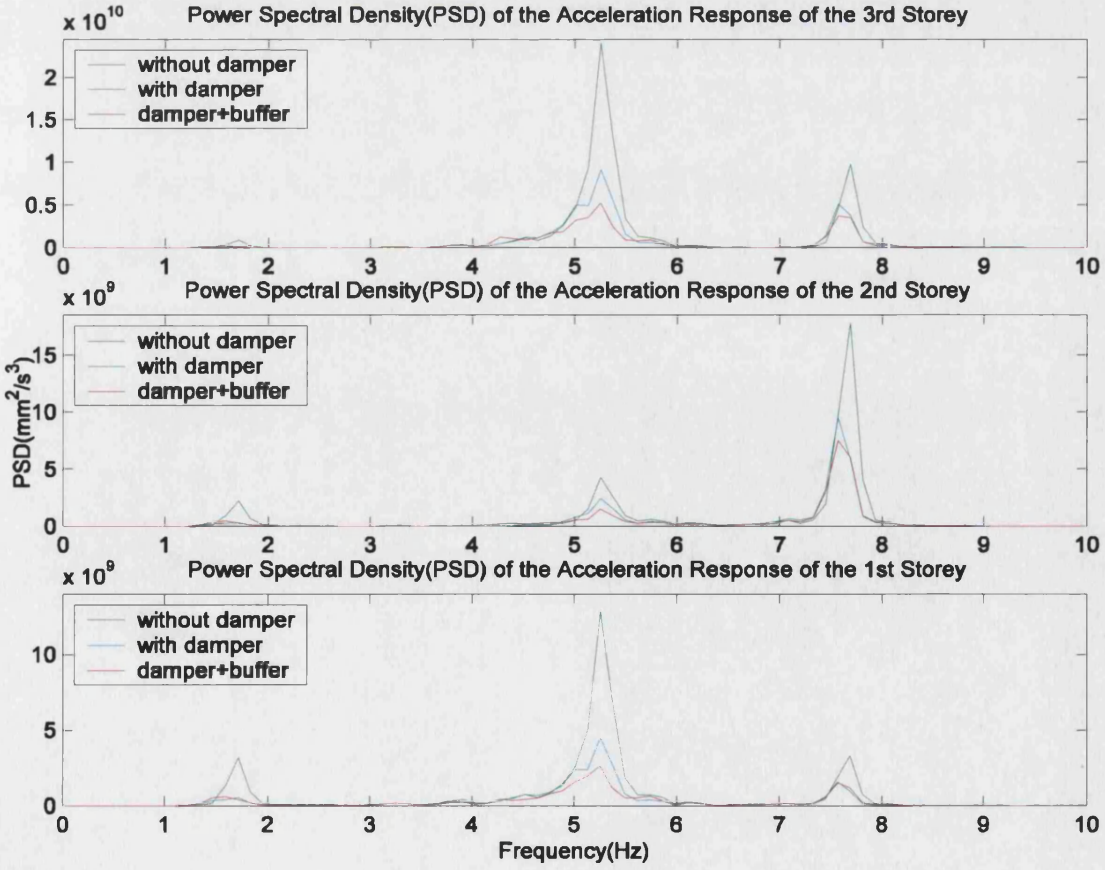


Figure 6.37: Power spectral density

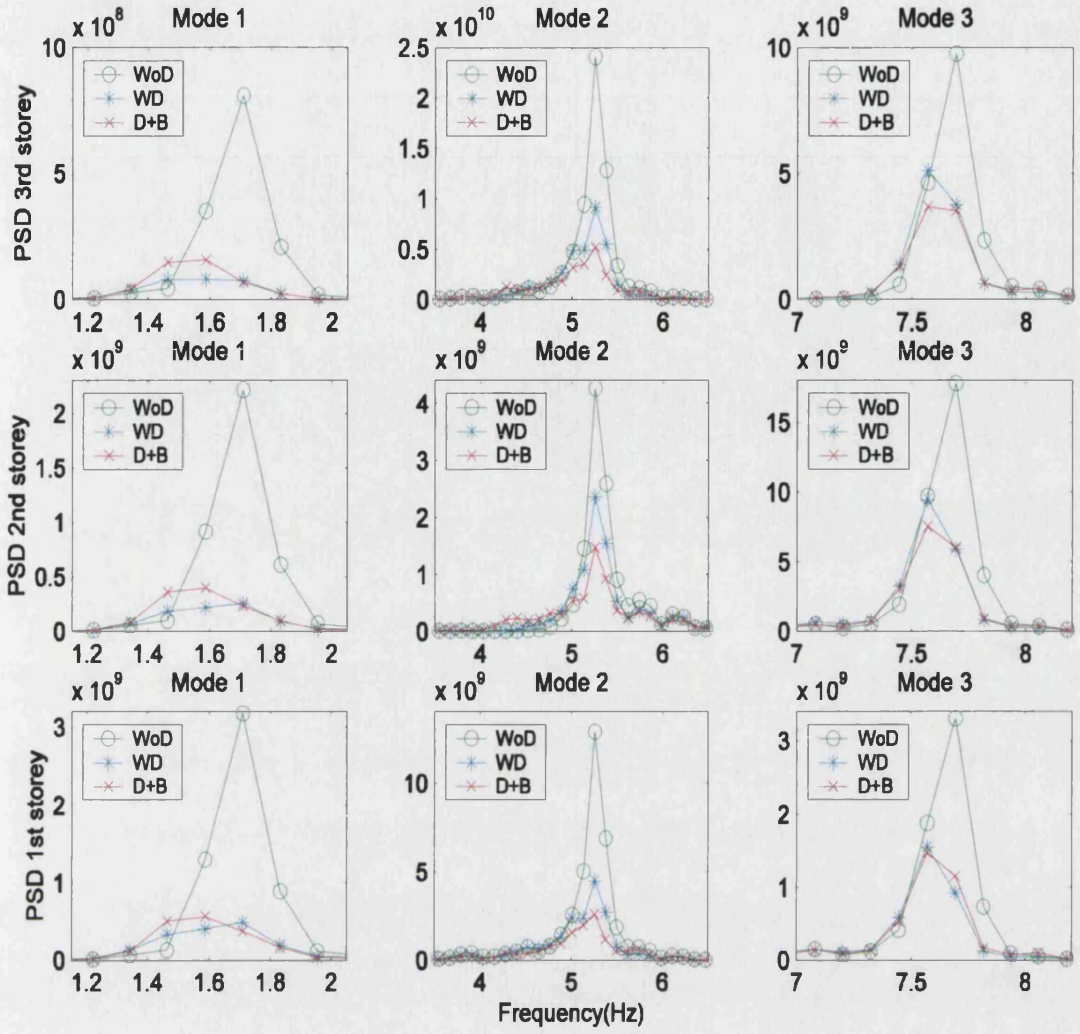


Figure 6.38: Power spectral density—zoomed around each natural frequency

*6.4.3 Remarks*

From the experimental investigation on a MDOF primary structure equipped with a buffered impact damper and comparisons with the corresponding experimental results of conventional impact damper, the following points can be drawn:

- Both free and forced vibration experiments demonstrate that a buffered impact damper eliminates the high accelerations (and associated high contact force and high level of noise) occurring at the moment of impact, which is inevitably associated with a conventional impact damper. With a suitably designed buffered impact damper, the acceleration of the structure always remains smaller than that without an impact damper.
- Both the buffered impact damper and conventional impact damper result in significant control of the first mode of the structure with the control effect of

conventional impact damper slightly better than that of the buffered impact damper in some cases. However, for higher modes, the buffered impact damper can always achieve a better control result than the conventional impact damper.

- Compared with a conventional impact damper, a buffered impact damper is more tolerant of variation in the intensity of excitation and variation of damper parameters, such as clearance.

## 6.5 Optimum buffer design for a buffered impact damper

Extensive experiments on both SDOF and MDOF primary structures have demonstrated that a buffered impact damper can not only eliminate the high accelerations (and high contact force and high level of noise) occurring at the moments of impact, but in most cases enhances the control effect as well. Experiments have also revealed that not all buffers perform equally well. Therefore, a procedure for the optimal design of the buffer of a BID is required to allow practical engineering implementation.

### *6.5.1 Modelling*

The problem posed here is how to design the buffer, modelled as a spring and a damper, for the buffered impact damper to result in maximum impulse momentum subject to a limit on the maximum impact force. Figure 6.39 depicts an impact damper with buffer. The damper mass, $m_2$, collides with the buffer, which is represented by the spring-damper pair $(k_b, c_b)$, with an initial relative velocity $v_0$. The buffer is fixed onto the primary structure of mass $m_1$.

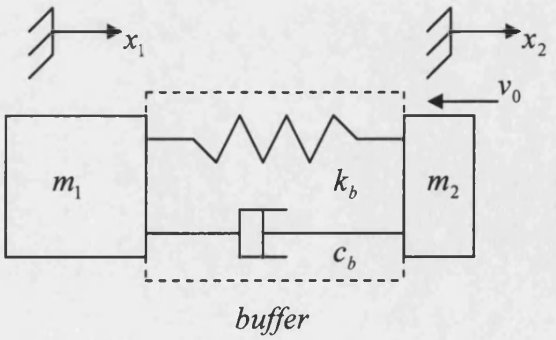


Figure 6.39: Model of impact of a BID

The equations of motion for this system after impact are:

$$m_2\ddot{x}_2 + c_b(\dot{x}_2 - \dot{x}_1) + k_b(x_2 - x_1) = 0 \tag{6.4}$$

$$m_1\ddot{x}_1 + c_b(\dot{x}_1 - \dot{x}_2) + k_b(x_1 - x_2) = 0 \tag{6.5}$$

By introducing the relative displacement:

$$y = x_2 - x_1$$

the following equation can be derived from Eq(6.4) and Eq(6.5):

$$\ddot{y} + 2\zeta\omega_n\dot{y} + \omega_n y = 0 \tag{6.6}$$

where

$$\omega_n = \sqrt{\frac{k_b}{m_2}(1+\mu)} \tag{6.7a}$$

$$\zeta = \frac{c_b\sqrt{1+\mu}}{2\sqrt{k_b m_2}} \tag{6.7b}$$

and mass ratio

$$\mu = \frac{m_2}{m_1} \tag{6.7c}$$

At the beginning of the collision

$$t = 0,\ y(0) = 0, \dot{y}(0) = v_0 \tag{6.8}$$

The force on mass $m_1$ during the collision is given by:

$$F = c_b\dot{y} + k_b y \tag{6.9}$$

The peak value of $F$ should be controlled (to remain below a certain level) to make sure no excessive accelerations, local damage or excessive noise are produced, i.e.

$$F \le F_{m0} \tag{6.10}$$

Here $F_{m0}$ is the highest value of $F$ which is acceptable.

Denoting the contact time, defined as the duration that the moving damper mass $m_2$ stays in contact with the buffer, by $T_c$, in section 2.3 the following equation was derived:

$$T_c = \frac{\pi}{\omega_n \sqrt{1-\varsigma^2}} \tag{6.11}$$

The impulse produced during the collision is:

$$I = \int_0^{T_c} F dt \tag{6.12}$$

To achieve the best vibration control effect, the impulse momentum, $I$, should be as high as possible. From this point of view, the contact force should be as high as possible but below $F_{m0}$. Therefore, the problem becomes the choice $k_b$ and $c_b$ which maximise $I$ under condition of Eq(6.10). To meet this condition, a limit on $y$ must be set, for without a constraint on $y$, the contact force $F$ can be made arbitrarily small. Let us denote the limit on $y$ by $y_m$.

*6.5.2 Nondimensional response*

To solve the problem posed above, the first step is to reduce the number of variables through non-dimensional groupings. $y$, $t$ and $F$ are non-dimensionalized as $z$, $\tau$ and $f$ by the following transformation[82][83]:

$$\left.\begin{aligned} z &= \frac{\omega_n y}{v_0} \\ \tau &= \omega_n t \\ f &= F y_m / (m_2 v_0^2) \end{aligned}\right\} \tag{6.13}$$

By denoting: $\frac{d(\ )}{d\tau} = (\ )^{\bullet}$, a set of nondimensional dynamic equations in terms of only one unknown parameter, $\varsigma$, yields:

$$\ddot{z}+2\varsigma\dot{z}+z=0 \tag{6.14}$$

with the corresponding initial conditions:

$$\left.\begin{aligned} z(0)&=0\\ \dot{z}(0)&=1\end{aligned}\right\} \tag{6.15}$$

The nondimensionalized contact time is:

$$\tau_c=\frac{\pi}{\sqrt{1-\varsigma^2}} \tag{6.16}$$

The solution of Eq(6.14) under the initial conditions of Eq(6.15) can be obtained as:

$$z=\frac{1}{\sqrt{1-\varsigma^2}}e^{-\varsigma\tau}\sin(\sqrt{1-\varsigma^2}\tau) \qquad \text{for} \quad \varsigma<1 \tag{6.17}$$

The nondimensionalized contact force can be expressed as:

$$f=z_m(2\varsigma\dot{z}+z)=-z_m\ddot{z} \tag{6.18}$$

Here $z_m$ is the maximum value of $z$. $z_m$ can be found out by taking the derivative of Eq(6.17) with respect to $\tau$ and setting it equal to zero:

$$\dot{z}=\frac{1}{\sqrt{1-\varsigma^2}}e^{-\varsigma\tau_f}[\sqrt{1-\varsigma^2}\cos(\sqrt{1-\varsigma^2}\tau_f)-\varsigma\sin(\sqrt{1-\varsigma^2}\tau_f)]=0 \tag{6.19}$$

Here $\tau_f$ is the moment at which the maximum $z$, $z_m$, occurs.

Solving Eq(6.19) gives:

$$\sqrt{1-\varsigma^2}\tau_f=\cos^{-1}\varsigma=\sin^{-1}\sqrt{1-\varsigma^2}=\tan^{-1}(\frac{\sqrt{1-\varsigma^2}}{\varsigma}) \tag{6.20}$$

Substituting Eq(6.20) into Eq(6.17), the maximum value of $z$ is found to be:

$$z_m=e^{-\varsigma\tau_f} \tag{6.21}$$

*6.5.3. Optimum $\varsigma$*

The largest $f$ for a given $\varsigma$ can only occur during the collision, not at the beginning or end of the collision. The maximum of $f$ can be found by differentiation of Eq(6.18) and setting it equal to zero:

$$\dot{f} = z_m(2\varsigma\ddot{z} + \dot{z}) = z_m[(1-4\varsigma^2)\dot{z} - 2\varsigma z] = 0 \tag{6.22}$$

Since $z_m$ can not be zero, Eq(6.22) leads to:

$$(1-4\varsigma^2)\dot{z} - 2\varsigma z = 0 \tag{6.23}$$

Substituting Eq(6.17) into Eq(6.23) and denoting the moment at which the highest value of $f$, $f_m$, occurs, by $\tau_m$, the following equation is obtained:

$$(1-4\varsigma^2)\cos(\sqrt{1-\varsigma^2}\tau_m) - \frac{(1-4\varsigma^2)\varsigma + 2\varsigma}{\sqrt{1-\varsigma^2}}\sin(\sqrt{1-\varsigma^2}\tau_m) = 0 \tag{6.24}$$

The resulting solutions for $\tau_m$ and $f_m$ are given by:

$$\sqrt{1-\varsigma^2}\tau_m = \cos^{-1}[\varsigma(3-4\varsigma^2)] = \sin^{-1}[\sqrt{1-\varsigma^2}(1-4\varsigma^2)] \tag{6.25}$$

and

$$f_m = z_m e^{-\varsigma\tau_m} = e^{-\xi(\tau_f+\tau_m)} \tag{6.26}$$

From Eq(6.25), it can be seen that for positive $\tau_m$ the maximum $f$ can occur only for:

$$0 \le \varsigma \le \frac{1}{2} \tag{6.27}$$

Two limiting cases are:

i) $\varsigma = 0, f_m = 1, \tau_m = \frac{\pi}{2}$

It can be seen that in this case ($\varsigma = 0$), $\tau_m = \frac{\pi}{2} = \tau_f$, i.e. the moment at which maximum $z$, $z_m$, occurs is also the moment that maximum $f$, $f_m$, occurs.

ii) $\varsigma = 1/2, \tau_m = 0, f_m = 0.5463$

To meet the condition of Eq(6.10), we need to minimize $f_m$. From Eq(6.26) it can be found that to minimize $f_m$ with respect to $\varsigma$ is equivalent to minimizing:

$$T = \varsigma(\tau_f + \tau_m) = \varsigma[\frac{1}{\sqrt{1-\varsigma^2}}\cos^{-1}\varsigma + \frac{1}{\sqrt{1-\varsigma^2}}\cos^{-1}(\varsigma(3-4\varsigma^2))] \tag{6.28}$$

The minimization can be achieved by solving:

$$\frac{dT}{d\varsigma} = 0 \tag{6.29}$$

This will be dealt with numerically later.

From Eq(6.12), the nondemensionalized impulse momentum is given by

$$\bar{I} = \int_0^{\tau_c} f d\tau$$

$$= \int_0^{\frac{\pi}{\sqrt{1-\varsigma^2}}} z_m[2\varsigma e^{-\varsigma\tau}\cos(\sqrt{1-\varsigma^2}\tau) - 2\varsigma^2 e^{-\varsigma\tau}\sin(\sqrt{1-\varsigma^2}\tau) + \frac{1}{\sqrt{1-\varsigma^2}}e^{-\varsigma\tau}\sin(\sqrt{1-\varsigma^2}\tau)]d\tau$$

$$= z_m(1+e^{-\frac{\pi\varsigma}{\sqrt{1-\varsigma^2}}}) = e^{-\varsigma\tau_f}(1+e^{-\frac{\pi\varsigma}{\sqrt{1-\varsigma^2}}}) \tag{6.30}$$

To achieve the goal of maximum impulse momentum under the condition set by Eq(6.10), there is some choice available in $\varsigma$.

Figure 6.40 is a plot of $\bar{I}$ vs. $\varsigma$ and $f_m$ vs. $\varsigma$. From Figure 6.40 it can be seen that for a minimum of the maximum contact force the optimum value of $\varsigma$ is $\varsigma$=*0.4*. The corresponding value of normalized contact force is $f_m$=*0.52*. However, at this value of $\varsigma$, the impulse momentum is quite low ($\bar{I}$=*0.783*). The maximum normalized impulse moment occurs at $\varsigma = 0$, but, here, the contact force is high, $f_m = 1.0$. Fortunately, the

curve of the normalized contact force vs. damping ratio is quite flat at the bottom, so a balance in the choosing of $\varsigma$ can be made in the design of the buffer. For example, taking $\varsigma = 0.2$, a large impulse momentum ($\bar{I}$ =1.168) can be achieved whilst the contact force remains relatively low ($f_m$ =0.63).

### *6.5.4 Considerations for buffer design*

Taking both the maximum impulse momentum and a low value of contact maximum force, as shown in Figure 6.40, the damping ratio might be taken between *0.2* and *0.3,* i.e.

$$0.2 \le \varsigma \le 0.3 \tag{6.31}$$

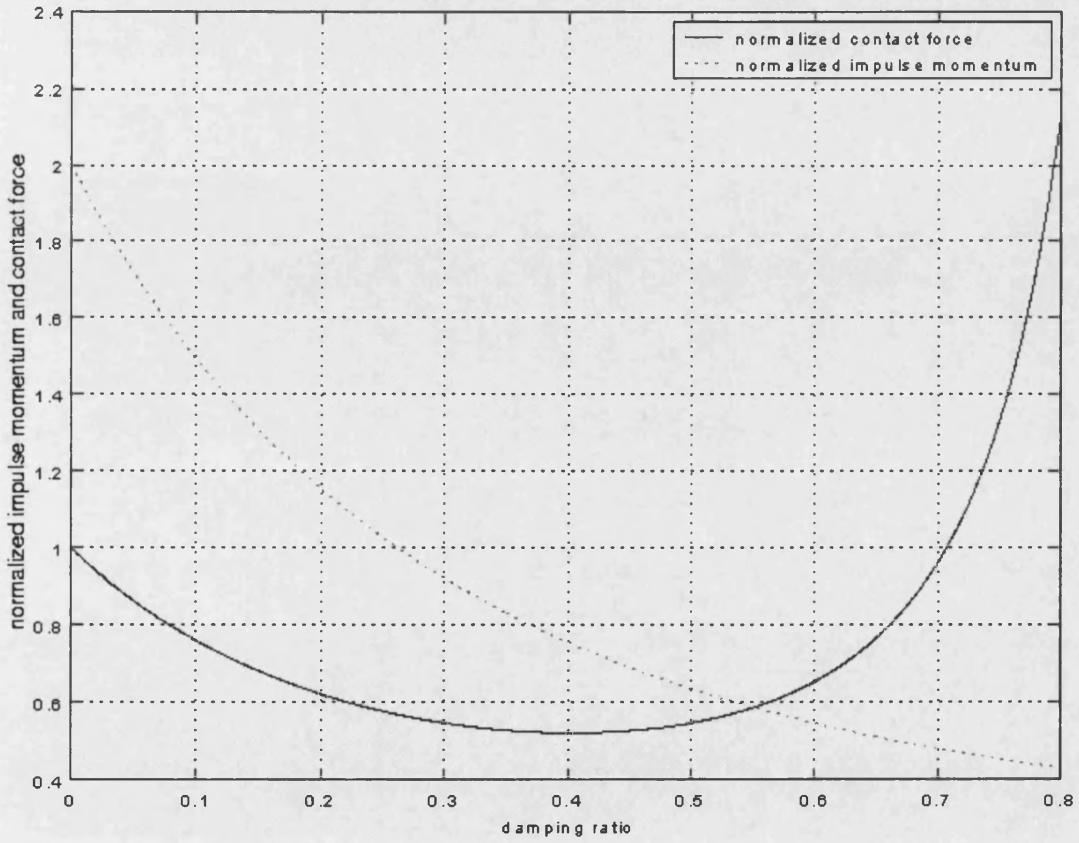


Figure 6.40: Normalized impulse momentum and contact force versus damping ratio

The following procedure can be used for the design of a buffer for a buffered impact damper:

a) Choose the damping ratio $\varsigma_0$ within the range described by Eq(6.31).

b) Find the corresponding maximum normalised contact force, $f_{m0}$, from curve given in Figure 6.40

c) Substitute the chosen damping ratio $\varsigma_0$ into Eq(6.20) and Eq(6.25) to evaluate the corresponding values of $\tau_f$ and $\tau_m$, denoting them by $\tau_{f0}$ and $\tau_{m0}$.

d) Substitute $\tau_{f0}$ and $\varsigma_0$ into Eq(6.21) to find the corresponding value of $z_m$, denoted by $z_{m0}$.

e) Recover the original dimensional values by substituting the nondimensional values back into Eq(6.13). For a given $y_m$, this yields:

$$\left.\begin{aligned} \varsigma &= \varsigma_0 \\ \omega_n &= \frac{z_{m0} v_0}{y_m} \end{aligned}\right\} \tag{6.32}$$

From Eq(6.7a) and Eq(6.7b), the dimensional values can also be given in terms of buffer stiffness and damping $k_b$ and $c_b$:

$$\left.\begin{aligned} k_b &= \frac{\omega_n^2 m_2}{1+\mu} = \frac{z_{m0}^2 v_0^2 m_2}{y_m^2 (1+\mu)} \\ c_b &= \frac{2\varsigma_0 z_{m0} v_0 m_2}{y_m (1+\mu)} \end{aligned}\right\} \tag{6.33}$$

From Eq(6.13), given the maximum likely velocity of the impact mass, the maximum contact force can be found as:

$$F_m = \frac{f_{m0} m_2 v_0^2}{y_m} \tag{6.34}$$

f) Check if the condition given by Eq(6.7) is met. If not, choose a higher damping ratio and repeat procedure above.

Although Eq(6.33) gives the parameters of the buffer, it is not convenient to use them in real buffer design since, as has been established, they do not represent real material

parameters. Section 2.3 gives the relationship between the parameters of the $k_b$ and $c_b$ and the coefficient of restitution $c_r$ and contact time $T_c$, which are easy to measure and can give more direct information for the practical design of the buffer:

$$\left.\begin{aligned} T_c &= \frac{2\pi m_2}{\sqrt{(1+\mu)[4m_2k_b-(1+\mu)c_b^2]}} \\ c_r &= e^{-\pi c_b R} \\ R &= \sqrt{\frac{1+\mu}{4m_2k_b-(1+\mu)c_b^2}} \end{aligned}\right\} \tag{6.35}$$

Thus, the values of $k_b$ and $c_b$, given by Eq(6.33), can be further transformed into an equivalent coefficient of restitution $c_r$ and contact time $T_c$ by means of Eq(6.35). These can be used to direct the practical design of the buffer, allowing the choice of material, the form and size of the buffer to be established.

The following is a buffer design example:

The parameters of a SDOF primary structure, the structure to be controlled, are: $m_1 = 1.2kg$, $k = 771N/m$ and $c = 0.3042Ns/m$. The damper mass is $m_2 = 0.0984kg$, so the mass ratio is $\mu = 0.082$. The maximum elastic deformation of the buffer during collision is set to $y_m = 0.0015m$ and the relative velocity of collision to $v_0 = 0.27m/s$. The maximum contact force acceptable is set at $F_{m0} = 5N$. The design of the buffer is as follows:

a) The damping ration is taken as $\varsigma_0 = 0.2$,

b) From Figure 6.40 the corresponding normalized contact force is:

$f_{m0} = 0.6207$

c) Substituting $\varsigma_0$ into Eq(6.20) and Eq(6.25) respectively gives:

$\tau_{f0} = 1.3977$ and $\tau_{m0} = 0.9867$

d) Putting $\tau_{f0}$ and $\varsigma_0$ into Eq(6.21) gives:

$z_{m0} = 0.7561$

e) Recovering the original dimensional values by means of Eq(6.32)

$\varsigma = 0.2$, $\omega_n = 0.7561 v_0 / y_m = 136.098(1/s)$

f) Making use of Eq(6.33) the parameters of the buffer are:

$k_b = 1684.5N/m, c_b = 4.9508Ns/m$

g) Substituting $k_b$ and $c_b$ into Eq(6.35) gives:

$c_r = 0.5269$ and $T_c$=*0.0236* (This is close to one of the buffers we used in the experiments described in this thesis).

h) Assuming the impact velocity $v_0 = 0.27m/s$, and using Eq(6.34) the maximum contact force can be obtained as: $F_m = 3.0114N < F_{m0} = 5N$, so the limiting condition on contact force is met. From Eq(6.34), it should be noted that the maximum contact force is proportional to the impact velocity.

To check this buffer design scheme, simulation studies have been performed.

*Case 1: free vibration*

Figure 6.41 is the simulated acceleration response and the power spectral density of acceleration, without a damper and with the BID using the buffer designed above. It shows that the control effect of the BID with the buffer as designed is significant. Figure 6.42 presents the displacement response and the simulated contact force. From Figure 6.42, it can be seen that the maximum contact force is about *4.9N*, remaining below the limit on contact force (although greater than $F_m = 3.0114N$ since the actual maximum velocity at impact is $v_0 = 0.35m/s$ rather than the assumed value of *0.27m/s*.). Another point of interest which can be seen from Figure 6.42 is that the simulated contact time, $T_c$=*0.024* seconds, is close to the calculated contact time *0.0236* seconds.

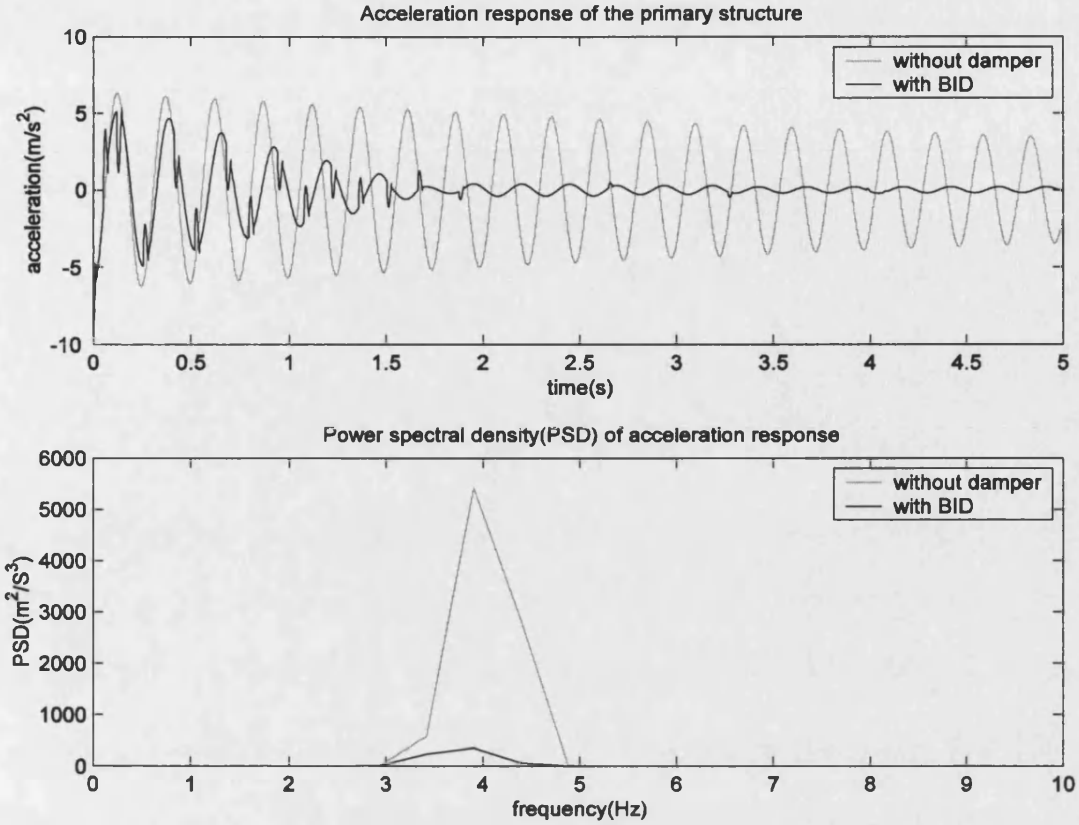


Figure 6.41: Simulation study on the buffer design scheme (free vibration)

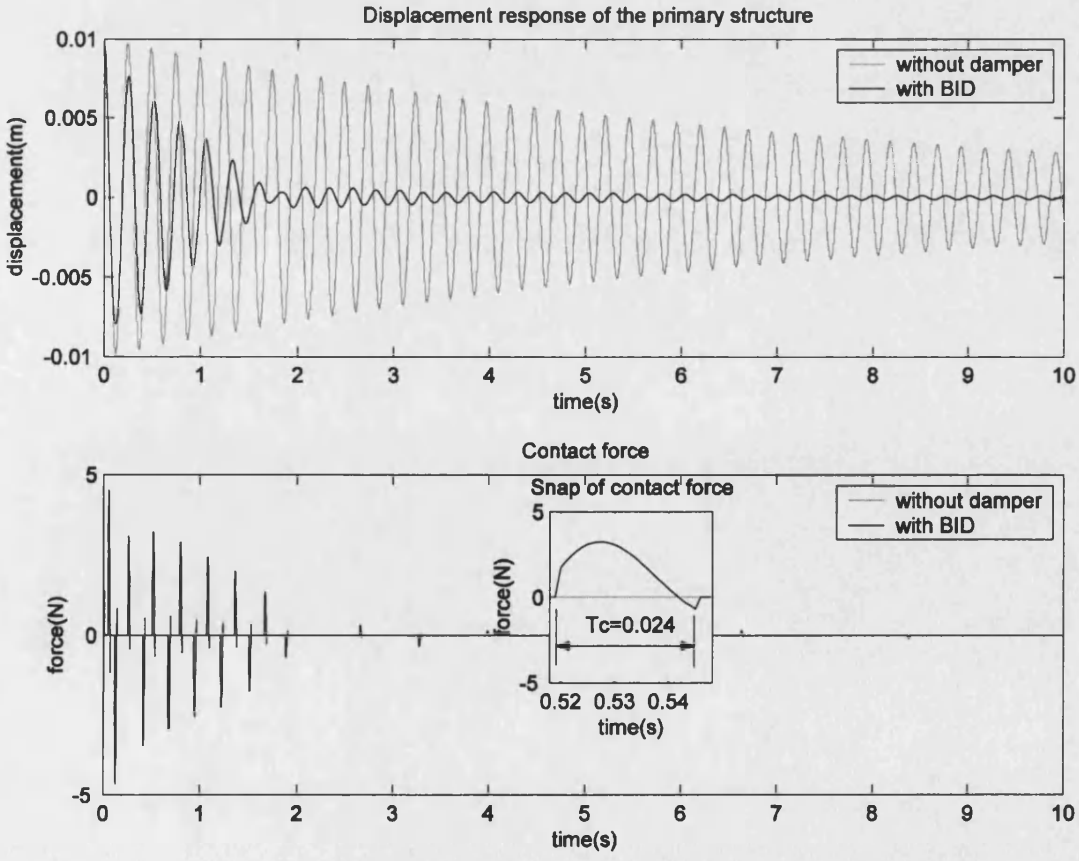


Figure 6.42: Checking the buffer design scheme by simulation (free vibration)

*Case 2: forced vibration*

When the primary structure is excited by *4 Hz* sinusoidal excitation, without a damper and with the designed BID, the simulated acceleration response and the PSD of acceleration response are as presented in Figure 6.43. Significant control effect of the BID with the buffer designed above can be seen from Figure 6.43 once the response is great enough for collision to occur. Figure 6.44 shows the simulated displacement response and the simulated contact force. It can be seen, again, that the maximum contact force is below the limit on the contact force and that the contact time obtained from the contact force time history is close to the calculated contact time.

From simulation of both free and force vibration, it can be demonstrated that the suggested buffer design scheme can produce a BID that can achieve good control and meet the limiting conditions on contact force.

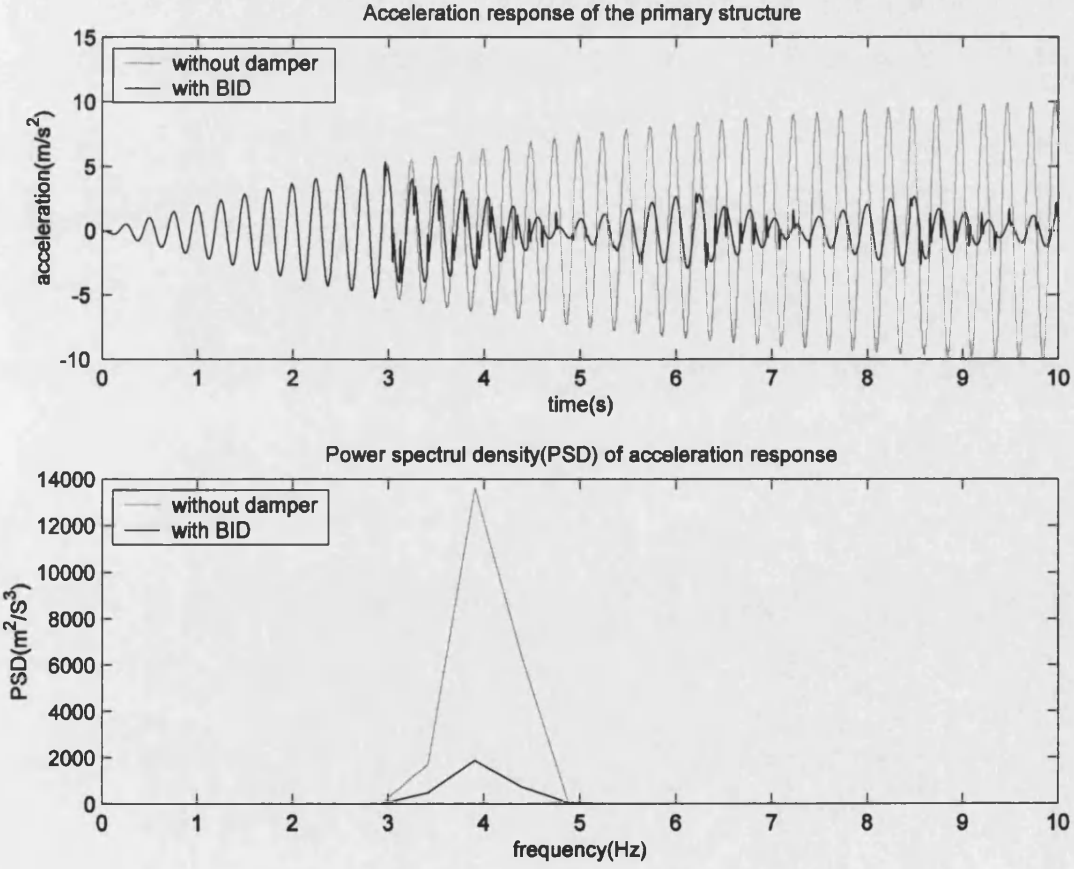


Figure 6.43: Simulation study on the buffer design scheme (forced vibration)

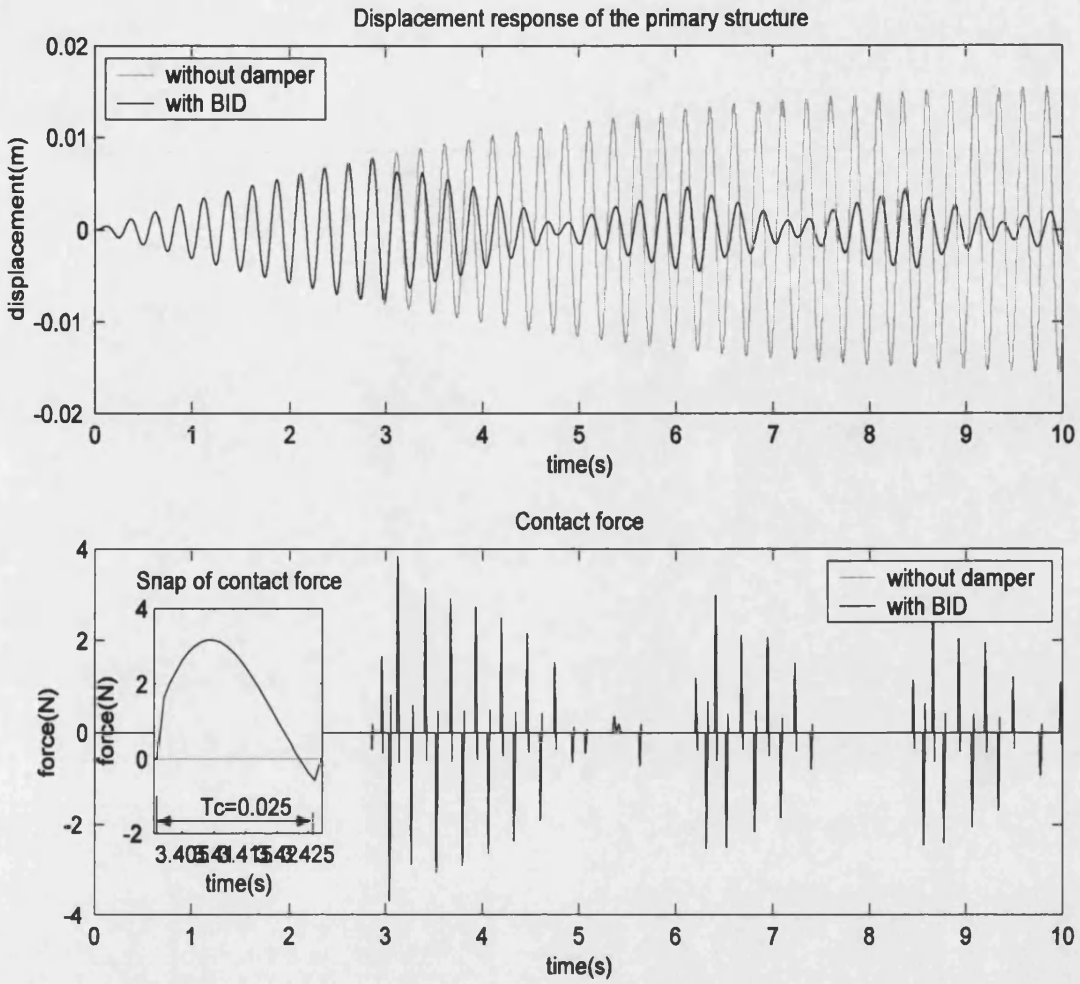


Figure 6.44: Checking the buffer design scheme by simulation (forced vibration)

# Chapter 7

# Numerical Simulation vs. Experiment

Introduction: Based on the mathematical models developed in Chapter 2 and the algorithms presented in Chapter 3, a numerical scheme for simulating a structure with an impact damper has been developed. Both the impulse momentum model and spring–damper model of impact can be applied in the simulation. Simulation results obtained with both the impulse momentum model and the spring-damper model of impact are compared with corresponding experimental results. The mathematical models developed in Chapter 2 and algorithms presented in Chapter 3 are tested and verified. The advantage of the spring-damper model over the impulse momentum model is demonstrated. Parametric studies of impact dampers are also performed.

## 7.1 Numerical simulation scheme

Based on the impulse momentum model of impact and the corresponding simulation strategy described in section 3.2.1, making use of the variable time step high precision direct (HPD) integration scheme described in section 3.3, a numerical simulation scheme for the structure-impact damper system can be formed as shown schematically in Figure 7.1.

Similarly, with the spring damper model of impact and the mathematical models developed in Chapter 2 and employing the high precision direct integration scheme for non-linear systems (HPD-NL), developed in chapter 3, a numerical simulation scheme for the structure-impact damper system can be formed as shown schematically in Figure 7.2.

Comparing Figures 7.1 and 7.2, it can be seen that simulation with the impulse momentum model requires establishing the timing of the collisions accurately (missing a collision will lead to failure of the simulation). This is not necessary for the simulation using the spring-damper model of impact.

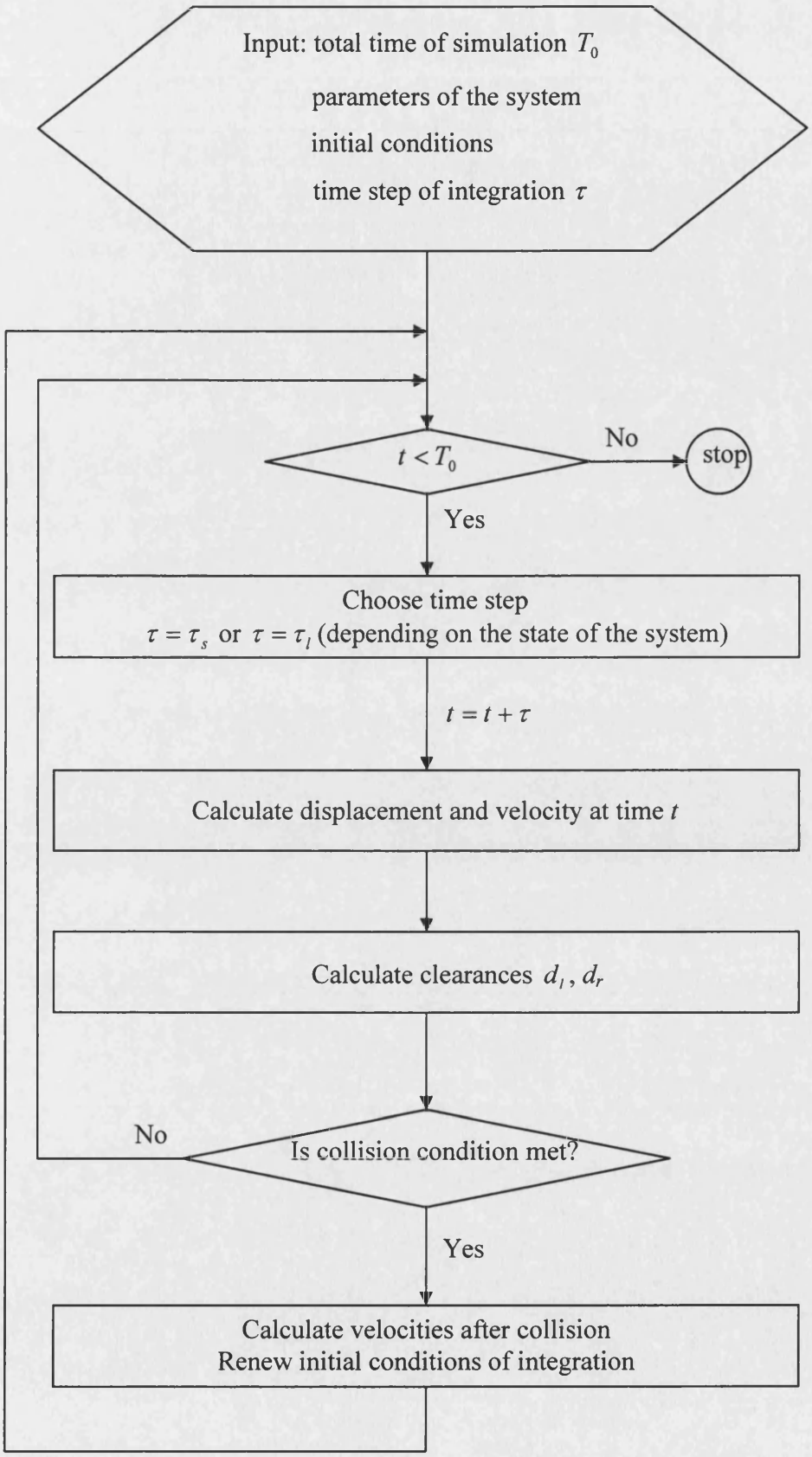


Figure 7.1: Flowchart of numerical simulation based on the impulse momentum model of impact

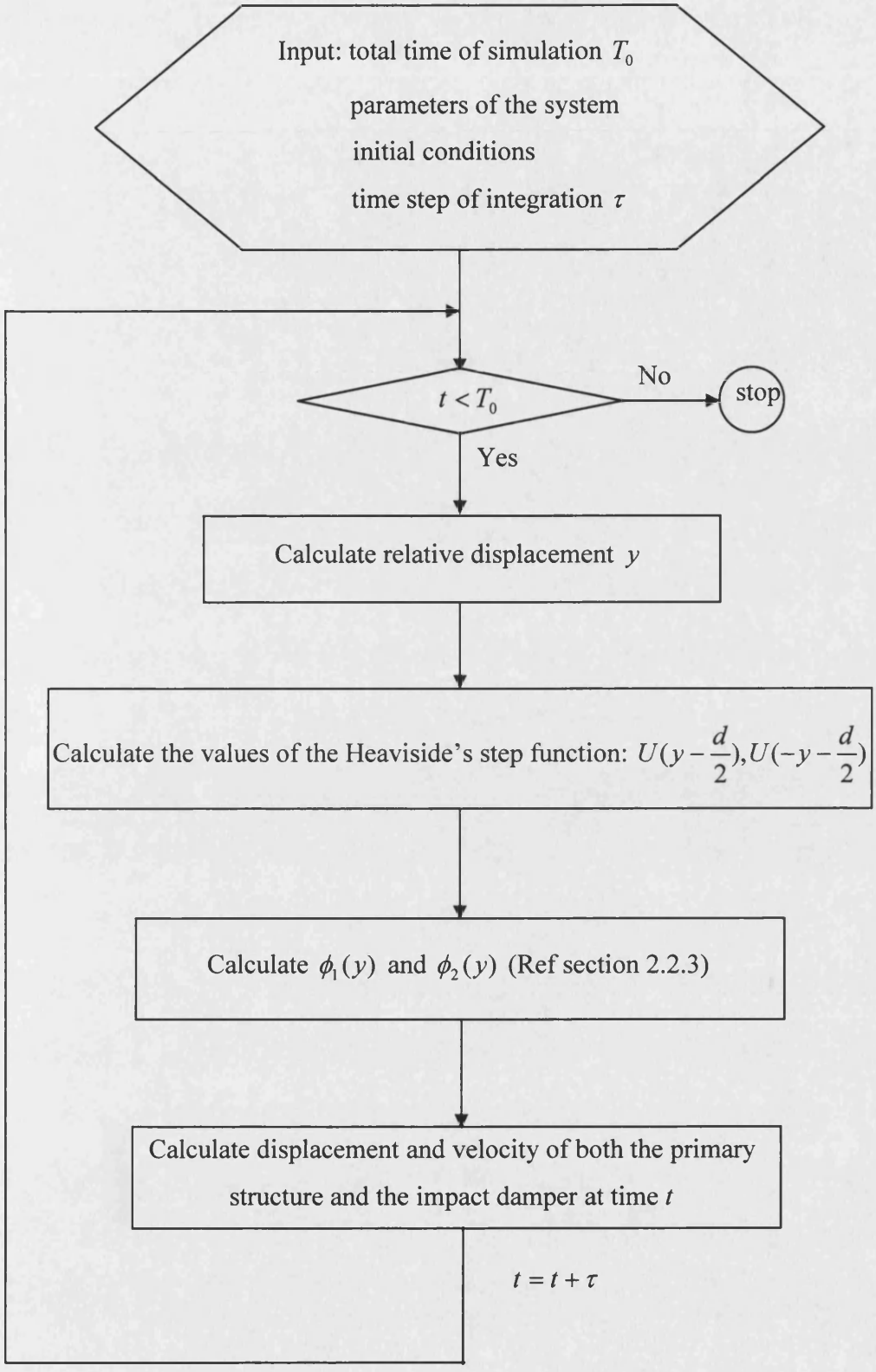


Figure 7.2: Flowchart of numerical simulation based on the spring-damper model of impact

## 7.2 Simulation vs. experiment—SDOF primary system

*Introduction:* This section presents comparisons between simulations and experimental results. The primary structure examined is a SDOF structure. Both free and forced vibrations are studied. Both simulations using the impulse momentum model of impact and simulations employing the spring-damper model of impact are performed and the results are compared with the corresponding experimental results.

### *7.2.1 Primary structure and its model*

A SDOF primary structure is preferable to be the subject of both experiments and simulations, since it can be modelled more easily and accurately in comparison with a MDOF structure and, thus, comparison becomes more direct and reliable. The SDOF primary structure chosen for both simulation and experiment is as shown in Figure 6.7.

The parameters of the physical structure are: mass $M=1.35kg$, which is obtained by weighing the beam; lateral stiffness $K=864.8N/m$, which is obtained by static load/displacement measurements on the strip; damping $C = 2 \times \varsigma \times \sqrt{\frac{K}{M}} = 1.092Ns/m$, where $\varsigma = 0.017$ is the damping ratio, which is evaluated from the experimentally obtained transfer function using the half-power points method.

### *7.2.2 Free vibration*

#### *7.2.2.1 simulation vs. experiment—without damper*

To demonstrate the accuracy of the numerical simulation scheme, the system was first tested without an impact damper under free vibration. Excitation was provided by an initial displacement $X_0 = 15\ mm$ in both the simulation and experiment. The time history of acceleration and the power spectral density of the acceleration response, are presented in Figure 7.3. It can be seen that the simulation matches the experimental results very well and, therefore, any errors from modelling the structure itself can be considered negligible. Therefore, it seems reasonable to assume that the simulation is comparable with the experimental results for the case when an impact damper is in operation.

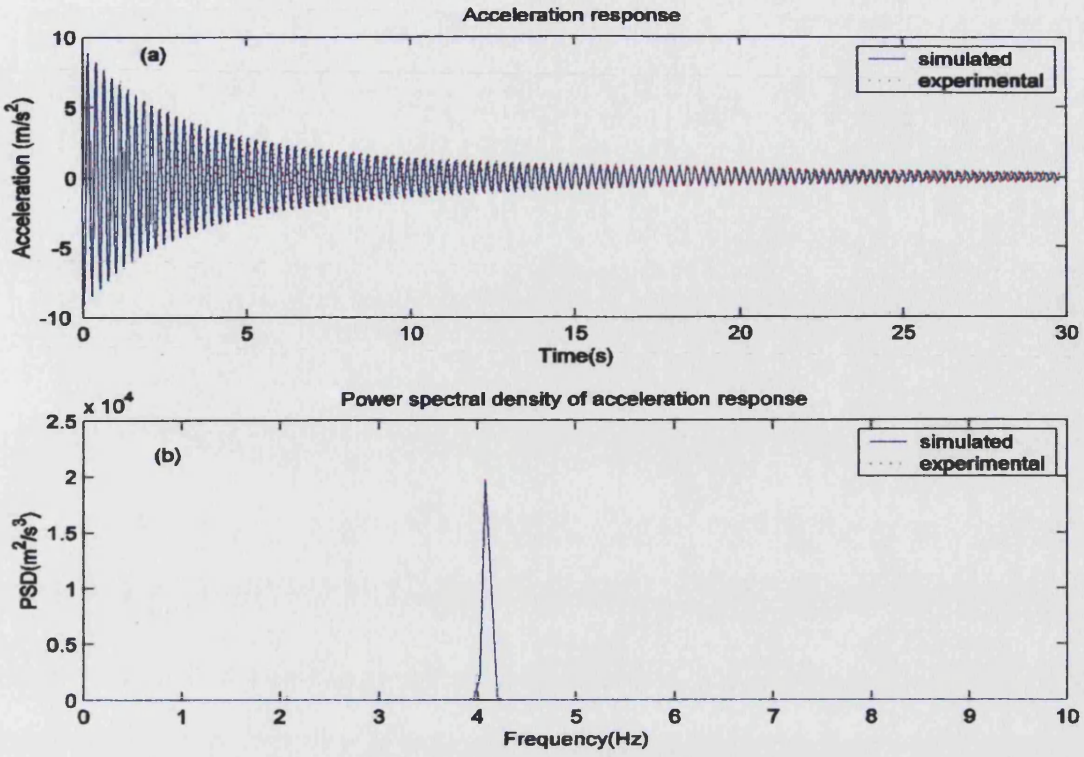


Figure 7.3: Simulation vs. experiment—without damper

*7.2.2.2 simulation vs. experiment—with conventional impact damper*

*7.2.2.2.1 simulation with impulse momentum model (IMM) of impact*

Both experiments and simulations with the impulse momentum model were performed when using a conventional (unbuffered) impact damper. For both the experiment and simulation, the mass ratio used was $\mu = 0.082$ and clearance *d=15mm.* In this case, the impacts occur between two steel objects, the damper mass and the stop. The coefficient of restitution used in the simulation is $c_r = 0.46$, which was obtained by the drop test described in section 6.2.1. The results of the simulation and experiment are shown in Figure 7.4. It can be seen that the simulated acceleration response matches the experimental acceleration response well, except that the high acceleration peaks produced by collisions can not be simulated. From Figure 7.4(b), it can be seen that the simulated PSD is a little lower for the simulation than that of the experiment. However, generally speaking, for the case of a conventional impact damper, the simulation using the impulse momentum model of impact matches the experimental result well.

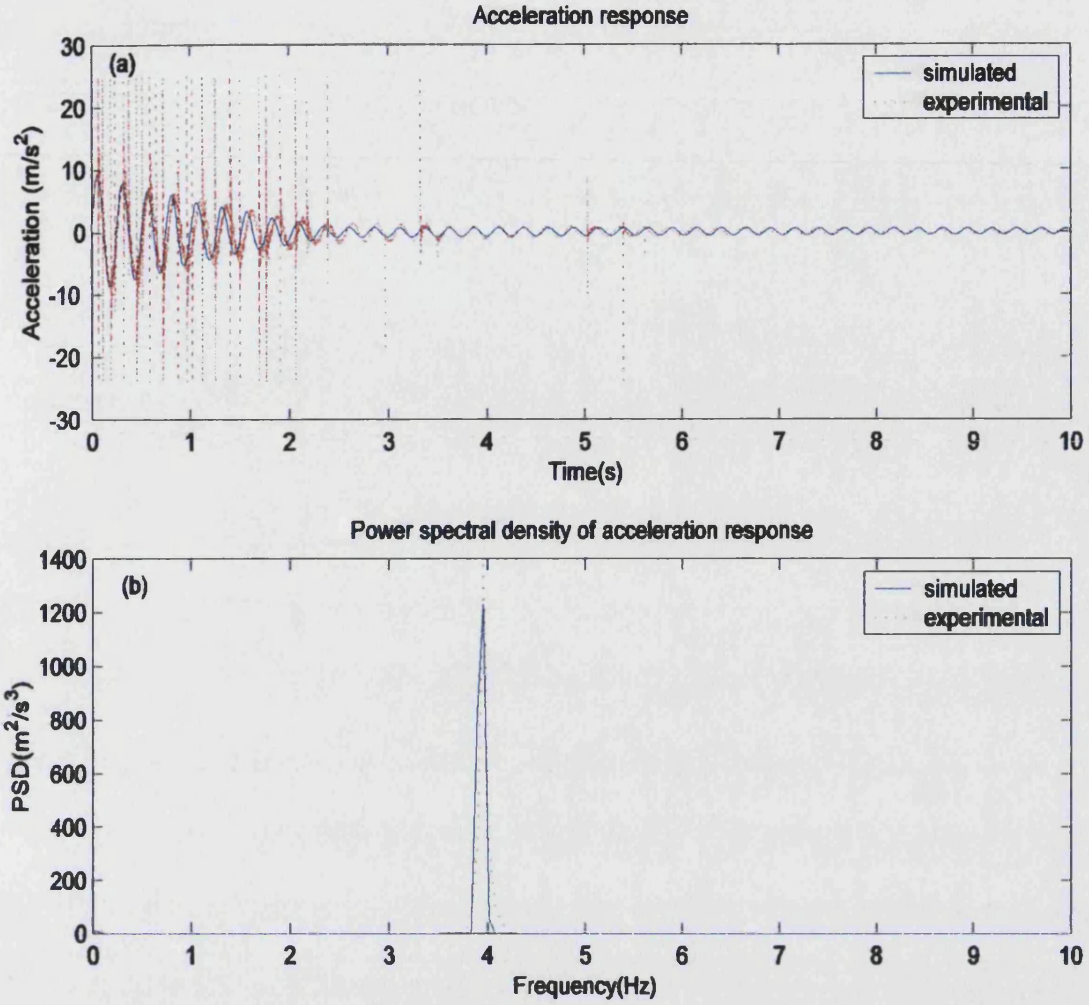


Figure 7.4: Simulation vs. experiment—impulse momentum model

*7.2.2.2.2 simulation with spring-damper model (SDM) of impact*

To compare the impulse momentum model with the spring-damper model of impact, developed in Chapter 2, a simulation with the spring-damper model, using the HPD-NL algorithm developed in Chapter 3, was also performed for the same free vibration case. The parameters of the spring-damper model were found by putting the experimentally obtained coefficient of restitution $c_r = 0.46$ and the measured contact time $T_c = 0.0003$ into Eq(2.36) and Eq(2.41) resulting in: $k_b = 11905000N/m$ and $c_b = 529.65Ns/m$. The results of the simulation compared with the experiment are shown in Figure 7.5.

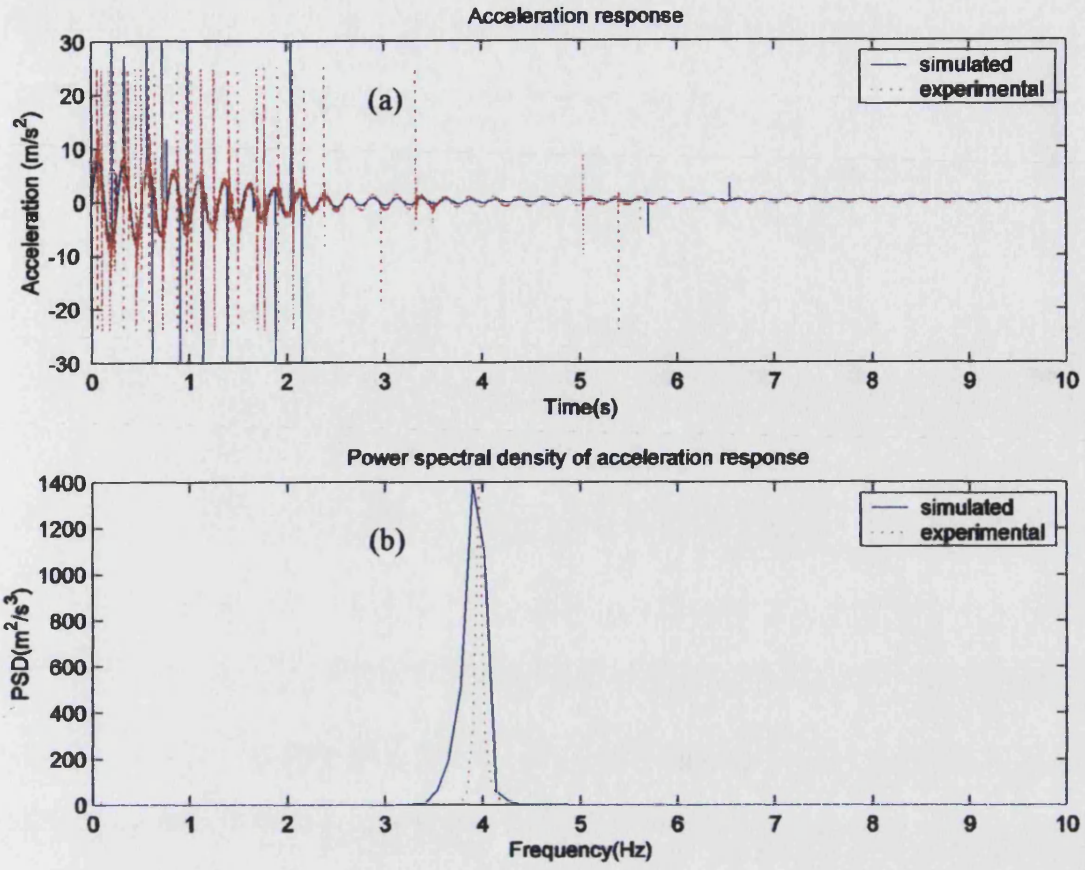


Figure 7.5: Simulation vs. experiment—spring-damper model

From Figure 7.5(a), the time history of the acceleration response, it can be seen that the simulated acceleration matches the experimental acceleration well. Peaks similar to those shown in the experiment can also be observed in the simulated acceleration response. From Figure 7.5 (b), it can be seen that the peak value of the PSD of the acceleration response from the simulation matches that from experiment well, although the frequency range is slightly larger. Comparing Figures 7.4 and 7.5, it can be seen that there is little overall difference between the simulation using the spring-damper model and that using the impulse momentum model other than the ability to simulate accelerations caused by collisions.

*7.2.2.3 simulation vs. experiment—with buffered impact damper*

*7.2.2.3.1 simulation with impulse momentum model of impact*

Buffer 1, as described in section 6.2.1, is employed in both the experiment and simulation. The coefficient of restitution between the steel damper mass and buffer *1* is $c_r = 0.61$, which was again obtained by the drop test described in section 6.2.1. All other conditions were kept the same as the previous tests described in section *7.2.2.2.1*.

The results of the simulation and the experiment are compared in Figure 7.6. It can be seen that for the buffered impact damper, the simulation using the impulse momentum model does not match the experimental result well. There are significant differences between the simulation and the experimental results for both the time history and the peak PSD values. This is not surprising, since for this buffered impact damper the contact time of impact is *0.025* seconds, two orders of magnitude greater than for the conventional impact damper. Therefore, the contact time of impact is not negligible, whilst the impulse momentum model is based on the assumption of an instantaneous impact, i.e. the contact time of impact is effectively zero.

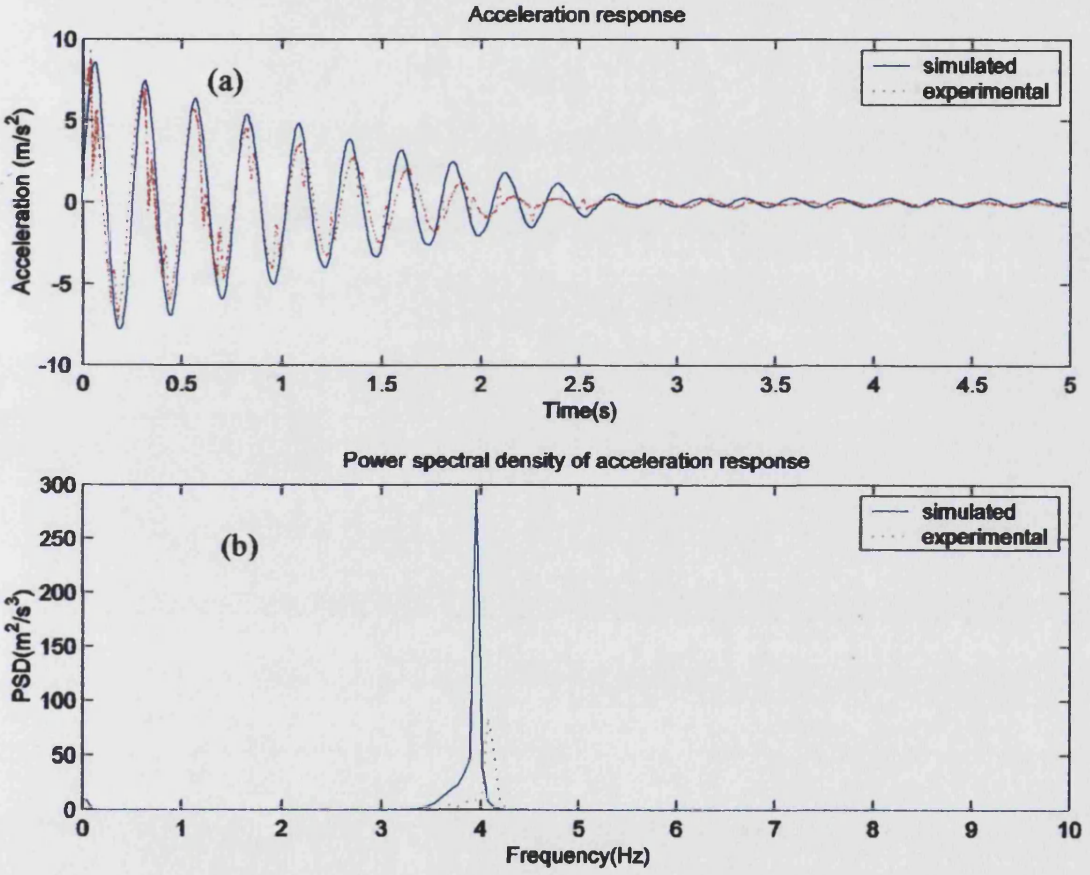


Figure 7.6: Simulation vs. experiment—impulse momentum model

*7.2.2.3.2 simulation with spring-damper model of impact*

The parameters of the spring-damper model can be found by putting the experimentally obtained coefficient of restitution $c_r = 0.61$ and the measured contact time $T_c = 0.025$ into Eq(2.36) and Eq(2.41) to give: $k_b = 1655.6N/m$ and $c_b = 4.0457s/m$. The

results of the simulation compared with the experimental results are shown in Figure 7.7.

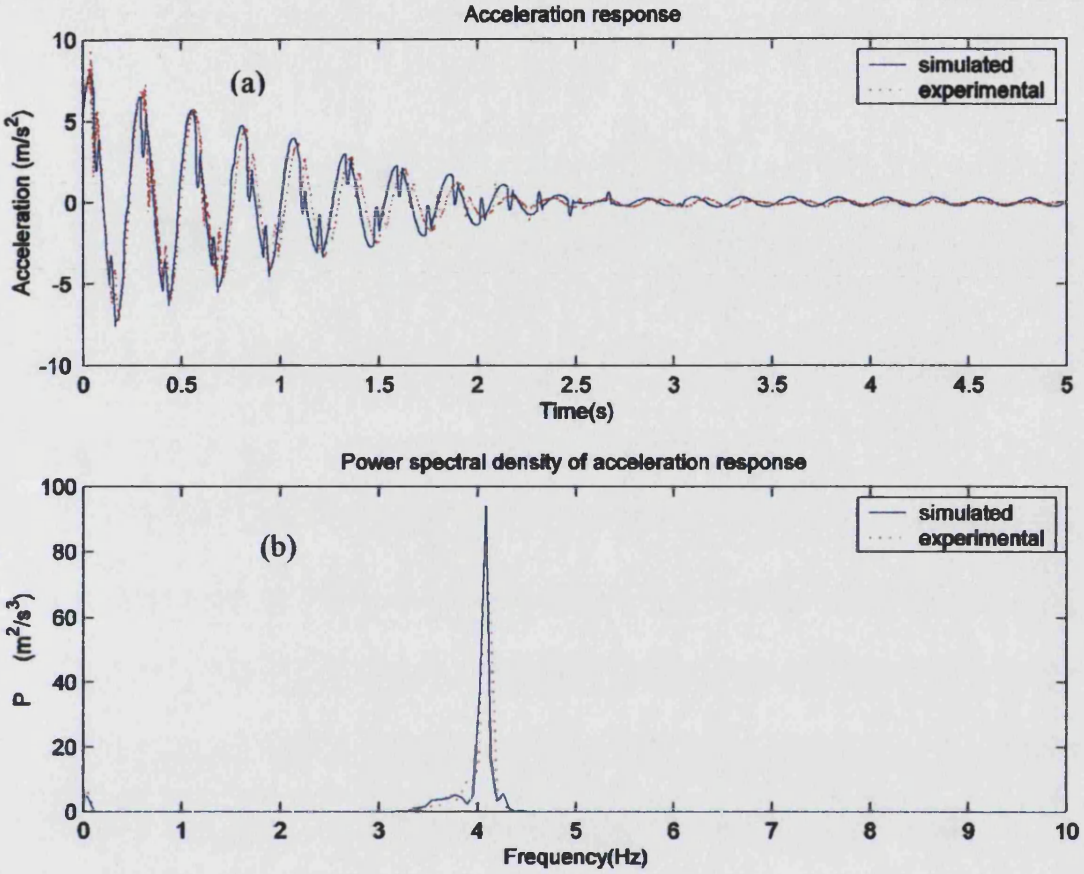


Figure 7.7: Simulation vs. experiment—spring-damper model

From Figure 7.7(a), it can be seen that the simulated and experimental acceleration responses match very well. The sudden changes in acceleration caused by collisions, represented by the peaks on the sine curve, can be clearly identified from both the simulation and the experiment, and match well. From Figure 7.7(b) it can also be seen that the PSD for the simulation matches the experimental PSD very well. The results clearly show that, when contact time is not negligible, the spring-damper model of impact simulates the actual response well, whereas the impulse momentum model is poor.

*7.2.3 Forced vibration—band limited white noise base excitation*

Similar tests to those described above have been carried out under forced vibration. In this case, tests have been performed using random base excitation with a band-limited frequency content between *0* and *15 Hz*.

*7.2.3.1 simulation vs. experiment—without damper*

Again, to demonstrate the accuracy of the numerical simulation, the response was first simulated without an impact damper and compared to the experimental response. The simulated and experimental results, i.e. the acceleration response and the power spectral density of the acceleration response, are shown in Figure 7.8. It can be seen that the simulation matches the experimental results well, suggesting that the numerical scheme is accurate.

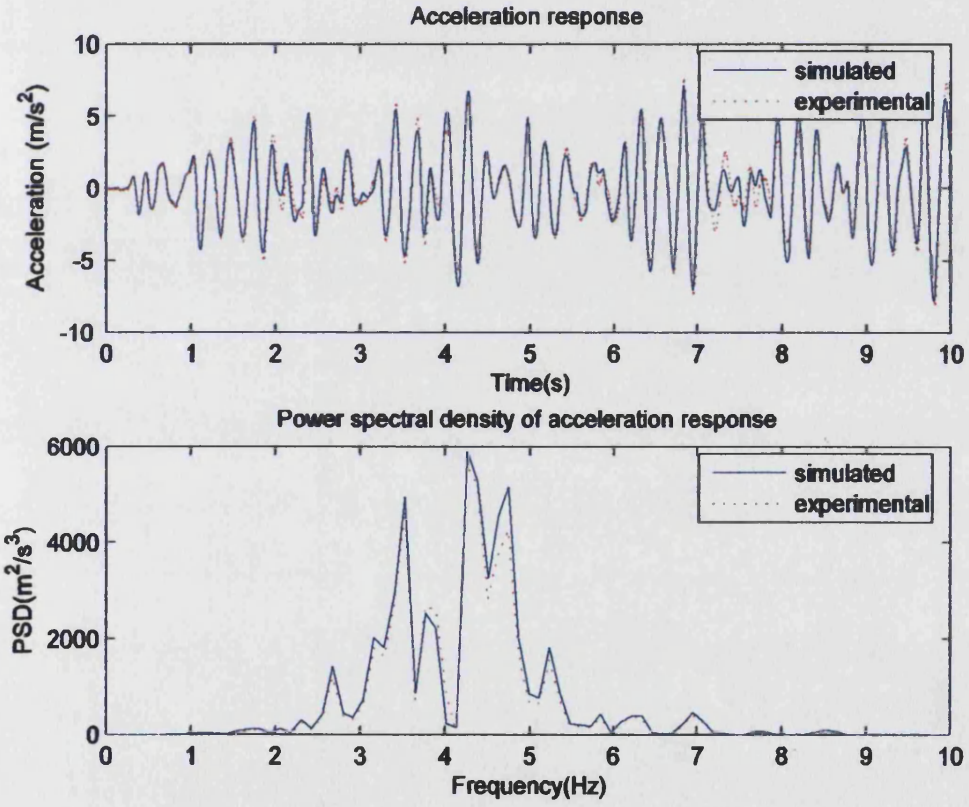


Figure 7.8: Simulation vs. experiment—without damper

*7.2.3.2 simulation vs. experiment—with conventional impact damper*

For the case of random base excitation with the conventional impact damper in operation, the simulations using the impulse momentum model and the spring-damper model were performed and the results compared with the experimental results.

*7.2.3.2.1 simulation with impulse momentum model of impact*

For both the experiment and simulation, the mass ratio used was $\mu = 0.082$ and clearance *d=15mm.* In this case, the collision is between two steel objects, the damper mass and the stop. The experimentally derived coefficient of restitution used in the simulation is $c_r = 0.46$ . The results are presented in Figure 7.9. It can be seen that for a conventional impact damper, the simulation using the impulse momentum model of impact matches the experimental results reasonably well, both in terms of the time history and the peak PSD, although there are some discrepancies in the PSD at higher frequencies.

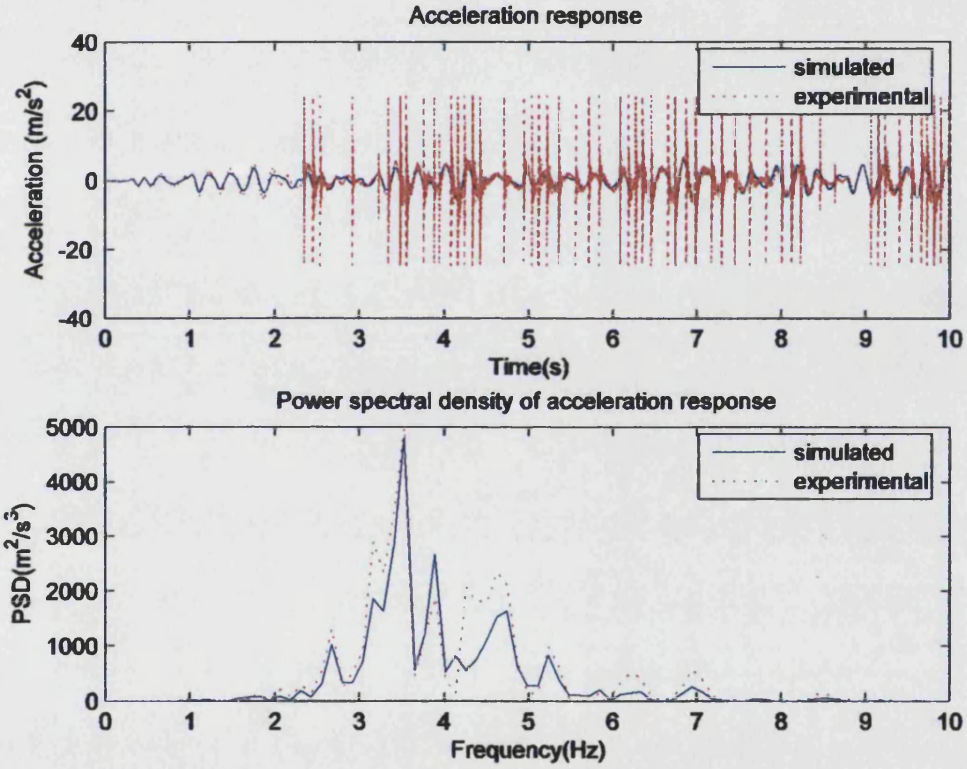


Figure 7.9: simulation vs. experiment—impulse momentum model

*7.2.3.2.2 simulation with spring-damper model of impact*

The parameters of the spring and damper used in the simulation, which are derived from the measured contact time and coefficient of restitution, are: $k_b = 11905000N/m$ and $c_b = 529.65Ns/m$. The results are shown in Figure 7.10. The simulation matches the experiment as well as for the impulse momentum model. However, it can be seen from the acceleration response, that the peaks caused by collisions are simulated and are at

about the same level as those which occurred in the experiment. Another point which can be noted is that in the simulation the fist collision of the impact damper came earlier than that of the experiment. This may be due to neglecting friction between the damper mass and the primary structure and simplifying the motion of the rolling ball damper mass.

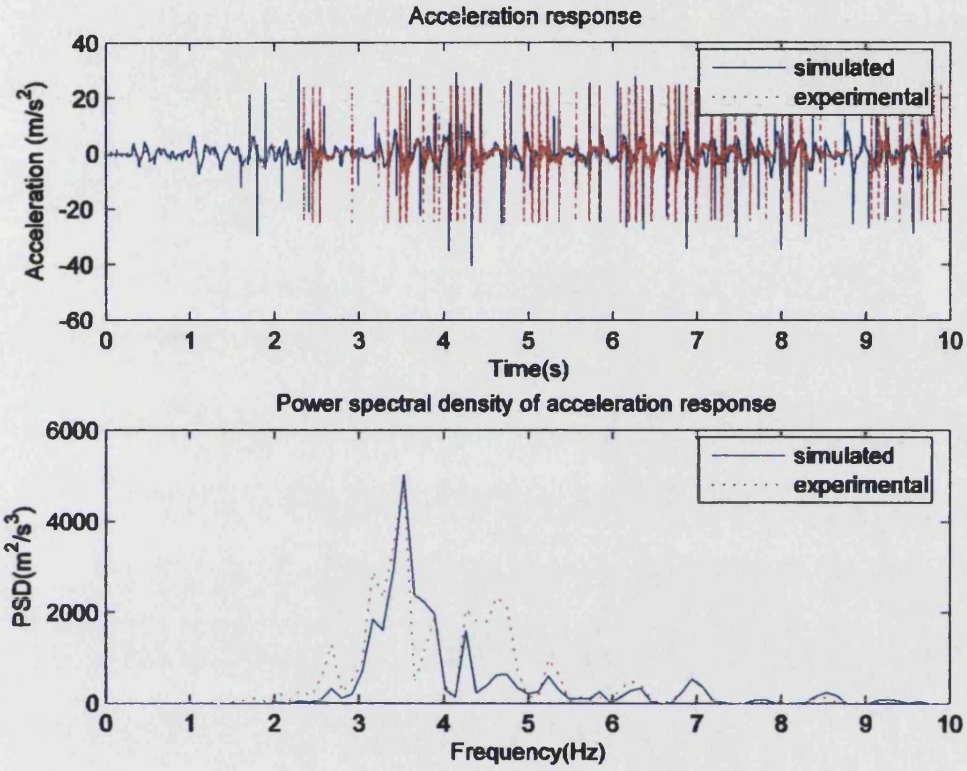


Figure 7.10: Simulation vs. experiment—spring-damper model

*7.2.3.3 simulation vs. experiment—with buffered impact damper*

For the case of base random excitation with a buffered impact damper in operation (using buffer 1), simulations using the impulse momentum model and the spring-damper model were performed and the results compared with the experimental results.

*7.2.3.3.1 simulation with impulse momentum model of impact*

The coefficient of restitution between the steel damper mass and buffer *1* is $c_r = 0.61$. All other conditions are the same as those described in section *7.2.2.3.1*. The results of the simulation using the impulse momentum model of impact and that from experiment are shown in Figure 7.11. There is a significant difference between the simulation and the experimental results, which can be seen from both the time history and the PSD.

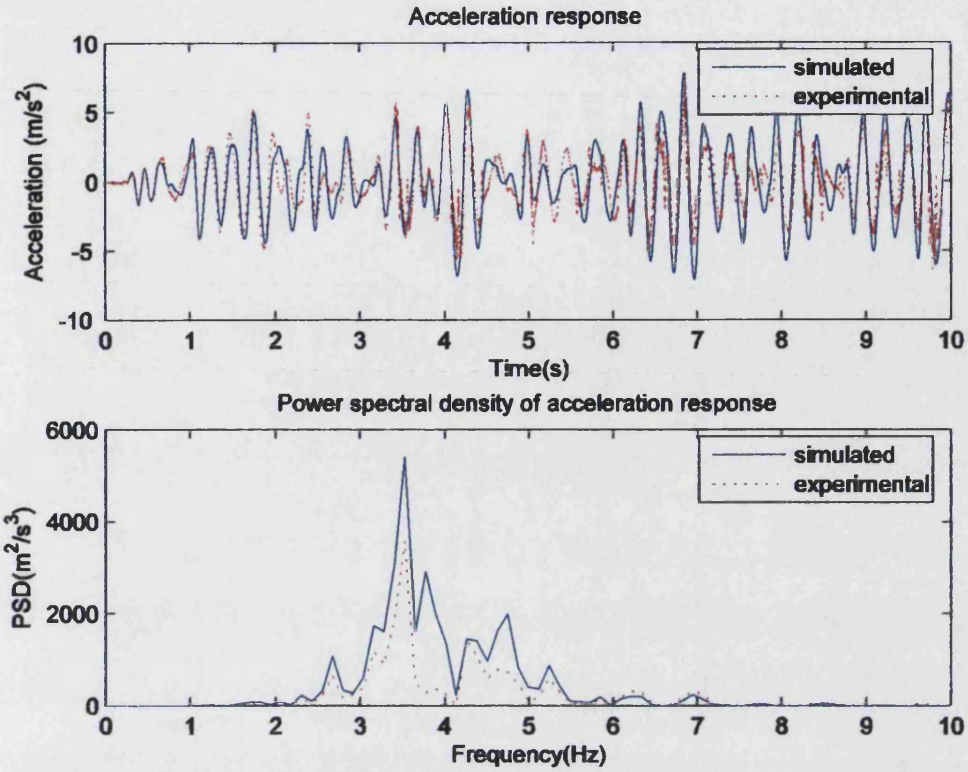


Figure 7.11: simulation vs. experiment—impulse momentum model

*7.2.3.3.2 simulation with spring-damper model*

The parameters of the spring-damper model used in the simulation are: $k_b = 1655.6N/m$ and $c_b = 4.0457s/m$. These are obtained by putting the coefficient of restitution $c_r = 0.61$ and the contact time $T_c = 0.025$ into Eq(2.36) and Eq(2.41). All other conditions are the same as those in section *7.2.3.3.1*. The results from both the simulation and the experiment are presented in Figure 7.12. It can be seen that the simulation with spring-damper model matches the experimental results well, particularly in terms of peak PSD.

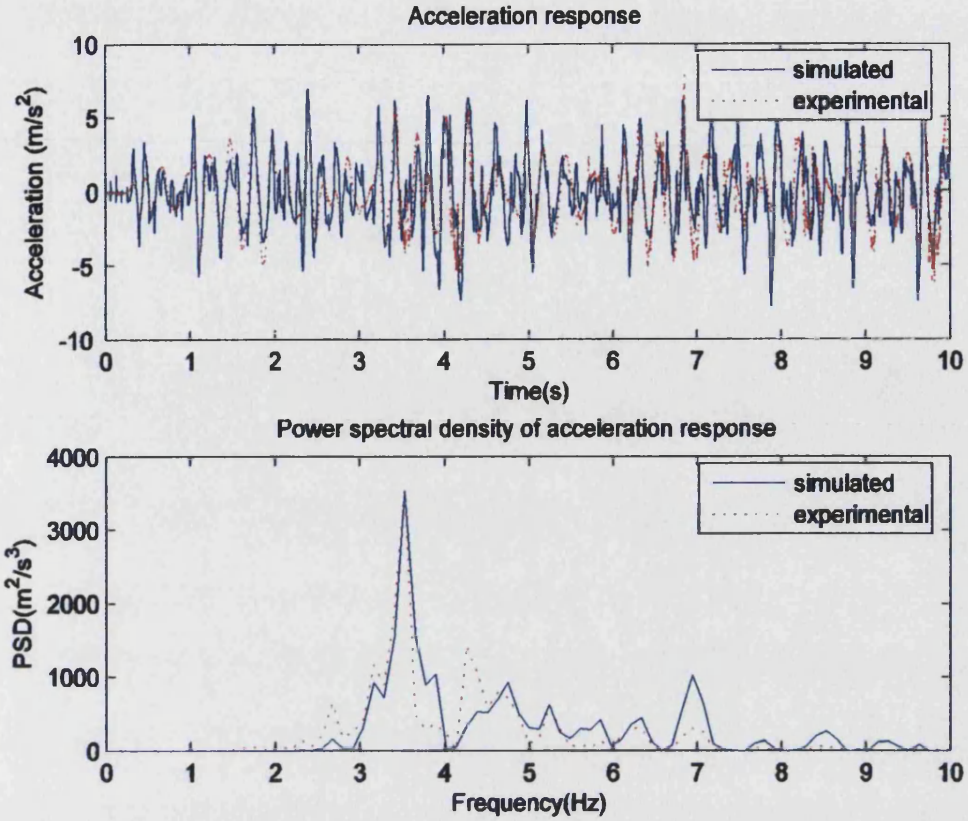


Figure 7.12: simulation vs. experiment—spring-damper model

From the above investigations of both free and forced vibration, it can be concluded that for the conventional rigid impact damper, simulations using both the impulse momentum model and the spring-damper model of impact produce results which match the corresponding experimental results well. However, for a buffered impact damper, where the contact time of impact is not negligible, the simulation using the impulse momentum model of impact can not match the experimental result whilst simulations using spring-damper model with parameters derived from the measured contact time and coefficient of restitution match the experimental result well.

### 7.3 Simulation vs. experiment—MDOF primary system

*Introduction:* Presented in this section are comparisons between simulations and experimental results for a MDOF primary structure under base sinusoidal sweep excitation. Both simulations using the impulse momentum model of impact and the spring-damper model of impact are performed and the results compared with corresponding experimental results.

*7.3.1 Primary structure and its model*

The MDOF primary structure chosen for both simulation and experiment is as shown in Figure 5.1. The parameters of the system representing the physical structure are:

$$\text{mass matrix } \mathbf{M} = \begin{bmatrix} 1.105 & 0 & 0 \\ 0 & 1.105 & 0 \\ 0 & 0.12 & 1.35 \end{bmatrix} (Kg)$$

$$\text{stiffness matrix } \mathbf{K} = \begin{bmatrix} 1572 & -786 & 0 \\ -786 & 1572 & -786 \\ 0 & -786 & 786 \end{bmatrix} (N/m)$$

The damping is assumed to be: $\mathbf{C} = [0.6541 \times \mathbf{M} + 0.00024 \times \mathbf{K}]$ $(Ns/m)$

The stiffness matrix is obtained by simple static measurements on the steel strips. The mass matrix is determined by weighing the beams with adjustment by fitting to the experiment results (which is why the off diagonal term of *0.12* exists, although it is recognized that this has no sound physical basis). The assumed damping matrix is based on the experimentally derived transfer function. The natural frequencies of the structure are $f_1 = 1.76Hz, f_2 = 5.22Hz$ and $f_3 = 7.72Hz$ . The excitation employed is base sinusoidal sweep. The sweeping range is from *0.5Hz* to $10Hz$ (to encompass the natural frequencies of the structure).

*7.3.2 Simulation vs. experiment—without damper*

When without a damper, the acceleration response of each storey, for both simulation and experiment, are as presented in Figure 7.13. The transfer functions between the base and each storey are shown in Figure 7.14. From Figure 7.13 and Figure 7.14, it can be seen that the simulation matches the experimental results well, demonstrating that the primary structure is modelled well and that the numerical integration scheme is appropriate.

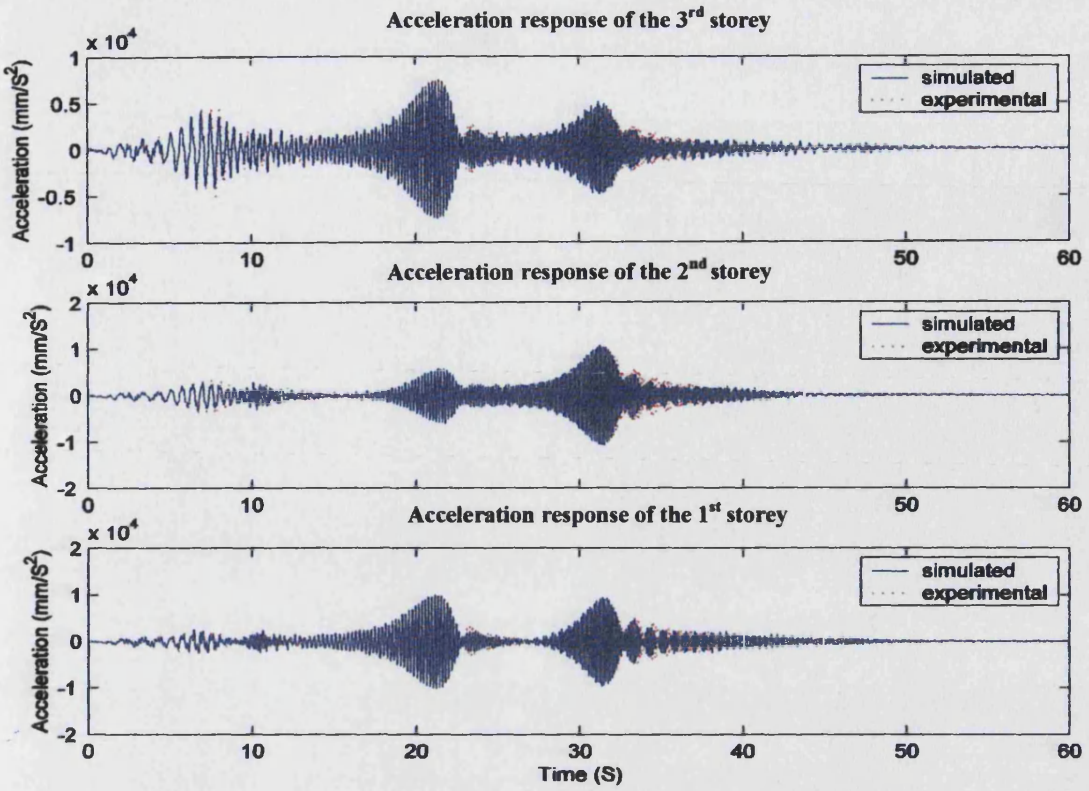


Figure 7.13: Simulation vs. experiment—acceleration (without damper)

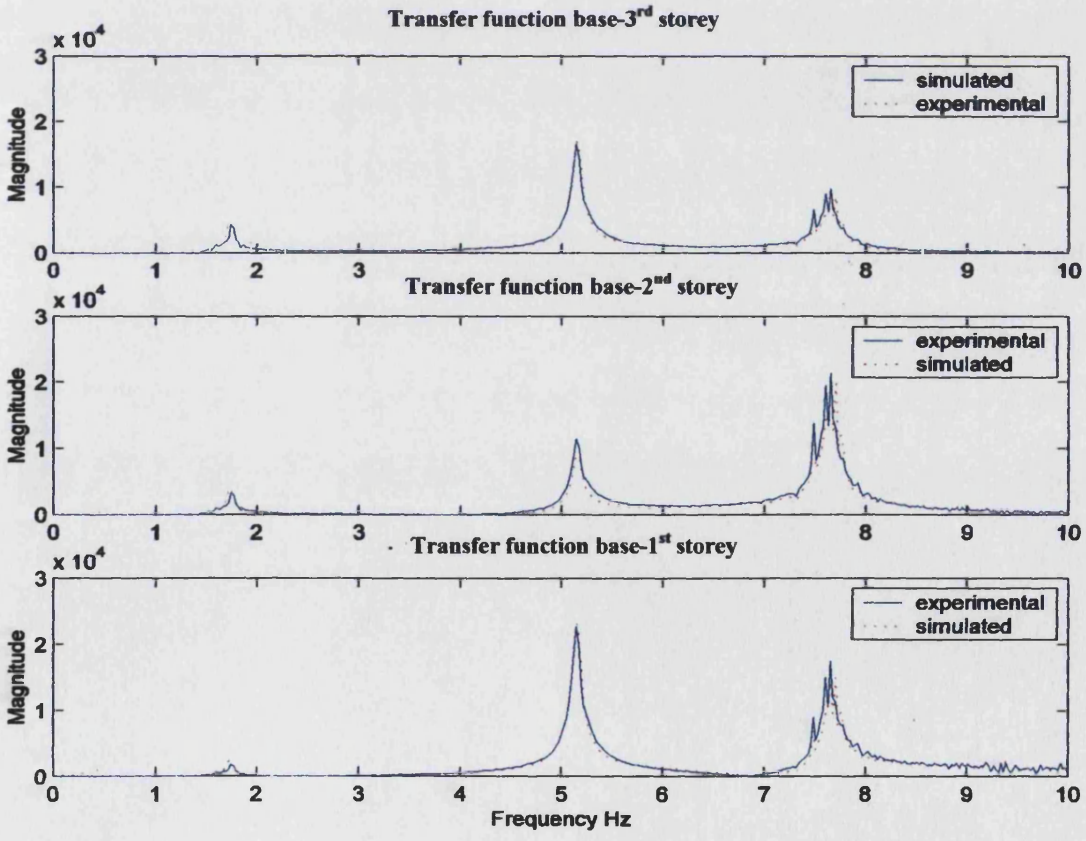


Figure 7.14: Simulation vs. experiment—transfer function (without damper)

*7.3.3 Simulation vs. experiment—with conventional impact damper*

*Introduction:* With a conventional impact damper in operation, simulations using the impulse momentum model and the simulation using the spring damper model of impact are performed and the results compared with experimental results.

*7.3.3.1 simulation with impulse momentum model of impact*

For both the simulation and the experiment the clearance used was $d=15mm$ and the mass ratio, defined as the ratio of the damper mass to the mass of the third storey of the primary structure (not the mass of the whole structure), is $\mu = \frac{m}{M_3} = 0.082$ . The coefficient of restitution between the steel damper mass and the steel stop is $c_r = 0.46$. The simulated and experimental accelerations of each storey are shown in Figure 7.15 and the transfer functions between the base and each storey are presented in Figure 7.16. From Figure 7.16 it can be seen that the difference between the simulation and experiment is significant on the second mode, which, looking at Figure 7.15, is the frequency where most impacts are observed in the experiment. For the first and third modes, there is good agreement but, as can be observed by comparing with Figure 7.14, there is little control effect for these modes.

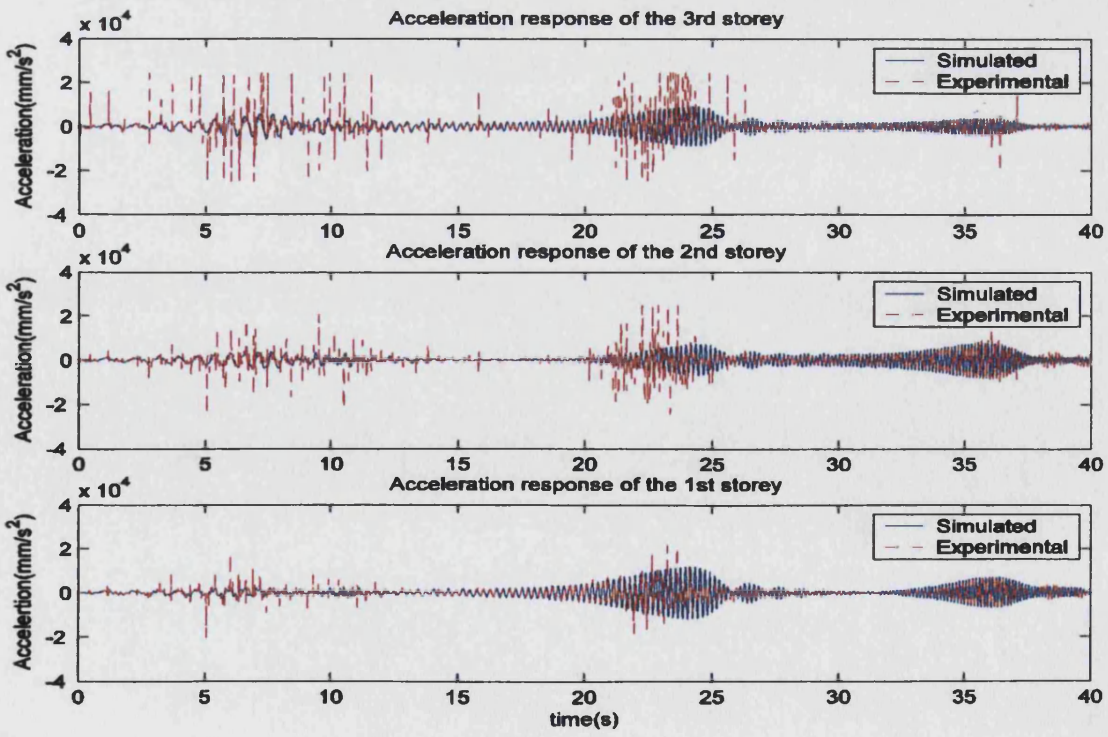


Figure 7.15: simulation (IMM) vs. experiment— acceleration

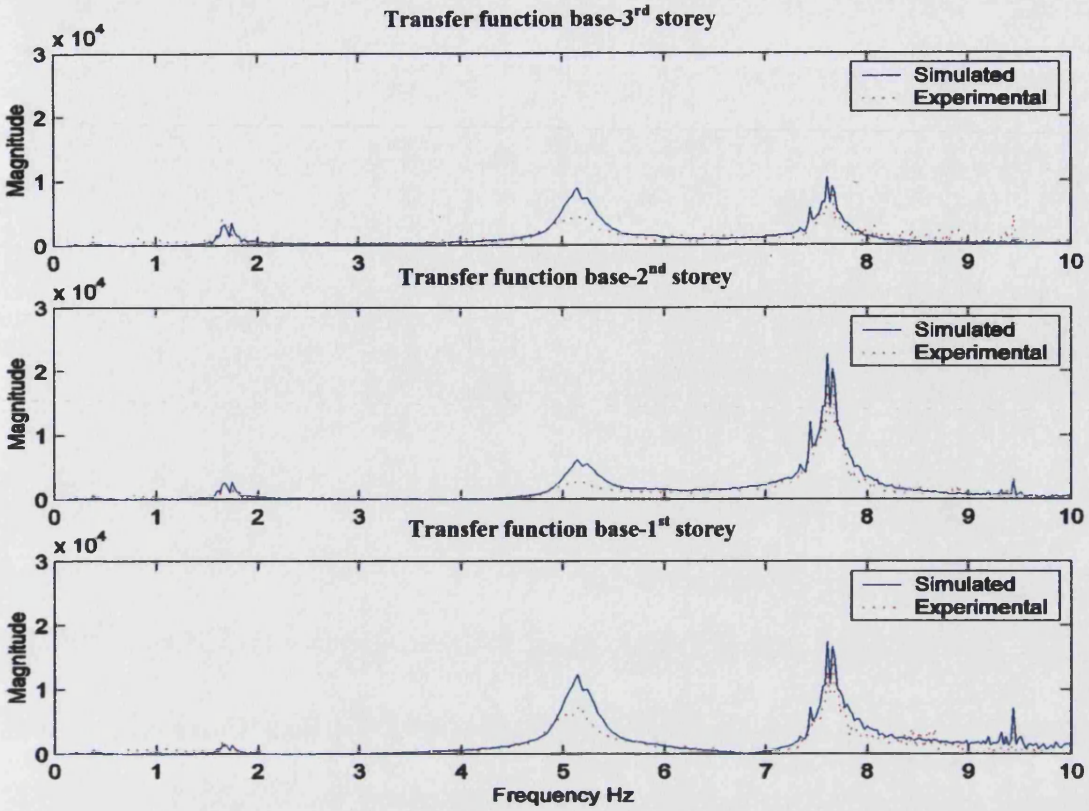


Figure 7.16: Simulation (IMM) vs. experiment— transfer function

*7.3.3.2 simulation with spring-damper model of impact*

The parameters of the spring and damper used in the simulation are: $k_b = 11905000N/m$ and $c_b = 529.65Ns/m$, which, again, are derived from the experimentally measured contact time and coefficient of restitution. The clearance and mass ratio are the same as in section 7.3.3.1. The results are presented in Figures 7.17 and 7.18. From Figure 7.17, the acceleration peaks caused by collisions can be seen from the simulated acceleration response of the third storey, where the impact damper is located. However, acceleration peaks also occur in the experimental responses of the second and first storey but this is not found in the simulated acceleration response. This may mean the effect of impact on the other DOFs of a MDOF structure except the DOF where the impact damper is located is not well modelled and may provide the basis for further modelling improvement. Comparing Figure 7.18 with Figure 7.16, it can be seen that the simulation with the spring-damper model matches the experimental result better than the simulation with impulse momentum model does, particularly for the second mode, where the control effect is most significant.

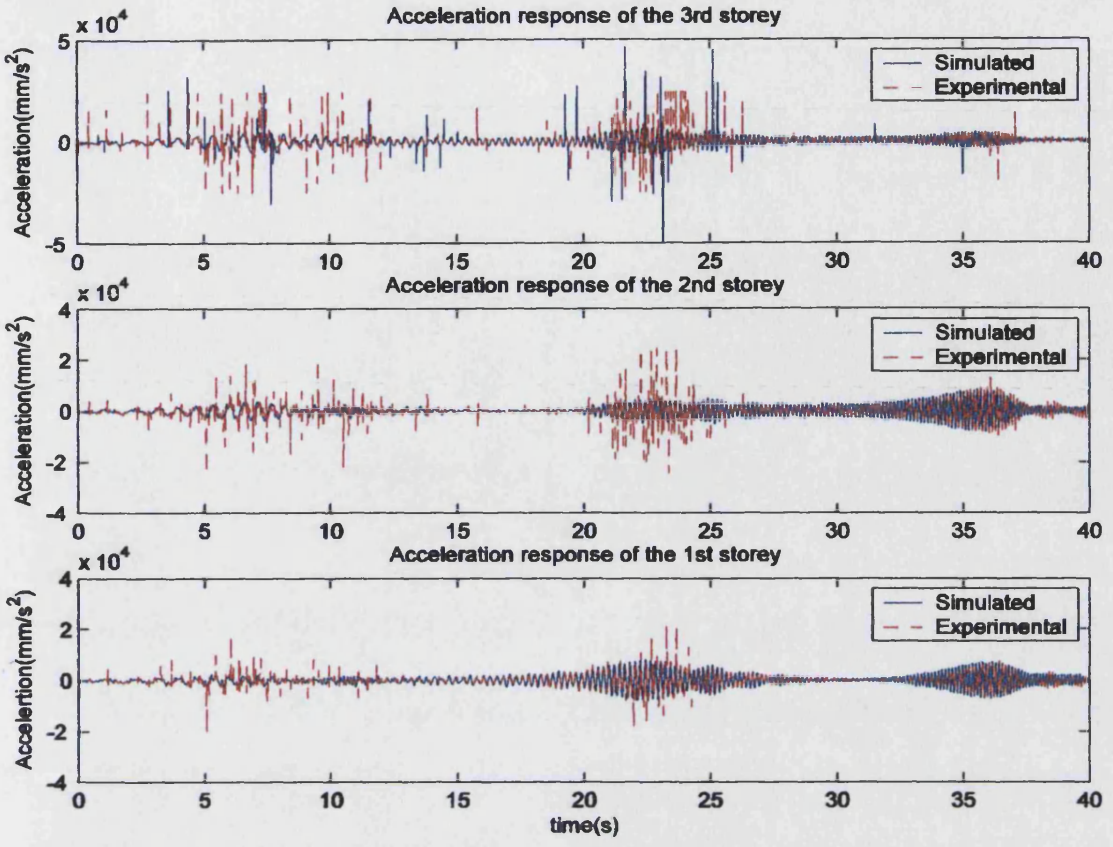


Figure 7.17: Simulation (SDM) vs. experiment—acceleration

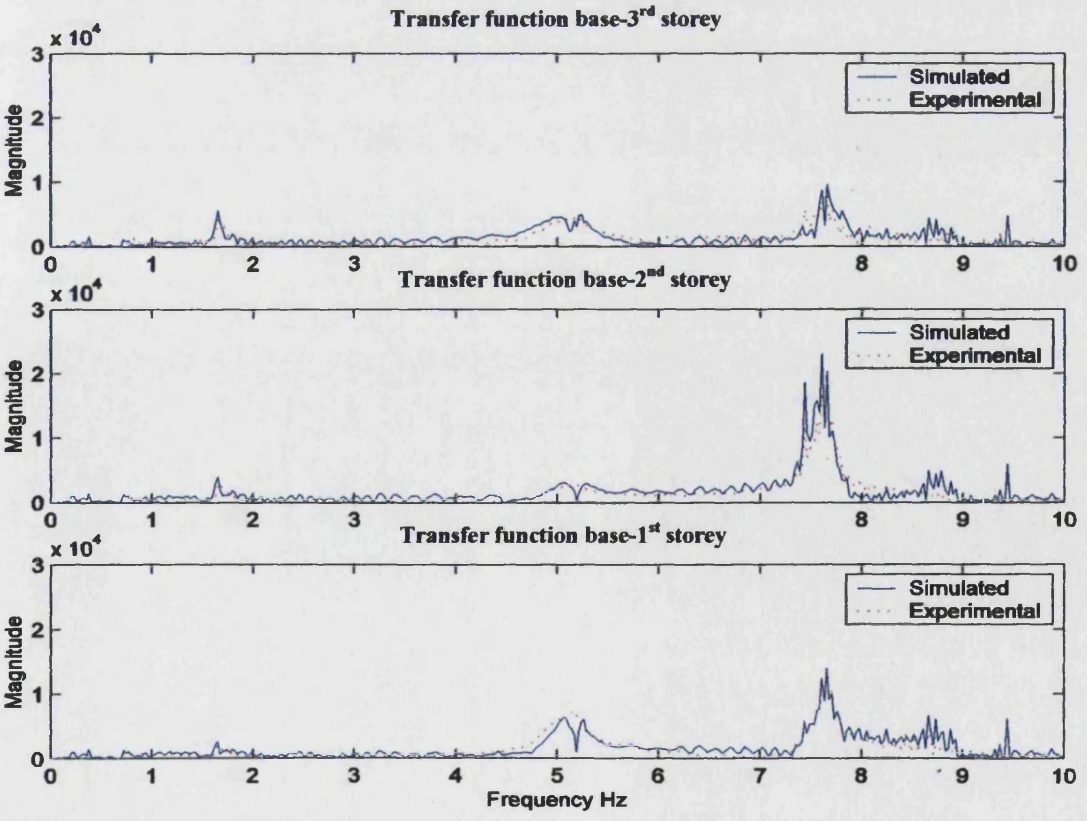


Figure 7.18: Simulation (SDM) vs. experiment— transfer function

*7.3.4 simulation vs. experiment—with buffered impact damper*

*Introduction:* With a buffered impact damper in operation, simulations using the impulse momentum model and the spring-damper model of impact were performed. The results are compared with the corresponding experimental results.

*7.3.4.1 simulation with impulse momentum model of impact*

The buffer used in both the experiment and simulation is buffer *1*. The coefficient of restitution between the steel damper mass and buffer *1* is $c_r = 0.61$. The clearance and mass ratio remain the same as that of the conventional impact damper case. The results from both the simulation and experiment are presented in Figures 7.19 and 7.20. From Figure 7.20 it can be seen that for both the second and the third modes of each story, the differences between the simulation and the experimental results are significant. For the first mode at the second and third storey, the simulation matches the experiment well. However, for the first mode of the first storey, the difference between the simulation and the experiment is also significant as can also be observed from the time history in Figure 7.19.

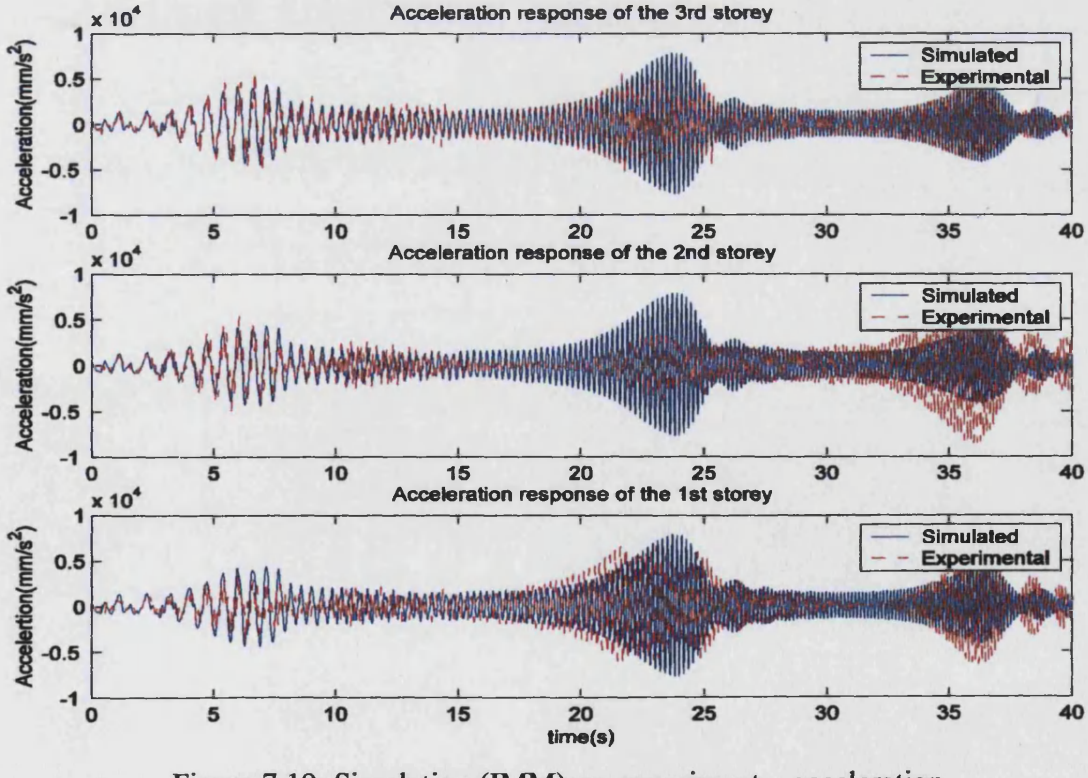


Figure 7.19: Simulation (IMM) vs. experiment—acceleration

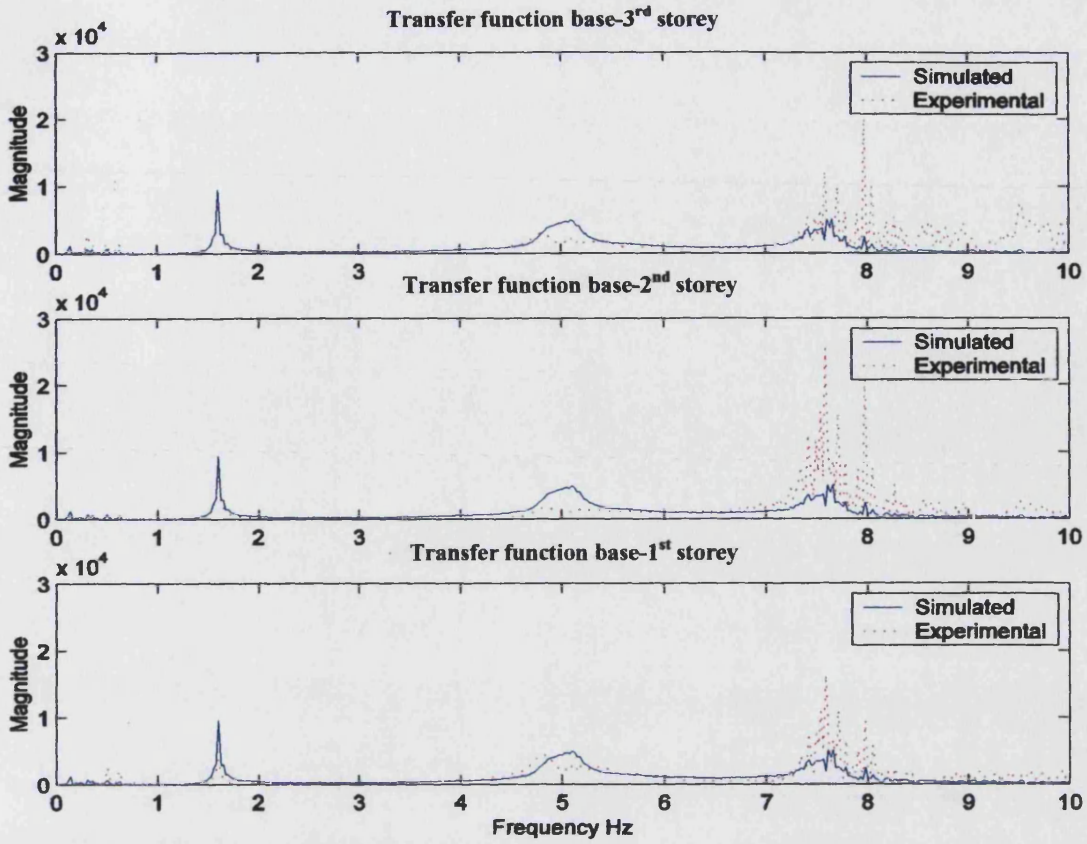


Figure 7.20: simulation (IMM) vs. experiment— transfer function

*7.3.4.2 simulation with spring-damper model of impact*

The parameters of the spring-damper model used in the simulation are: $k_b = 1655.6N/m$ and $c_b = 4.0457Ns/m$. The simulated and experimental acceleration responses of each storey are presented in Figure 7.21. Figure 7.21 is re-plotted, taking only the first *10* seconds, as shown in Figure 7.22, in order to allow the behaviour at impact be observed. From the simulated acceleration of the third storey in Figure 7.22, it can be observed that the acceleration peaks, caused by collision, are similar to those of the experimental acceleration record. Figure 7.23 shows the transfer function between the base and each storey. Comparing Figure 7.23 with Figure 7.20, it can be seen that the simulation with the spring damper model of impact matches the experimental results better than the simulation with impulse momentum model does, particularly for the third mode although there are still discrepancies evident.

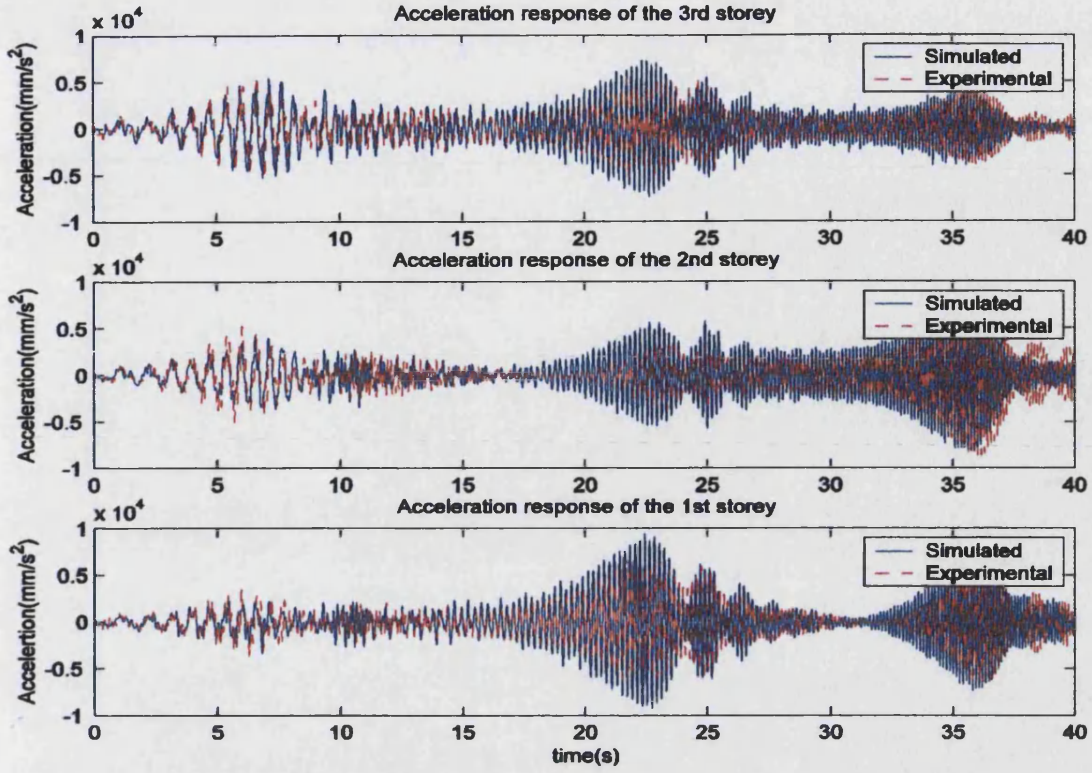


Figure 7.21: Simulation (SDM) vs. experiment—acceleration

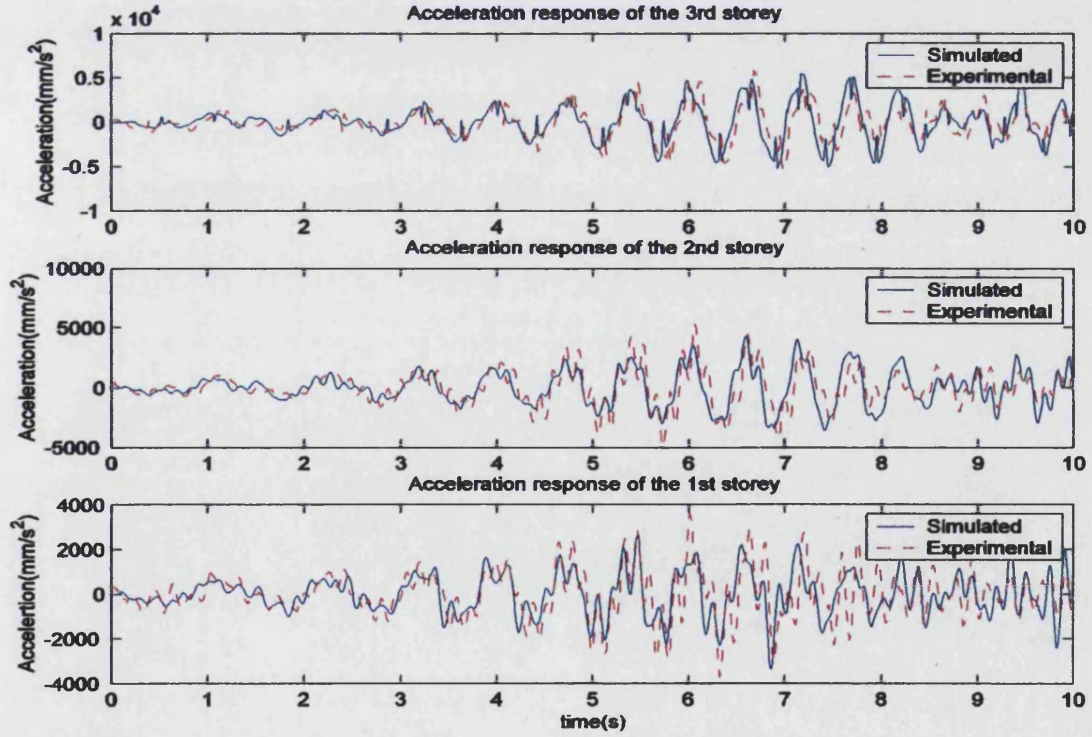


Figure 7.22: Simulation (SDM) vs. experiment—acceleration (first 10 seconds)

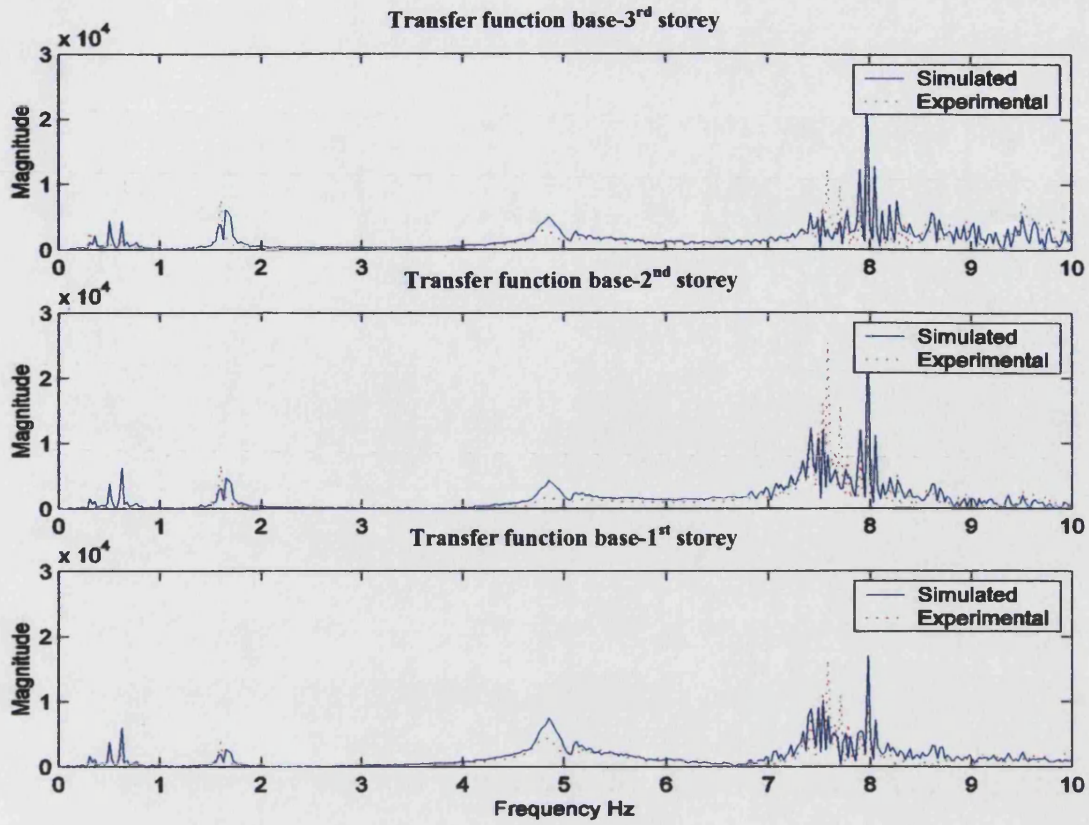


Figure 7.23: simulation (SDM) vs. experiment— transfer function

## 7.4 Simulation studies on impact damper parameters

The above comparison of simulations with experimental results has demonstrated the effectiveness of the simulation (in particular using the spring-damper model of impact) in predicting the response of a structure incorporating an impact damper. The following examples employ the simulation using the spring damper model of impact to investigate the effect of parametric variation on the performance of an impact damper in the control of a primary structure.

### *7.4.1 Effect of clearance—SDOF primary structure*

A SDOF primary structure is employed to investigate the effect of clearance of a BID on control effect. The parameters of the primary structure are chosen to be: mass *M=1.2Kg*, stiffness *K= 767N/m* and damping *C=0.25Ns/m*. The parameters of the impact damper are: mass ratio $\mu = 0.08$, $k_b = 110260N/m$ and $c_b = 41.66Ns/m$. The primary structure is excited by an initial displacement of *20mm* to provide free vibration.

Figure 7.24 shows the simulated displacements for different clearances, $d = 20, 30$ and $40mm$, compared with the response without an impact damper. From Figure 7.24 it can be seen that when the clearance of the impact damper is smaller than twice the initial displacement ($2 \times 20mm$) of the primary structure, the control effect of the impact damper is significant. When the clearance of the impact damper is *40mm*, exactly twice the initial displacement (*20mm*) of the primary structure, there is no control effect at all. This can also be seen from the PSD of the acceleration response and the time history of acceleration presented in Figure 7.25. However, for a clearance of *39mm*, only very slightly smaller than twice the initial displacement, there is a significant control effect. Clearances greater than *40mm* were also simulated, although the simulation results are not presented here. They also showed that there is no control effect at all when the clearance is greater that twice of the initial displacement of the primary structure. This result is consistent with the results of the analytical study on free vibration of a SDOF primary structure equipped with an impact damper by Chen and Wang [81].

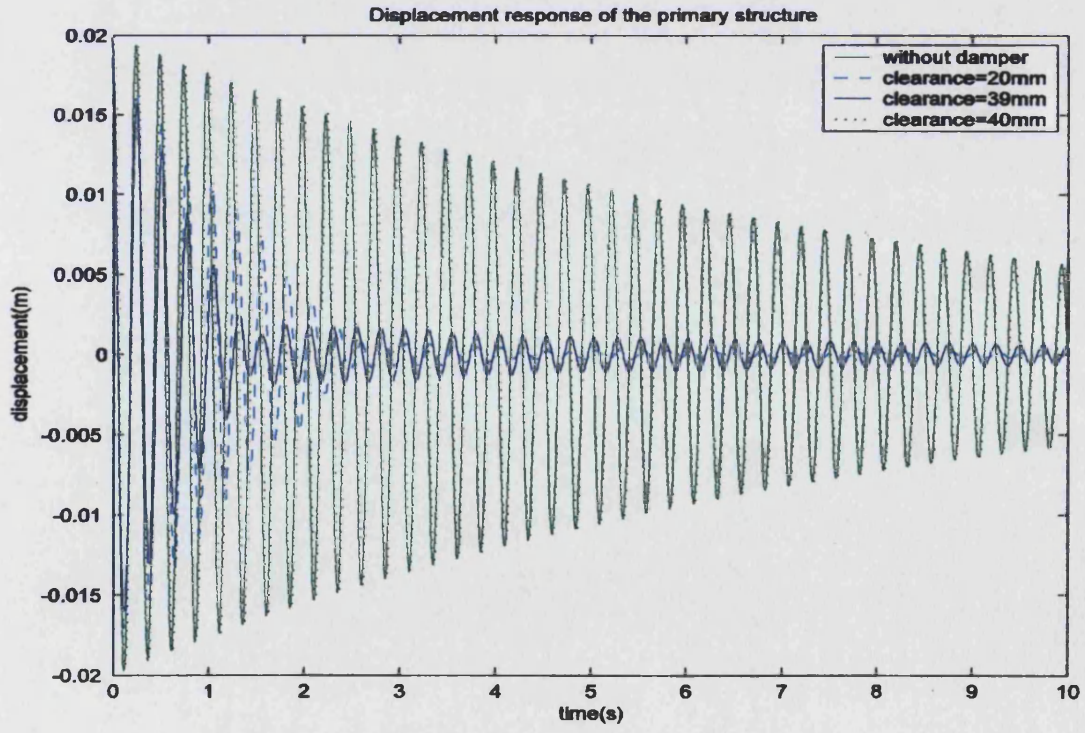


Figure 7.24: simulation on the effect of clearance.

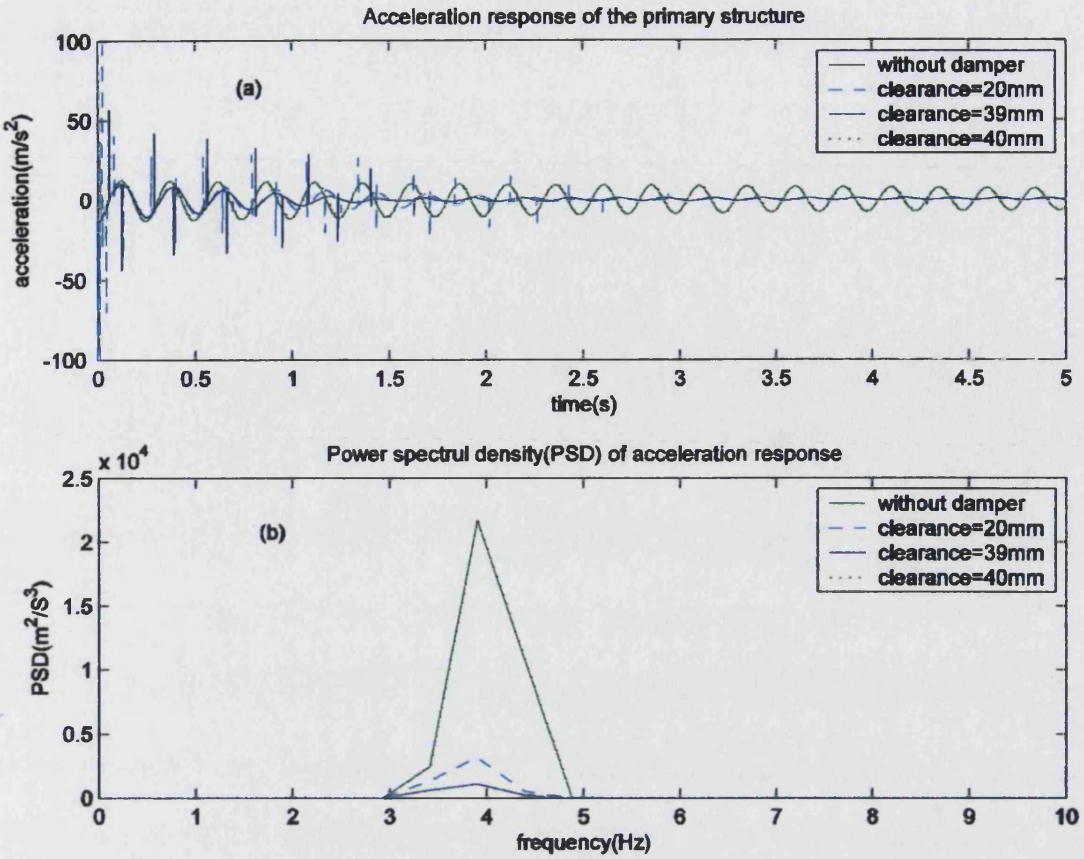


Figure 7.25: Simulated contact force and PSD at different clearance

*7.4.2 Effect of clearance—MDOF primary structure*

Whilst for SDOF systems under simple excitation it is possible to calculate the response analytically, for a MDOF primary structure, it is more difficult, even for the simplest case of a system excited by an initial displacement. However, with numerical simulation, the effect of clearance on the performance of impact damper can be predicted and an optimal clearance chosen for a particular application.

For the following example, the parameters of the 3DOF primary structure are:

$$\text{mass matrix: } \mathbf{M} = \begin{bmatrix} 1.105 & 0 & 0 \\ 0 & 1.105 & 0 \\ 0 & 0 & 1.350 \end{bmatrix} (kg),$$

$$\text{stiffness matrix: } \mathbf{K} = \begin{bmatrix} 1800 & -660 & 0 \\ -660 & 1320 & -660 \\ 0 & -660 & 660 \end{bmatrix} (N/m)$$

and damping matrix **C**=[0.3**M**+0.0003**K**](Ns/m). The initial displacement of the primary system is $X_0$ =[*0,0,0*] and the initial velocity $\dot{X}_0$=[0,0,0.3]m/s, i.e. the primary structure is stimulated by an initial velocity of the third storey. The parameters of the impact damper are: $c_b = 61.95N.m/s$, $k_b = 1.54e5N/m$ and mass ratio $\mu = \frac{m}{M_3} = 0.082$.

Several impact damper clearances, *d*, are investigated in the simulation. The displacement response of each storey is presented in Figure 7.26. It can be seen that the maximum displacement of the third storey, where the impact damper is located, is *27.5 mm*. From Figure 7.26, it can be seen that when the clearance is 55mm, i.e. twice of the maximum displacement of the third storey, there is no control effect at all.

Figure 7.27 presents the corresponding acceleration response. From the acceleration response of the third storey, it can be seen that when the clearance is *55mm*, twice the maximum displacement of the third storey, there are no acceleration peaks, indicating that there are no collisions and, therefore, as expected, no control effect.

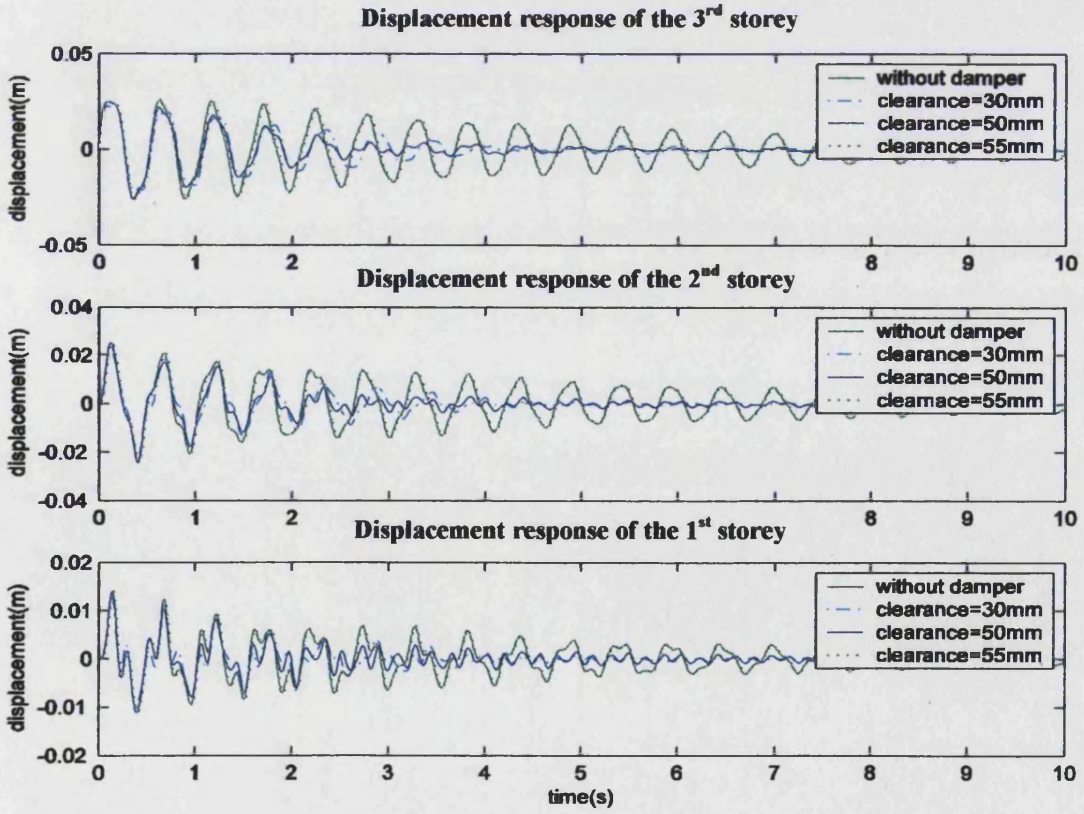


Figure 7.26: Effect of clearance—MDOF primary structure

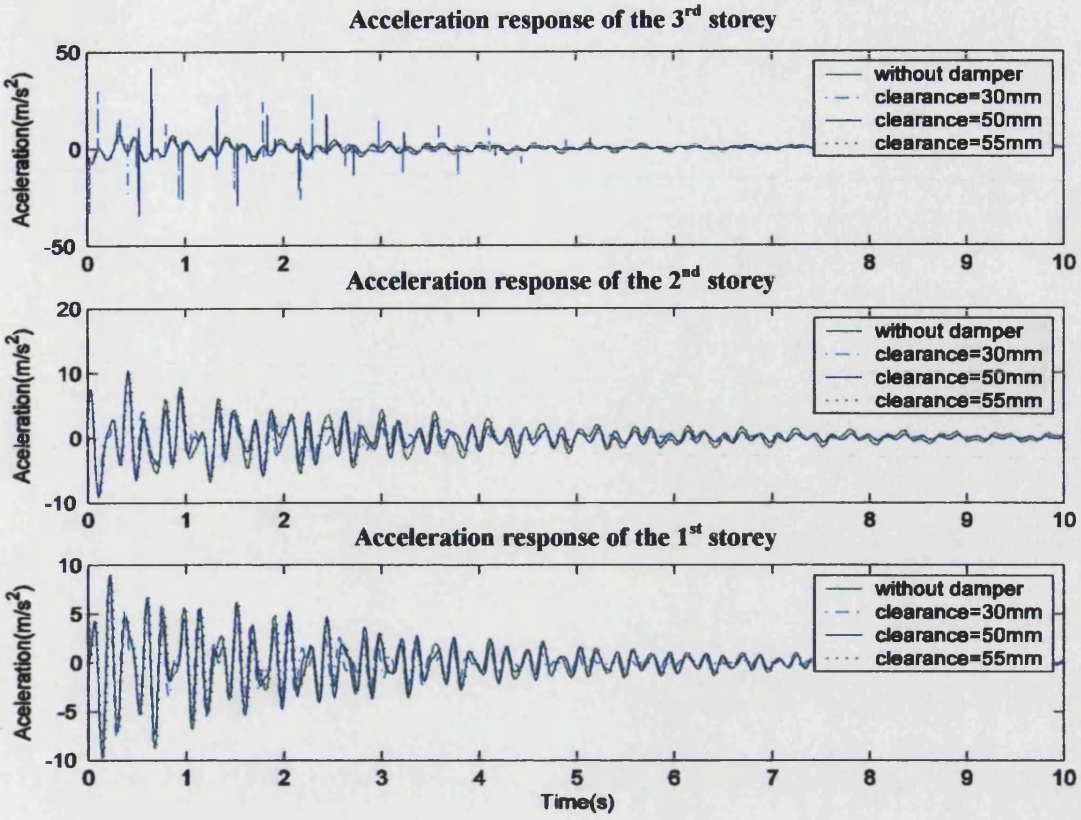


Figure 7.27: Acceleration responses at different clearances

Figure 7.28 presents the PSDs of the acceleration response. From Figure 7.28, it can be seen, once again, that when the clearance is *55mm*, there is no control effect at all. It can also be seen that control of the first mode is significant with a clearance of 30mm and even a clearance of *50mm* (only slightly smaller than twice the maximum displacement of the third storey). However, for the second mode, a clearance of *30mm* results in significant control whilst a clearance of *50mm* results in only a small degree of control. For the third mode, for both clearances the impact damper makes the response a little worse. Further investigations would result in an optimal clearance for control although it is clear that no control will occur if the clearance is greater than twice the maximum displacement of the third storey.

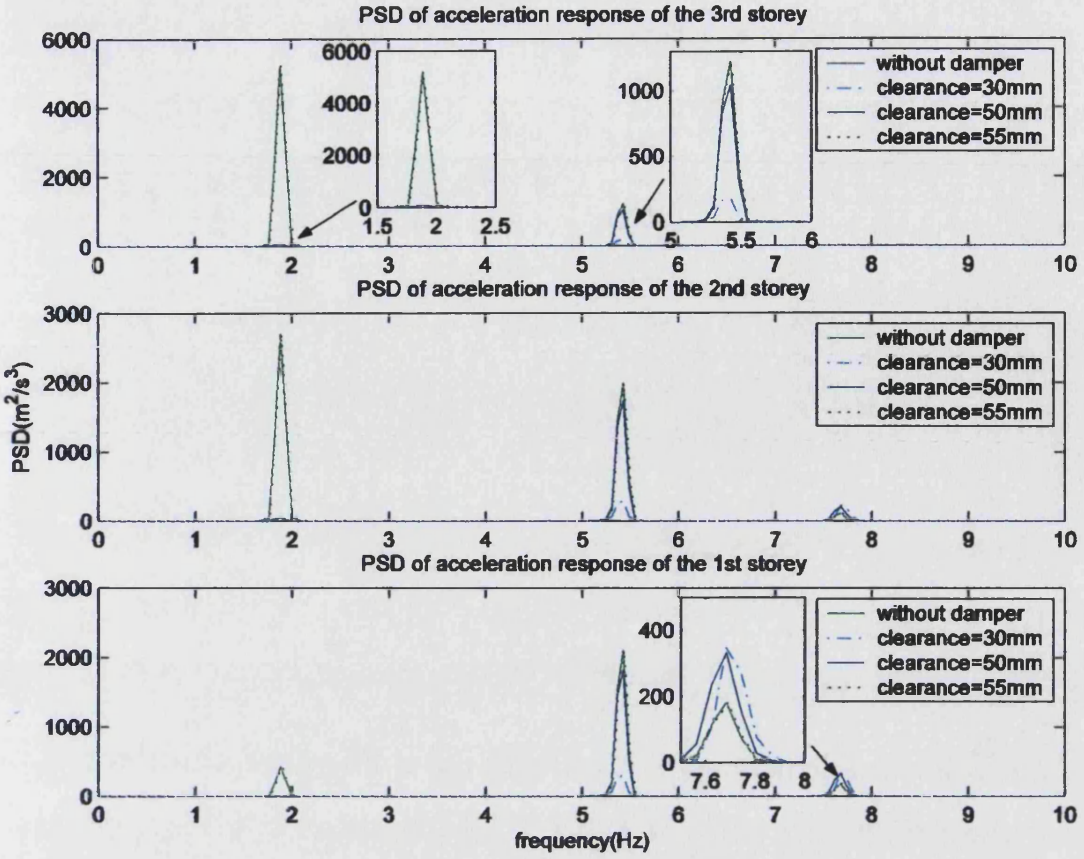


Figure 7.28: PSDs of acceleration response at different clearances

### *7.4.3 Effect of mass ratio—MDOF primary structure*

In this example, the simulation is used to investigate the effect of mass ratio on the control of a MDOF structure. The parameters of the primary structure remain same as in section *7.4.2.* The initial displacement of the primary system is $X_0$ =[*0,0,0*] and the initial velocity $\dot{X}_0$ =[0,0,0.3]m/s. The clearance used in this case is *d=0.02m.* Simulations with a mass ratio of $\mu = \frac{m}{M_3}$=*0.05*, *0.08* and *0.19* are performed.

The displacement responses of the $3^{rd}$, $2^{nd}$ and $1^{st}$ storey, with and without an impact damper for the different mass ratios, are shown in Figure 7.29. The acceleration responses are shown in Figure 7.30 and the corresponding PSDs of acceleration response are shown in Figure 7.31

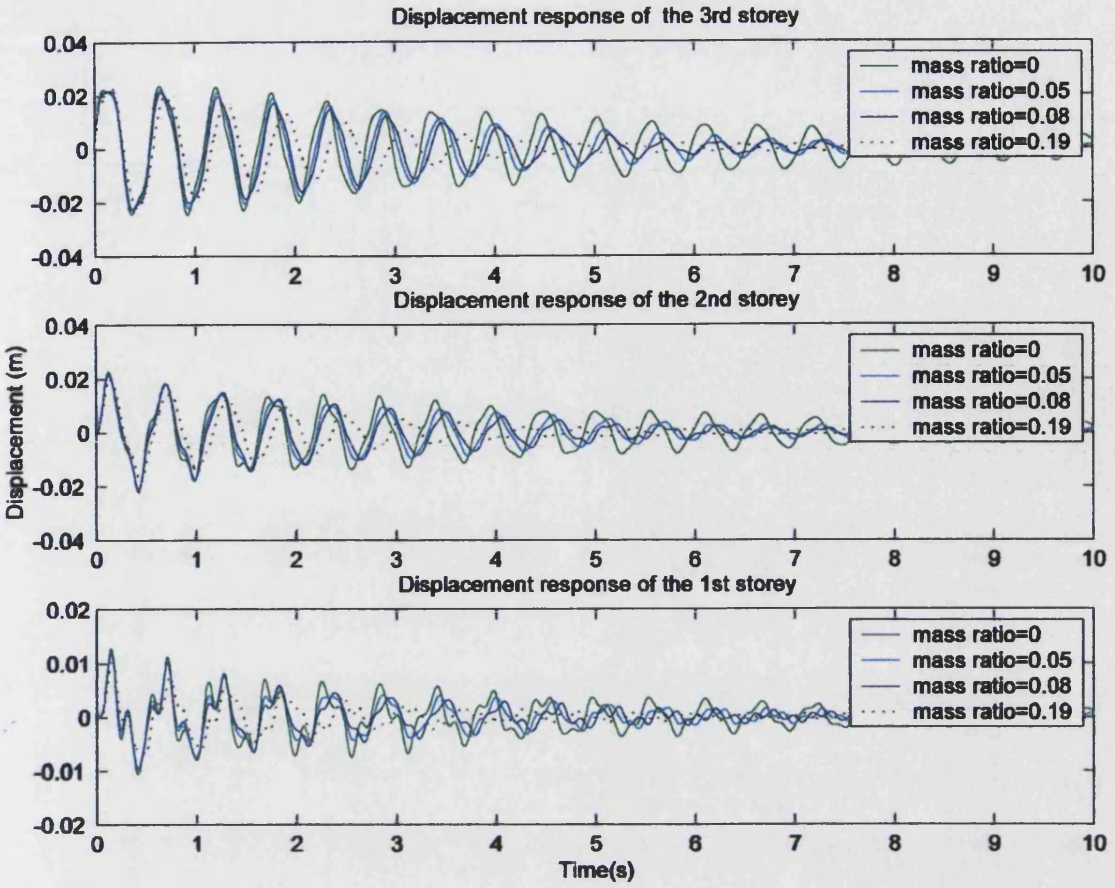


Figure 7.29: Effect of mass ratio—displacement response

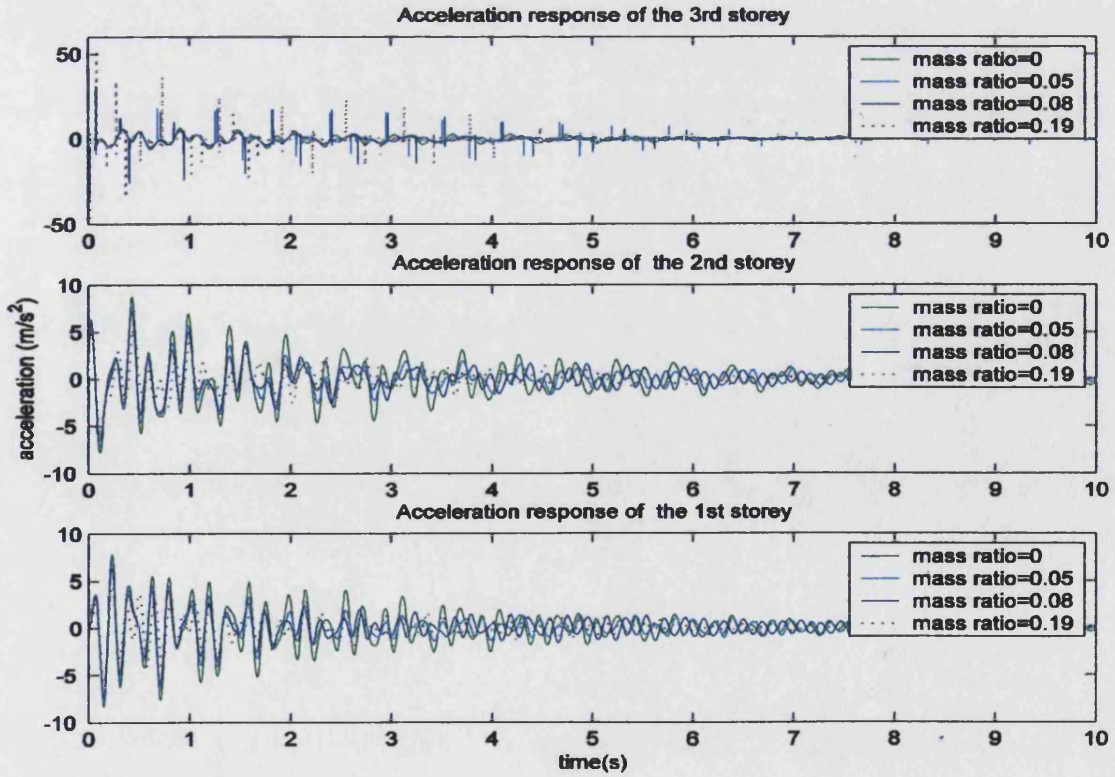


Figure 7.30: Effect of mass ration—acceleration response

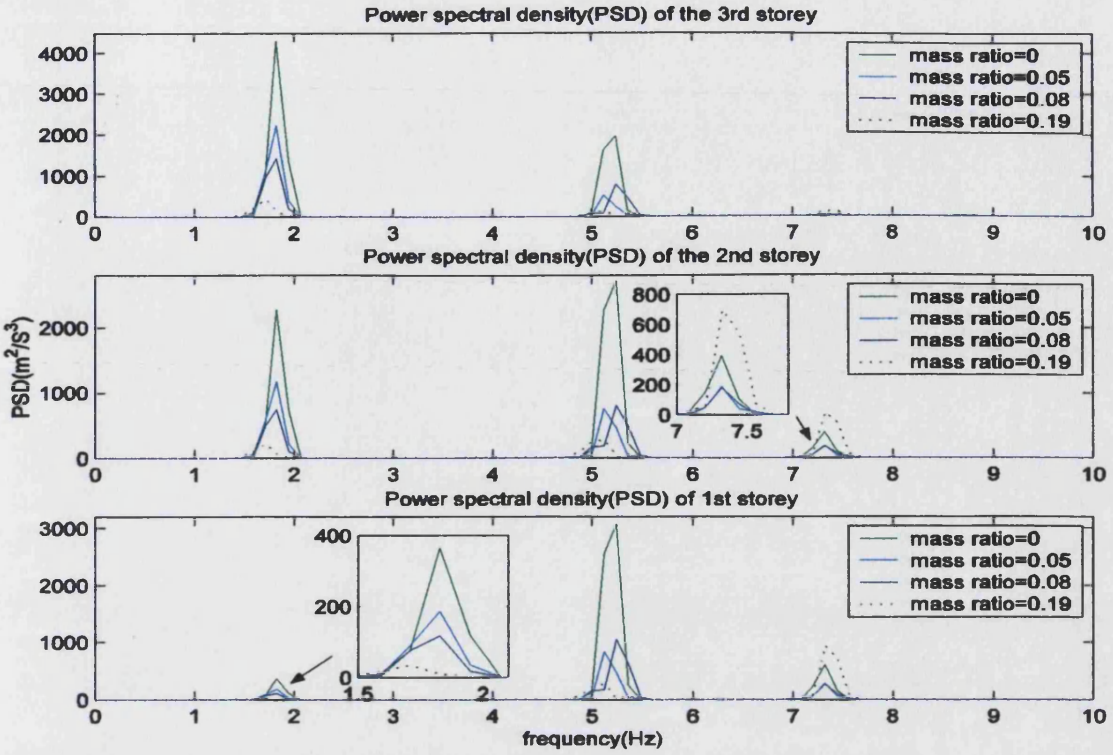


Figure 7.31: Effect of mass ration—PSDs of acceleration response

From Figure 7.29 and 7.30 the control effect can be observed. Figure 7.30 also clearly shows that the acceleration peaks caused by collision are different with impact dampers of different mass ratio. A greater mass ratio leads to higher acceleration peaks as expected. From Figure 7.31 it can be seen that for the first mode, a higher mass ratio produces a better control result. However, this is not necessarily true for the higher modes. It can be seen that control of the second mode is better with a mass ratio of *0.05* than with a bigger mass ratio of *0.08*, and in the case of the greatest mass ratio, $\mu = 0.19$, the third modes is made worse. This finding is consistent with the experimental results presented in Chapter 5.

### 7.5 Summary and conclusions

Numerical simulations of the interaction between an impact damper and a primary structure under various types of excitation have been performed. Comparisons with experimental investigations have also been carried out. The results from experiments have verified the simulation schemes, both the scheme based on the impulse momentum model and the scheme based on the spring-damper model of impact. Also verified are

the integration algorithms presented in Chapter 3, on which these numerical simulation schemes are based.

For a conventional impact damper, both the numerical simulations based on the impulse momentum model and the spring-damper model of impact work well. However, for the buffered impact damper, the impulse momentum model of impact produces results which significantly differ from the experimental results whilst the spring-damper model, in general, matches the experimental results well. This is not surprising, since for the buffered impact damper the contact time of impact and the deformation caused by impact are not negligibly small. The impulse momentum model is based on the assumption that collision is instantaneous, i.e. the contact time is zero, and that collision occurs between rigid bodies. The spring-damper model, however, can take both deformation and contact time into consideration despite the fact that it too makes use of the coefficient of restitution. It should be pointed out that even for a conventional impact damper the spring-damper model leads to good simulation, although the impulse momentum model matches the experiment results almost as well.

In terms of the simulation itself, the simulation with the impulse momentum model requires accurate timing of the collisions. Missing a collision may lead to the failure of the simulation. For simulations with the spring-damper model, timing is not critical since it is automatically taken into account in the algorithm.

Using the simulation with the spring-damper model of impact, examples of parametric studies on SDOF and MDOF primary structures equipped with an impact damper have been performed. The results of the studies are in agreement with published results and the experimental results described in Chapters 5 and 6. This demonstrates the usefulness of the simulation as a predictive design tool for a vibro-impact system.

# Chapter 8

# Experimental Investigation of a Hybrid Pendulum Impact Damper and a Twin-unit Impact Damper

Introduction: Presented in this chapter are the results of preliminary experiments on a hybrid pendulum impact damper (HPID) (i.e. a combination of a tuned pendulum mass damper (TPMD) and an impact damper) and on a twin-unit impact damper (TUID). An initial insight into the possible benefits and application of HPID or TUID for vibration control of structures is offered. The intention of both systems is to improve control effect whilst reducing accelerations of impact.

## 8.1 Experimental investigation of a hybrid pendulum impact damper

*8.1.1 HPID—a combination of a tuned pendulum mass damper with an impact damper*

Tuned mass dampers can effectively control a single mode of a structure (usually the first mode), which might be excited by wind loading for instance. For higher intensity excitation over a wider frequency range such as that caused by earthquake loading, an impact damper has been shown to be effective, but at the cost of high accelerations and impact forces. The purpose of these experiments is to investigate a combination of both systems to control the dynamic response of the structure. The combined system will be referred to as a hybrid pendulum impact damper (HPID). Using the MDOF structure described in section 4.1, a pendulum mass damper has been designed and tuned to control the first mode and an impact damper is used to control the system when the vibration of the structure becomes severe. The combined system is shown in Figure 8.1. It can be seen that the same mass is used for the tuned mass damper and impact damper. When the stops are set far from each other and no collision between the moving damper mass and the stops occur, the HPID is reduced to a tuned pendulum mass damper (TPMD). The TPMD is designed according to the equation described in section 3.5:

$$R = r + \frac{5g}{28\pi^2 f_1^2} \tag{8.1}$$

where $R$ is the radius of the orbit, as shown in Figure 8.2, $r$ is the radius of the rolling ball, $g$ is the acceleration due to gravity and $f_1$ is the first natural frequency of the test structure, i.e. the TPMD is tuned to the fundamental frequency of the primary structure.

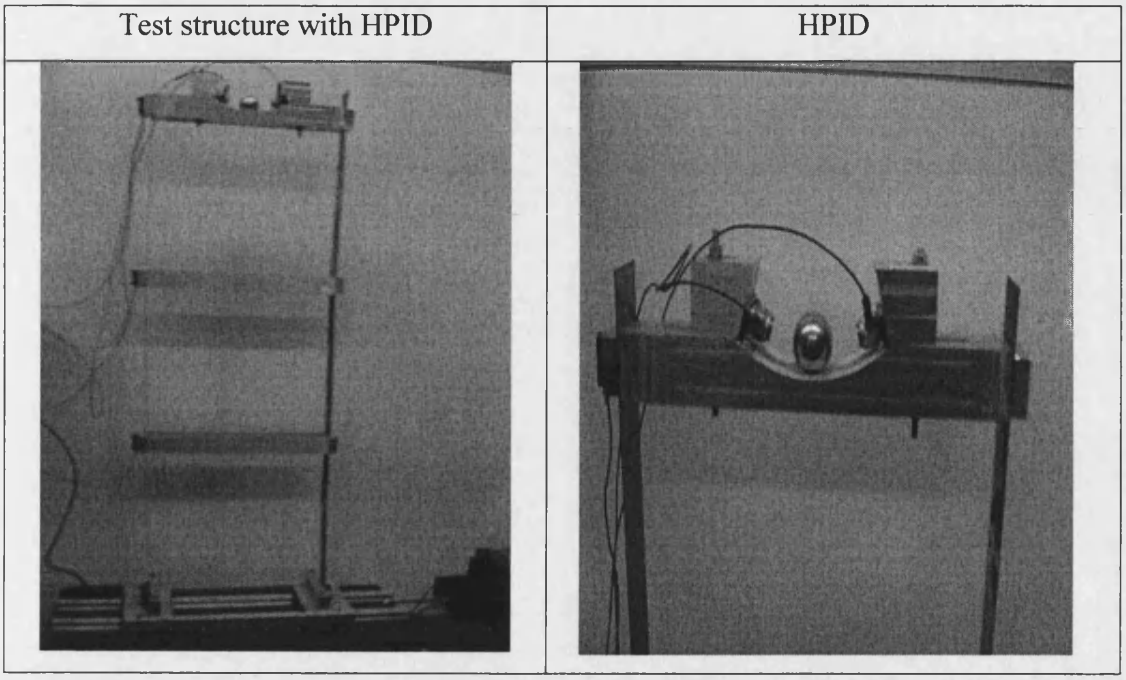


Figure 8.1 HPID—a combination of a tuned pendulum damper with an impact damper

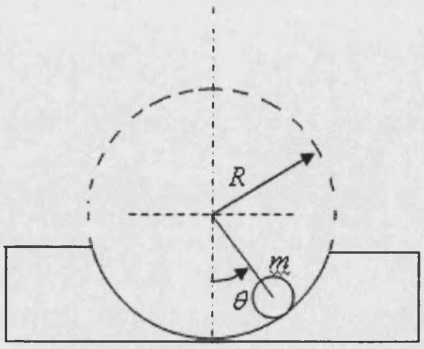


Figure 8.2: Tuned pendulum mass damper

For the system using the medium ball of radius $r = 15mm$ and with a fundamental natural frequency of $f_1 = 1.79\,Hz$, the radius of the pendulum is $R = 70mm$. A specially shaped top storey beam was made for this purpose.

*8.1.2 Experimental results*

*8.1.2.1 free vibration*

Free vibration experiments were performed either by releasing the structure from an initial displacement or by striking the primary structure to provide an impulse input. The base of the structure, connected to the shaking table, is fixed rigidly and statically. The response of each storey of the structure was measured using the accelerometers. This procedure was repeated with the HPID, with the TPMD alone and with no damper for each case investigated.

8.1.2.1.1 *initial displacement excitation*

The primary structure is excited by releasing from an initial displacement. The mass ratio used in the experiments is $\mu = 0.08$ and the clearance is $d = 20mm$. The time histories of the acceleration response with the TPMD, the HPID and without a damper are presented in Figure 8.3. The corresponding PSDs of the acceleration responses, focusing around each natural frequency, are presented in Figure 8.4. The acceleration peaks caused by collisions when the HPID is in operation can be observed for the top storey in Figure 8.3. From Figure 8.4 it can be seen that for the first mode of each storey, the control effect of the HPID is better than that of the TPMD, although both show a similar degree of control effect. The control effect of the HPID on the third mode is significantly better than that of the TPMD. For the second mode, the control effect of TPMD is slightly detrimental whilst that of the HPID is, typically, much worse. It should be pointed out that although the TPMD is tuned to the first frequency of the primary structure it affects the other modes of the structure as well due to the change in frequency response of the complete system and the non-linear behaviour of the damper (since the angular displacement, $\theta$, is not necessarily small as assumed in the linear theory).

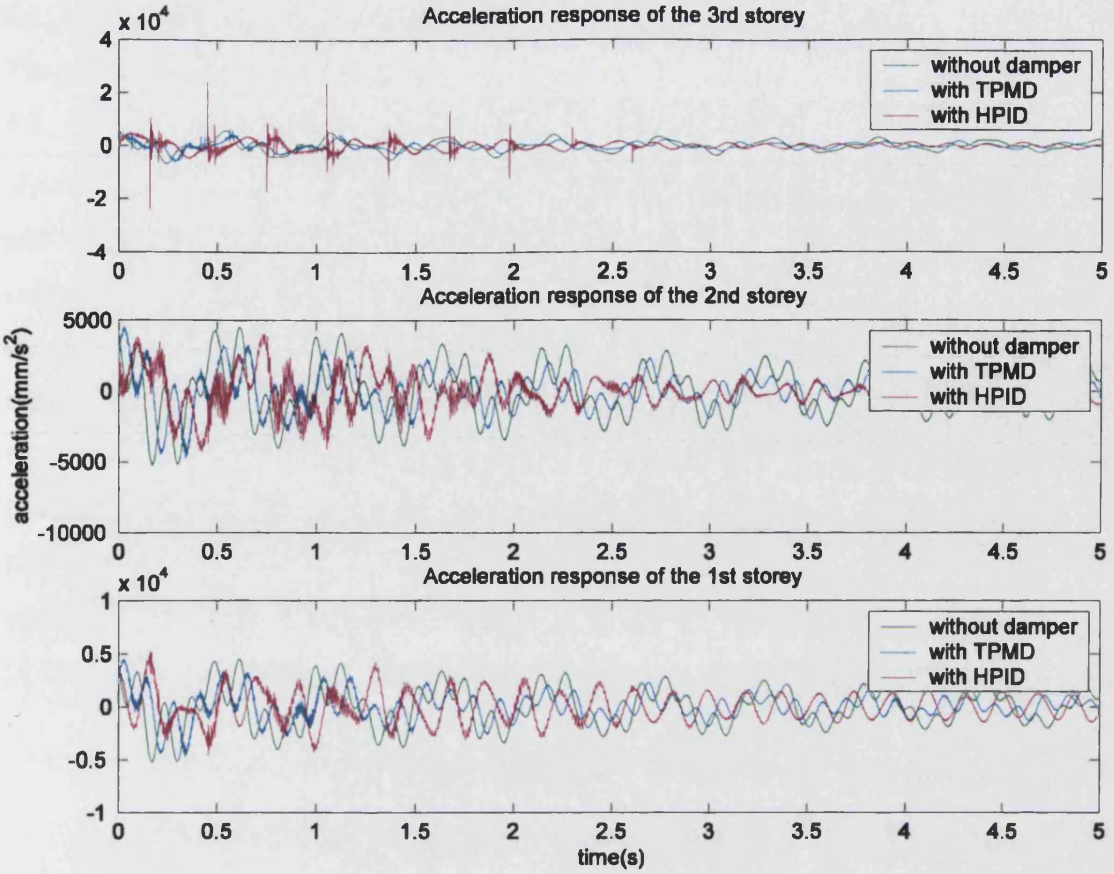


Figure 8.3: Time history of acceleration response (initial displacement excitation)

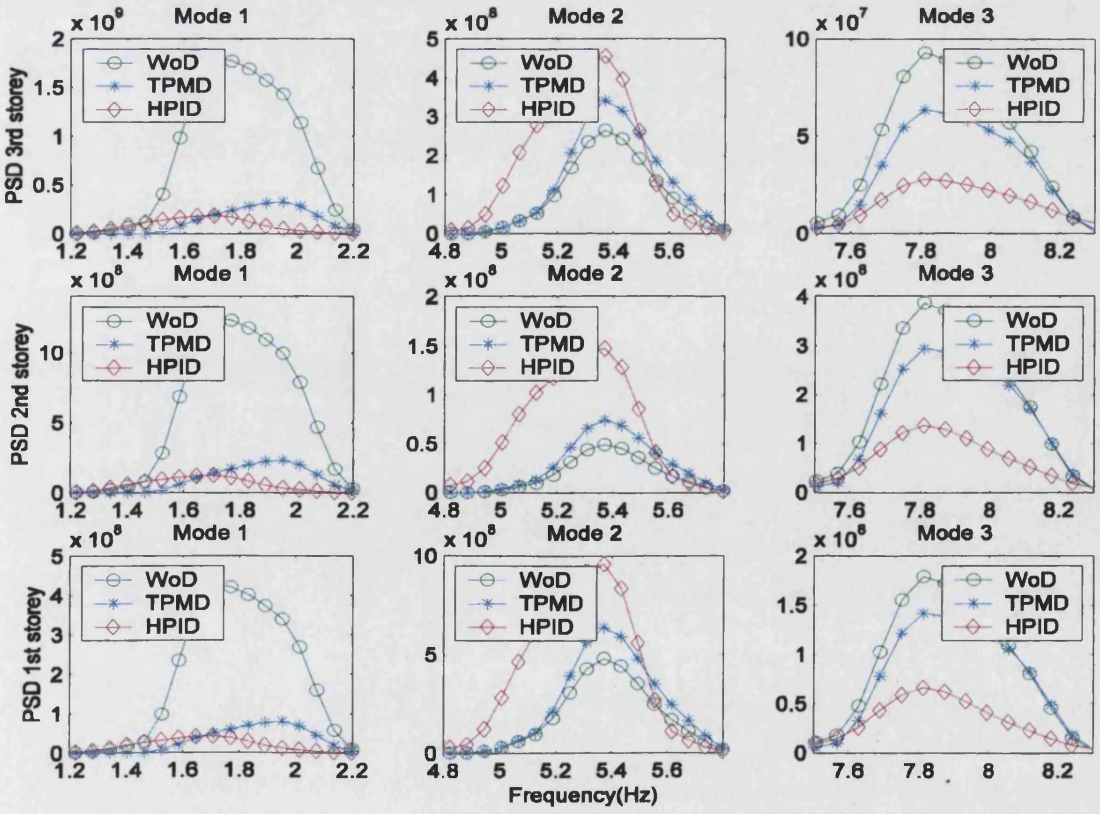


Figure 8.4 PSDs of acceleration (initial displacement excitation)

8.1.2.1.2 *initial velocity excitation—striking at A*

The primary structure is excited by striking it at $A$, the first storey, as shown in Figure 4.1. Again the mass ratio used in the experiments is $\mu = 0.08$ and the clearance is $d = 20mm$. The time histories of the acceleration response with the TPMD, the HPID and without a damper are presented in Figure 8.5. The acceleration peaks caused by collision when the HPID is in operation can be observed. There are only two such peaks since the excitation is not strong. The corresponding PSDs of the acceleration responses are presented in Figure 8.6. From Figure 8.6 it can be seen that for the first mode of each storey, again, the control effect of the HPID is better than that of the TPMD even though only two impacts occurred. For the second and third modes, the control effect of the TPMD is detrimental whilst the HPID showed control of all modes except the second mode of the second storey.

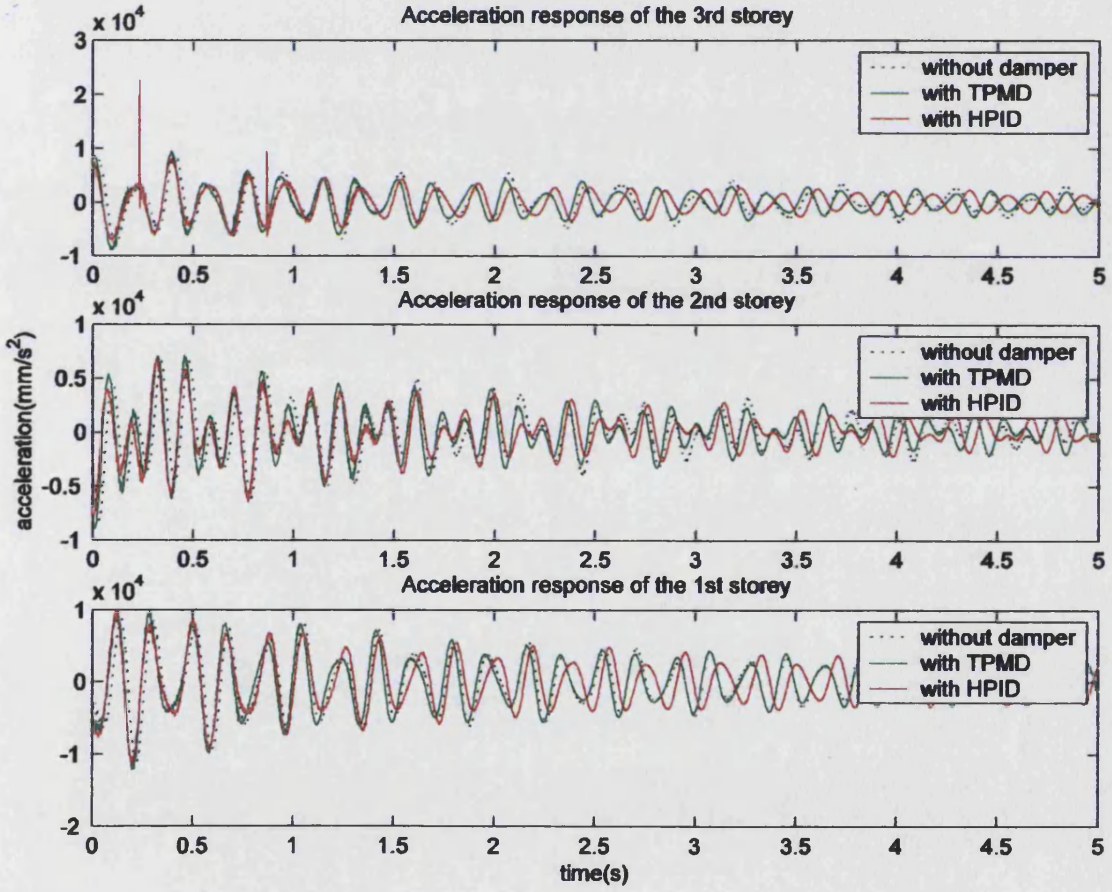


Figure 8.5: Time history of acceleration response (excitation by striking at $A$)

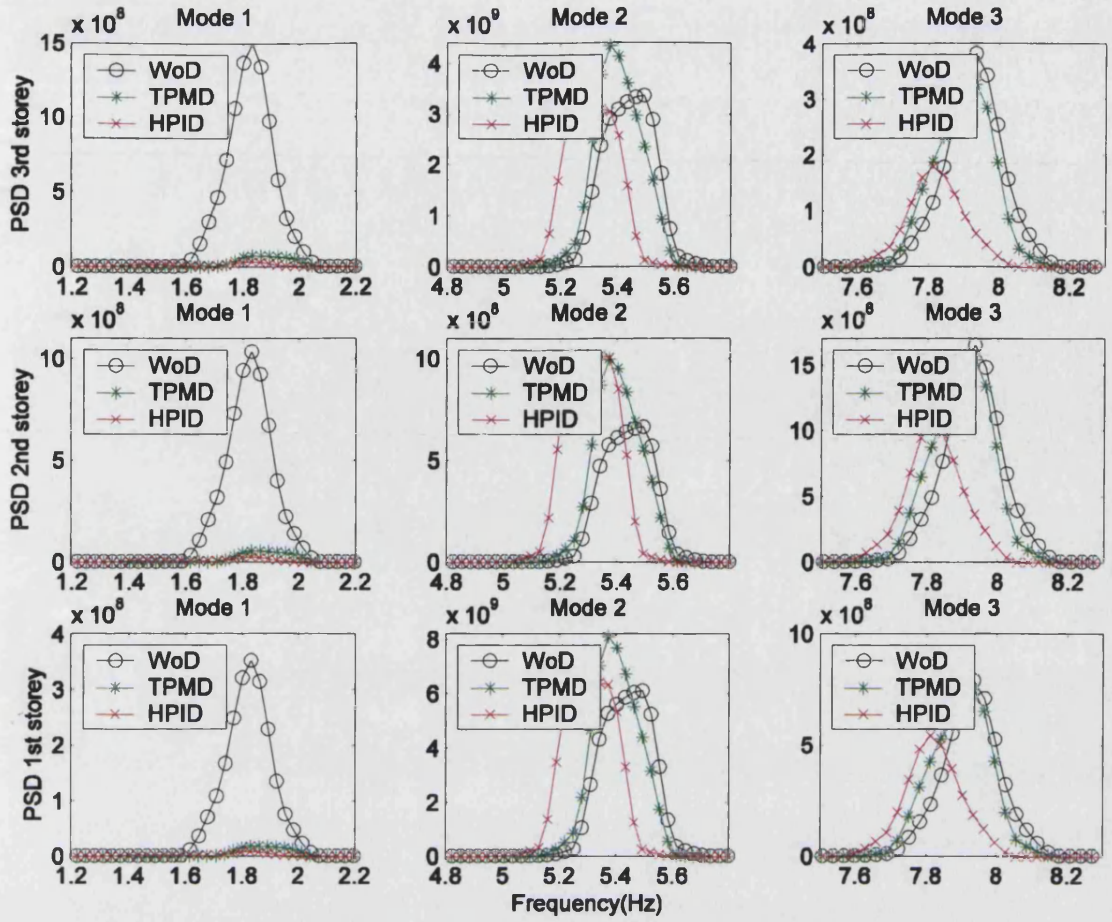


Figure 8.6: PSDs of acceleration response (excitation by striking at *A*)

*8.1.2.2 forced vibration*

*8.1.2.2.1 base sinusoidal excitation*

For forced vibration experiments, the structure is excited with base motion using the shaking table onto which the test structure is fixed. Experiments are first carried out with a sine dwell excitation. The frequency of the excitation is chosen to be the first natural frequency of the test structure, i.e. $f = f_1 = 1.79Hz$. The time histories of acceleration response without a damper, with the TPMD and with the HPID are presented in Figure 8.7 and the corresponding PSDs of the acceleration response are shown in Figure 8.8. From Figure 8.7 the acceleration peaks caused by collisions when the HPID is in operation can be observed. It can also be observed that the acceleration response curve is not smooth and small peaks occur when TPMD is in operation. This might be caused by jumping of the mass as it rolls around the arc. Figure 8.8 shows that both the TPMD and the HPID can produce very good control in this case, with slightly better control effect for the HPID, although not significant considering the amount of impacts occurring.

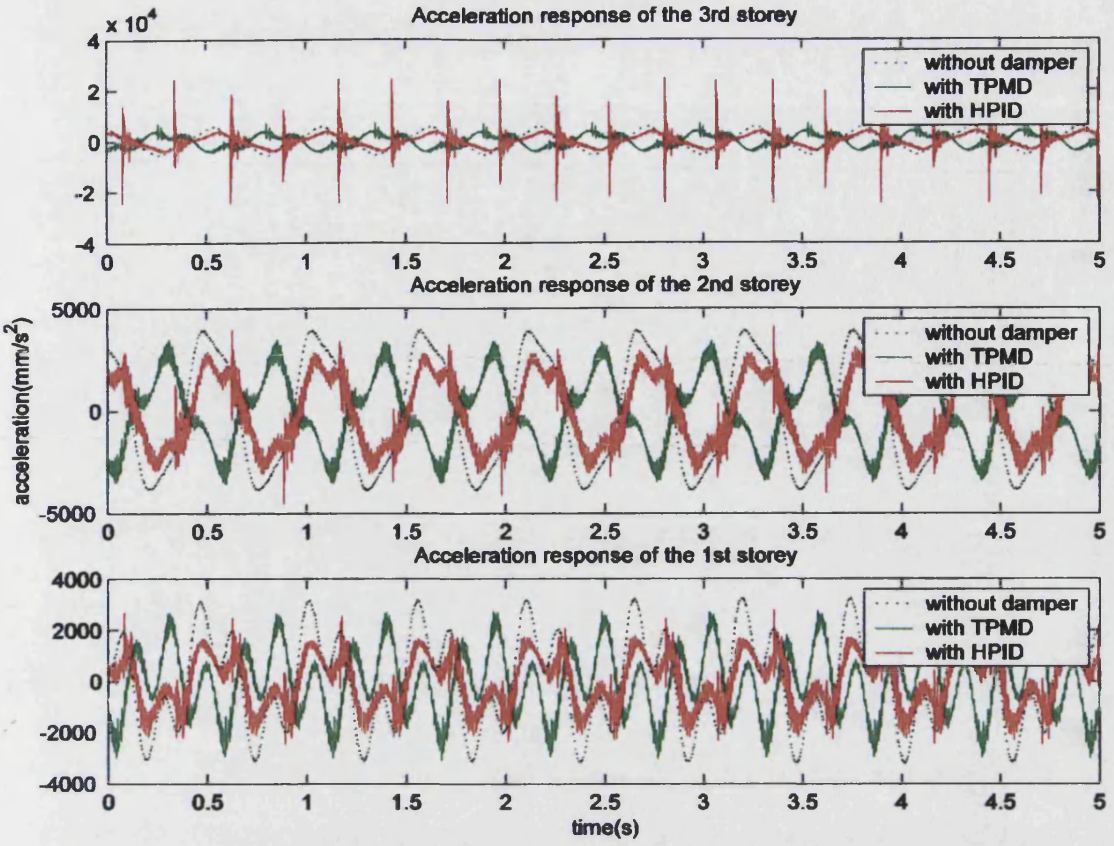


Figure 8.7: Time history of acceleration response (base sinusoidal excitation)

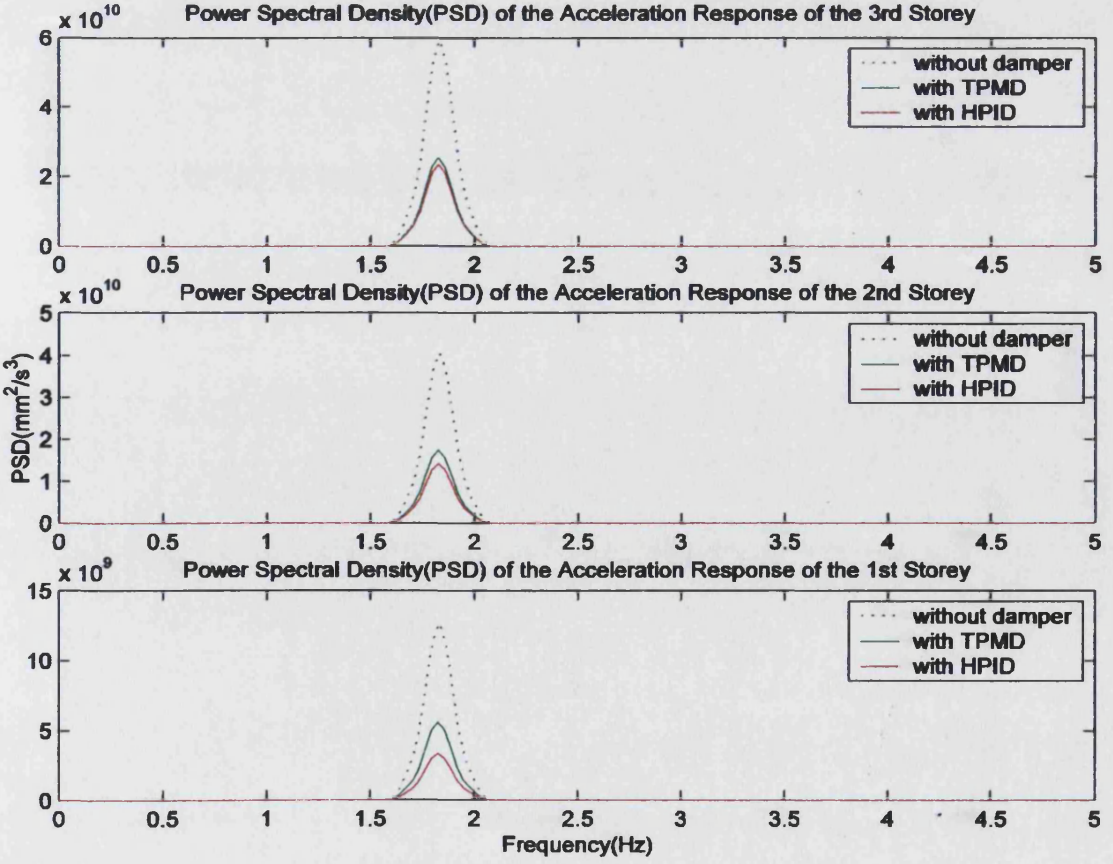


Figure 8.8: PSDs of acceleration response (base sinusoidal excitation)

To study the effect of excitation frequency on the performance of the TPMD and the HPID, experiments are carried out for a series of sine dwell excitation frequencies either side of the first natural frequency, $f_1 = 1.79Hz$, i.e. taking $f = 0.7f_1$, $0.8f_1$, $0.9f_1$, $f_1, 1.1f_1, 1.2f_1$. For the tests, the excitation amplitude was $A = 5mm$, the mass ratio of the HPID is $\mu = 0.08$ and clearance is $d = 15mm$. The peak value of the PSD of acceleration response at the excitation frequency when with the TPMD, with the HPID and without a damper are obtained. The results are shown in Figure 8.9. It can be seen that TPMD produces good control only when the frequency ratio lies between *0.9* and *1*. Outside of this range, the control effect of the TPMD is either not significant or detrimental. The HPID shows substantial control effect for the frequency ratio range between *r=0.9* and *r=1.2*. However, for lower frequencies the control effect is more detrimental than the TPMD, as demonstrated in chapter 6.

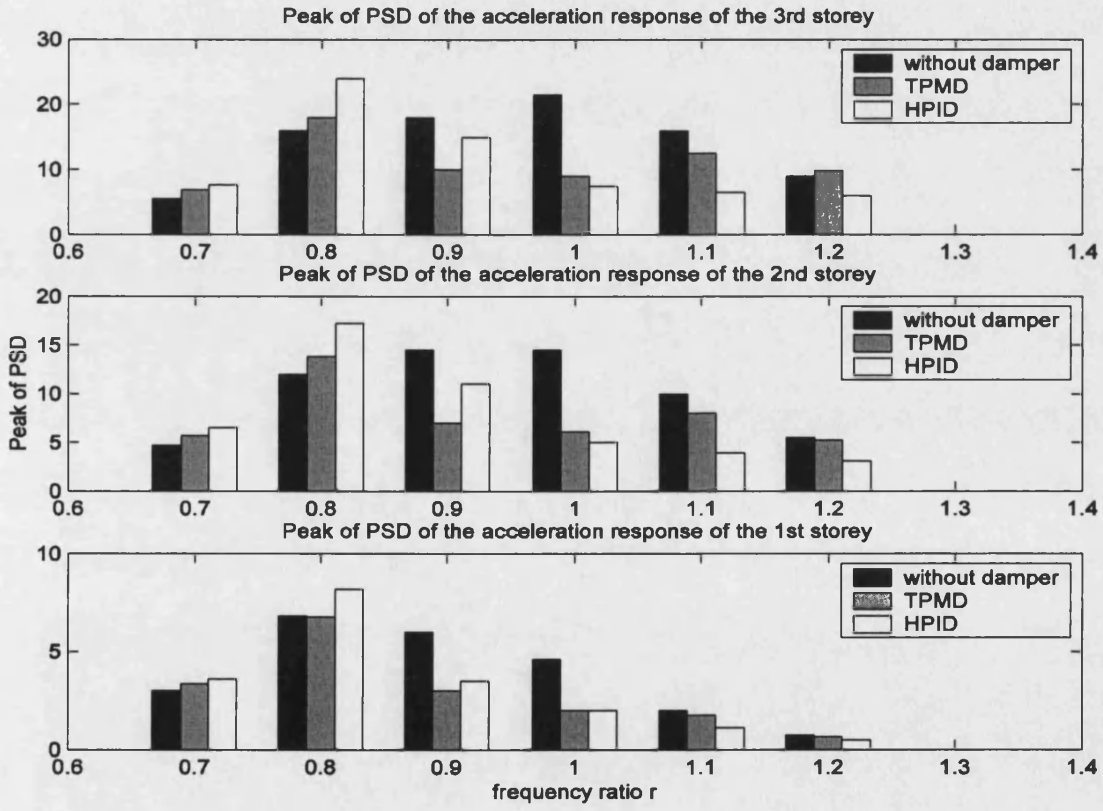


Figure 8.9: Effect of excitation frequency (base sinusoidal excitation)

*8.1.2.2.2 base sinusoidal sweep excitation*

Experiments with sinusoidal sweep base excitation were also performed. The sweeping range is *0.1* to *10 Hz* (encompassing the three natural frequencies of the structure) and

the sweep rate is *0.1Hz/s*. The mass ratio of the HPID is $\mu = 0.08$ and the clearance is *d=12mm*. The time histories of the acceleration response when without a damper, with the TPMD and with the HPID are presented in Figure 8.10. It can be seen that when the HPID is in operation, collisions only occur when exciting the first natural frequency of the test structure. There are no collisions following this period even though the clearance is small, since the TPMD is tuned to the first natural frequency of the primary structure and the motion of the rolling ball becomes very weak when the excitation frequency is higher than the first natural frequency of the structure. This can also be seen from the corresponding PSDs of the acceleration response shown in Figure 8.11.

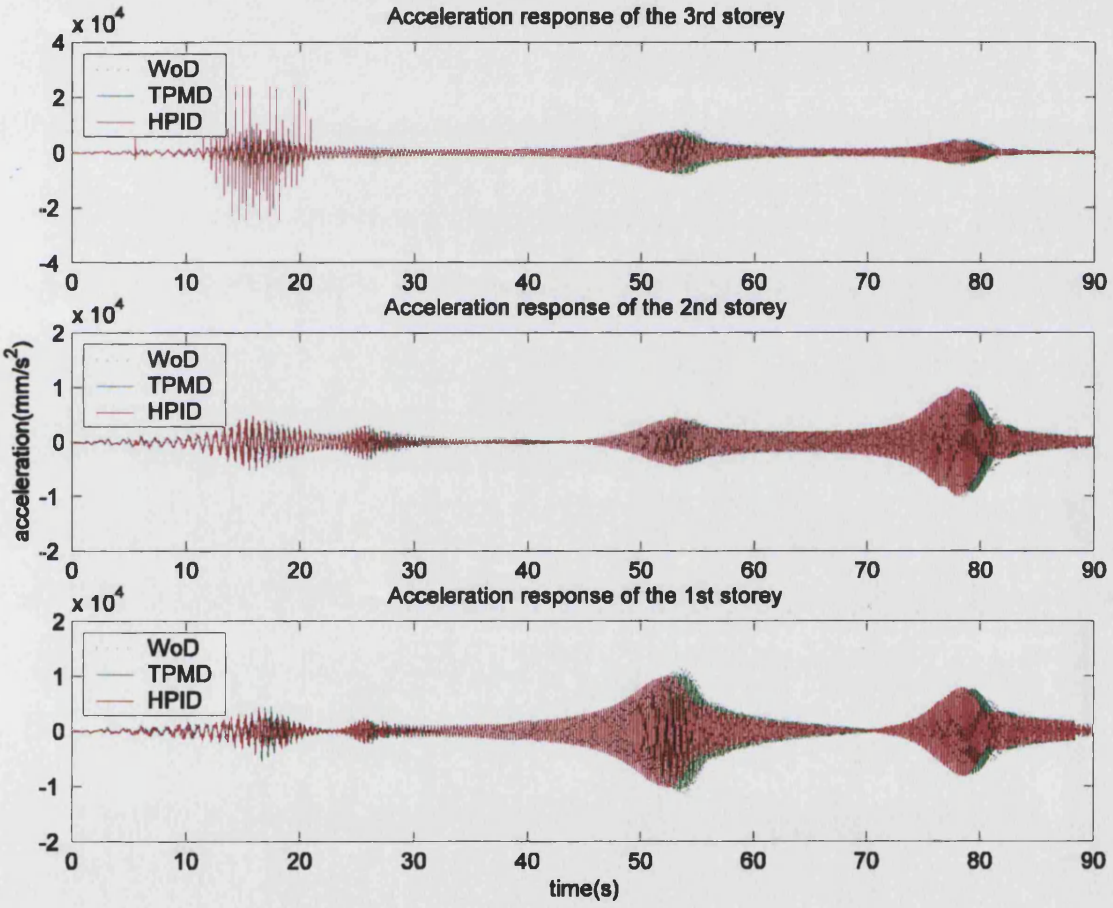


Figure 8.10: Time history of acceleration response (base sinusoidal sweep excitation)

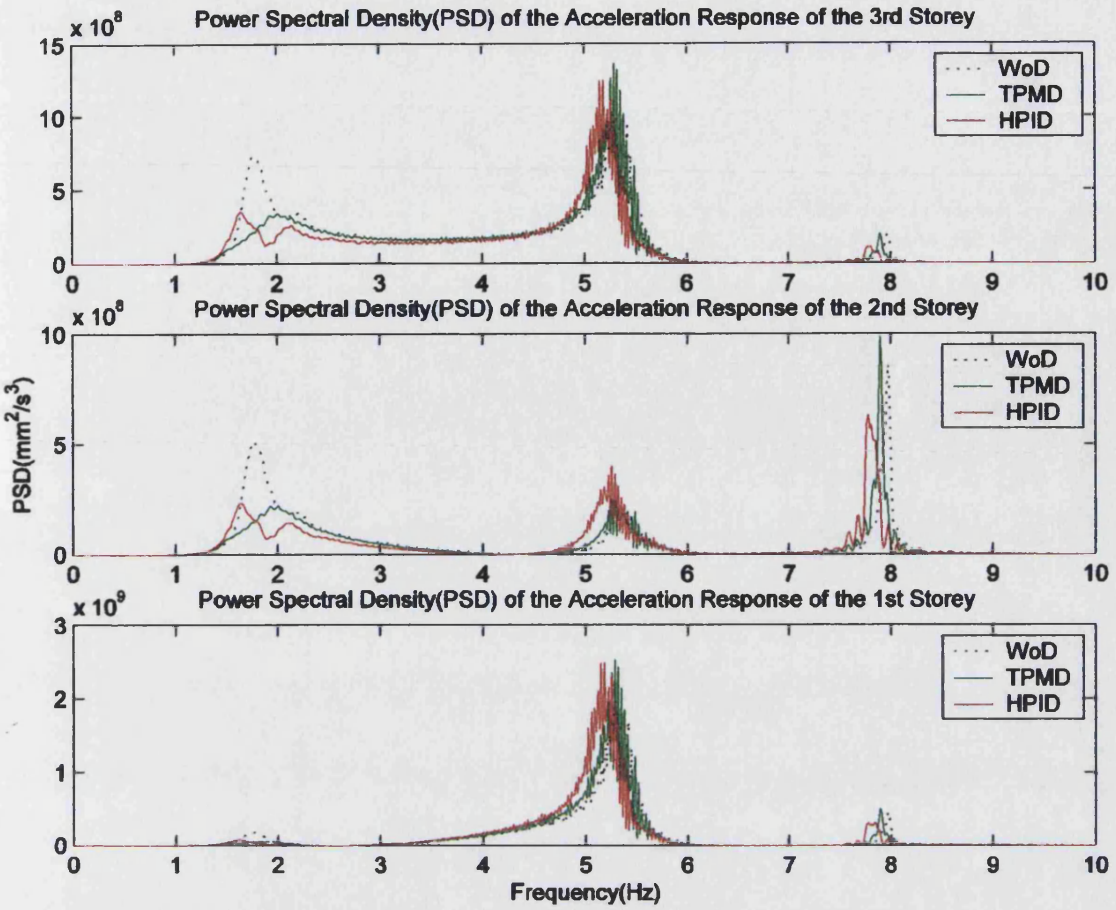


Figure 8.11: PSDs of acceleration response (base sinusoidal sweep excitation)

The preliminary experimental investigations presented above show that for the first mode of the test structure the HPID can always achieve better control than the TPMD. Therefore, the HPID might be a good choice for the vibration control of a SDOF primary structure allowing the TPMD to operate during weak excitation and to combine with an impact damper during more severe excitation. The behaviour of the HPID on the control of higher modes becomes more complicated with the possibility of significant detrimental effect. Therefore it may not be a good choice for the control of MDOF structure but further investigations are required.

There are two aspects of the system behaviour which harm the performance of the HPID. Firstly, unlike the case of a conventional impact damper where the direction of the impact force is parallel to the direction of motion of the structure, the direction of the impact force of the HPID acts at an angle so that not all the energy is effectively transferred. Secondly, and more significantly, since the mass must roll up a slope of the arc, the velocity at impact is lower than for a conventional impact damper and,

therefore, less momentum is exchanged. This is particularly the case when the vibration frequency is away from the frequency that the TPMD is tuned to and often no impact occurs even with a small clearance.

## 8.2 Experimental investigation on a twin-unit impact damper (TUID)

*8.2.1 Twin-unit impact damper*

Another possible means of reducing the detrimental effect of a single unit impact damper, i.e. the high contact force and associated high accelerations and high noise level, whilst retaining its vibration control performance is by replacing the single unit impact damper with multiple impact dampers with the same total mass. A twin-unit impact damper, as shown in Figure 8.12, has been designed, to experimentally investigate and compare it with an equivalent single unit impact damper. The structure tested is the MDOF system described in section 4.1. The parameters of the impact masses of the twin-unit impact damper and that of the single unit impact damper are given in Table 8.1. The mass ratios of the two systems are similar.

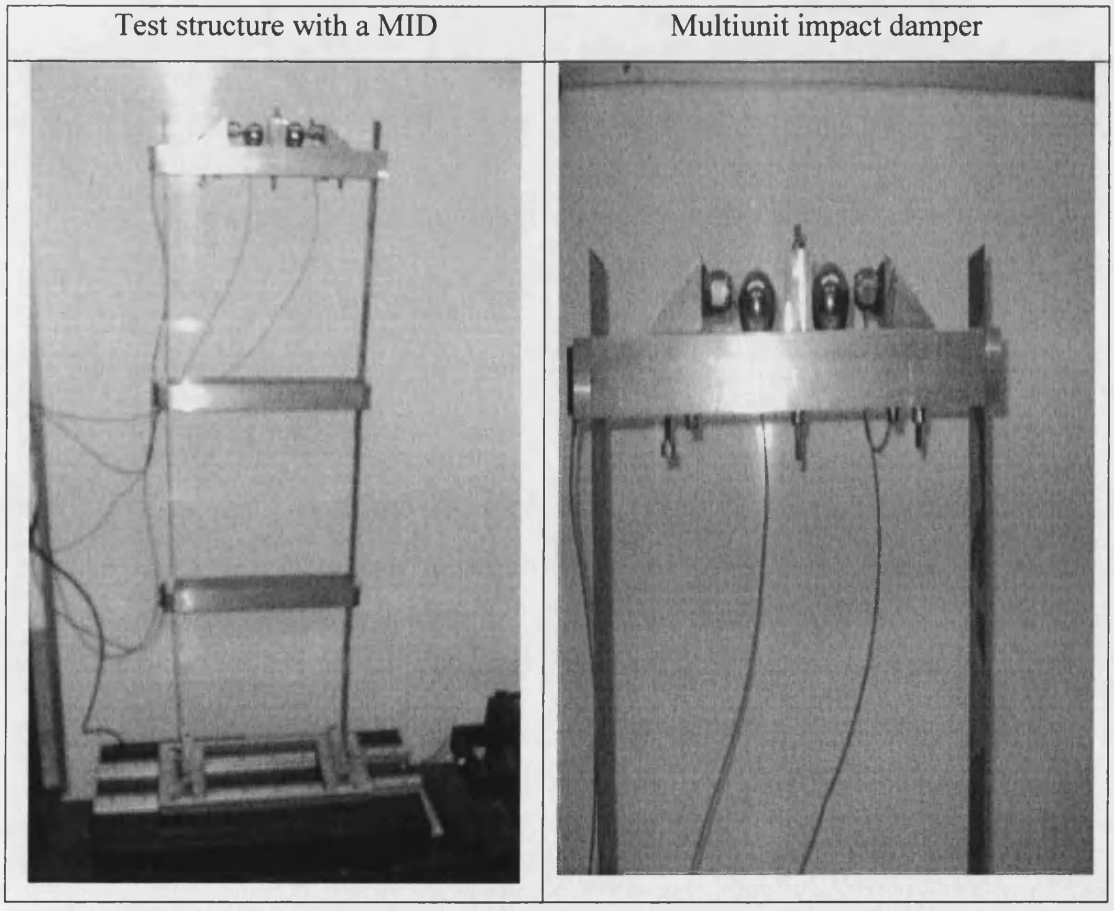


Figure 8.12: Twin-unit impact damper and the test structure

Table 8.1: Parameters of the impact mass

| | Single unit impact damper | Twin-unit impact damper | |
|---|---|---|---|
| | | Unit 1 | Unit 2 |
| Impact mass size | Big ball 40mm diameter | Medium ball 30mm diameter | Medium ball 30mm diameter |
| Mass | $m=0.26kg$ | $m_1 = 0.11kg$ | $m_2 = 0.11kg$ |
| Mass ratio | $\mu = \frac{m}{M_3} = 0.194$ | $\mu = \frac{m_1 + m_2}{M_3} = 0.164$ | |

* $M_3 = 1.35kg$ is the mass of the third storey of the test structure

*8.2.2 Experimental results*

*8.2.2.1 free vibration*

The primary structure is excited by striking it at *A*, the first storey, as shown in Figure 4.1. For the single unit impact damper, the clearance is $d=15mm$. The clearances for the twin-unit impact damper are $d_1 = 15mm$ for both units. The time histories of the acceleration response with the single unit impact damper (SUID), with the twin-unit impact damper (TUID) and without a damper (WoD) are presented in Figure 8.13. The corresponding PSDs of the acceleration responses, focusing on each natural frequency, are presented in Figure 8.14. From Figure 8.13, it can be seen that the acceleration peaks produced with the SUID are higher than those produced by the TUID. However, the difference is not as significant as might be expected, although the difference in contact force per impact damper unit, as shown in Figure 8.15, is more significant. Comparing the control effect of the SUID and that of the TUID shown in Figure 8.14, it can be seen that, generally, there is no substantial difference between the control effect of the SUID and that of the TUID, except that the SUID achieves slightly better control of the second mode and is slightly more detrimental for the third mode. Both achieve excellent control of the first mode.

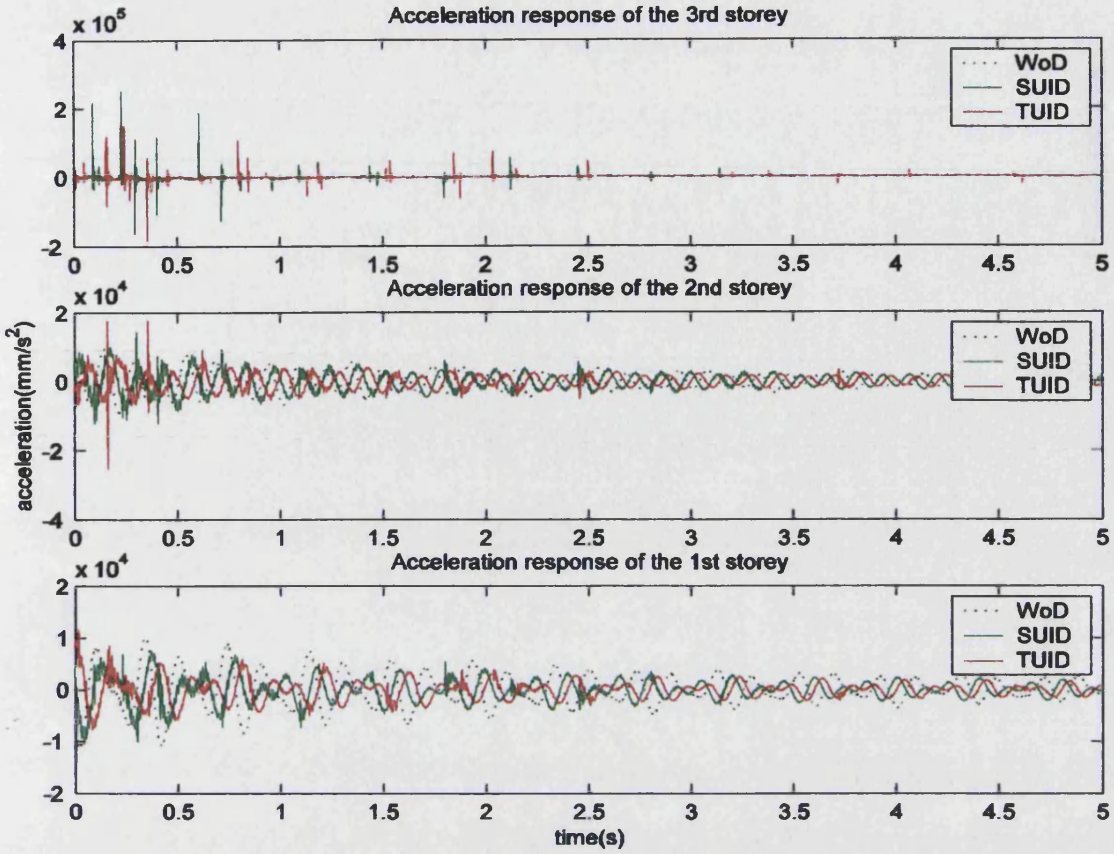


Figure 8.13: Time history of acceleration response (free vibration)

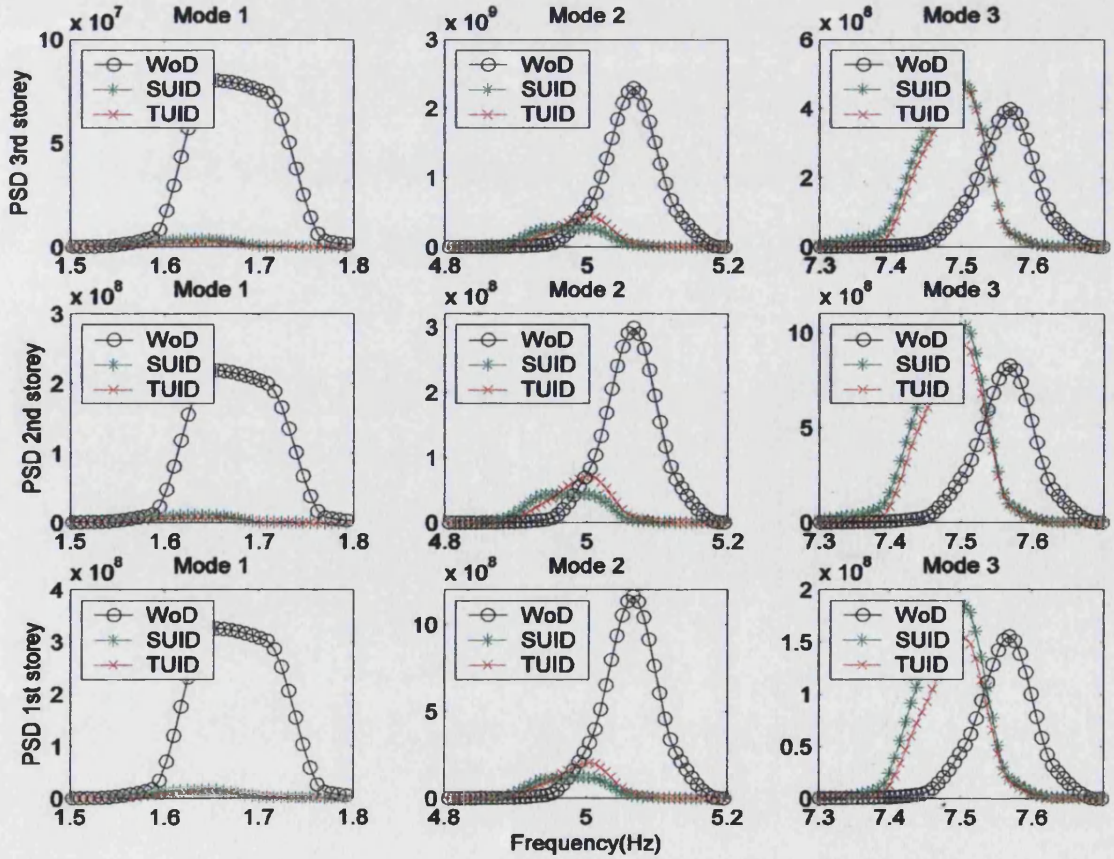


Figure 8.14: PSDs of acceleration response (free vibration)

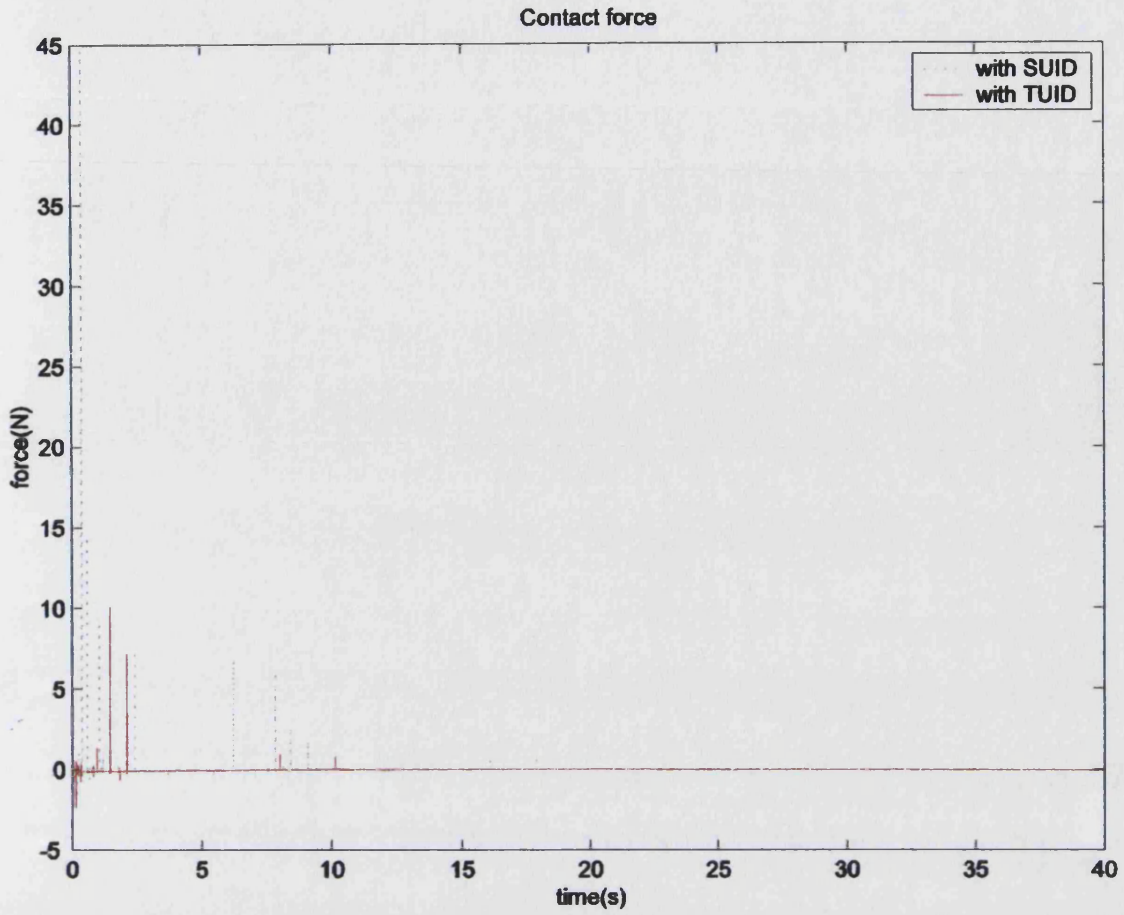


Figure 8.15: Contact force of SUID and TUID

*8.2.2.2 forced vibration—base sinusoidal excitation*

Forced vibration of the structure was achieved by base motion using the shaking table onto which the test structure was fixed. First experiments are under sine dwell excitation. The frequency of the excitation is first chosen to be the first natural frequency of the test structure, i.e. $f = f_1 = 1.65Hz$. The clearance used is $d=15mm$ for both the SUID and the TUID. The time histories of the acceleration response without a damper, with the SUID and with the TUID are presented in Figure 8.16 with the corresponding PSDs of the acceleration response shown in Figure 8.17. Figure 8.16 shows that the acceleration peaks caused by collisions with the SUID are no higher than those with the TUID, although the contact force of the SUID is obviously higher than that of a single unit of the TUID, as shown in Figure 8.18. Therefore, replacing the SUID with an equivalent TUID can not reduce the acceleration peaks. Figure 8.17 reveals that for the first and second storey, the control effect of the SUID is only slightly better than that of the TUID (even though the mass ratio of the SUID is a little higher than that of the TUID). However, for the third storey, where the impact damper is located, the control effect of the TUID is better than that of the SUID.

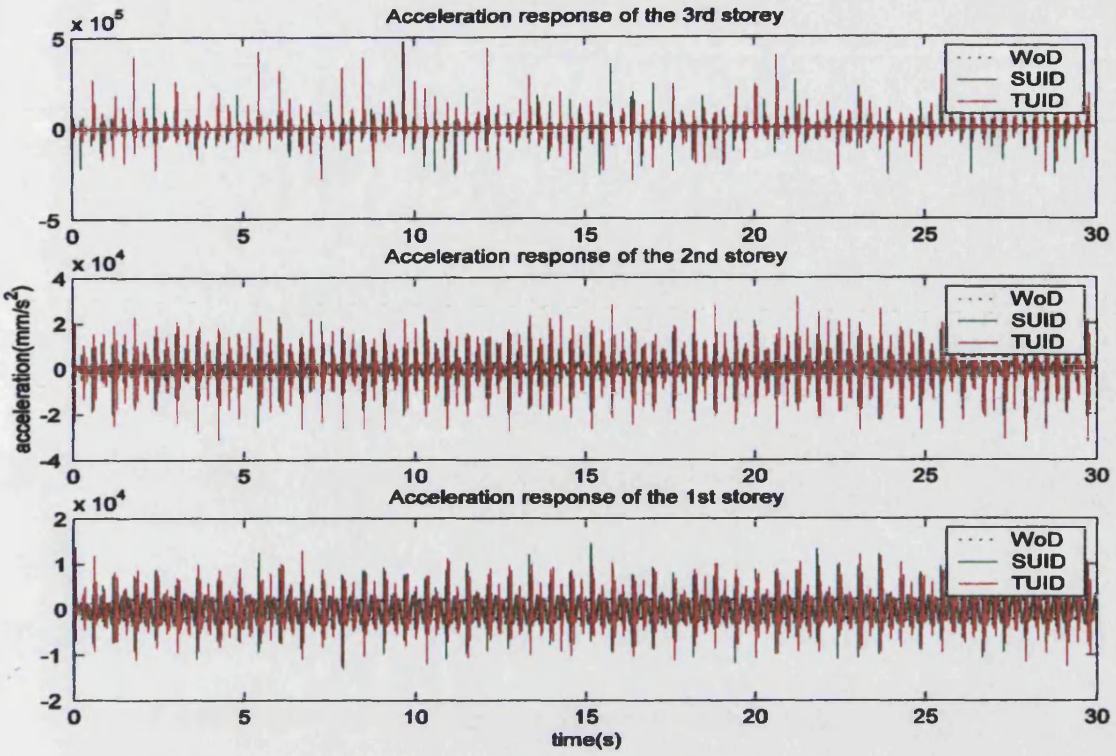


Figure 8.16: Time history of acceleration response (base sinusoidal excitation)

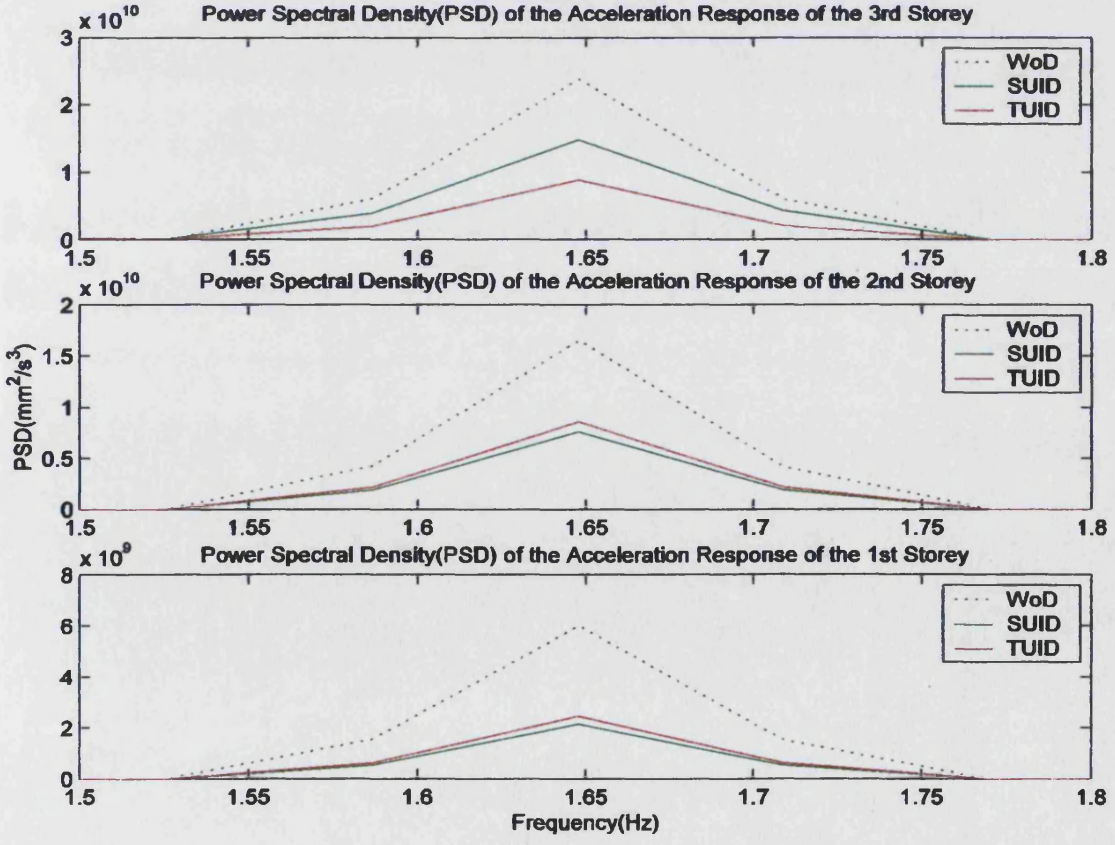


Figure 8.17: PSDs of acceleration response (base sinusoidal excitation)

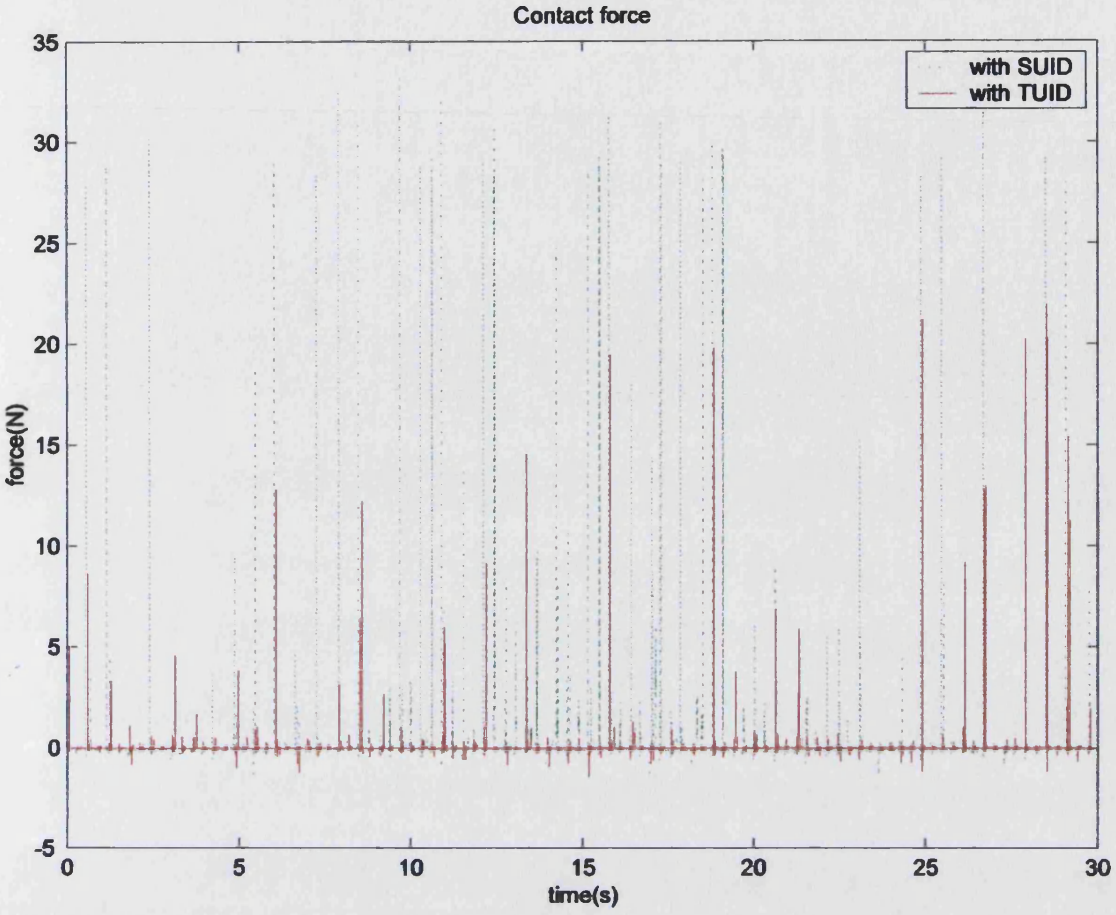


Figure 8.18: Contact force of SUID and TUID (base sinusoidal excitation)

Experiments have also been performed using excitation frequencies $f = 0.8f_1$ (lower than the first natural frequency) and $f = 1.6f_1$ (higher than the fist natural frequency) with all other parameters the same. The PSDs of acceleration responses when the excitation frequency is $f = 0.8f_1$ are shown in Figure 8.19. It can be seen that the control effect of the SUID and that of the TUID are equally detrimental. The PSDs of acceleration response when the excitation frequency is $f = 1.6f_1$ are shown in Figure 8.20. It can be seen that both the SUID and the TUID show a similar control effect, except at the third storey where the control of the TUID is a little better than that of the SUID. It must be pointed out that in both these two cases, the acceleration peaks produced by the TUID are, again, at about the same level as those produced by the SUID, although the time histories of the acceleration response are not presented here to save space.

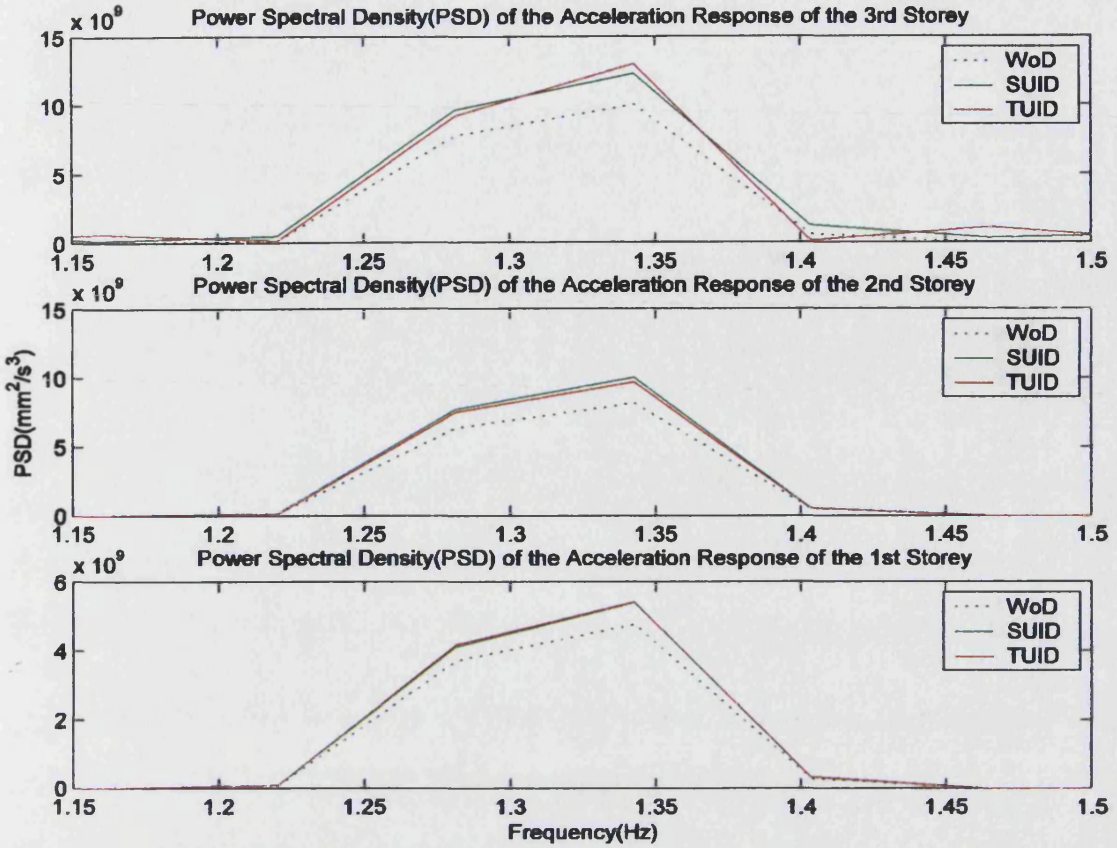


Figure 8.19 PSDs of acceleration response (base sinusoidal excitation $f = 0.8f_1$)

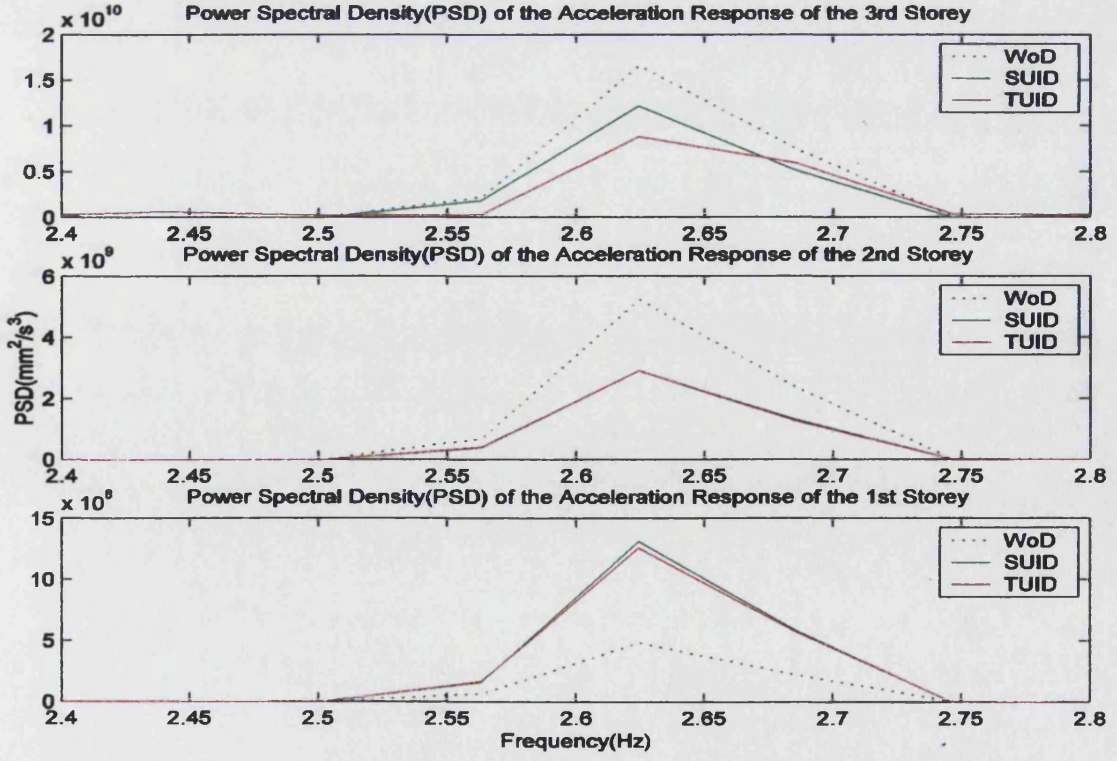


Figure 8.20: PSDs of acceleration response (base sinusoidal excitation $f = 1.6f_1$)

It seems that the TUID retains the main performance of an equivalent SUID, but does not reduce accelerations. This is perhaps to be expected where the same parameters are used for both systems. However, it may be that different parameters for each unit of the twin-unit impact damper may produce beneficial results. The following tests investigate this possibility.

*8.2.2.3 forced vibration—base sinusoidal sweep excitation*

In this case, experiments with sinusoidal sweep base excitation are performed. The sweep range is *0.1* to *10 Hz* and the sweep rate is *0.1Hz/s*. The performance of the TUID with the same clearance, with different clearances and with different mass ratios are studied and compared with that of the SUID.

*1)* SUID *d=15mm,* TUID $d_1 = d_2 = d = 15mm$

In this case the clearances are the same for both the SUID and the two units of the TUID. The time histories of the acceleration response without a damper, with the SUID and with the TUID are presented in Figure 8.21. It can be seen, again, that the acceleration peaks produced by the TUID are similar to those produced by the SUID. The difference in contact force for a single unit of the TUID is, as might be expected, about half that of the SUID as shown in Figure 8.22.

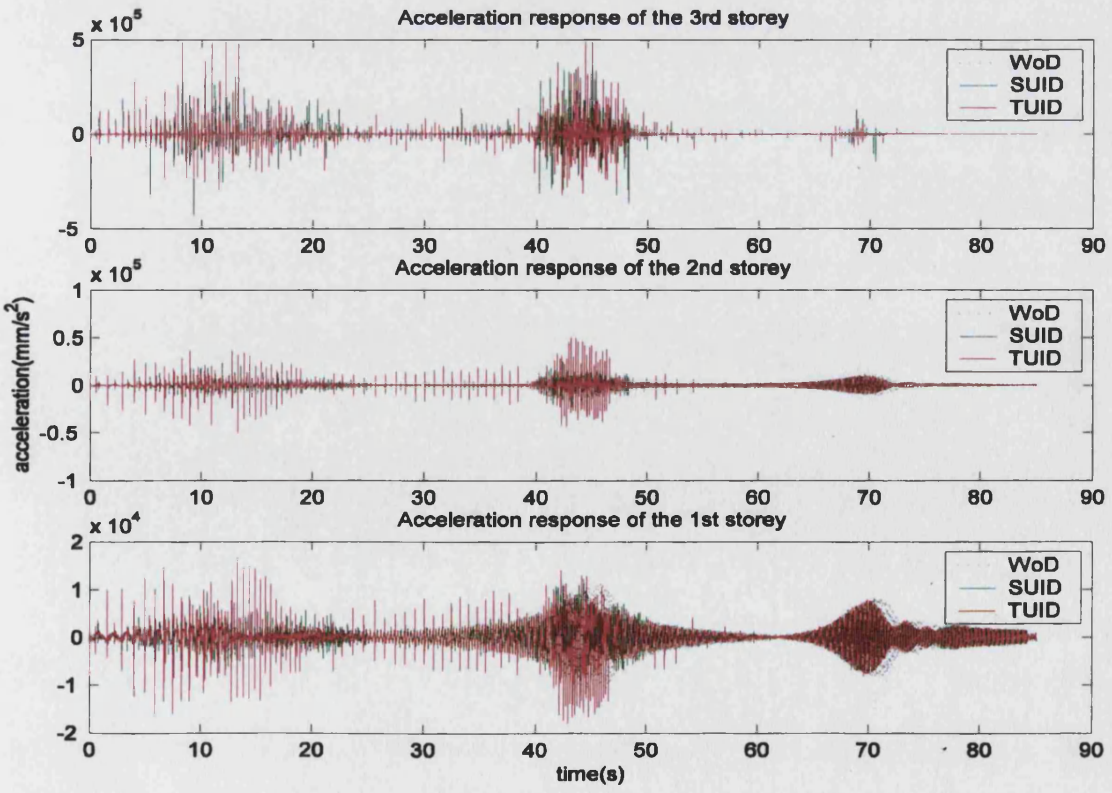


Figure 8.21: Time history of acceleration response (base sinusoidal sweep excitation)

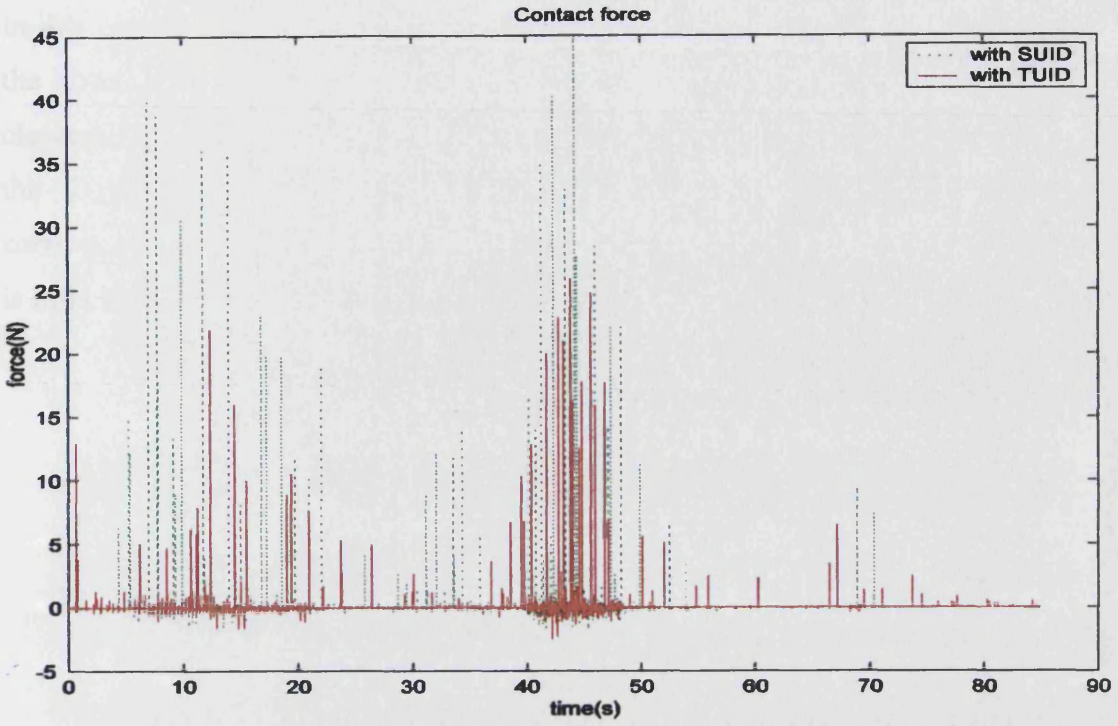


Figure 8.22: Contact force of SUID and TUID (base sinusoidal sweep excitation)

The corresponding PSDs of the acceleration response are shown in Figure 8.23. Again, there is no significant difference in the control effect between the SUID and the TUID.

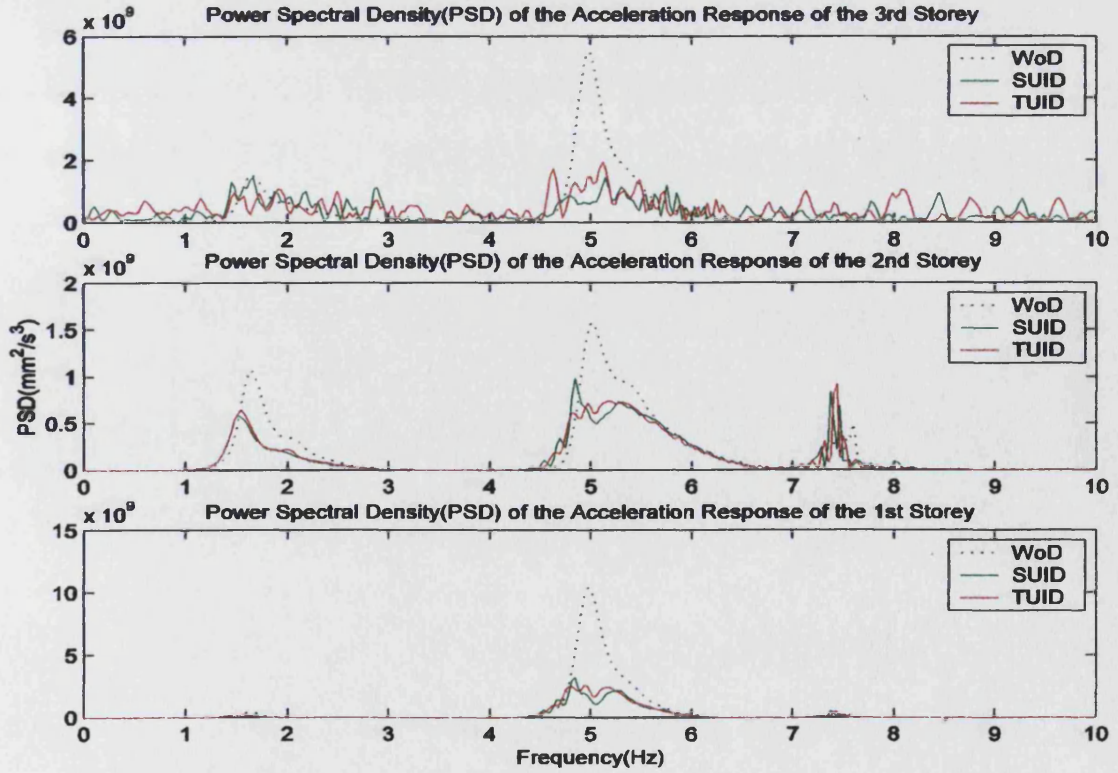


Figure 8.23: PSDs of acceleration response (base sinusoidal sweep excitation)

*2)* SUID $d$=*15mm,* TUID $d_1$ = *15mm*, $d_2$= *3mm*

In this case the two units of the TUID have different clearances. The time histories of the acceleration response are shown in Figure 8.24. It can be seen that, when the clearance of the two units are substantially different, the acceleration peaks produced by the TUID are, in general, no smaller than those produced by the SUID. The corresponding PSDs of the acceleration responses are given in Figure 8.25. Again, there is little difference between the control effect of the TUID and that of the SUID.

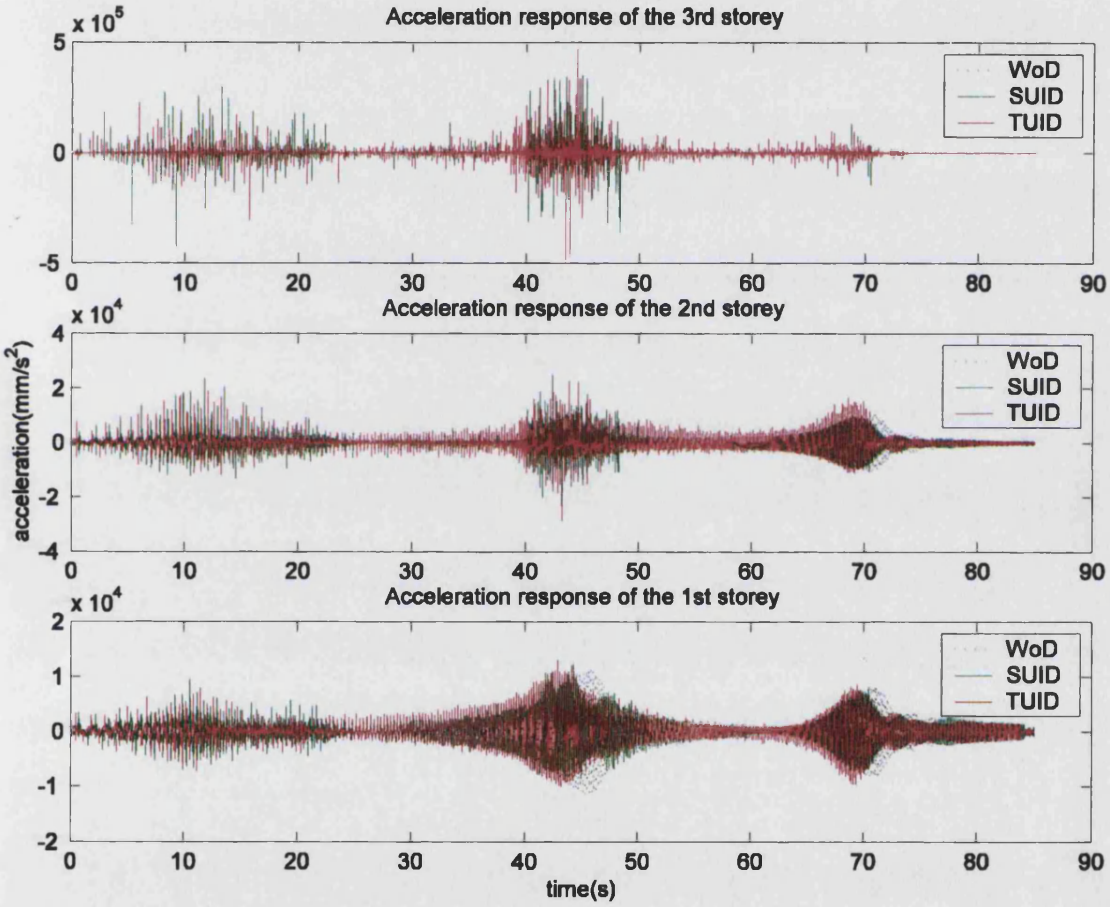


Figure 8.24: Time history of acceleration response (base sinusoidal sweep excitation)

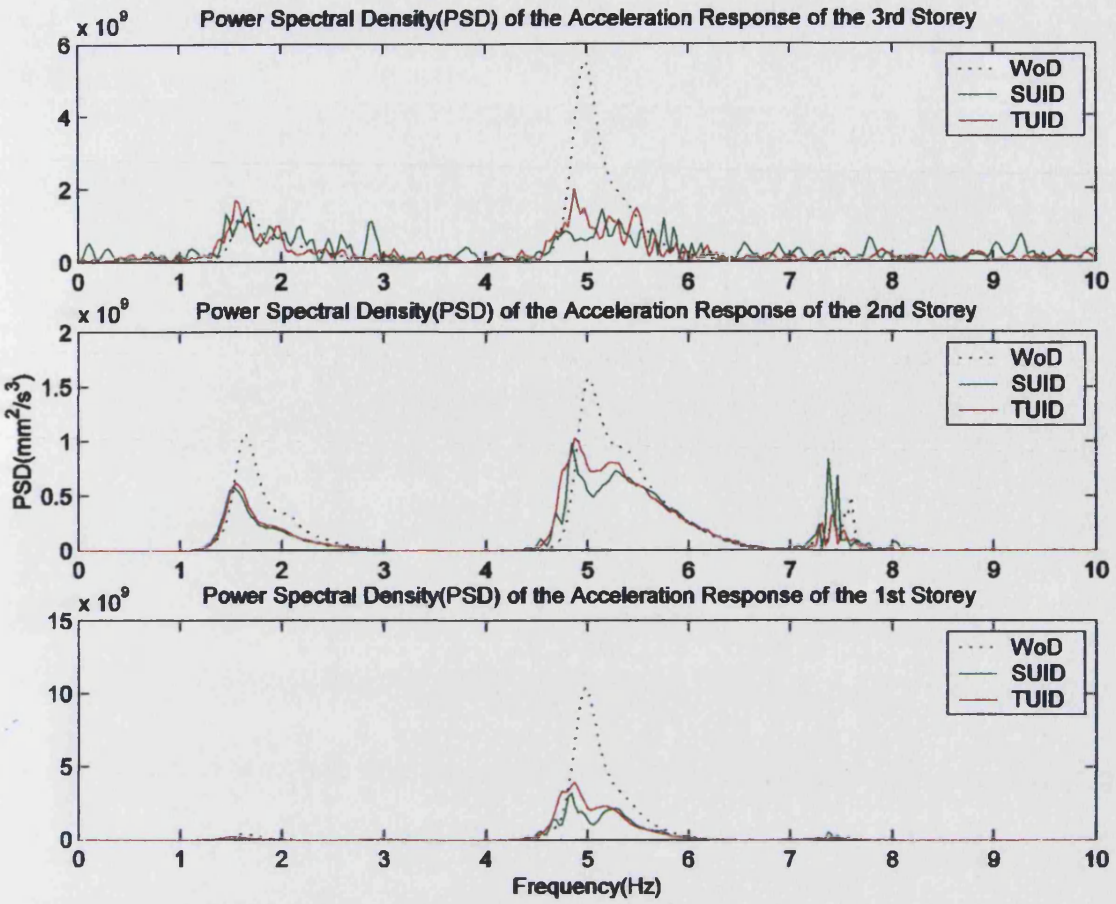


Figure 8.25: PSDs of acceleration response (base sinusoidal sweep excitation)

Experiments with:

a) SUID $d$=*15mm*, TUID $d_1 = d = 15mm, d_2 = 12mm$

b) SUID $d$=*15mm*, TUID $d_1 = d = 15mm, d_2 = 10mm$

c) SUID $d$=*15mm*, TUID $d_1 = d = 15mm, d_2 = 5mm$

were also performed. The results, not presented here to save space, show that in all cases the control effect of the TUID is not substantially different from that of the SUID. Similarly, the acceleration peaks produced by the TUID are, in general, no smaller than those produce by the SUID.

*3)* SUID $d$=*15mm*, $\mu = 0.192$ TUID $d_1 = d_2 = 15mm$, $\mu = 0.14$ (medium+ small ball)

In this case, the mass of each unit of the TUID are different. The time histories of the acceleration response are shown in Figure 8.26. Again, the acceleration peaks produced by the TUID are generally no smaller than that produced by the SUID, even though the mass ratio of the SUID is higher than that of the TUID. Figure 8.27 presents the corresponding PSDs of the acceleration response. It can be seen that for the third storey,

the control effect of the SUID is a little better than that of the TUID but, generally the difference in the control is not significant.

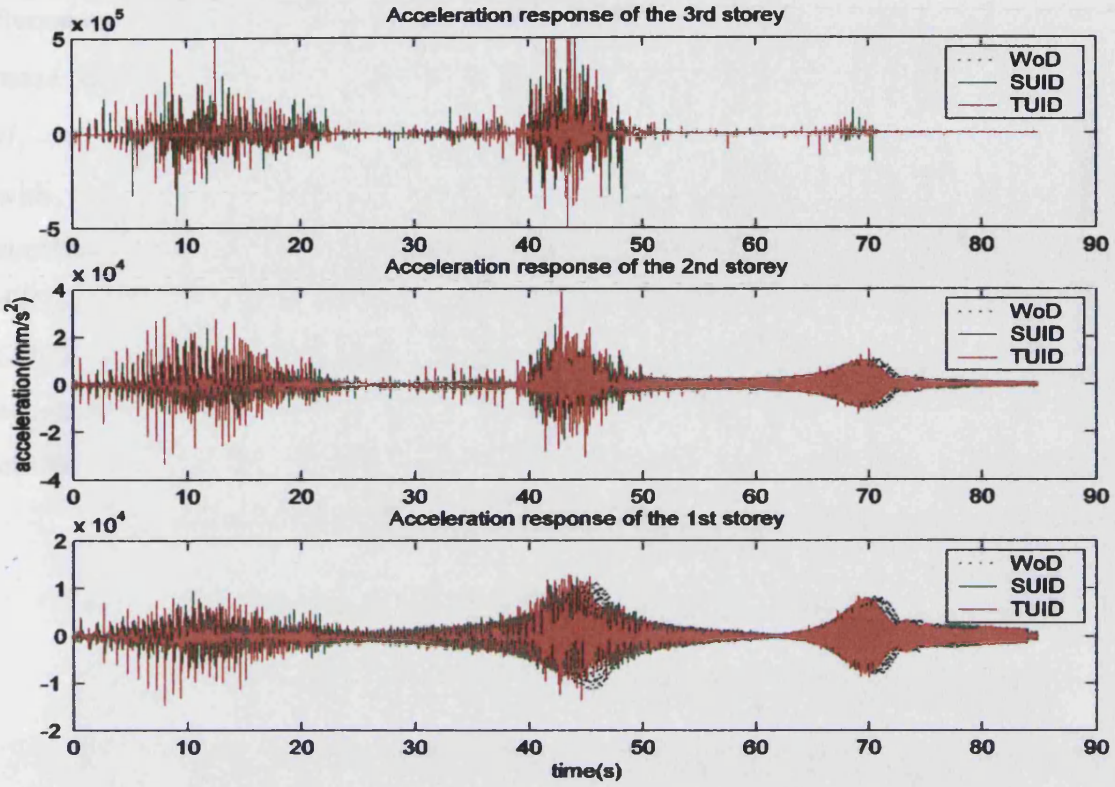


Figure 8.26: Time history of acceleration response (base sinusoidal sweep excitation)

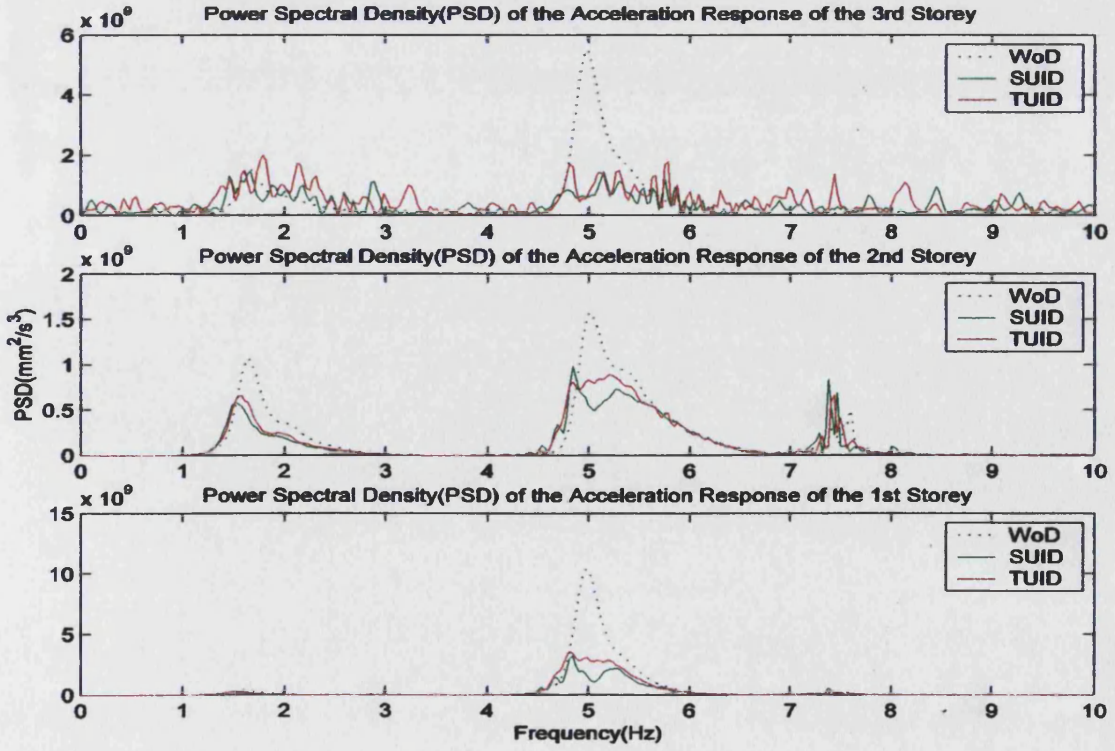


Figure 8.27: PSDs of acceleration response (base sinusoidal sweep excitation)

*8.2.2.4 forced vibration—base random excitation*

Finally, tests have been performed using random base excitation with a band-limited frequency content between 0 and 15 Hz. The mass ratio if the SUID is $\mu = 0.192$ and the mass ratio of the TUID is $\mu = 0.164$. The clearances of both the SUID and the TUID are $d_1 = d_2 = d = 15mm$. The time histories of the acceleration response without a damper, with the SUID and with the TUID are presented in Figure 8.28. As expected, the acceleration peaks produced by TUID are similar to those produced by the SUID. The difference in contact force produced by each unit of the TUID and that produced by the SUID, as shown in Figure 8.29, is not significant either. The corresponding PSDs of acceleration response are presented in Figure 8.30. It can be seen that the control effect of the TUID is approximately the same as that of the SUID.

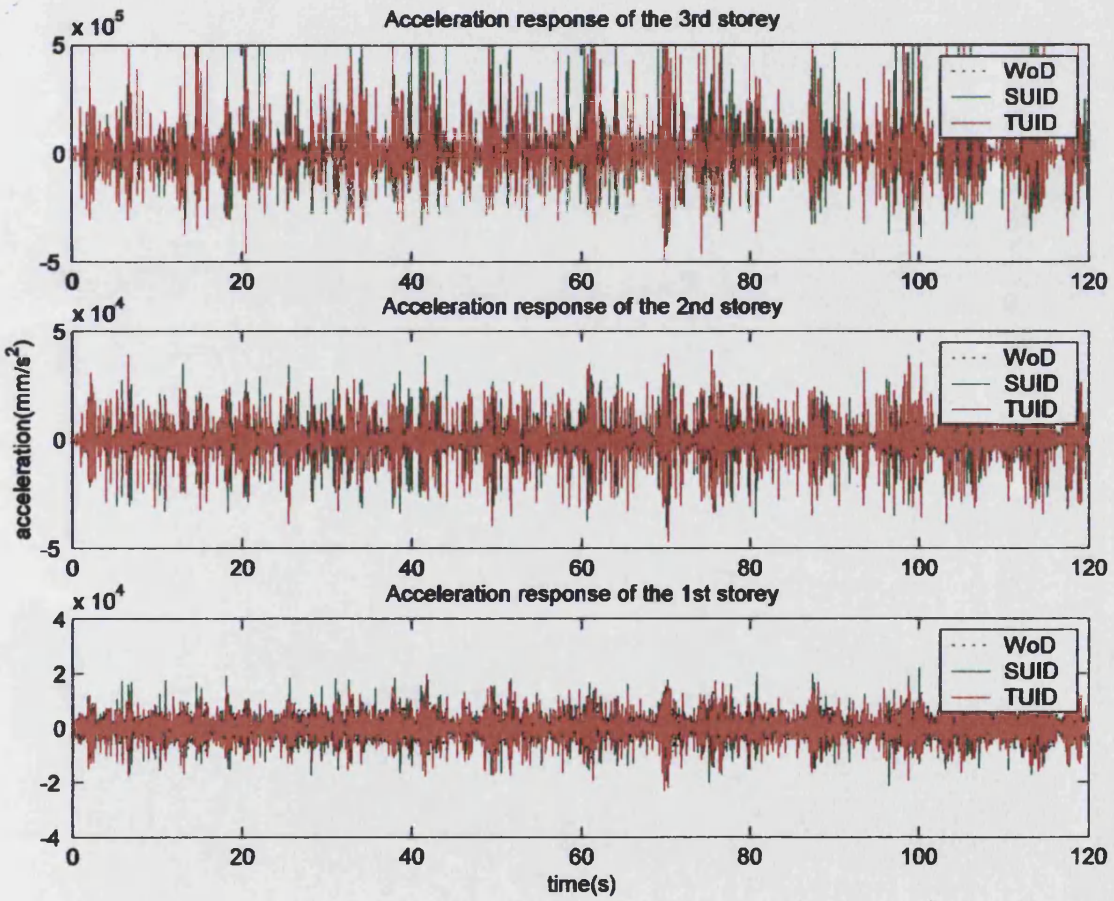


Figure 8.28: Time history of acceleration response (base random excitation)

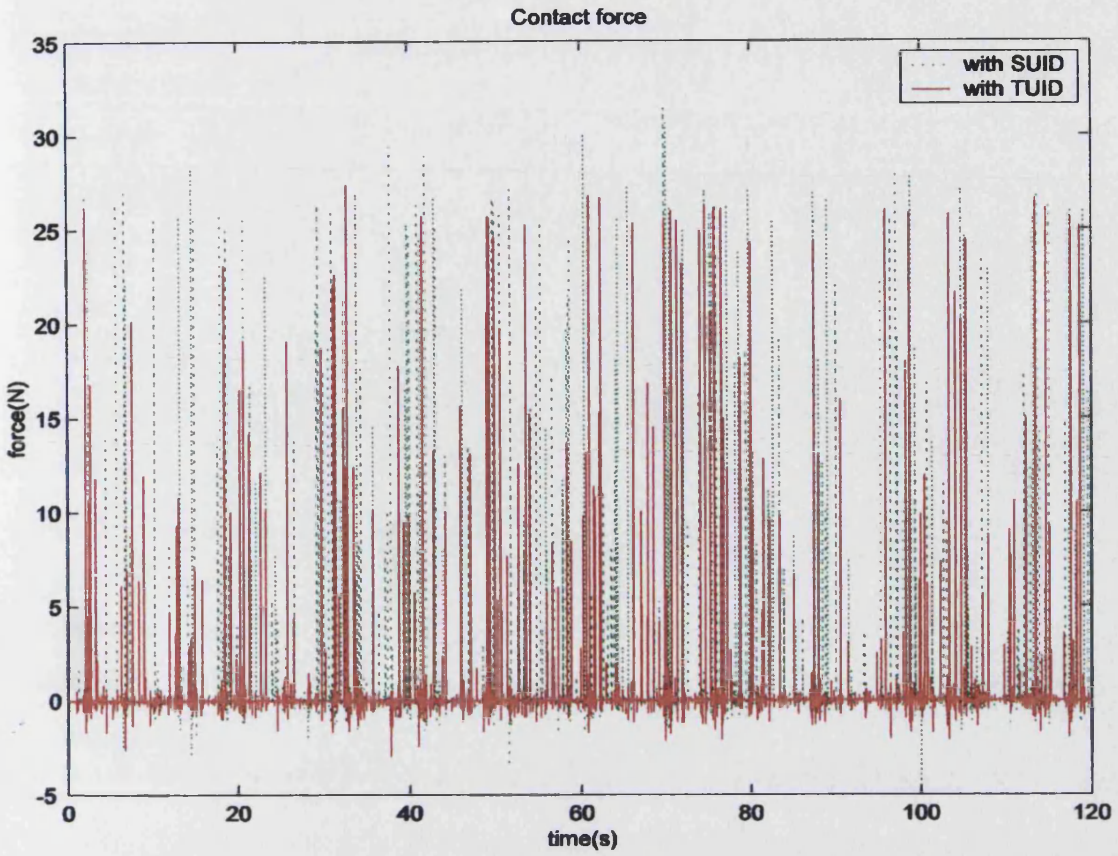


Figure 8.29: Contact force of SUID and TUID (base random excitation)

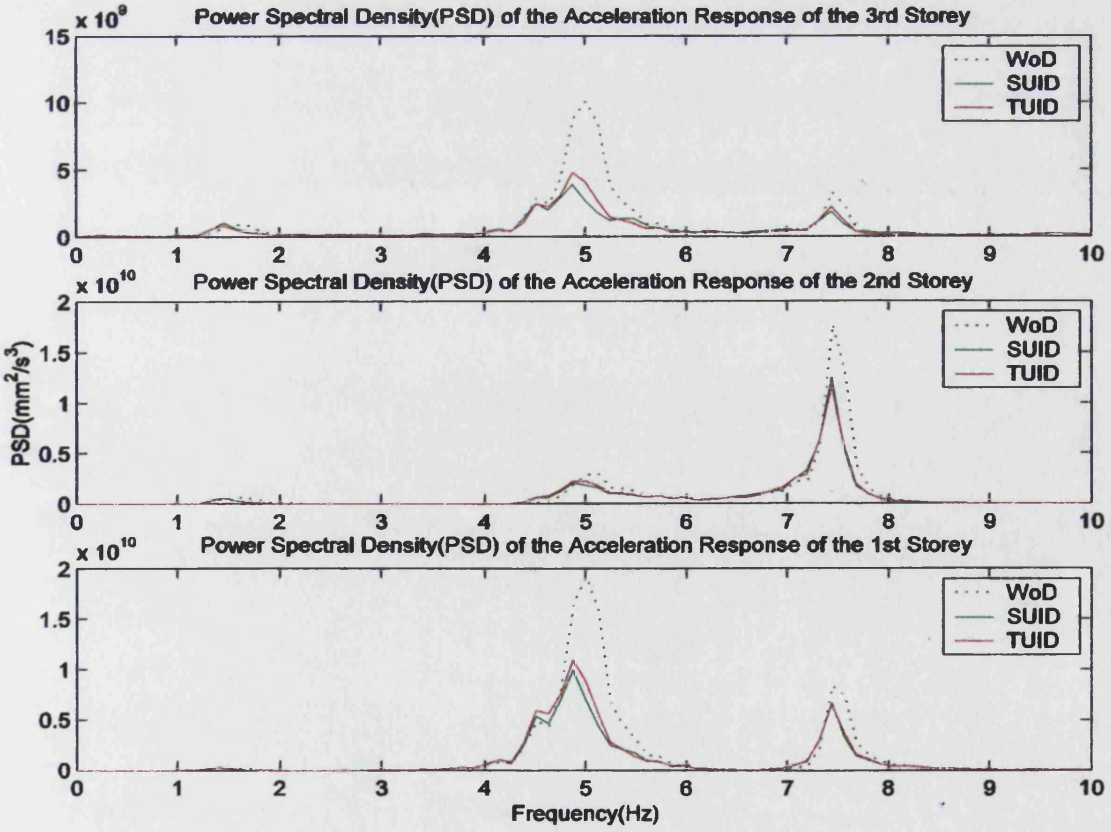


Figure 8.30: PSDs of acceleration response (base random excitation)

*8.2.3 Summary*

Experiments on a twin-unit impact damper compared with an equivalent single-unit impact damper show that the twin-unit impact damper retains the performance characteristics of the single unit impact damper, both good and bad. It appears not to be effective in reducing the high accelerations caused by collisions. This might be expected since, whatever the clearance, the motion of the impact masses remain synchronised with the motion of the structure. Thus impacts of each mass occur simultaneously with a similar overall impact force. It also appears not to be effective to use a twin-unit impact damper to reduce the contact force. Although some reduction in contact force can be achieved, there is not a significant reduction, although more, smaller masses will reduce the impact force further. It might be possible to achieve better control or reduced accelerations by increasing the number of masses, distributing the masses around the structure or by allowing impacts to occur between impact masses. Further investigation is required.

# Chapter 9

# Conclusions and Suggestions for Further Work

Introduction: Passive control devices are especially attractive for civil engineers to use for structural dynamic control, although other methods such as base isolation and active or semi-active control are also available. As a passive control device, an impact damper has the unique feature that it is synchronised to the excitation frequency, and a reduction in dynamic response can be achieved over a large excitation frequency range. At the outset of the project in 2001, issues concerning the use of impact dampers for MDOF structural control and problems associated with its application to civil engineering practice, such as high contact force; high accelerations and high level of noise caused by impacts had not been resolved. Overcoming these problems was the motivation behind this research. Significant progress has been made in this respect. The main conclusions drawn from the experimental, analytical and numerical investigations are as follows.

## 9.1 Conclusions

*State of the art in 2001*: Theoretical, analytical and experimental investigations on impact dampers have been reviewed. It is observed that most of the studies deal with the interaction of an impact damper with a SDOF primary structure, especially under sinusoidal excitation. In most cases, a civil structure, such as a multi storey building, would be subject to more varied environmental disturbances, such as wind loads and earthquakes, and can not be simplified as a SDOF system. To apply impact dampers to civil structural control, therefore, further understanding of the interaction between an impact damper and a MDOF primary structure under various types of excitation is required and practical issues associated with the application need to be addressed. The work presented in this thesis addresses the issues.

*Modelling of vibro-impact system:* The key to the modelling of the interaction between an impact damper and a primary structure lies in the modelling of the impact process itself. An impulse momentum model of impact has been employed in almost all previous studies on impact dampers. Such an approach inherently fails to take the deformation during contact and the contact time of impact into account, since the impulse momentum model stems from rigid body dynamics and is based on the assumption of an instantaneous collision. A spring-damper model of impact has

therefore been proposed in this work. The contact surface is modelled as a spring-damper pair. The stiffness and damping properties cannot be directly calculated from material properties due to the rapid rate of loading. However, a novel method for determining the parameters of the spring and damper has been developed based on experimentally measured contact time and coefficient of restitution. This model can automatically take the deformation during a collision and the contact time of impact into account quantitatively. With the spring-damper model of impact, the governing equations of motion of the primary structure (either SDOF or MDOF) under various types of excitation have been developed. Unlike the model developed with the impulse momentum model of impact, where the governing equations are applicable only between impacts, the governing equations with the spring damper model of impact are valid both during the impact process and between impacts. Therefore, the accurate timing of impacts becomes unnecessary in numerical simulations with this model.

*Direct integration of the differential equation of motion:* Only in a few simple cases, such as for a SDOF primary structure under sinusoidal excitation, can an analytical solution of the governing equations of a vibro-impact system be found. For most cases, the equations must be solved numerically. A high precision direct (HPD) integration scheme has been described. To improve the efficiency and reliability of the method, modifications to this scheme have been made to form a variable time-step HPD scheme allowing cubic interpolation of the load. To solve the governing equations developed with the spring-damper model of impact, which are non-linear, even though the primary structure is linear, a high precision direct integration scheme for non-linear systems (HPD-NL) was developed for this work. Numerical examples demonstrate significant performance advantages of the HPD-NL scheme over the popular forth order Runge-Kutta explicit algorithm.

*Experimental system and control:* To carry out experimental studies, a shaking table and the associated test apparatus have been constructed. Signal generation, data acquisition and signal processing software were developed. To allow the shaking table to produce accurate movement, a PID controller was developed and incorporated into the experimental system. The good tracking ability and robustness of the controller have been demonstrated.

*Experimental investigation on an impact damper for MDOF structure control:* Experimental investigations on the effect of an impact damper on a MDOF primary system under free and various forms of forced vibration have been performed. In particular, the effects of the parameters of impact damper itself, such as mass ratio and clearance, upon damping efficiency and system dynamics have been investigated. The following points can be drawn from these investigations:

- With a properly designed impact damper, it is possible to control all modes of a MDOF primary system to a certain extent.
- Compared with higher modes, the control of the fundamental mode is more easily achieved and it is more tolerant of variations in damper parameters and excitation type.
- A higher mass ratio does not necessarily result in better control of modes other than the first mode.
- For certain parameters, the control effect on higher modes can be detrimental.
- The performance of an impact damper on the control of a MDOF primary structure is closely related to the parameters of the damper, the dynamics of the primary structure and the excitation. Therefore, the ability to simulate the response of the complete impact damper/MDOF system is a useful design tool.

Also clearly revealed by the experiments is one of the main issues associated with the application of impact dampers to civil engineering, namely, the high accelerations occurring at the moment of collision. They occur not only at the story where the impact damper is located, but may also occur at other storeys.

*Development and investigation of buffered impact dampers:* To reduce the contact force and the corresponding high accelerations and noise level of a conventional impact damper, a new type of impact damper, a buffered impact damper (BID) has been developed by introducing a buffer zone between the moving damper mass and the stop. The performance of a BID has been studied and compared with that of a conventional impact damper by an extensive experimental investigation on both SDOF and MDOF primary system under free and various forms of forced vibration. With a properly chosen buffer, the BID can not only significantly reduce the contact force, peak value of acceleration and noise generated by collisions but also substantially enhance the vibration control effect, making it ideal for many engineering applications, not only civil engineering applications. Tests on buffers of different materials and sizes together with experimental investigations on the contact characteristics of collision have been

performed. The damping mechanism of the BID has been explored and reasons for the improved control performance suggested. To simplify its use in engineering practice, a procedure for optimum buffer design has also been developed.

*Numerical simulation and comparison with experimental results:* To verify the simulation schemes, both the scheme based on the impulse momentum model of impact and the scheme based on the spring-damper model of impact, extensive simulations have been performed and compared with the experimental results conducted for this research. It is demonstrated that the numerical HPD algorithm is reliable and efficient. Comparing the two simulation schemes, for a conventional impact damper, both the simulation based on the impulse momentum model of impact and that based on the spring-damper model of impact work well since the impact time and deformation can reasonably be considered to be negligible. However, for a buffered impact damper, the simulation with the spring-damper model results in a substantially better match with the experimental results. Therefore, the advantages of the spring-damper model of impact over the impulse momentum model have been demonstrated. The accuracy of the method for determining the parameters of the spring-damper model has also been demonstrated. This simulation provides a tool for performance prediction and impact damper design.

## 9.2 Summary of contributions

1. A spring-damper model of impact is suggested. The parameters of the spring and damper can not be directly calculated. Previous studies have used a trial and error approach to match such an impact model with observed behaviour. In this research, a novel method has been developed to determine the parameters of the spring-damper model *a priori* by making use of the contact time and coefficient of restitution of impact, which can be obtained by experiments. The important feature of this model is that the contact time of impact and deformation during collision can be taken into consideration quantitatively. The conventional impulse momentum model of impact stems from rigid body dynamics with the assumption of instantaneous collision and, therefore, neither the deformation nor the contact time can be included. The spring-damper model is valid for modelling the collision between two objects of various materials (such as collision between two steel objects or collision between a steel object and a

very soft sponge material) whilst the impulse momentum model of impact can only result in a good approximation of behaviour for collisions between hard metal objects (such as two steel objects), since only in this case are both the deformation and the contact time very small. With the spring-damper model of impact, a mathematical model of a vibro-impact system has developed. This model is valid both during collisions and between collisions, not just between impacts, as the mathematical model based on the impulse momentum model of impact is. This results in a consistent framework for the whole simulation process.

2. A high precision direct integration scheme for non-linear systems (HPD-NL) has been developed and successfully applied in simulations based on the spring-damper model of impact.

3. An insight into applying an impact damper for the vibration control of a MDOF primary structure is offered by experimental investigations and numerical simulations.

4. A buffered impact damper has been developed and investigated. With the buffered impact damper, the inherent shortcoming of a conventional impact damper, i.e. the inevitable high accelerations and noise caused by collisions (which is the main issue associated with the use of impact dampers in civil engineering), can be eliminated. Moreover, the control effect is actually enhanced, which makes the buffered impact damper attractive in many other engineering applications.

5. The damping mechanism of the buffered impact damper has been explored and a procedure for the optimum design of a buffer has been suggested.

6. As a tool of performance prediction and impact damper design, a numerical simulation has been developed and verified by comparison with experimental results.

## 9.3 Suggestions for further work

*Improving on the spring-damper model of impact:* Both contact time and the coefficient of restitution are related to the impact velocity. However, the spring-damper model developed can not at present include the effect of impact velocity on contact time and the coefficient of restitution, although experiments have demonstrated that both can be taken as approximately constant within the velocity range experienced by an impact damper. To gain a further understanding of the relationship between contact time, coefficient of restitution and impact velocity, further work, both experimental and analytical, is required. This work could result in more accurate modelling of impact, which will not only improve the modelling and simulation of a vibro-impact system but also benefit other studies or applications related to impact processes. Another possible way to improve the spring-damper model of impact is the use of nonlinear spring and/or nonlinear damper. Both the spring and the damper in the present spring damper model are linear. The deformation, especially for collision between a hard (such as steel) object and a soft (such as the sponge buffer), could be significant and the strain rate could be very high since impact lasts only a short time. Therefore, nonlinearity in deformation might be expected, and, a nonlinear spring and/or damper could lead to a better model of impact. Moreover, a spring-damper model with nonlinear spring and/or damper could include the effect of impact velocity on contact time and coefficient of restitution. It should be pointed out that either improvement suggested above can easily be implemented in the simulation, since the mathematical model and the algorithm developed for the simulation have been validated for nonlinear systems.

*Design of impact dampers:* To make an impact damper more easily applied in engineering, easily usable design tools, such as formulae or design graphs, are still required, although simulations can be employed for performance prediction, parametric studies and design of impact dampers. It is difficult, if not impossible, to derive analytical formulae to decide the optimum parameters of an impact damper except for a few simple cases. A possible way to solve this problem is to forget the details of the system and make use of the overall dynamics of the system, such as dynamic compliance, X/F. Figure 9.1 presents the model of a vibro-impact system, where P represents the primary structure, the structure to be controlled. This can be a SDOF, a MDOF, or an infinite degree of freedom system. To simplify the description of this suggestion, the damper in the spring-damper pair for the modelling of impact is neglected temporarily.

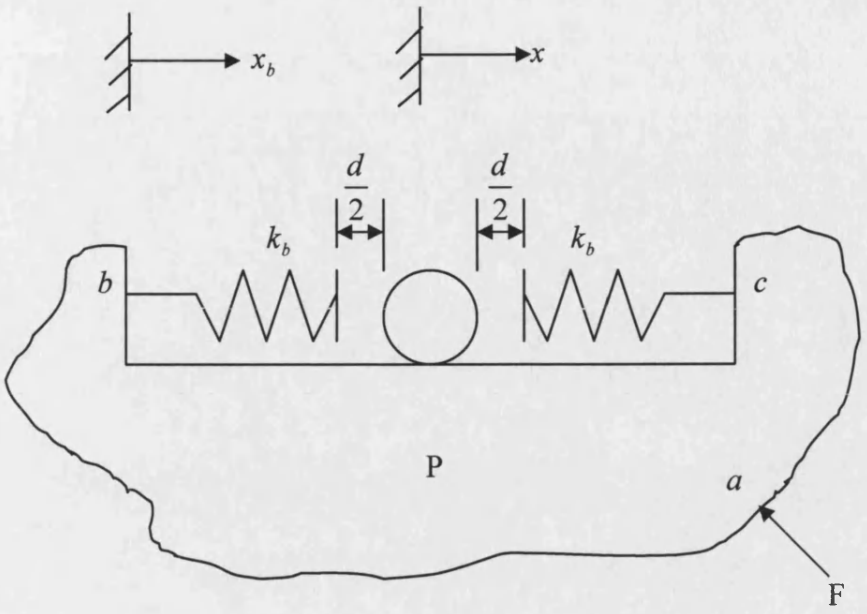


Figure 9.1: A general model of a vibro-impact system

The displacement of the damper mass can be expressed as:

$$x = F_b H_{00} + F_c H_{00} \tag{9.1}$$

and displacement at point b of the primary structure is:

$$x_b = F H_{ba} + F_b H_{bb} + F_c H_{cb} \tag{9.2}$$

where $H_{00}$ is the dynamic compliance from one end to the other end of the spring $k_b$, $H_{ba}$ is the dynamic compliance from *a* to *b*, $H_{bb}$ is the dynamic compliance from *b* to *b*, i.e. local compliance, and $H_{cb}$ is the dynamic compliance from *c* to *b*.

By denoting: $y = x_b - x$, $F_b$ and $F_c$ can be expressed as:

$$F_b = k_b (y - \frac{d}{2}) U(y - \frac{d}{2}) \tag{9.3}$$

$$F_c = k_b (y + \frac{d}{2}) U(-y - \frac{d}{2}) \tag{9.4}$$

where $U(\circ)$ is the Heaviside step function defined as:

$$U(\rho)=\begin{cases}0 & \rho \le 0\\ 1 & \rho > 0\end{cases} \tag{2.7}$$

The optimum design of the impact damper comes down to choosing the clearance $d$ to minimize the displacement $x_b$. The related dynamic compliances can be obtained by experiment or calculation. This may lead to a general solution for the design of impact dampers, especially solving the problem of optimization of clearances in different directions to achieve a good control effect whichever direction the primary structure vibrates (the differences in dynamics when the primary structure vibrates in different directions can be represented through the different dynamic compliances) .

*Further study on the application of impact damper:* Although impact dampers have been used on many occasions for vibration control, further efforts to widen its application are still needed. The following are some suggestions for further application of impact dampers.

- Impact dampers should be applied to real civil structures or full-scale test structures to investigate its performance, especially its performance on vibration control in different lateral directions, such as $x$ direction and $y$ direction as shown in Figure 9.2. This will also provide a platform to test findings from small scale experimental study and validating design methods for impact damper.

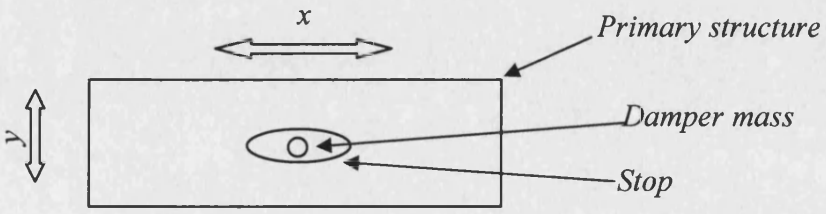


Figure 9.2: Impact damper for control of vibration in different direction

- A group of impact dampers could control torsion vibration, as sketched in Figure 9.3. Setting several impact damper units symmetrically to form an impact damper group may form an efficient and simple torsional vibration absorber. It can retain the unique feature of impact dampers, i.e. synchronisation with the excitation frequency and thus, attenuation over a large frequency range.

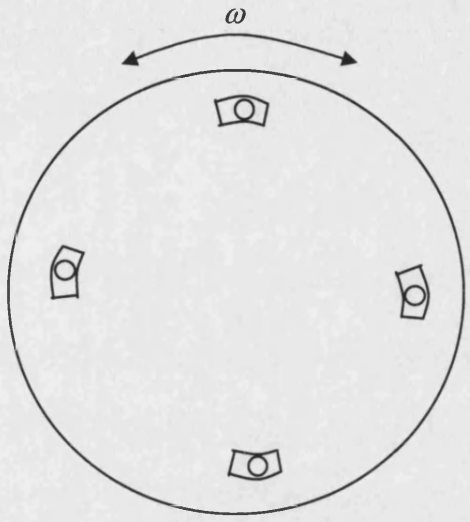


Figure 9.3 Impact damper group for torsion vibration control

- Buffered impact dampers could be applied to mechanical, aeronautical and many other engineering systems for vibration control. It has been demonstrated that buffered impact dampers can not only eliminate the inherited disadvantage of conventional rigid impact damper, i.e. high contact force and associated high accelerations and noise level caused by collision, but also significantly enhance vibration control effect. This is attractive for many engineering applications. The significant advantages of buffered impact dampers should be thoroughly employed, for example, using a buffered impact damper to replace the conventional impact damper for chatter vibration control of machine tools. Moreover, the principle of buffered impact dampers can also be used to improve pile-driving techniques, ground moling and so on.

# Appendix

## Test Point file of the PID controller

*Action list of the Start button:*

**1) Clear Errorvector** % **Errorvector** is a container used for store the error
% vector

**2) Clear Errorlaststep** % **Errorlaststep** is a container used to store the error of
% last step

**3) Set Zero to *0*** % set the value of variable **Zero** to *0*

**4) Input from DisD** % **DisD** is a file in which the data of a reference signal,
% such as the displacement of an earthquake record, is
% stored

**5) Append to Errorvector from Zero** % the error at he first step is supposed to be *0*

**6) Start A/D A/D1 samples =127960 , rate=2000 Hz, Channel(s)=0,1,2,3,4,5, event after 40 samples** % set the parameters of sampling for A/D

*Action list of A/D 1*

**1) Calculate step** % record the steps

**2) Calculate Expect with V3=DisD, aa= step** % in $i^{th}$ step, pick out the $i^{th}$ data (number)
% from the vector **DisD**
% **Expect**=index(V3,aa)

**3) Calculate MeasuredV with V4=A/D1** % pick out the measured displacement (in
% voltage at the moment)
% **MeasuredV**=index(select(V4,0),39)
% The displacement signal of the shaking
% table is acquired through Channel 0

**4) Calculate MeasuredD with V5= MasuredV** % turn voltage into mm
% **MeasuredD**=(V5-2.095)*150/4.19

**5) calculate ErrorD with V6= Expect,** **% ErrorD=-V5+V6**

**V7= MeasuredD**

**6) Append to Errorvector from ErrorD** **% Errorvector** get a new element (add to

% the end)

**7) Calculate Sumerror with Ver=** % Calculate the sum of error

**Errorvector** % **Sumerror**= sum(**Ver**)

**8) calculate ControlV1 with K3= P control** % P Control is a slider. It provide a

**ErrorD=ErrorD** % value for k3

**9) Calculate ControlV2 with K4= I control,** % **ControlV2=K4*Sumerr**/60

**Sumerr=Sumerror**

**10) calculate ControlV with CV1=ControlV1,** % **ControlV=CV1+CV2**

**CV2=ControlV2**

**11) Output D/A D/A1 once Channel=0, value=** % output corrected voltage

**ControlV**

**12) Add points to Graph1 from Expect,** % display the reference signal and

% measured signal

**MeasuredD**

Note: 1) the A/D data from all cannels are sent to a file

2) the DC voltage required by the displacement sensor is provided by hardware, not by D/A channel 1

## Reference


1. R.I. Skinner, W.H. Robinson and G.H. McVerry (1993) *An Introduction to Seismic Isolation*. John Wiley & Sons Ltd, Chichester, England
2. K. Li and A.P. Darby (2002) Unevenly modulated non-stationary seismic response of structure with isolation base. *Proc. of 12th European earthquake engineering conference*, CD-ROM Paper, paper no. 850, London
3. T.T. Soong and G.F. Dargush (1996) *Passive Dissipation Systems in Structural Engineering*. John Wiley & Sons Ltd, Chichester, England
4. A. Filiatrault (1990) Analytical predictions of the seismic response of friction damped timber shear walls. *Earthquake Engrg. Struct. Dyn.* **19**, 259-273
5. N. Makris and J. Zhang (1995) Dynamic analysis of visco-elastic fluid dampers. *J. of Engineering Mechanics. ASCE*, **121**(10), 1114-1121
6. R.J. McNamara (1997) Tuned mass damper for buildings *J. of Engineering Mechanics. ASCE*, **103**(9), 1785-1789
7. R.E. Roberson (1952) Synthesis of a non-linear vibration absorber. *J. of the Franklin Institute* **254**, 205-220
8. M.C. Constantinou (1998) Passive energy dissipation systems for structural design and retrofit. *Monograph series*, Vol. 1, Multidisciplinary centre for earthquake engineering research
9. A.L. Paget (1937) Vibration in steam turbine buckets and damping by impact, *Engineering* **143**, 305-307
10. J. B. Hunt (1979) *Dynamic Vibration Absorber*, Mechanical Engineering Publication LTD, London
11. M.M Sadek. (1965) The behaviour of the impact damper, *Proc. Instn mech. Engrs*, **180**, 895-906
12. P. Lieber and D.P. Jensen (1945) An acceleration damper: development, design, and some application. *Trams Am. Soc. Mech. Engrs.* **67**, 523-530
13. C. Grubin (1956) On the theory of the acceleration damper. *J. of Appl. Mech.* **23**, 373-378
14. R.N. Arnold (1956) The acceleration damper. *Proc. of international conference of applied mechanics*. 367-372

15. G.B. Warburton (1957) On the theory of the acceleration damper. *J. Appl. Mech.* **24**, 322-324
16. S.F. Masri and T.K. Caughey (1966) On the stability of the impact damper. *J. Appl. Mech. ASME*, **33**, 586-592
17. D.M. Egle (1967) An investigation of an impact vibration absorber. *J. of engineering for industry.* **89**, 653-661
18. M.M. Sadek (1966) The behaviour if the impact damper. *Proc. of the institution of mechanical engineers.* **180**, 895-906
19. S.F. Masri (1970) General motion of impact dampers. *J. of the Acoustical Society of America.* **47**, 229-237
20. C.N. Bapat and N. Popplewell (1983) Stable periodic vibroimpacts of an oscillator. *J. of sound and vibration.* **87**(1), 41-59
21. C.N. Bapat (1995) The general motion of an inclined impact damper with friction. *J. of Sound and Vibration* **184**(3), 417-427
22. Xu Zhiwei (1999) Simulation of vertical impact damper system (in Chinese). *J. of Xian Jiaotong University.* **7**, 66-70
23. M.C. Thomas (1974) The effectiveness of the impact damper with a spring-supported auxiliary mass. *J. of Mechanical Engineering Science.* **16**, 109-116
24. C.N. Bapat (1998) Periodic motion of an impact oscillator. *J. of sound and vibration.* **209**(1), 43-60
25. C.N. Bapat and S. Sankar (1985) Multiunit impact damper—re-examined. *J. of sound and vibration.* **103**(4), 457-469
26. M.M. Nigm and A.A. Shabana (1983) Effect on an impact damper on a multi-degree of freedom system. *J. of sound and vibration.* **89**(4), 541-557
27. S.F. Masri (1973) Response of impact damper to stationary random excitation. *J. of Acoust. Soc. Amer.* **53**, 200-211
28. S. Aoki (2000) Effect of impact vibration absorber with hysteretic damping to earthquake excitation. *Proc. of 12$^{th}$ world conference on earthquake engineering.* Auckland, New Zealand
29. S. Ma and S.E. Semercigil (1997) A modified passive tuned absorber for secondary system under random excitation. *J. of sound and vibration.* **208**(3), 349-366
30. Goldsmith and Werner (1960) *Impact*, Edward Arnold Publishers, London

31. M. Fandrich (1998) Modelling non-destructive impacts macroscopically. *J. of Mathl. Comput. Modelling.* Vol. 28, No. 4-8, pp. 205-224
32. D. Gugan (2000) Inelastic collision and the Hertz theory of impact, *American Journal of Physics,* Vol. 68, No. 10, pp. 920-924
33. O.R. Walton (1983) Particle-dynamics calculation of shear flow, In *Mechanics of Granular Materials: New Models and Constitutive Relations,* pp. 327-338, Elsevier Science
34. S.F. Masri (1972) Theory of dynamic vibration neutralizer with motion-limiting stops. *J. of Applied Mechanics, ASME,* **39**, 563-568
35. C.N. Bapat and N. Popplewell (1983) Stable periodic motions of an impact-pair. *J. of Sound and Vibration* **87**, 19-40
36. E.H. Dowell (1982) Flutter of a buckled plate as an example on chaotic motion of a deterministic autonomous system. *J. of Sound and Vibration* **85**, 333-344
37. S.W. Shaw (1983) Periodically forced linear oscillator with impacts: Chaos and long period motions. *Physical review letters.* **51**, 623-626
38. G.S. Whiston (1987) The vibro-impact response of a harmonically excited and pre loaded one-dimensional linear oscillator. *J. of Sound and Vibration* **115**, 303-319
39. C.K. Sung and W.S. Yu (1992) Dynamics of a harmonically excited impact damper: bifurcation and chaotic motion. *J. of Sound and Vibration* **158**(2), 317-329
40. F. Peterka (1992) Transition to chaotic motion in mechanical systems with impacts. *J. of Sound and Vibration* **154**(1), 95-115
41. F. Peterka (2001) Vibro-Impact Systems. Chapter in *Encyclopaedia of Vib*ration. Vol. 3, pp. 1531-1548, Academic Press Ltd, London
42. M.D. Thomas, W.A. Knight and M.M. Sadek (1975) The impact damper as a method of improving cantilever boring bars. *J. of Engineering for Industry, ASME* **87**, 859-866
43. P. Hong (1992) A passive controller for the flexible robot arm. *Proc. of the Engineering Systems Design and Analysis Conference*, ASME, Vol. 47-1 192-202 Istanbul, Turkey,
44. L. Jo (1989) Development of highway light pole with resistance to wing vortex-induced oscillations. *Kawasaki Steel Technical Report*, **21**, 86-94
45. S.F. Masri S. F. Analytical and experimental studies of multi-unit impact dampers. *J. of the Acoustical Society of America* Vol.45 No.5 1111-1117

46. S. Ekwaro-orsire and I.C. Desen (2001) Experimental study on an impact vibration absorber. *J. of Vibration and Control* **7**, 475-493
47. F.S. Collette (1998) A combined tuned absorber and pendulum impact damper under random excitation. *J. of Sound and Vibration* **216**(2), 199-213
48. S.E. Semercigil, F.S. Collette and D. Huynh (2002) Experiments with tuned absorber-impact damper combination. *J. of Sound and Vibration* **256**(1), 179-188
49. N. Popplewell and S.E. Semercigil (1989) Performance of the bean bag impact damper for a sinusoidal external force. *J. of Sound and Vibration* **133**(2), 193-223
50. Y. Araki, Y. Yuhki, I. Yokomichi and Y. Jinnouchi (1985) Impact damper with granular materials. *Bulletin of JSME*, Vol. 28, No. 240 1121-1217
51. A. Papalou and S.F. Masri (1996) Performance of particle dampers under random excitation. *J. of Vibration and Acoustics, ASME* Vol.118 615-621
52. G.R. Tomlinson, D. Pritchard and R. Wareing (2001) Damping characteristics of particle dampers—some preliminary results. *Proc Instn Mech Engrs* Vol. 215 Part C, pp. 253-257
53. L.B. Erlikh (1952) Vibration absorber with impact action and its use in machine tools. *Stanki instru.*, No.7 17-19
54. W.H. Reed (1967) Hanging chain impact dampers: A simple method of damping tall, flexible strictures. *Wind Effects on Buildings and Structures* (Proceedings of international research Seminar, Ottowa), **2**, 283-321
55. K. Ogawa T. Ide and T. Saitou (1997) Application of impact mass damper to a cable-stayed bridge pylon. *J. of Wind Engineering and Industrial Aerodynamics.* **72**, 301-312
56. S. Ema and E. Marui (2000) Suppression of chatter vibration off boring tools using impact dampers. *International Journal of Machine Tools and Manufacture* Vol.40 No.8 ,1141-1156
57. A.S. Velichkovich and S.V. Velichkovich (2001) Vibration-impact damper for controlling the dynamic drillstring conditions. *Chemical and Petroleum Engineering.* Vol.37, No.3/4, 213-215
58. A. Benamar (2000) Dynamic pile response using two pile-driving techniques. *J. of Soil Dynamics and Earthquake Engineering.* **20**, 243-247
59. M. Wiercogroch (1999) Material removal rate predition for ultrasonic drilling of hard materials using impact oscillator approach. *Physics Letters A.*: **259**(2), 91-96

60. E. Pavlovskaia, M. Wiercigroch, K.C. Woo and A.A. Rodger (2003) Modelling of ground moling dynamics by an impact oscillator with a friction slider. *Meccanica*, Vol. 38, No.1, 85-97
61. H. Dittrich (1966) Unterschungen uber einen unstetig arbeitenden stosschwingungsdampfer. Ing.-Arch., **35**, 150-171
62. N. Popplewell and M. Liao (1991) A simple design procedure for optimum impact dampers. *J. of Sound and Vibration* **146**(3), 519-526
63. S. Chatterjee, A.K. Mallik and A. Ghosh (1995) On impact dampers for non-linear vibration systems. *J. of Sound and Vibration* **187**(3), 403-420
64. S. Chatterjee, A.K. Mallik and A. Ghosh (1996) Impact dampers for controlling self-excited oscillation. *J. of Sound and Vibration* **193**(5), 1003-1014
65. W. Zhong and F.W. Williams (1990) Computational structural mechanics optimal control and semi-analytical methods for PDE. *Computers and Structures.* **37**, 993-1004
66. J. Lin, W. Shen and F.W. Williams (1995) A high precision direct integration scheme for structures subject to transient dynamic loading. *J. of computer and structure* **56**, 113-120
67. J. Pang (1982) *Practice Problems in Vibration* (in Chinese). Tinhua University Press, Beijing
68. K.J. Bathe and E.L. Wilson (1976) *Numerical Methods in Finite Element Analysis*, Prentice-Hall, Englewood Cliffs, N.J.
69. P.B. Bornemann, U. Galvanetto and M.A. Crisfield (2002) Some remarks on the numerical time integration of non-linear dynamical systems. *J. of Sound and Vibration* **252**(5), 935-944
70. Y.M. Xie (1996) An assessment of time integration schemes for non-linear dynamic equations. *J. of Sound and Vibration* **192**(1), 321-331
71. P.D. Stoten and E. Gomez (1998) Progress on the adaptive control of shaking table. *11th European Conference on Earthquake Engineering (XI ECEE)*, CD-ROM paper, Balkema, Rotterdam
72. T.H. Chen and C.M. Liaw (1999) Vibration acceleration control of an inverter-fed electrodynamic shaker. *IEEE/ASME Transaction on Mechatronics*, Vol. 4, No. 1, 60-70

73. K.Y. Swarop, K. Ahsan, K. Scott and L.K. Fred (2001) Dynamic load simulator: development of a prototype. *J. of Engineering Mechanics. ASCE*, Vol. 127, No. 12, 1310-1315

74. M.J. Hochrainer , C. Adam, R. Heuer and F. Ziegler (2000) A novel experimental setup to model earthquake excited elastic-pastic structures. *Proc. of 12th World Conference on Earthquake Engineering (12WCEE),* CD-ROM paper, paper no. 0835, Auckland, New Zealand.

75. K. Wei, Y. Wang and Z. Chen (1997) *MATLAB and the design of control systems (in Chinese).* Mechanical Industry Press, Beijing

76. C.N. Bapat and S. Sankar (1985) Single unit impact damper in free and forced vibration. *Journal of Sound and Vibration*, **99**, 885-894

77. S.F. Masri (1969) Analytical and experimental studies if multiunit impact dampers. *J. of the Acoustical Society of America*, **45**, 1111-1117

78. C.N. Bapat and S. Sankar (1985) Multiunit impact damper—re-examined. *J. of Sound and Vibration* **103**(4), 457-469

79. A. Papalou and S.F. Masri (1996) Performance of particle dampers under random excitation. *Journal of Vibration and Acoustics* **118**, 615-621.

80. S.E. Olsen (2003) An analytical particle damping model. *Journal of Sound and Vibration* **264**, 1155-1166.

81. C.C. Chen and J.Y. Wang (2003) Free vibration analysis of a resilient impact damper. *International Journal of Mechanical Science* **45**, 589-604.

82. L. Meirovitch (1996) Elements of Vibration Analysis, McGraw-Hill, New York

83. D.A. Peters (1997) Optimum spring-damper design for mass impact, *Society for Industrial and Applied Mathematics Review* (SIAM REV.) Vol.39, No. 1,118-122